# University of Nottingham
UK | CHINA | MALAYSIA

# Hybrid Gamma Camera Imaging: Translation from Bench to Bedside

*A thesis submitted to the University of Nottingham for the degree of*

## Doctor of Philosophy

*by*

# Aik Hao Ng
*MMed.Phys.*

Radiological Sciences, Division of Clinical Neuroscience, School of Medicine

**September 2017**

# Declaration

I, Aik Hao Ng declare that the work presented in this thesis is my own original work based on the research undertaken during my PhD study period unless otherwise referenced or acknowledged.

*"Life is like riding a bicycle.*
*To keep your balance, you must keep moving."*

*- Albert Einstein*

# Abstract

There is increasing interest in the use of small field of view (SFOV) portable gamma cameras in medical imaging. A novel hybrid optical-gamma camera (HGC) has been developed through a collaboration between the Universities of Leicester and Nottingham. This system offers high resolution gamma and optical imaging and shows potential for use at the patient bedside, or in the operating theatre. The aim of this thesis was to translate the HGC technology from *in vitro* laboratory studies to clinical use in human subjects.

Pilot studies were undertaken with the HGC as part of this thesis. Furthermore, efforts have been made to transform the HGC technologies into a new medical device, known as Nebuleye. Initial physical evaluation of the pre-production prototype camera was carried out as part of the device developmental process, highlighting some aspects of the design that require further modification. A complete and rigorous testing scheme to assess the pre-production prototype camera has been developed and successfully implemented. The newly introduced tests enabled the system uniformity, system sensitivity, detector head shielding leakage, optical-gamma image alignment and optical image quality of the hybrid camera to be assessed objectively. This harmonised testing scheme allows characterisation and direct comparison of SFOV gamma cameras.

*In vitro* and *in vivo* preclinical imaging was undertaken to examine the performance of the SFOV gamma cameras for experimental animal studies. The results of animal study have shown for the first time the feasibility and performance of these SFOV gamma cameras for imaging mice injected with a newly developed $^{111}$In labelled hybrid tracer. Further investigations are needed to improve the system resolution and prepare the camera system for combined gamma-near infrared fluorescence imaging in future.

A systematic *in vitro* laboratory assessment method has been established to examine the imaging performance of the SFOV gamma camera in radioguided sentinel lymph node biopsy (SLNB) and radioactive seed localisation procedures for breast cancer surgery. Further preparatory work was undertaken to carry out a pilot clinical trial of

the use of the pre-production prototype camera in sentinel node localisation procedures during breast cancer surgery. The clinical study protocol and routine quality control procedures have been established and are suitable for future use. Baseline data on the camera performance assessed using the routine quality control scheme have been obtained.

Finally, the capabilities of the SFOV gamma camera were assessed. This has provided baseline data on user feedback and the imaging consequences on operator motion effects, as well as examining the detectability of a range of radionuclides, including $^{99m}$Tc, $^{111}$In, $^{123}$I, $^{125}$I and $^{75}$Se. The first clinical results of the use of the HGC in clinical hybrid optical-gamma imaging in patients administered with $^{99m}$Tc and $^{123}$I labelled radiopharmaceuticals have been reported. This clinical study has demonstrated the feasibility and capability of HGC in various clinical applications performed at the patient bedside, which included patients undergoing bone, thyroid, lacrimal drainage and lymphatic imaging as well as DaTscan studies.

In conclusion, the work in this thesis has demonstrated the successful translation of an SFOV hybrid gamma camera for clinical use. This system would be ideally suited for use in the operating theatre for radioguided procedures such as sentinel node detection and tumour localisation. This system also offers potential for use with the new generation of hybrid fluorescent-radionuclide tracers currently under development.

# Acknowledgements

In autumn 2013, I left my comfort zone, full with family and friends love, and the nice hot weather that I am familiar with, to a four seasons country to embark on my PhD journey. From that time point, I knew it would be a tough doctoral world, from settling my family and myself in the new environment, to the discovery of sciences in my study field. I consider myself very fortunate indeed to have the opportunity to meet so many wonderful people and have had an enriched life experience in the United Kingdom. There are many organisations or people whom I would like to express my sincere gratitude for their help and support along my PhD journey.

Firstly, I would like to thank my three supervisors, Professor Alan C. Perkins, Professor John E. Lees and Professor Paul S. Morgan for sharing their knowledge and experiences. Without their advice and guidance, this thesis would not be possible. I am fortunate to have had the opportunity to work with Professor Alan C. Perkins, an experienced leader in the world of nuclear medicine. He has been a wonderful mentor, supervisor and friend. His broad knowledge and experience in medical physics as well as his patience in imparting wisdom to me are inspirational. Thanks for giving me the opportunities to extend my professional horizon in regional research collaboration. I also express my heartfelt gratitude to him for the time and effort he had to spend to discuss, proofread and correct my thesis.

I would like to thank Professor John E. Lees for his generosity and kindness in sharing his vast knowledge and expertise in the Hybrid Gamma Camera (HGC) technology and loaning me the camera and other necessary equipment for my experimental work. His enormous efforts in innovation and strong leadership has led the research team to develop a better camera for patient benefit. I would also like to thank Professor Paul S. Morgan for his advice and help with the image processing work and the use of MOCO software used in the operator motion effect study. He is a good friend and supervisor who provides continuous support and guidance whenever I needed during my study.

Secondly, I would like to thank the colleagues from Space Research Centre, University of Leicester that worked together on this camera development and clinical trial, who

for the HGC to be used in the clinical trial at NUH NHS Trust. I would also like to thank Jennifer Poveda, Mark Westby, Nick Gibson, Graham Love and Elizabeth Powell for their technical support.

During my short trip to LUMC, I had the opportunity to work with Marieke Stammes, Hein Handgraaf and Pauline. Thanks for their hospitality and providing necessary research facilities for the preclinical imaging, including the mice with tumour model and the probe.

I am grateful to Gamma Technologies Limited and Xstrahl Limited (Surrey, UK) for lending me the pre-production prototype Nebuleye, to LabLogic Systems Ltd. (Sheffield, UK) for allowing me to use CrystalCam gamma camera and to GE Healthcare (Arlington Heights, IL, USA) for providing the $^{125}$I seeds.

I would like to express my gratitude and appreciation to the Ministry of Health and the Government of Malaysia for providing my PhD scholarship. Thanks to my colleagues in the MOH for your support and friendship.

To my fellow office mates and friends: Thanks to everyone for sharing your laughter and support, in particular Dewen, Will, Stefan and Tom.

Last but not least, I am extremely thankful to my family for their endless encouragement, care, trust and love. To my wonderful wife Hwee Shin, my adorable kids Qian, Thong and Isaac, thanks for being together with me in a place called home. In particular to my wife, thanks for standing by me through thick and thin, sharing your love and care and undergoing our PhD journey together.

# Table of contents

# List of Figures

# List of Tables

# List of Abbreviations

A list of acronyms and abbreviations used in this thesis is given as follows:

| | |
|---|---|
| $^{111}$In | Indium-111 |
| $^{123}$I | Iodine-123 |
| $^{125}$I | Iodine-125 |
| 2-D | two-dimensional |
| 3-D | three-dimensional |
| $^{99m}$Tc | Technetium-99m |
| BCS | breast conserving surgery |
| CCD | charge-coupled device |
| CE | "Conformité Européene" which means "European Conformity" |
| CGC | Compact Gamma Camera |
| CNR | contrast-to-noise ratio |
| COM | centre of mass |
| CoV | coefficient of variation |
| cps | count per second |
| CRF | case report form |
| CsI(Tl) | thallium doped cesium iodide |
| CT | computed tomography |
| D | depth |
| DICOM | Digital Imaging and Communications in Medicine |
| DU | differential uniformity |
| EMCCD | electron multiplying charge-coupled device |
| ERF | edge response function |
| eV | electron volt |
| FFD | fixed focal distance |
| FWHM | full width at half maximum |
| GTL | Gamma Technologies Limited |
| H | height |
| HGC | Hybrid Gamma Camera |
| HRA | Health Research Authority |

| | |
|---|---|
| HRGI | High Resolution Gamma Imager |
| IP | intellectual property |
| IPEM | Institute of Physics and Engineering in Medicine |
| IPSD | intensified position-sensitive diode |
| IS | injection site |
| IU | intrinsic uniformity |
| kcps | kilo counts per second |
| L | length |
| LEGP | low energy general purpose |
| LEHR | low energy high resolution |
| LFOV | large field of view |
| LSF | line spread function |
| MAPMT | multi-anode photomultiplier tube |
| MBq | megabecquerel |
| MGRC | Mini Gamma Ray Camera |
| MHRA | Medicines and Healthcare products Regulatory Agency |
| MIBG | metaiodobenzylguanidine |
| MRI | magnetic resonance imaging |
| ND | node depth |
| NHS | National Health Service |
| NIR | node-to-injection site activity ratio |
| NIRF | near-infrared fluorescence |
| NS | node-to-injection site separation |
| OSEM | ordered subset expectation maximisation |
| PET | positron emission tomography |
| PIS | patient information sheet |
| PMMA | polymethyl-methacrylate |
| PMT | photomultiplier tube |
| PSF | point spread function |
| PSPMT | position-sensitive photomultiplier tube |
| RGB | red green blue |
| ROLL | radioguided occult lesion localisation |
| RSL | radioactive seed localisation |

| | |
|---|---|
| SCD | source-to-collimator distance |
| SFOV | small field of view |
| SLN | sentinel lymph node |
| SLNB | sentinel lymph node biopsy |
| SNOLL | sentinel node and occult lesion localisation |
| SPECT | single photon emission computed tomography |
| SSD | source-to-camera surface distance |
| UV | ultraviolet |
| W | width |
| WGL | wire guided localisation |

# List of Publications

1. **A.H. Ng**, P.E. Blackshaw, M.S. Alqahtani, L.K. Jambi, S.L. Bugby, J.E. Lees, and A.C. Perkins. 2017. A novel compact small field of view hybrid gamma camera: first clinical results. Nucl Med Commun, 38(9): 729-736.

2. M.S. Alqahtani, J.E. Lees, S.L. Bugby, P. Samara-Ratna, **A.H. Ng**, and A.C. Perkins. 2017. Design and implementation of a prototype head and neck phantom for the performance evaluation of gamma imaging systems. EJNMMI Physics, 4(1): 19.

3. J.E. Lees, S.L. Bugby, M.S. Alqahtani, L.K. Jambi, N.S. Dawood, W.R. McKnight, **A.H. Ng**, and A.C. Perkins. 2017. A Multimodality Hybrid Gamma-Optical Camera for Intraoperative Imaging. Sensors (Basel), 17(3).

4. A.C. Perkins, **A.H. Ng**, and J.E. Lees. 2017. Small Field of View Gamma Cameras and Intraoperative Applications, in Gamma Cameras for Interventional and Intraoperative Imaging, A.C. Perkins and J.E. Lees, Editors. CRC Press (Taylor & Francis Group): Boca Raton, FL.

5. L.K. Jambi, J.E. Lees, S.L. Bugby, B.S. Bhatia, M.S. Alqahtani, W.R. McKnight, N.S. Dawood, **A.H. Ng** and A.C. Perkins. 2016. Comparison of columnar and pixelated scintillators for small field of view hybrid gamma camera imaging. IEEE Nuclear Science Symposium and Medical Imaging Conference (NSS/MIC), Strasbourg, France. In Press.

6. S.L. Bugby, J.E. Lees, **A.H. Ng**, M.S. Alqahtani, and A.C. Perkins. 2016. Investigation of an SFOV hybrid gamma camera for thyroid imaging. Phys Med, 32(1): 290-296.

7. **A.H. Ng**, D. Clay, P.E. Blackshaw, S.L. Bugby, P.S. Morgan, J.E. Lees, and A.C. Perkins. 2015. Assessment of the performance of small field of view gamma cameras for sentinel node imaging. Nucl Med Commun, 36(11): 1134-42.

8. J.E. Lees, S.L. Bugby, B.S. Bhatia, L.K. Jambi, M.S. Alqahtani, W.R. McKnight, **A.H. Ng**, and A.C. Perkins. 2014. A small field of view camera for hybrid gamma and optical imaging. Journal of Instrumentation, 9(12): C12020.

# List of Conference Abstracts

1.  J.E. Lees, S.L. Bugby, M.S. Alqahtani, L.K. Jambi, N.S. Dawood, W.R. McKnight, B.S. Bhatia, **A.H. Ng** and A.C. Perkins. 2017. Hybrid gamma camera for medical applications. PSD11: 11th International Conference on Position Sensitive Detectors, Milton Keynes, UK.

2.  L.K. Jambi, J.E. Lees, S.L. Bugby, M.S. Alqahtani, B.S. Bhatia, W.R. McKnight, N.S. Dawood, **A.H. Ng** and A.C. Perkins. 2017. A hand-held hybrid gamma-near-infrared fluorescence imaging camera. Society of Nuclear Medicine and Molecular Imaging (SNMMI) Annual Meeting, Denver, USA. Abstract in:  J Nucl Med 58, supplement 1: 220.

3.  M.S. Alqahtani, J.E. Lees, S.L. Bugby, L.K. Jambi, B.S. Bhatia, W.R. McKnight, N.S. Dawood, **A.H. Ng** and A.C. Perkins. 2017. Capability of a novel small field of view hybrid gamma camera (HGC) for sentinel lymph node and small organ imaging. Society of Nuclear Medicine and Molecular Imaging (SNMMI) Annual Meeting, Denver, USA. Abstract in: J Nucl Med 58, supplement 1: 157.

4.  J.E. Lees, S.L. Bugby, M.S. Alqahtani, L.K. Jambi, N.S. Dawood, W.R. McKnight, B.S. Bhatia, **A.H. Ng** and A.C. Perkins. 2017. A multimodality camera for intraoperative imaging. Cancer Imaging Conference. London, UK.

5.  N.S. Dawood, J.E. Lees, S.L. Bugby, M.S. Alqahtani, L.K. Jambi, W.R. McKnight, **A.H. Ng** and A.C. Perkins. 2017. Radionuclide depth estimation using a novel SFOV hybrid gamma-optical camera with an anthropomorphic breast phantom. The 45th Annual Spring BNMS Meeting. Birmingham, UK.

6.  **A.H. Ng**, M.S. Alqahtani, L.K. Jambi, S.L. Bugby, J.E. Lees and A.C. Perkins. 2017. Use of a novel small field of view hybrid gamma camera (HGC) for Iodine-125 seed localisation. The 45th Annual Spring BNMS Meeting. Birmingham, UK.

7.  L.K. Jambi, J.E. Lees, S.L. Bugby, B.S. Bhatia, M.S. Alqahtani, W.R. McKnight, N.S. Dawood, **A.H. Ng** and A.C. Perkins. 2016. IEEE Nuclear Science Symposium (NSS) and Medical Imaging Conference (MIC). Strasbourg, France.

8.  S.L. Bugby, J.E. Lees, **A.H. Ng**, M.S. Alqahtani, L.K. Jambi, M.A. Stammes, H.J.M. Handgraaf and A.C. Perkins. 2016. Portable hybrid gamma-near-infrared fluorescence imaging. European Association of Nuclear Medicine

(EANM) Annual Congress. Barcelona, Spain. DOI: 10.1007/s00259-016-3484-4

9.    J.E. Lees, S.L. Bugby, M.S. Alqahtani, L.K. Jambi, **A.H. Ng**, N.S. Dawood and A.C. Perkins. 2016. A high-resolution hybrid gamma-optical camera for intraoperative imaging. European Association of Nuclear Medicine (EANM) Annual Congress. Barcelona, Spain. DOI: 10.1007/s00259-016-3484-4

10.   M.S. Alqahtani, J.E. Lees, S.L. Bugby, L.K. Jambi, B.S. Bhatia, W.R. McKnight, N.S. Dawood, **A.H. Ng** and A.C. Perkins. 2016. Quantitative analysis of sentinel node detection using a novel small field of view hybrid gamma camera (HGC). European Congress of Medical Physics (ECMP), Athens, Greece. Abstract in: Phys Med 32, Supplement 3, 256-257.

11.   A.C. Perkins, **A.H. Ng**, S.L. Bugby, P.E. Blackshaw, M.S. Alqahtani, L.K. Jambi, J.E. Lees. 2016. A novel compact hybrid optical gamma camera: First clinical results. Society of Nuclear Medicine and Molecular Imaging (SNMMI) Annual Meeting, San Diego, USA. Abstract in:  J Nucl Med 57, Supplement 2:531.

12.   L.K. Jambi, J.E. Lees, S.L. Bugby, M.S. Alqahtani, B.S. Bhatia, W.R. McKnight, N.S. Dawood, **A.H. Ng** and A.C. Perkins. 2016. Development of a small field of view gamma camera for medical imaging. European Congress of Radiology (ECR), Vienna, Austria. Abstract available in: http://dx.doi.org/10.1594/ecr2016/C-2206

13.   M.S. Alqahtani, J.E. Lees, S.L. Bugby, L.K. Jambi, B.S. Bhatia, W.R. McKnight, N.S. Dawood, **A.H. Ng** and A.C. Perkins. 2016. Investigation of a novel small field of view hybrid compact gamma camera (HCGC) for scintigraphic imaging. European Congress of Radiology (ECR), Vienna, Austria. Abstract available in: http://dx.doi.org/10.1594/ecr2016/B-0033

14.   M.S. Alqahtani, J.E. Lees, S.L. Bugby, L.K. Jambi, B.S. Bhatia, W.R. McKnight, N.S. Dawood, **A.H. Ng** and A.C. Perkins. 2016. Investigation of a novel small field of view hybrid compact gamma camera (HCGC) for scintigraphic imaging. European Congress of Radiology (ECR), Vienna, Austria. Abstract in: Insights Imaging (2016 ) 7 (Suppl 1):S162-S465, DOI 10.1007/s13244-016-0475-8

15.   **A.H. Ng**, S.L. Bugby, L.K. Jambi, M.S. Alqahtani, P.E. Blackshaw, P.S. Morgan, J.E. Lees and A.C. Perkins. 2015. Development of a hybrid optical-gamma camera: A new innovation in bedside molecular imaging. World Congress on Medical Physics and Biomedical Engineering, Toronto, Canada.

16.    J.E. Lees, A.C. Perkins, S.L. Bugby, B.S. Bhatia, L.K. Jambi, M.S. Alqahtani, W.R. McKnight, N.S. Dawood and **A.H. Ng.** 2015. A high-resolution handheld hybrid camera for gamma and optical imaging. British Nuclear Medicine Society (BNMS) Autumn Meeting, London, UK.

17.    **A.H. Ng**, S.L. Bugby, L.K. Jambi, M.S. Alqahtani, D. Clay, P.E. Blackshaw, P.S. Morgan, J.E. Lees and A.C. Perkins. 2015. Hybrid optical-gamma camera for intraoperative imaging: A flexible phantom to assess system performances for sentinel node detection. International Conference on Clinical PET-CT and Molecular Imaging (IPET), Vienna, Austria.

18.    L.K. Jambi, J.E. Lees, S.L. Bugby, B.S. Bhatia, M.S. Alqahtani, W.R. McKnight, **A.H. Ng** and A.C. Perkins. 2014. Performance of a hybrid gamma-optical camera for improved utility in diagnostic imaging. British Institute of Radiology (BIR) Annual Congress, London, UK. Abstract available in: http://www.eposters.net/poster/performance-of-a-hybrid-gamma-optical-camera-for-improved-utility-in-diagnostic-imaging.

19.    M.S. Alqahtani, J.E. Lees, S.L. Bugby, B.S. Bhatia, L.K. Jambi, **A.H. Ng** and A.C. Perkins. 2014. A lymphoscintigraphic phantom study using a novel hybrid optical-gamma camera. British Institute of Radiology (BIR) Annual Congress, London, UK. Abstract available in: http://www.eposters.net/poster/a-lymphoscintigraphic-phantom-study-using-a-novel-hybrid-optical-gamma-camera

20.    J.E. Lees, S.L. Bugby, B.S. Bhatia, L.K. Jambi, M.S. Alqhatani, **A.H. Ng** and A.C. Perkins. 2014. A small field of view camera for hybrid gamma and optical imaging. PSD10: 10th International Conference on Position Sensitive Detectors, Guildford, UK.

21.    **A.H. Ng**, D. Clay, P.E. Blackshaw, S.L. Bugby, B.S. Bhatia, J.E. Lees and A.C. Perkins. 2014. A phantom for testing gamma camera performance in sentinel node detection. British Nuclear Medicine Society 42nd Annual Meeting, Harrogate, UK. Abstract in: Nucl Med Commun 35 (5): 570.

# Chapter 1

# Introduction

## 1.1  Diagnostic Nuclear Medicine

The discovery of natural radioactivity in uranium ore in 1896 by Henri Becquerel led to the further discovery of other new radioactive elements by Marie Curie, who first used the terms 'radioactive' and 'radioactivity'. During the mid-1920s, George de Hevesy carried out studies of metabolic pathways by administering radionuclides to rats, thus establishing the principle of the radiotracer. Frédéric Joliot Curie and Irène Joliot Curie reported the first production of artificial radioactive material in 1934 [1] and it is believed that John H. Lawrence has successfully made his first attempt to treat leukaemia by using an artificial radionuclide, named phosphorus-32 [2]. These studies established the fundamental principles for the application of radionuclides in medicine.

There are three main types of nuclear medicine procedure practiced worldwide, namely imaging procedures, non-imaging procedures and therapeutic procedures. Diagnostic nuclear medicine is the medical speciality that utilises radioactive tracers in the diagnosis of disease. It is based on the understanding of the physiological uptake and clearance of an administered radiolabelled tracer known as a radiopharmaceutical. Once administered to the patient the radiopharmaceutical will concentrate in the organ or system of interest while emitting radiation, principally gamma rays due to the physical process of radioactive decay. The energy of these gamma photons allows a significant number to penetrate through body tissues and be detected using dedicated gamma cameras and scanners that can image the spatial distribution of the radioactivity in the body. Figure 1.1 gives a summary illustration of the processes of a nuclear medicine imaging.
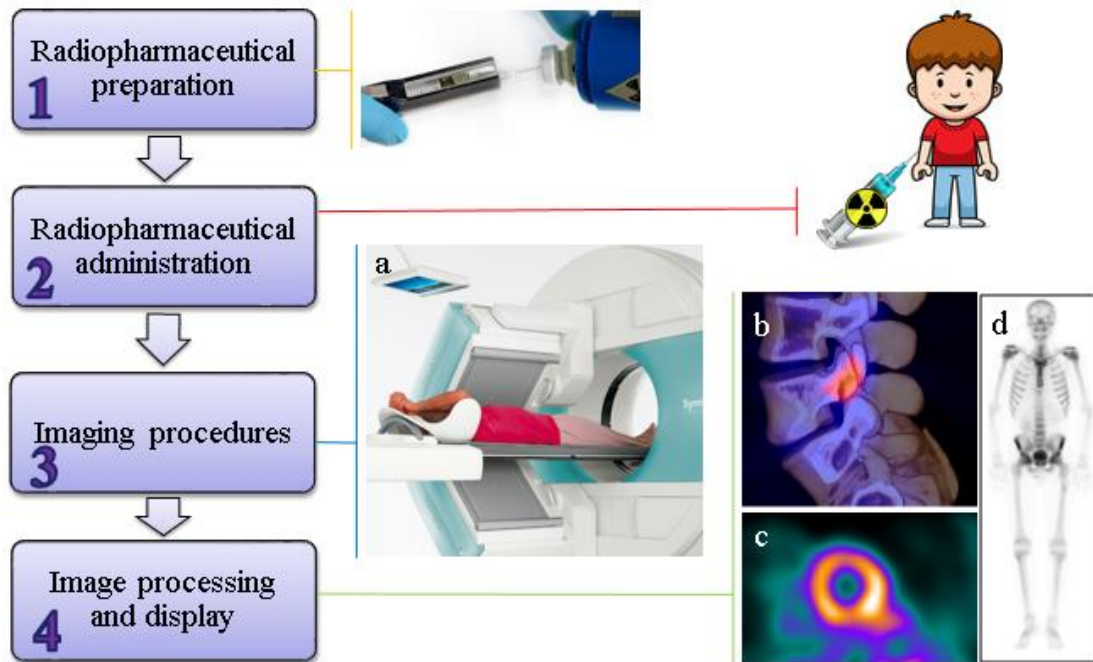
Figure 1.1: The typical processes of a nuclear medicine imaging procedure. (a) SPECT-CT imaging with patient lying on couch; (b) SPECT-CT image of lumbar spine with fracture; (c) myocardial perfusion image (Images taken from [3]); and (d) whole body bone scintigraphy (Image taken from [4])

Imaging studies require imaging systems such as gamma cameras, Single Photon Emission Computed Tomography (SPECT) and Positron Emission Tomography (PET) camera systems to acquire the gamma images of radioactivity distribution within the patient's body. This technology plays an important role in the identification of a range of medical conditions including malignant diseases, heart disease, brain disorders and organ function. These gamma images compliment other diagnostic information provided by imaging techniques such as computed tomography (CT), magnetic resonance imaging (MRI) and ultrasonography to improve the accuracy in disease diagnosis, cancer treatments planning and evaluating treatment response. With the widespread development of nuclear imaging and computer emission tomography technology, there are about 33 million diagnostic nuclear medicine examinations carried out globally in a year [5].

### 1.1.1   Physics in Nuclear Medicine

Radiation is a form of energy. There are two types of radiation used in nuclear medicine, particulate radiation and electromagnetic radiation, which are emitted from radionuclides through the radioactive decay processes. Particulate radiation is energy in the form of kinetic energy of mass in motion, originating from the process of

radioactive decay, nuclear reactions and from cosmic rays. Examples of these radiations are energetic electrons (*e*), protons (*p*), neutrons (*n*) and alpha particles (*α*).

Electromagnetic radiation is a form of energy in motion with no mass and charge. It propagates through space as either waves or discrete packets of energy, called photons or quanta, at the speed of light by oscillating electrical and magnetic fields. The relationship of wavelength, λ and frequency, ν of the electromagnetic radiation is given by Equation 1.1.

$$\lambda \times \nu = c$$

1.1

where *c* is the velocity of light in vacuum, which is approximately $3 \times 10^8$ m.s$^{-1}$. The basic unit of energy is the *electron volt* (eV). One eV is defined as the energy acquired by an electron when accelerated through an electric potential difference of one volt. The energy *E* (in kilo eV) and the wavelength of its associated electromagnetic field λ (in nanometers) are related by Equation 1.2. Figure 1.2 illustrates the examples of different form and applications over the range of the electromagnetic spectrum.

$$E = \frac{1.24}{\lambda}$$

1.2
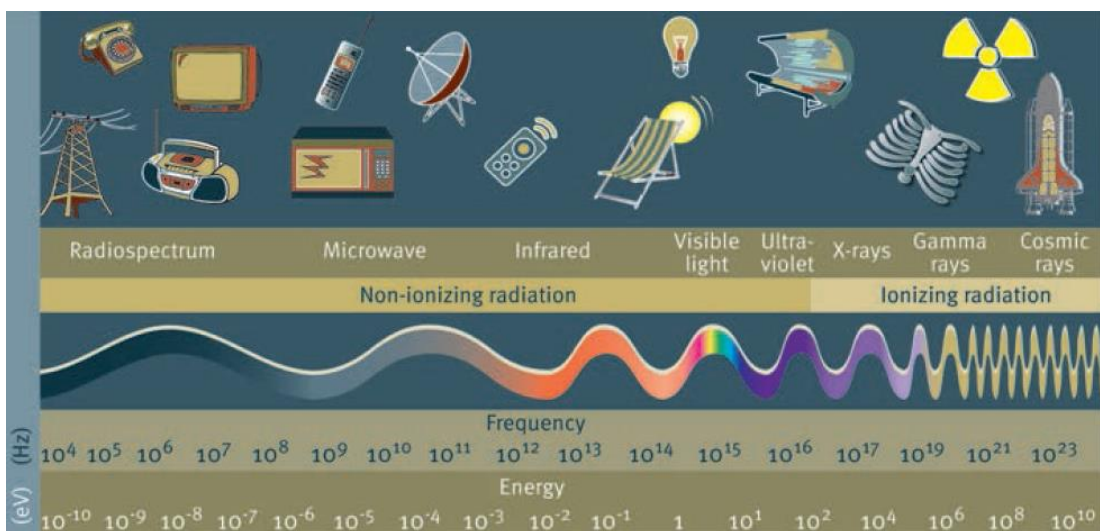


Figure 1.2: Electromagnetic spectrum taken from [6].

### 1.1.1.1 Radioactive decay

An atomic nucleus is characterised by the number of protons and neutrons within the positively charged core. The combinations of protons and neutrons produce either stable or unstable nuclei. The ratio of the number of neutrons to the number of protons ($N/Z$) determines the stability degree of a nucleus. A radionuclide, which has an unstable nucleus, emits radiation in the process of achieving a more stable configuration of protons and neutrons in the nucleus. The process is called radioactive decay or radioactive disintegration. It is spontaneous and involves the conversion of mass into energy. It is described in terms of probabilities and average disintegration rates during a period of time. If a number of radioactive atoms $N$ present in a radionuclide, the disintegration rate at that time ($t$) is given by Equation 1.3.

$$\frac{dN}{dt} = -\lambda N$$

1.3

where $\lambda$ is the decay constant of the radionuclide. The disintegration rate $A$ is referred to as the radioactivity or the activity of the radionuclide and has dimensions of disintegration per second (dps). The Systeme International (SI) unit of activity is the becquerel (Bq). From a knowledge of the decay constant and the initial amount of radioactivity, the total number of radioactive atoms can be determined by Equation 1.4.

$$N_t = N_0 e^{-\lambda t}$$

1.4

where $N_0$ and $N_t$ are the number of radioactive atoms at $t = 0$ and time $t$ respectively. Since activity $A$ is proportional to the number of atoms $N$, therefore it can be calculated by Equation 1.5.

$$A_t = A_0 e^{-\lambda t}$$

1.5

The decay factor $e^{-\lambda t}$ is an exponential function of time $t$. Each radionuclide has its characteristic properties include the decay mode and type of emissions, the transition energy and the average lifetime of a nucleus of the radionuclide prior decay process.

### 1.1.1.2  Physical half-life

The physical half-life ($t_½$) of a radionuclide is defined as the time required reducing its initial activity level to half. It is related to the decay constant $\lambda$ by Equation 1.6.

$$\lambda = \frac{0.693}{t_{½}}$$

1.6

The mean life $\tau$ of a radionuclide is the average lifetime of the atoms in a sample. It is related to the decay constant and half-life as follows:

$$\tau = \frac{1}{\lambda} = \frac{t_{½}}{0.693} = 1.44 \, t_{½}$$

1.7

For medical applications, the elimination of a radiopharmaceutical from any organ or tissue depends on both the physical half-life ($T_p$ or $t_½$) and biological half-life ($T_b$) of the radiopharmaceutical. The half-life associated with radioactive decay is categorised as the physical half-life while biological half-life is defined as the time required to excrete half of the administered radiopharmaceutical from biologic system. The effective decay constant ($\lambda_e$) is related to $\lambda_p$ and $\lambda_b$ by Equation 1.8.

$$\lambda_e = \lambda_p + \lambda_b$$

1.8

Therefore, the effective half-life, $T_e$ can be derived as Equation 1.9.

$$T_e = \frac{T_p \times T_b}{T_p + T_b}$$

1.9

### 1.1.2  Radionuclides

The radiation emitted following radioactive decay of a radionuclide during its natural tendency to achieve stability allows for many healthcare applications. Nuclear medicine procedures involve the mapping of radioactivity distributions in organs and tissues offers information on the physiology and metabolism of organs and biologic systems using sophisticated radiation detector. These radionuclides are all man-made and can be classified as reactor-produced radionuclides (e.g. Molydenum-99 and Iodine-131) or accelerator-produced radionuclides (e.g. Fluorine-18). Table 1.1 shows the physical

characteristic of radionuclides commonly used in nuclear medicine. The selection of the medicinal radionuclides for specific procedure needs to take into considerations of the following factors:

a) type and energy of emissions: gamma photons for imaging, alpha or beta particles with high energy (~1 MeV) for therapy;

b) physical half-life: relative short half-lives (measured in minutes, hours or days);

c) chemical properties: simple chemical technique for attaching the radionuclide to the ligand;

d) cost and/or complexity of preparation: ease and relative low cost of production and ready availability.

Table 1.1: Commonly used radionuclide in nuclear medicine adapted from [7].

| Nuclide | Physical half-life | Mode of decay (%) | γ-ray energy* (MeV) | γ-ray abundance (%) |
|---|---|---|---|---|
| *Positron Emission Tomography (PET) imaging* | | | | |
| $^{11}_{6}C$ | 20.4 min | $\beta^+$ (100) | 0.511 (annihilation) | 200 |
| $^{13}_{7}N$ | 10 min | $\beta^+$ (100) | 0.511 (annihilation) | 200 |
| $^{15}_{8}O$ | 2 min | $\beta^+$ (100) | 0.511 (annihilation) | 200 |
| $^{18}_{9}F$ | 110 min | $\beta^+$ (97) EC (3) | 0.511 (annihilation) | 194 |
| $^{68}_{31}Ga$ | 68 min | $\beta^+$ (89) EC (11) | 0.511 (annihilation) | 178 |
| *Single Photon Emission Computed Tomography (SPECT) imaging* | | | | |
| $^{67}_{31}Ga$ | 78 hr | EC (100) | 0.093 | 40 |
| | | | 0.184 | 20 |
| | | | 0.300 | 17 |
| | | | 0.393 | 5 |
| $^{75}_{34}Se$ | 119.78 days | EC | 0.136 | 59.2 |
| | | | 0.265 | 59.8 |
| $^{99}_{42}Mo$ | 66 hr | $\beta^-$ (100) | 0.181 | 6 |

| Nuclide | Physical half-life | Mode of decay (%) | γ-ray energy* (MeV) | γ-ray abundance (%) |
|---------|--------------------|--------------------|----------------------|----------------------|
| | | | 0.740 | 12 |
| | | | 0.780 | 4 |
| $^{99m}_{43}$Tc | 6.0 hr | IT (100) | 0.140 | 90 |
| $^{111}_{49}$In | 2.8 days | EC (100) | 0.171 | 90 |
| | | | 0.245 | 94 |
| $^{123}_{53}$I | 13.2 hr | EC (100) | 0.159 | 83 |
| $^{201}_{81}$Tl | 73 hr | EC (100) | 0.167 | 9.4 |
| | | | X-ray (0.069-0.083) | 93 |
| *Therapeutic* | | | | |
| $^{32}_{15}$P | 14.3 day | $\beta^-$ (100) | - | - |
| $^{90}_{39}Y$ | 64.1 hr | $\beta^-$ | - | - |
| $^{131}_{53}$I | 8.0 days | $\beta^-$ (100) | 0.284 | 6 |
| | | | 0.364 | 81 |
| | | | 0.637 | 7 |
| $^{177}_{71}Lu$ | 6.73 days | $\beta^-$ | 0.208 | 11 |
| $^{223}_{88}Ra$ | 11.44 days | α | 0.154 | 5.6 |

Note:

*γ-rays with abundance less than 4% have not been cited.

d, deuteron; EC, electron capture; f, fission; IT, isomeric transition; n, neutron; p, proton; min, minutes; hr, hours.

Data from Browne E, Finestone RB. Table of Radioactive Isotopes. New York: Wiley; 1986 and [8].

### 1.1.3 Radiopharmaceuticals

A radiopharmaceutical is a specific radiotracer in which the radionuclide is labelled to a molecule that has useful biomedical properties for diagnostic or therapeutic purposes. The biochemical and physiological behaviour can be traced, either *in vitro* or *in vivo*, following the administration of the radiopharmaceutical, subsequently resulting in diagnostic information or a therapeutic effect. The administration technique is usually either orally or intravenously in a single dose. These radiolabelled molecules are unique and easily detected, there are no differences in physical and chemical properties to the unlabelled molecules however the label between radionuclide and molecule must be firmly bounded [9]. In addition, the following factors should be considered when selecting a biochemical compound as a radiopharmaceutical:

a) non-toxic nature

b) the mechanism of localisation in the desired organ or compartment

c) the specific activity of chemical compound

d) the radiochemical purity

e) the biological half-life

The synthesis of radiopharmaceuticals involves the handling of radioactive substances and chemical processing in designated radiopharmaceutical production facilities. It ranges from simple preparation using radiopharmaceutical kits to complex synthesis process carried out in a purpose-built hot cell. Dispensing and supply of radionuclide at a hospital facility is usually carried out using a radionuclide generator, for example $^{99}$Mo/$^{99m}$Tc generator. The elution process of this generator is based on the separation of a short lived daughter radionuclide ($^{99m}$Tc) from a long parent lived radionuclide ($^{99}$Mo). The production methods of these radiopharmaceuticals are required to adhere to regulatory compliance as required by national authorities such as US Food and Drug Administration (FDA) and UK Medicines and Healthcare products Regulatory Agency (MHRA) and are subject to strict quality control tests. Table 1.2 summarises commonly used radiopharmaceuticals in nuclear medicine procedures, in particular SPECT imaging.

Table 1.2: Commonly used radiopharmaceuticals in SPECT imaging.

| Chemical form | Clinical Use |
| --- | --- |
| $^{99m}$Tc-nanocolloid human serum albumin | Lymphatic imaging |
| $^{99m}$Tc-Mercaptoacetyltriglycine | Renography |
| $^{99m}$Tc-Macroaggregated Albumin (MAA) | Pulmonary blood flow (lung scan) |
| $^{99m}$Tc-Diethylene Triamino Penta Acetic Acid (DTPA) | Renal blood flow, function and excretion (Renogram) |
| $^{99m}$Tc-Methylene DiPhosphonate (MDP) | Skeletal studies (bone scan) |
| $^{99m}$Tc-Sodium Pertechnetate | Thyroid, salivary gland, brain and nasolacrimal drainage imaging |
| $^{99m}$Tc-Red Blood Cells | Cardiac function and blood pool scans |

| Chemical form | Clinical Use |
|---|---|
| $^{99m}$Tc-Sestamibi | Myocardial perfusion |
| $^{99m}$Tc-Tetrofosmin | Myocardial perfusion |
| $^{99m}$Tc-Hexa Methylene Propylene Amine Oxime (HMPAO) | Cerebral blood flow and scans for infection |
| $^{123}$I-Ioflupane | Parkinson's disease/Dopamine transporter imaging |
| $^{123}$I-Sodium Iodide | Thyroid scan |
| $^{111}$In-pentetreotide | Somatostatin receptor scintigraphy |

## 1.2   Gamma Camera

The initial focus of nuclear medicine studies was related to the measurement of thyroid function. A Geiger counter was placed over the patient's neck to detect the gamma rays emitted from the thyroid after the administration of $^{131}$I [10]. The ratio between the detected count rates measured at neck and a known standard determined the percentage of thyroid uptake, and provided an indication of whether thyroid uptake was normal or abnormal. The disadvantages of this technology were that it did not outline which parts of thyroid were abnormal and it deposited a high radiation dose to the patient.

In 1951, Cassen *et al.* [11] from the University of California, Los Angeles developed a moving collimated scintillation detector, called a rectilinear scanner as shown in Figure 1.3(a). The automated detector was moved backwards and forwards in a series of parallel lines across patient's neck while another part of the system held a pen which moved synchronously over a sheet of paper producing black marks and later used a colour display to plot the distribution in proportion to the intensity of gamma rays detected.

The concept of the gamma camera was invented by Hal Anger in 1952 whilst working at the Donner Laboratory, the University of California in Berkeley, USA. The early prototype consisted of a pinhole collimator and a sodium iodide flat intensifying screen placed in front of a photographic plate which was able to produce a clinical relevant image showing gamma-ray distributions emitted from the patient (Figure 1.3 (b)). The sensitivity of the camera was low resulting in long imaging times and requiring

relatively high amounts of radioactivity to be administered to the study subject to produce images.

Anger enhanced the prototype design by replacing the gamma ray detector with a 4-inch diameter scintillator coupled to an array of seven photomultiplier tubes (PMTs) and applied 'Anger arithmetic' to determine the position of the scintillation event that occurred in the crystal by comparing the voltages collected in individual PMTs. Typically, a gamma camera consists of a collimator, scintillation detector, PMTs, pulse height analyser, X-Y positioning circuits and an image display with an image recording or storage device.
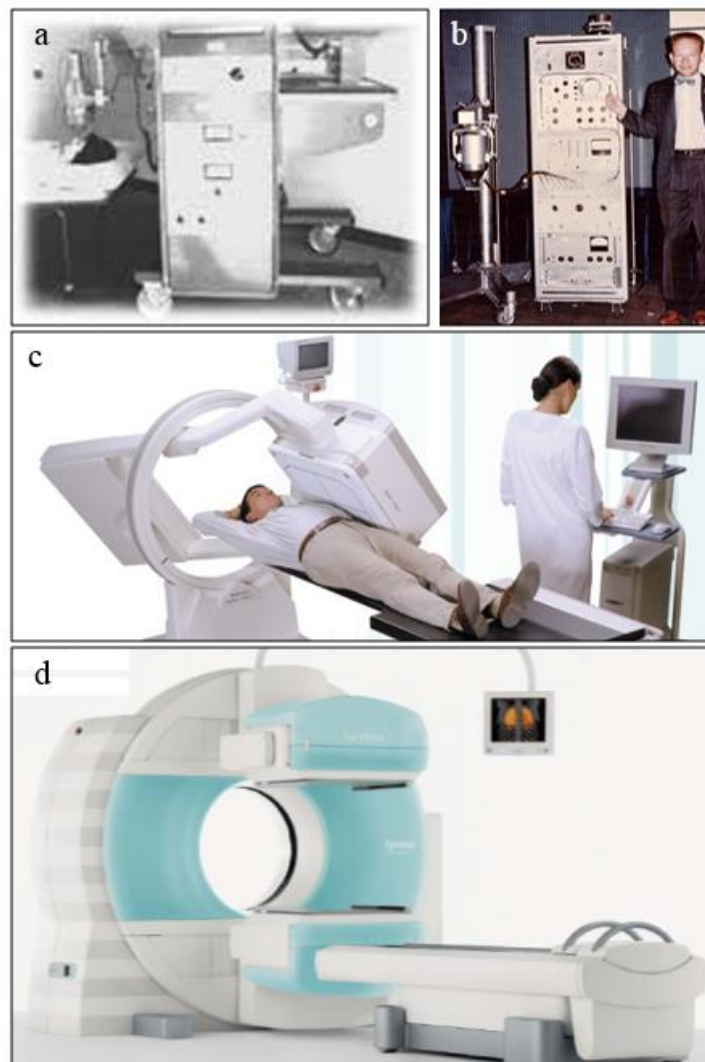


Figure 1.3: The evolution of gamma camera technologies from early (a) rectilinear scanner "Picker Magna Scanner" [12], (b) Anger camera [12], single-head LFOV gamma camera [13] to state-of-art SPECT-CT imaging system [3].

When a radiation source is placed nearby the camera system, the incoming gamma rays will pass through the collimator and interact with the detector. The detector, usually made of a scintillation crystal (such as NaI(Tl)), converts the energy from the gamma ray to a flash of light. The light photons are detected by an array of PMTs adjacent to the detector and the events are computed and mapped out as the gamma image display. In modern gamma camera systems, advanced digital electronics and software are used to process the image data obtained from the PMT units.

### 1.2.1  Detector head

The functions of the detector head are to detect gamma rays and produce analysable electrical signals that represent the incident radiation events. The head is covered by lead shielding around the back and sides to prevent gamma rays from entering from these directions. A collimator is fitted at the front of the detector to allow incoming gamma photons travelling in the desired directions to pass through and reach the detector. Figure 1.4 shows the schematic diagram of a detector head of gamma camera.
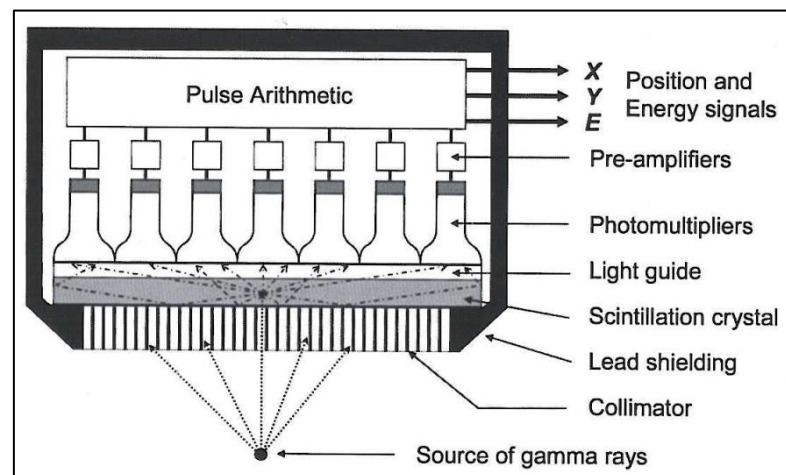


Figure 1.4: Components in the detector head of a gamma camera taken from [12].

### 1.2.1.1  Collimator

Collimators are made of lead or other materials with high atomic number that can absorb gamma radiation. They have holes to allow gamma rays travelling along the direction of holes to reach the detector crystal. Photons emitted in any other direction are absorbed by the septa between the holes. Figure 1.5 shows different types of collimator that may be used to project incident gamma rays onto the detector of a gamma camera.
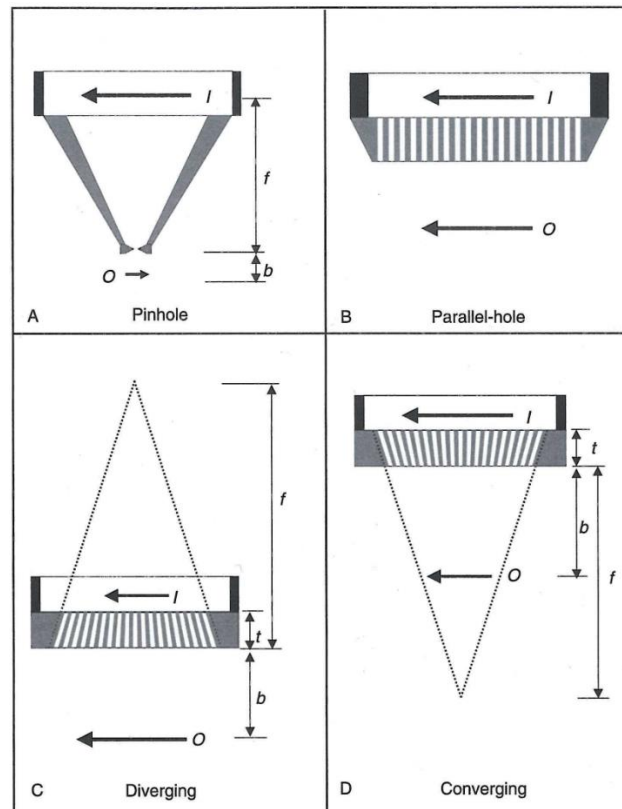
Figure 1.5: Four types of collimator used in gamma camera system. O, radioactive object; I, projected image. Image taken from [14].

#### 1.2.1.1.1   Parallel hole collimators

Parallel-hole collimators are the most commonly used collimator on modern gamma cameras. They are constructed with holes that are parallel to each other and perpendicular to the detector face. The lead walls between the holes are called collimator septa, with thicker walls for higher energy radionuclides. Parallel-hole collimators are categorised based on the energy of radionuclide used and the resolution and sensitivity they provide in imaging as following:

   a)  Low energy general purpose collimator (LEGP)
   b)  Low energy high resolution collimator (LEHR)
   c)  Low energy high sensitivity collimator (LEHS)
   d)  Medium energy collimator
   e)  Ultra-high energy collimator

#### 1.2.1.1.2   Pinhole collimator

A pinhole collimator has a single and small pinhole aperture, usually 2-4 mm in diameter. It is constructed using lead, tungsten or platinum. The size of aperture

determines both the spatial resolution and the sensitivity; a smaller aperture giving increased spatial resolution and decreased sensitivity and vice versa for a larger aperture. During image acquisition, gamma rays passing through the pinhole aperture, project an inverted image of the original sources onto the crystal. The image is magnified when the distance *b* from the source to the pinhole is smaller than the collimator cone length *f*; while it is minified if the sources are further away (refer Figure 1.5(a). The relationship between image size *I* and object size *O* is given by Equation 1.10.

$$\frac{I}{O} = \frac{f}{b}$$

<div align="right">1.10</div>

The size of the imaged area may vary with distance from the pinhole collimator. The diameter of the image area projected onto the detector, $D'$ can be determined by

$$D' = \frac{D}{I/O}$$

<div align="right">1.11</div>

where *D* is detector diameter and *I/O* is the magnification factor.

### 1.2.1.1.3   Converging and diverging collimators

Converging collimators are designed with tapered holes converging towards object direction. It is used to magnify the image where the organ of interest is smaller than the size of detector. Diverging collimators are made with tapered holes that are divergent from the crystal site. It demagnifies images of objects which are larger than the size of the detector.

### 1.2.1.2   Scintillation crystal detector

Scintillation detector technologies have been widely used as gamma-ray converters in medical imaging. Most gamma cameras have traditionally utilised inorganic scintillation crystals such as thallium doped sodium iodide (NaI(Tl)) or thallium doped cesium iodide CsI(Tl) with typical thickness of 6.4 - 18.4 mm as the gamma detector. Table 1.3 summarises various inorganic scintillation crystal used in gamma camera and PET camera systems. This material emits scintillation photons following the absorption

of the energy deposited by the incident gamma photons that are detected by an electronic light sensor such as photomultiplier tube. Impurities (known as activators) are added to the pure crystal to modify the energy structure so that multiple energy states are created between the conduction and valence bands. These energy states have narrower energy gaps resulting in a lower energy of the emitted photons, usually in the visible range and prevents self-absorption.

Table 1.3: Properties of various inorganic scintillation crystal used in gamma camera [15-17].

| Scintillator | NaI(Tl) | CsI(Tl) | LaCl$_3$(Ce) | LaBr$_3$(Ce) | YAlO$_3$(Ce) |
|---|---|---|---|---|---|
| Density (g cm$^{-3)}$ | 3.67 | 4.51 | 3.86 | 5.30 | 5.50 |
| Effective atomic number (Z) | 50 | 54 | - | - | 39 |
| Linear attenuation coefficient at 140 keV (cm$^{-1}$) | 3.12 | 4.53 | 2.82 | 3.42 | 1.81 |
| Peak emission wavelength (nm) | 415 | 550 | 330 | 358 | 350 |
| Decay time (ns) | 230 | 1000 | 20 (70%), 231 (30%) | 35 (90%) | 30 |
| Light yield (photons/keV) | 38 | 54 | 49 | 61 | 21 |

Figure 1.6 illustrates the energy band structure of an inorganic scintillator. During the interaction of the incident gamma photons with the scintillator, many electron-hole pairs are created. The positive holes move to a location with lower ionisation energy, usually the activator, and subsequently ionise it. The excited electrons elevate to the conduction band and move freely through the crystal until they encounter an ionised site. The recombination of the excited electron and the ionised site makes the configuration unstable (activator excited states), then the de-excitation process occurs with the emission of scintillation photons [18].
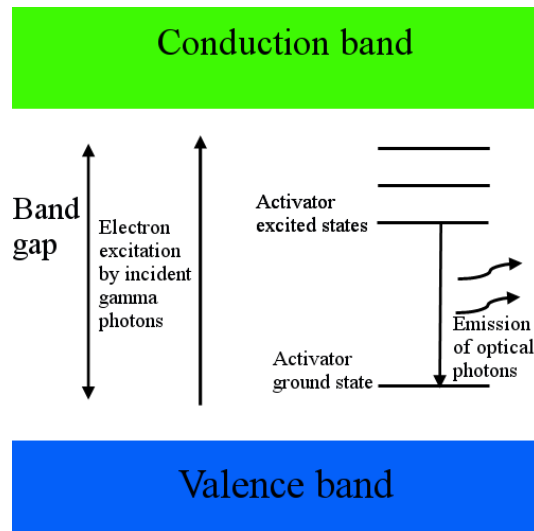
Figure 1.6: Energy band structure of an inorganic scintillation crystal.

The main characteristics of a scintillator are the intrinsic detection efficiency, the light conversion efficiency and the phosphorescent decay time. The intrinsic detection efficiency depends on the linear attenuation coefficient of the scintillator which could determine the optimum thickness of the crystal in stopping incoming gamma photon. Light conversion efficiency is the amount of light produced per keV of absorbed photon. Phosphorescent decay time is the time required for the light to be emitted. Each parameter partly determines the energy resolution and the maximum counting rate of the detector respectively.

### 1.2.1.3   Photomultiplier tube

The scintillation photons emitted are sparse and weak for image formation, so they must be amplified. Amplification is achieved using the photomultiplier tubes (PMT) attached to the back of the crystal. A PMT consists of a vacuum glass tube with a photocathode at the front which converts light photons into electrons and a series of electrodes known as dynodes that amplify the number of electrons produced for each incident event. A gamma camera can have a number of tubes in its array, typically $30 - 100$ in most modern cameras. These are closely packed for example in a hexagonal pattern to ensure minimum gaps are left between the tubes. The base of each PMT is connected to a pre-amplifier circuit. The amplified output from the PMT is passed to the position logistic circuits, where signals detected are recorded and processed. This information is then output to a computer system where the data is analysed.

#### 1.2.1.4 Solid State Detector

In recent years, there has been an increased use of semiconductor detectors in gamma cameras. The most commonly used semiconductor detector materials for this application are cadmium telluride (CdTe) or cadmium zinc telluride (CdZnTe or CZT). Table 1.4 summarises various semiconductor detector used in gamma camera systems. When a gamma ray interacts with a semiconductor detector, it is converted to an electronic signal within a single process. Semiconductor detectors are normally poor electrical conductors. However, an incident photon will produce ionisation in the depletion region, where it enables excited electrons flow freely. The electrical charge produced can be collected by an external applied voltage. The size of the electrical signal is proportional to the amount of radiation energy absorbed.

Table 1.4: Properties of semiconductor detectors used in gamma camera [15, 16].

| Detector | Si | CdTe | CZT | HgI$_2$ |
|---|---|---|---|---|
| Density (g cm$^{-3}$) | 2.33 | 5.85 | 5.82 | 6.40 |
| Effective atomic number (Z) | 14 | 48-52 | 30-52 | 53-80 |
| Linear attenuation coefficient at 140 keV (cm$^{-1}$) | 0.02 | 3.22 | 3.07 | 8.03 |
| Average energy per electron-hole pair (eV) | 3.61 | 4.43 | ~5 | 4.20 |
| Electron mobility (cm$^2$/V.s) | 1500 | 1000 | 1350 | 100 |
| Hole mobility (cm$^2$/V.s) | 600 | 80 | 120 | 4 |

Note: Si-Silicon; HgI$_2$-mercuric iodide
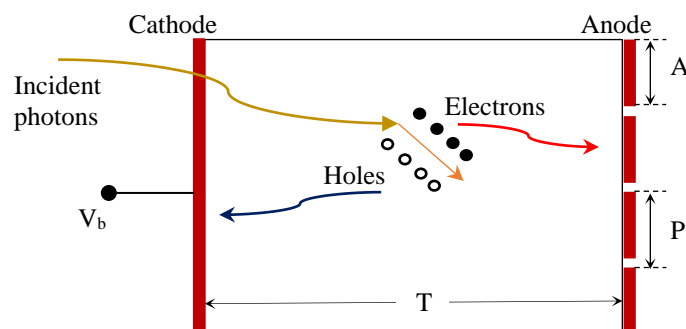


Figure 1.7: Schematic diagram of a CZT semiconductor detector (V$_b$: bias voltage, T: material thickness, A: anode, P: pixel size).

#### 1.2.1.5 Pulse height analyser

The pulse height analyser (PHA) analyses the amplitude of the output pulse from the amplifier and determines the energies of detector photon events. The feature selects

only those photons of desired energy range to be counted by the use of appropriate peak and window settings.

### 1.2.2  Positioning Circuit

The X-Y positioning circuit uses a 'voltage divider' to weight the output of each tube corresponding to the X, Y location of the point of interaction of the gamma rays on the crystal [19]. All PMTs are connected through capacitors to four directional terminals: $X^+$, $X^-$, $Y^+$ and $Y^-$. A resistive or capacitive network assigns relative values proportionally to the four signals obtained from the PMTs registering the event.

### 1.2.3  Gantry

The purpose of the gantry is to hold the detector head firmly and allow it to be positioned near to patient during image acquisition. The gantry is designed to support the heavily mounted detector head whilst providing motorised features for gantry movement and positioning. For modern gamma cameras, ring-style gantries are more common. All the motions of gantry are motorised and controlled by the operator or set for scanning procedures by computer.

## 1.3  SPECT and other hybrid modalities

The introduction of scanning gamma camera technology has formed the basis of Single Photon Emission Computed Tomography (SPECT), an emission tomographic imaging technique which utilises a single or multiple-headed gamma camera mounted on a mechanical rotating gantry as shown in Figure 1.3 (c). These camera detectors can rotate around the patient detecting gamma events and producing a cross sectional tomographic image using reconstruction software (in the same way as X-ray computed tomography (CT) image formation) or a whole body image as shown in Figure 1.8 (a). In 1963, Kuhl and Edwards [20] has demonstrated the early concept of SPECT. Early attempts in producing 3-D images on a conventional gamma camera was achieved by rotating the patient in front of a stationary camera. Over the decades, SPECT technologies have expanded to become reliable, robust and widely accepted nuclear imaging procedures. The same cameras can scan over the patient to produce a whole body image or can be controlled as organ-specific SPECT systems for abdominal, brain,

cardiac or breast imaging. These techniques allow the three-dimensional (3-D) visualisation of radiotracer distributions in the body.
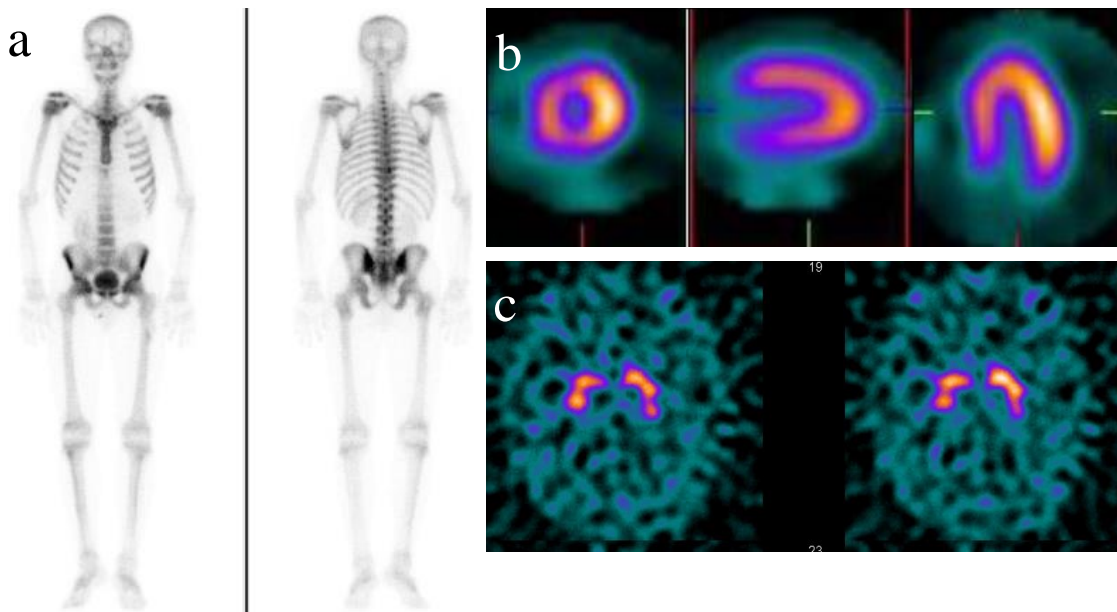


Figure 1.8: Example of (a) whole body bone scintigraphy (anterior and posterior views; images taken from [4]) and 3-D SPECT images. ((b) Myocardial perfusion study (short axis, horizontal and vertical long axis views) showing the radiotracer distribution in the different regions of the myocardium ( images taken from [3]); (c) Transverse slices of the reconstructed brain SPECT image of $^{123}$I-Ioflupane (DaTscan$^{TM}$)).

More recently, the fusion of dual modalities into a single multimodality imaging device has resulted in the creation of Single Photon Emission Computed Tomography-Computed Tomography (SPECT-CT) camera systems. In 1990 Hasegawa *et al.* [21] reported the simultaneous transmission-emission imaging which formed the basis of SPECT-CT development. The first commercial SPECT-CT was introduced in 1999, a year earlier than the official launch of Positron Emission Tomography-Computed Tomography (PET-CT).

These hybrid imaging modalities offer the fusion of gamma and CT images to enable the overlay of physiological tracer uptake with the cross sectional anatomical detail. The CT information also aids in attenuation correction and organ localisation, as well as providing diagnostic quality CT images. Figure 1.9 shows an example of fused SPECT-CT images in a patient with an ectopic parathyroid adenoma. The tremendous success of these hybrid cameras, led to the integration of the magnetic resonance (MR) scanner with either the PET or SPECT camera, allowing the fusion of nuclear images with MR images having superior soft tissue contrast when compared with CT [22].
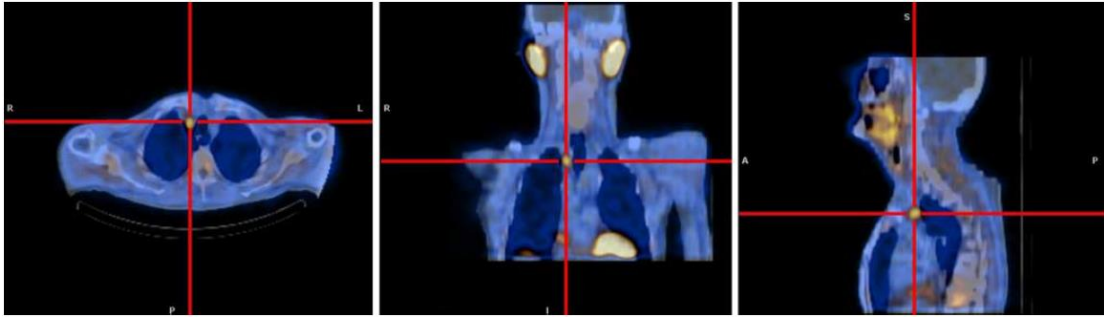
Figure 1.9: Example SPECT-CT images in a patient with an ectopic parathyroid adenoma in the upper mediastinum, right paratracheal region (as indicated by the centre of the red-cross). The fused anatomical and physiological details provides valuable information to aid surgical procedures [23].

## 1.4   Bedside imaging

Most nuclear medicine procedures are carried out in the nuclear medicine department since gamma cameras are large bulky devices, installed in purpose built rooms. This requires the patient to attend the department in order to undergo the imaging investigation. As a consequence, this restricts the type of patient who can access the services and patients from the operating theatre, intensive care unit and accident and emergency department cannot always attend. The use of mobile or portable gamma cameras enables bedside investigations which may be of value in those hospital departments.

The application of nuclear medicine techniques outside of the department has a long history. The concept of radioguided surgery using a gamma probe, which was reported approximately 60 years ago [24], enabled the intraoperative detection of radionuclide in the operating theatre. Selverstone *et al.* [24] at Harvard Medical School reported on the use of a Geiger Müller tube device to detect the beta radiation emitter, phosphorus-32 in patients with brain tumours. The counts in the area of suspected tumour and normal brain tissue were detected by the device at various time intervals and various depths beneath the cerebral cortex to demarcate the boundary of tumour margins.

Perkins *et al.* [25, 26] described a range of bedside nuclear medicine investigations employing gamma probes in the intensive care unit and operating theatre. These developments originated from the use of gamma probes for the detection of the uptake of $^{99m}$Tc bone scanning agents, in particular osteoid osteoma, a benign condition that predominantly occurs in young children and adolescents. In addition, the increasing use of gamma probes in sentinel lymph node biopsy procedures in the staging and

management of breast cancer drove the evolution of gamma probe technology and the widespread acceptance of nuclear medicine procedures during surgery. Since then, the evolution of gamma detection probe technology in intraoperative procedures has immensely developed and has become an established discipline within the practice of surgery.

The development of small field of view (SFOV) gamma cameras offers the capability of intraoperative imaging during surgical procedures. For use in the operating theatre, gamma cameras must be compact enough to be handheld by the surgeon or other theatre staff. As indicated by the name, SFOV gamma cameras are considerably smaller in comparison with conventional large field of view (LFOV) gamma cameras. Advances in low profile detector technologies have enabled the introduction of smaller imaging systems with the cameras held on an articulated arm mounted on a small trolley or handheld by the operator during use.

### 1.4.1 Mobile Gamma Cameras

Small single-headed cameras mounted on a mechanical trolley have been available over the past 20 years. These cameras enabled a range of clinically important imaging investigations to be undertaken whilst the patient is lying on a standard bed outside of nuclear medicine department. In 1973, Hurwitz *et al.* [27] reported preliminary experience with a "portable" scintillation camera in the operating room or other locations previously believed to be inaccessible for diagnostic nuclear medicine. The camera was a modified standard Anger scintillation camera with a 0.5-inch NaI(Tl) crystal of 12 inches in diameter, mounted on a movable stand.

Figure 1.10 shows a mobile digital gamma camera from Digirad Corporation (San Diego, CA, USA) which is currently available. This system has a field of view measuring 311 mm × 396 mm produced by a solid-state segmented CsI(Tl) crystal detector with a silicon photodiode and is suitable for detecting gamma energies between 50 keV and 350 keV with the aid of the interchangeable collimators. The camera can be manoeuvred manually despite having a weight of 305 kg.

Figure 1.10: A solid-state mobile gamma camera-Digirad ergo™ Imaging System by Digirad (Taken from [28]).

Figure 1.11 shows another example of commercially available mobile gamma camera produced by Mediso Medical Imaging (Budapest, Hungary), namely Nucline™ TH. The camera detector comprises an NaI(Tl) scintillation crystal with a thickness of 6.5 mm backed by PMTs. The detector head is available in sizes of 230 mm $\times$ 210 mm, 260 mm $\times$ 246 mm and 300 mm $\times$ 300 mm. The system weighs 180 kg and the gantry is equipped with motorised height adjustment and interchangeable collimators. A separate computer console is used for image acquisition.



Figure 1.11: A mobile gamma camera-Mediso 'Nucline™ TH' (Taken from [13]).

Another example of an organ-specific gamma camera is called the Cardiotom$^{TM}$ system [29]. This gamma camera system combines a commercially available detector system attached with a rotatable parallel and slanted-hole collimator (ectomography) to produce tomographic images. The camera weighs 320 kg and is primarily designed for cardiac studies at the patient bedside. Table 1.5 provides summary of mobile gamma cameras available at the time of writing.

Table 1.5: Examples of clinical mobile gamma camera systems.

| Camera | Detector | Nominal FOV (mm) | Weight (kg) | Applications |
|---|---|---|---|---|
| Nucline$^{TM}$ TH (Mediso) | NaI(Tl), PMT | $260 \times 246$ | 180 | Cardiac, thyroid imaging [13] |
| ergo™ Imaging System (Digirad) | CsI(Tl), silicon photodiode | $311 \times 396$ | 305 | Cardiac, breast, and other bedside imaging [28] |
| 2020tc imager (Digirad) | CsI(Tl), silicon photodiode | $212 \times 212$ | 386 | Lung, thyroid, cardiac, mammoscintigraphy, bedside imaging [30] |
| Cardiotom$^{TM}$ (Adolesco) | NaI(Tl), PMT (Sopha DS7) | Ø 400 | 320 | Cardiac imaging [29] |
| Picola − Scintron® | NaI(Tl), PMT | Ø 254 | NA | Thyroid imaging [31] |
| Solo Mobile™ (DDD-Diagnostic A/S) | NaI, PMT | Ø 210 | < 270 | Thyroid, parathyroid, cardiac, sentinel node imaging [32] |

Ø denotes diameter of circular FOV.

### 1.4.2 Handheld Gamma Cameras

More recent technological advancement in gamma camera detector design has led to the innovation of portable compact SFOV gamma cameras. Possibly the earliest concept of the handheld gamma imaging system was introduced by Barber *et al.* [33], in which prototype devices were small enough to be inserted into the upper or lower

gastrointestinal tract to image the distribution of tumour-seeking radiotracers. The design provided flexibility for handheld use in additional areas of clinical investigation when compared to a mobile gamma camera. These cameras were not intended to replace the standard LFOV gamma cameras, but have been used for additional clinical applications, in particular for intraoperative imaging. This has resulted in a number of vibrant research initiatives worldwide for exploring the development of robust, user-friendly and ergonomical SFOV gamma camera systems [34-37].

Similar to standard gamma cameras, the main features of compact imaging devices are the imaging detector, collimator, shielding, electronic readout circuitry and image acquisition and image processing software. The size and weight of the camera head represents the most important characteristic of an SFOV camera in terms of ease of use and manoeuvrability near the patient. From the literature it can be seen that the weight of SFOV gamma camera heads used for clinical application has been between 320 g [38] and 2490 g [39] while the detector size varied from 8.192 mm × 8.192 mm [40] up to 127 mm × 127 mm [41]. Based on the literature review, there are five commercially available SFOV gamma cameras whilst at least 10 prototype cameras are still at an experimental stage. Table 1.6 summarises the characteristics of SFOV gamma cameras that are currently in development, or in clinical use.

Table 1.6: Characteristics of SFOV imaging systems.

| Camera | Detector | | | Detector head | | Collimator | | Energy range (keV) /radionuclide detected | Clinical application & reference |
|---|---|---|---|---|---|---|---|---|---|
| | Type/material | Size (FOV) (xyz) (mm) | Matrix size | Size (mm) | Weight (g) | Type | Material | | |
| IOGC | Hg1$_2$, electrodes | 23.75 × 23.75 × 1 | 16 × 16 | 43 × 45 | NA | PA | Tungsten | $^{99m}$Tc, $^{57}$Co, $^{241}$Am | NA [42] |
| HGC | CsI(Tl), EMCCD | 8.192 × 8.192 × 1.5 | 128 × 128 | Ø 115 × 171 (L) | 1500 | Pinhole | Tungsten | 30 – 245 | Bone imaging, lacrimal drainage scan, thyroid imaging, lymphatic scan [43-45] |
| POCI 2 | CsI(Na), IPSD | Ø 40 × 3 | 50 × 50 | Ø 95 × 90 | 1200 | PA | lead | $^{99m}$Tc, $^{57}$Co | SLN detection with breast cancer [46, 47] |
| TreCam | LaBr3:Ce, MAPMT | 49 × 49 × 5 | 16 × 16 | NA | 2200 | PA | lead | $^{99m}$Tc, $^{57}$Co | SNOLL [48-50] |
| Mediprobe | CdTe:Cl | 14.08 × 14. 08 × 1 | 256 × 256 | 200 × 70 × 30 | 1500* | Pinhole | Tungsten | $^{99m}$Tc, $^{57}$Co | SLN detection with melanoma cancer [51] |
| eZ Scope † | CZT | 32 × 32 × 5 | 16 × 16 | 74 × 72 × 210 | 820 | PA | NA | 71 - 364 | Intraoperative imaging for primary hyperparathyroidism [52, 53] |
| MGC500 | CdTe | 44.8 × 44.8 | 32 × 32 | 82 × 86 × 205 | 1400* | PA | Tungsten | 550 keV | Lymphoscintigraphy with oral cancer [54-56] |
| IHGC | NaI(Tl), PSPMT | 50 × 50 × 6 | 29 × 29 | 64 × 64 × 76 | 1100 | PA | lead | 30-300 | SLN detection with breast or melanoma cancer [57, 58] |
| IP † | CsI(Tl), PSPMT | 44.1 × 44.1 × 5 | 18 × 18 | NA | 1200 | PA | tungsten | 50-250 | SLN detection with breast cancer [59-61] |
| GE | CZT | 40 × 40 | 16 × 16 | 150 (L) | 1200 | PA | NA | 40 - 200 | NA [62] |
| Sentinella 102 † | CsI(Na), PSPMT | 40 × 40 | 300 × 300 | 80 × 90 × 1500 | 1000* | Pinhole | lead | 50 - 200 | SLN detection with breast, penile, prostate cancer, intraoperative imaging for primary hyperparathyroidism [63-68] |
| GCOI | CsI(Tl), PSPMT | 38.4 × 38.4 × 4 | 24 × 24 | NA | NA | PA | NA | 60 - 300 | NA [69] |

Note: NA-information not available; L-length; PA-parallel hole; *-without collimator; Ø-diameter of circular FOV; †-commercially available; IPSD- intensified position-sensitive diode; MAPMT-multi-anode photomultiplier tube; PSPMT-position-sensitive photomultiplier tube.

Table 1.6: Characteristics of SFOV imaging systems (cont'd).

| Camera | Detector | | | Detector head | | Collimator | | Energy range (keV) /radionuclide detected | Clinical application & reference |
|---|---|---|---|---|---|---|---|---|---|
| | Type/ material | Size (FOV) (xyz) (mm) | Matrix size | Size (mm) | Weight (g) | Type | Material | | |
| CrystalCam † | CZT | $40 \times 40$ | $16 \times 16$ | $65 \times 65 \times 180$ | 800 | PA | Tungsten | 30-250 | SLN detection with breast and melanoma cancer [34, 70-72] |
| Minicam 2 † | CdTe | $40 \times 40$ | $16 \times 16$ | $250 \times 70 \times 170$ | 700 | PA | Tantalum | 30-200 | SLN localisation [73] |
| MRG15 | CsI(Tl), SiPM | $13.2 \times 13.2 \times 5$ | $4 \times 4$ | $114 \times 32 \times 26$ | 320 | PA | NA | $^{99m}$Tc, $^{57}$Co | NA [38] |
| CarollRes | GSO:Ce, MAPMT | $50 \times 50$ | $8 \times 8$ | $78 \times 78 \times 275$ | 2490 | PA | Lead | $^{99m}$Tc, $^{57}$Co | SLN detection with breast cancer [39, 74] |
| Medica GammaCAM/OR | NaI(Tl), PSPMT | $127 \times 127 \times 6$ | $56 \times 56$ | NA | NA | PA | NA | $^{99m}$Tc | SLN detection with breast cancer [41, 75] |
| DEPICT | CZT | $44 \times 44 \times 5$ | $22 \times 22$ | $216 \times 200 \times 93$ | NA | PA | Lead/ Tungsten | 30 – 3000 | dosimetry of molecular radiotherapy [76, 77] |

Note: NA-information not available; L-length; PA-parallel hole; *-without collimator; Ø-diameter of circular FOV; †-commercially available; IPSD- intensified position-sensitive diode; MAPMT-multi-anode photomultiplier tube; PSPMT-position-sensitive photomultiplier tube; SiPM-silicon photomultiplier.

### 1.4.2.1  Camera Detectors

One of the main factors that made the innovation of a miniature-size SFOV gamma camera possible was the availability of suitable compact detectors. Based on the reports published since 1997, most SFOV gamma cameras have used either scintillation crystals [43, 50, 64, 78-81] or semiconductor [51, 52, 56, 62, 71, 73, 77, 82] detectors. The most commonly used scintillation crystals are thallium or sodium-doped cesium iodide (CsI(Tl) and CsI(Na)), NaI(Tl) and cerium-doped lutetium oxyorthosilicate (LSO). The semiconductor detector materials used in SFOV gamma cameras are either cadmium telluride (CdTe) or cadmium zinc telluride (CdZnTe or CZT).

During earlier development, Patt *et al.* [42] developed a 256-element mercuric iodide ($HgI_2$) detector array which was intended to be used as an intraoperative gamma camera. A novel SFOV gamma camera based on yttrium aluminium perovskite activated by cerium (YAP:Ce) coupled with intensified position-sensitive diode (IPSD) [83] has also been developed. A few years later, the compact position-sensitive photomultiplier tube (PSPMT) was recognised as a key development in small camera design and these have been used in cameras with CsI(Tl) [78, 79], NaI(Tl) [75, 80], cerium doped orthosilicate of gadolinium ($Gd_2SiO_5$:Ce or GSO) [81] and cerium-doped halide (LaBr3:Ce) scintillators [50]. Lees, *et al.* have developed a high resolution SFOV gamma camera using a columnar CsI(Tl) coupled to electron multiplying charge coupled device (EMCCD) [84, 85] which is described in more detail in Chapter 2. Figure 1.12 shows an example of the SFOV gamma camera, IP Guardian 2 with detector consisting of CsI(Tl) scintillator coupled to PSPMT.

Figure 1.12: Example of SFOV gamma camera with CsI(Tl) scintillation detector coupled to PSPMT (IP Guardian2, Li-Tech, Roma, Italy). Photograph courtesy of Domenico Rubello, MD, Rovigo, Italy.

As for semiconductor-based gamma cameras, several camera systems have been produced using CdTe [51, 56, 73, 79] or CZT [52, 62, 71]. Figure 1.13 shows an example of compact gamma camera equipped with CZT semiconductor detector, the CrystalCam (Crystal Photonics GmbH, Berlin, Germany). This system is designed to be an "imaging gamma probe" and has a range of tungsten collimators for use with different energy radionuclides.



Figure 1.13: CrystalCam imaging probe with a semiconductor detector. Image courtesy of Thomas Barthel, Crystal Photonics GmbH, Berlin, Germany.

### 1.4.2.2 Camera Collimators

The most common types of collimator used in SFOV gamma camera are either pinhole [36, 43, 51, 86, 87] or parallel-hole [46, 50, 52, 56, 62, 71, 73, 77-79, 81, 88, 89]. These have been constructed from dense metal radiation absorbers, namely lead or tungsten. A range of pinhole collimators with different aperture sizes have been used. These range between 0.5 mm and 4 mm, which providing different choices for various clinical applications. On the other hand, parallel-hole collimators have been fabricated with parallel holes, either in square or hexagonal shape. These include low energy high sensitivity (LEHS), low energy high resolution (LEHR) and low energy general purpose (LEGP) collimators.

Figure 1.14 (left) shows an example of an SFOV gamma camera with a pinhole collimator, Sentinella 102 (Oncovision, Valencia, Spain). The camera consists of an interchangeable pinhole collimator and a single CsI(Na) crystal backed by a position sensitive photomultiplier tube. Figure 1.14 (right) gives another example of an SFOV gamma camera with parallel-hole collimator, namely Mini Gamma Camera 500 (MGC500) (Acrorad Co. Ltd, Okinawa, Japan). The parallel-hole collimator is a combination of 100 pieces of tungsten mesh sheets with the thickness of 0.1 mm respectively. Each sheet having square openings measuring 1.2 mm × 1.2 mm with 0.2 mm pitch.

Figure 1.14: SFOV gamma camera mounted on an articulated arm and cart based system (left) with pinhole collimator, Sentinella 102 (image courtesy of Victoria García, OncoVision, Spain) and (right) MGC 500 with parallel-hole collimator (Taken from [54]).

## 1.5 Aims of the thesis

The previous sections have provided an introduction to the gamma camera and nuclear medicine techniques. The work of this thesis was carried out between 2014 and 2017 to investigate the clinical use of a newly developed prototype SFOV Hybrid Gamma Camera (HGC) and its pre-production prototype device (Nebuleye).

This thesis aims to translate the HGC technology from *in vitro* laboratory studies to clinical use in human subjects. In order to achieve the aims, the following objectives needed to be addressed:

a) to characterise the pre-production SFOV hybrid optical-gamma camera;

b) to assess the performance of the SFOV hybrid optical-gamma cameras in clinical settings;

c) to assess the application of the SFOV hybrid optical-gamma cameras in preclinical imaging;

d) to characterise and gain knowledge of the pre-production camera prior to use in the clinic;

e) to explore the clinical applications of the HGC.

## 1.6 Thesis organisation

- Chapter 2 provides an overview of the design of SFOV gamma cameras, in particular the prototype Hybrid Gamma Camera (HGC) and the pre-production prototype Nebuleye mini gamma camera.

- Chapter 3 investigates the characteristics of the pre-production prototype Nebuleye mini gamma camera and compares these with HGC.

- Chapter 4 explores the potential use of the cameras in preclinical imaging.

- Chapter 5 examines the performance capabilities of the camera for future use in breast cancer surgery.

- Chapter 6 presents the preparatory studies of the pre-production prototype Nebuleye mini gamma camera prior to surgical use.

- Chapter 7 assesses the capabilities of the pre-production prototype Nebuleye mini gamma camera.

- Chapter 8 describes the first use of the HGC in a clinical setting.

- Chapter 9 provides the conclusions of the current work and suggests future research studies.

Throughout this thesis, the term of the SFOV gamma camera was used to indicate either HGC, Nebuleye or other portable gamma cameras. The HGC indicates the laboratory prototype hybrid optical-gamma camera developed by the Universities of Nottingham and Leicester. The Nebuleye indicates the pre-production prototype hybrid optical-gamma camera fabricated by the industrial partner for commercialisation purposes.

# Chapter 2

# The SFOV Hybrid Optical Gamma Cameras

## 2.1  Introduction

Advances in radiation detector technologies have led to a reduction in the size of gamma cameras, leading to the production of compact devices. The Space Research Centre at the University of Leicester in collaboration with Radiological Sciences at the University of Nottingham and Medical Physics at the Nottingham University Hospitals NHS Trust have successfully transferred the use of a charge-coupled device (CCD) from space research to an imaging system suitable for biomedical applications [84]. Further equipment development has resulted in the production of the first laboratory prototype of the handheld SFOV Hybrid Gamma Camera (HGC).

The first prototype camera head consisted of a pinhole collimator, photon detector and cooling unit contained in a plastic enclosure which was connected to an electronics control unit and controlled by a personal computer (PC). The detector was a CsI(Tl) columnar scintillation crystal (Hamamatsu Photonics UK Ltd., Welwyn Garden City, UK) coupled to a CCD (CCD97 BI, e2v Technologies Ltd., Chelmsford, UK) surrounded by 3-mm thick tungsten shielding. A Peltier cooling element and a thermoelectric cooler was used to regulate the operating temperature of the CCD.

With the aid of Biomedical Catalyst Funding awarded by Innovate UK, the camera design was further developed in partnership with industrial partners, Gamma Technologies Limited (Leicester, UK) and Xstrahl Limited (Surrey, UK). This mini gamma camera system was known as Nebuleye and was designed as a medical device intended for commercialisation. The camera system comprised of a cart with the camera head mounted on a positioning arm, two touch screen monitor displays with integrated

PC and an electronic control unit. This chapter summarises the evolution of the prototype HGC and introduces the newly manufactured Nebuleye as show in Figure 2.1. The following sections provide detailed descriptions of the HGC used in the experimental work.
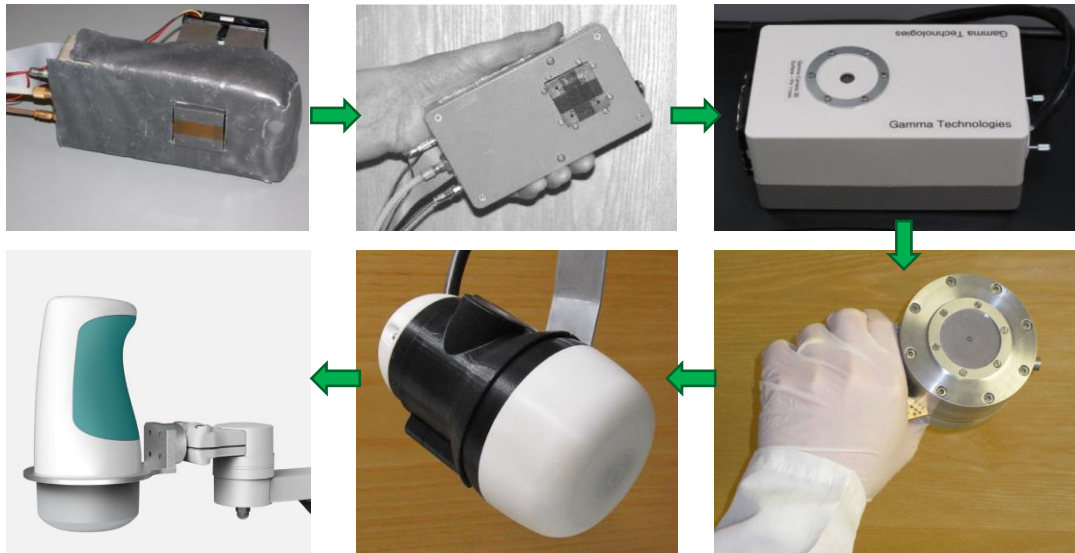


Figure 2.1: Evolution of HGC from early laboratory prototype towards medical device standard.

## 2.2 Early development

The initial design concept of the handheld gamma camera was pioneered in the Space Research Centre, University of Leicester. Lees *et al.* [84] reported a low cost, scintillator-coated, collimated imager, known as High Resolution Gamma Imager (HRGI). The device utilised a charge-coupled device CCD38-20 manufactured by e2v Technologies (formerly EEV Ltd.) as the photon detector which was originally used for dental x-ray imaging. A layer of scintillation crystal gadolinium oxysulfide ($Gd_2O_2S$), which is also known as Gadox, with various thicknesses ranging from 100 to 500 µm was coupled to the CCD and encapsulated within a plastic casing. The CCD detection technology had originally been developed for use in X-ray astronomy [90, 91]. It was used on XMM-Newton EPIC for high performance x-ray imaging while the scintillator materials was utilised on Chandra HRI for improving x-ray detector efficiency. With an increase in the scintillator thickness, the detection efficiency of the imager increased with a consequent degradation of spatial resolution from 0.44 to 0.60 mm. The first image of a $^{99m}$Tc line source (Figure 2.2) were obtained demonstrating potential use in nuclear medicine [84].
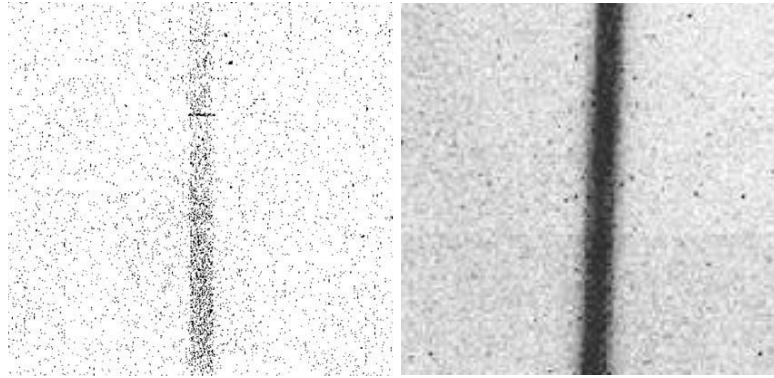
Figure 2.2: (Left) Image of a 1 mm diameter [99mTc] line source with acquisition time of 300 s using HRGI. (Right) [241]Am slit image with acquisition time of 100 s using modified HRGI. Images taken from [84, 92].

Improvements in the performance of the imager were subsequently reported [92] to address several shortfalls which were identified in the previous work. The upgraded HRGI consisted of CCD55-30 (e2v Technologies, UK) coated with 500 µm-thick terbium-doped gadolinium oxysulfide ($Gd_2O_2S(Tb)$) scintillator layer [93], parallel hole lead collimator and a Peltier cooler (Melcor thermoelectric device) [94] with a finned forced-air heat-sink. The detector was packed in a protective plastic box which made it easier to use and compact enough to be handheld (Figure 2.3). This version of the camera was operated in photon counting mode in order to reduce the multiplicative noise associated with the amplification process. The Peltier cooler aided in reducing the operating temperature to approximately -5 ºC subsequently enabling a drop of dark current to 10 electrons/pixel/second. A dry nitrogen atmosphere was maintained in the detector housing to prevent condensation on the CCD.
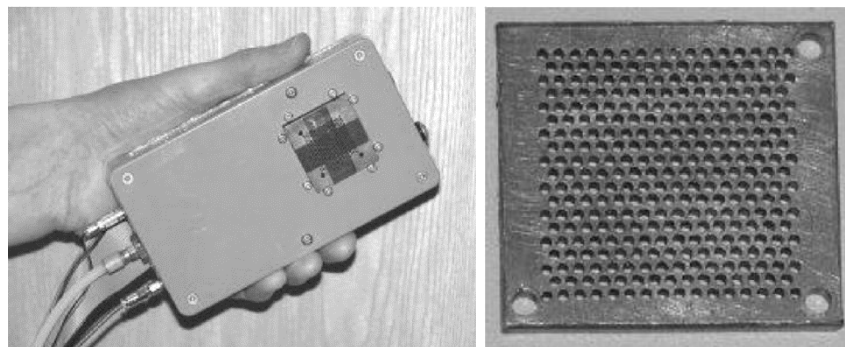


Figure 2.3: (Left) High Resolution Gamma Imager showing water cooling tubing and electronics cables (right) high resolution parallel holes collimator (Taken from [92]).

## 2.3   Mini Gamma Ray Camera

Further development of the camera resulted in the fabrication of a new prototype, called the Mini Gamma Ray Camera (MGRC) (Figure 2.4). The design of the gamma camera was enhanced to offer high spatial resolution imaging with potential for medical and veterinary applications [43]. The gamma ray detector was changed from the Gadox scintillator to thallium-doped cesium iodide (CsI(Tl)) (Hamamatsu Photonics UK Ltd., Welwyn Garden City, UK). The CCD was an inverted mode, back illuminated electron multiplying CCD (EMCCD) (CCD97 BI, e2v Technologies Ltd., Chelmsford, UK) [95]. It was coupled to the scintillation crystal with Dow Corning optical grease. The same thermoelectric technology used in HRGI was utilised in this camera. The sides and back of the detector were surrounded by 4 mm thick lead shielding to minimise detection of scattered photons and background radiation. The outer cover of the camera was a 10 mm-thick aluminium casing.

This version of the camera design allowed interchangeable collimators, either parallel hole as mentioned in Section 2.2 or pinhole.  Two pinhole collimators of 0.5 mm and 1.0 mm in pinhole diameter with an angular aperture of 60 degrees were fabricated from tungsten discs, with dimensions of 6 mm in thickness and 45 mm in diameter. Image acquisition was carried out using a bespoke programme (IDL software, Exelis Visual Information Solutions, Inc., Boulder, CO, USA).  The design of the MGRC offered detection of photons with an energy range between 20 and 140 keV, spatial resolution of approximately 1 mm (full width at half maximum (FWHM)) and better detection efficiency. Pilot clinical gamma imaging was carried out in Medical Physics at Queen's Medical Centre to study the feasibility of using the MGRC in clinical environment. A gamma image of the thumb of a volunteer who was administered with ^{99m}Tc-hydroxymethylene diphosphate (HDP) for a bone scan was reported [43].
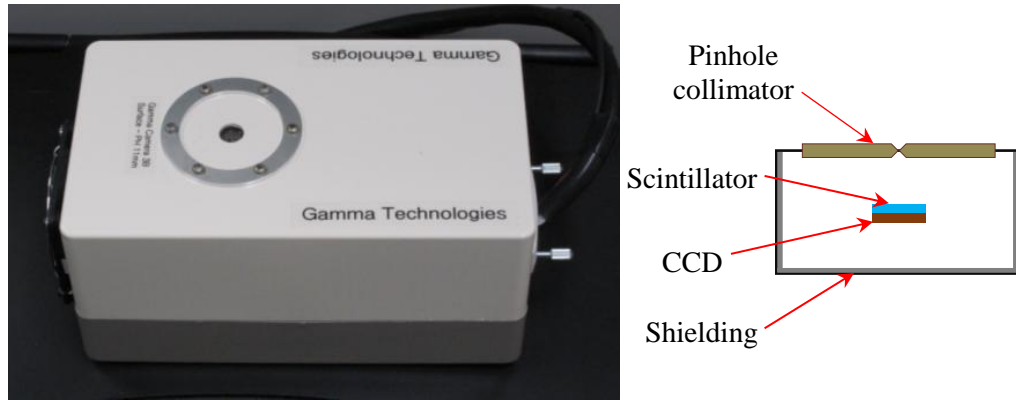
Figure 2.4: (Left) MGRC prototype in a box shaped and (right) schematic of the main camera head components.

## 2.4  Compact Gamma Camera

The box shaped camera head of the MGRC was relatively bulky and difficult to hold by the operator during use. In addition, based on the initial assessment of the gamma images, it was found that there was high level of noise present in the images which degraded the image quality [43]. This may have been due to insufficient shielding around the camera head. As a result, further improvements particularly on the cooling system and shielding were made in the new version of the camera, which was named Compact Gamma Camera (CGC). The heat exchanger was changed to a paraffin based phase-change material (PCM) which reduced the CCD temperature to -13℃ in a cooling process without the need for electrically powered fans. This minimised the risk of contamination as the PCM was encapsulated in the camera head allowing heat exchanges to take place without the involvement of air flow. Further development of the camera was in collaboration with De Montfort University's Regional Design Unit to consider the camera ergonomics and manufacturing design. The camera head was designed with a ridged surface to provide good grip for holding during imaging. Figure 2.5 shows a photograph and schematic of the CGC. A non-toxic plastic enclosure provided both thermal and electrical isolation, as well as being easy to clean in case of contamination with dirt or biological fluids. The shielding material around the back and side of the detector was changed to 3 mm-thick tungsten material having a gamma-ray transmission of $1.74 \times 10^{-5}$ at 140 keV.
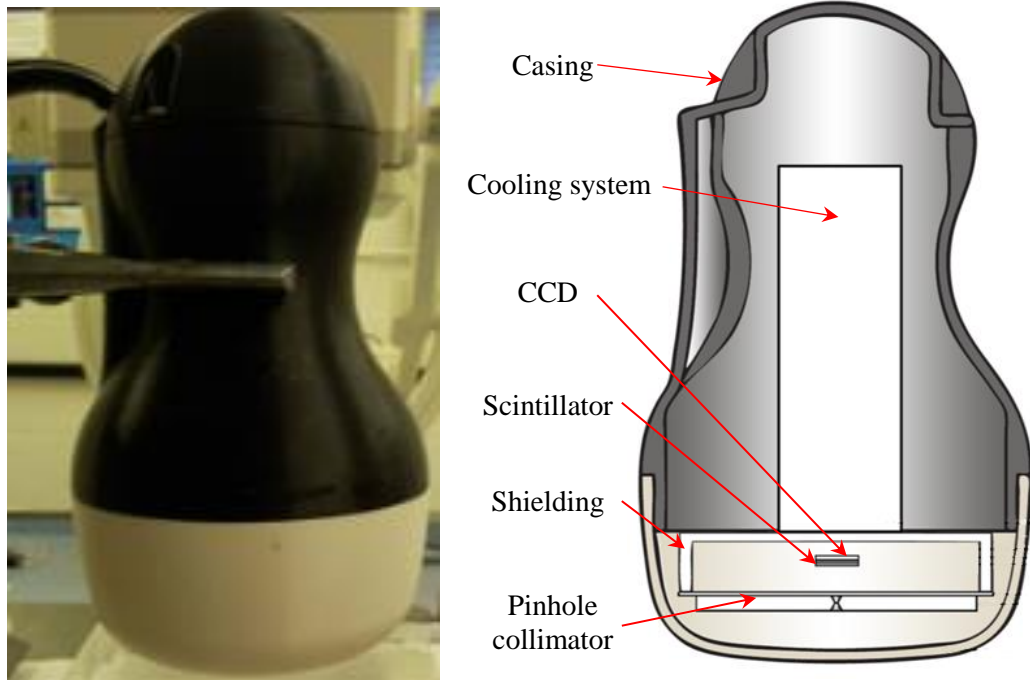
Figure 2.5: (Left) Photograph and (right) schematic diagram of the CGC with ergonomic casing design.

## 2.5  Hybrid Gamma Camera

The combination of dual imaging modalities in medical applications such as Positron Emission Tomography (PET) and Single Photon Emission Computed Tomography (SPECT) combined with Computed Tomography (CT) has provided considerable added value in patient diagnosis and management. These technologies provide both functional and anatomical information to clinicians to assist with disease management. Inter-modality image fusion has provided registration of functional and anatomical details corresponding to the tissue metabolism along with its associated spatial location within the anatomical structures. Building on the success of the development work between Leicester and Nottingham resulted in the innovation of the Hybrid Gamma Camera (HGC) (Figure 2.6) [40, 44]. This was a new concept in portable imaging systems, which was not only applicable for medical diagnosis purposes, but also for environmental surveying and monitoring and the localisation of radioactive sources [96].
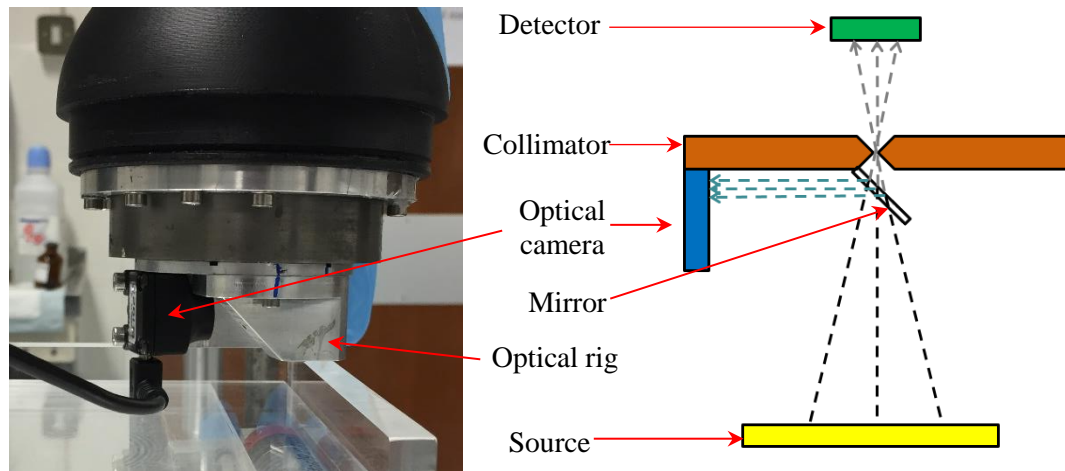
Figure 2.6 (Left) Photograph of the detector head of the HGC prototype (protective casing removed) with the optical camera and mirror fixed on the optical mount. (Right) Diagram of the HGC illustrating the transmission of gamma and optical photons from the source to reach the detectors.

A simple modification was made to the CGC (as described in Section 2.4) where a mount was designed to hold a small optical camera and mirror. This allowed the gamma photons from the source to pass through the mirror and collimator to reach the scintillator detector and subsequently to form a gamma image; while the reflection of optical photons by the mirror to the optical camera generated an optical image. Both gamma and optical cameras were co-aligned in a position that provided fused gamma and optical images with corresponding spatial alignment. Figure 2.7 shows a photograph and schematic diagram of a HGC.

Both optical and gamma cameras were connected to the readout and control electronic systems by a USB cable and D-type cable respectively and were controlled by a standard desktop computer or laptop. Further improvement to the HGC involved an increase of the thickness of the crystal scintillator, fabrication of an additional 1 mm diameter pinhole collimator and incorporation of uEye XS Industrial Camera (IDS Imaging Development Systems GmbH, Obersulm, Germany) [97]. The camera head weighed approximately 1.2 kg.
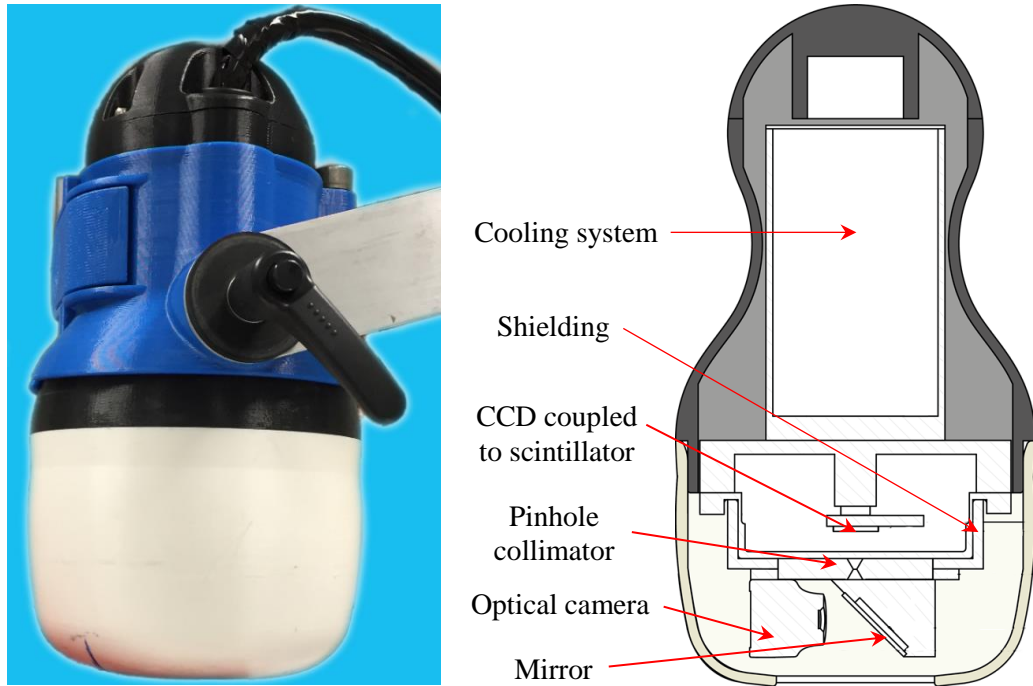
Figure 2.7: (Left) Photograph of the HGC held on an articulated arm. (Right) Cross-sectional schematic diagram of the HGC.

### 2.5.1   Gamma camera components

#### 2.5.1.1   Scintillator

The HGC utilised either a 600 µm or 1500 µm thick columnar scintillator (Hamamatsu Photonics UK Ltd., Welwyn Garden City, UK) (Figure 2.8). This detector enabled the design of the camera to detect over an energy range between 30 and 140 keV with an expected photon absorption ranging from ~38% to 100% [37]. The advantages of the CsI(Tl) scintillation detector are high atomic number (54), high density (~4.5 g cm$^{-3}$) and good light yield (54 photons/keV). The maximum wavelength of the photon emission is 565 nm which has a good match to the spectral sensitivity of the CCD and quantum efficiency of over 90 % at the peak wavelength. The columnar-shaped CsI(Tl) (Figure 2.9) enabled the reduction of spread of the light in the scintillator along the transmission path to the CCD. The crystal was held in place on the CCD using a flexible Kapton window.
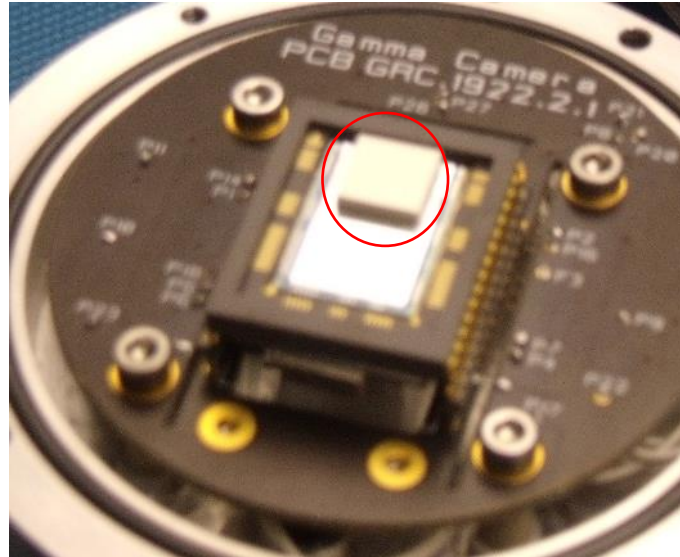
Figure 2.8: Photograph of the scintillator (red circle) coupled to the CCD. Image courtesy of Space Research Centre, University of Leicester.
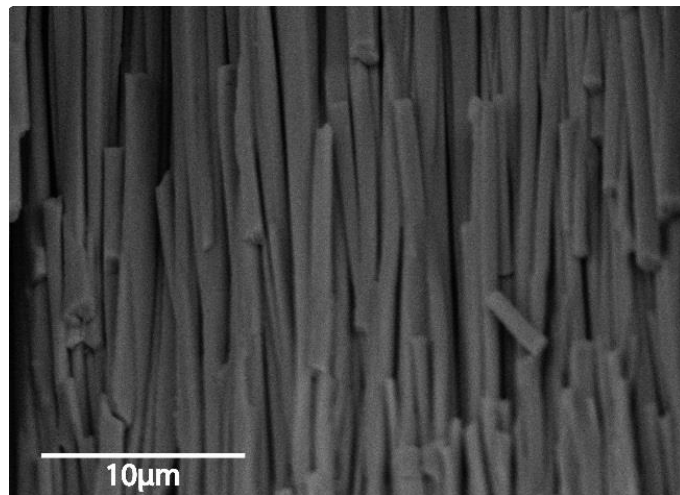


Figure 2.9: The image of the crystal sample acquired by a scanning electron microscope (SEM) illustrates the columnar shape of the material which acts as a light tunnel to guide the scintillation photons to CCD. Image courtesy of Space Research Centre, University of Leicester.

### 2.5.1.2   CCD

A CCD is an electronic device that converts light into an electric charge and processes it into electronic signals. The EMCCD is a frame transfer device which includes an imaging and storage section on the CCD chip. Light photons exposed to the image section are converted to charge within the integration time to form an image. This image is then shifted to the storage section prior to read out register. Next, the individual pixel charge is passed to the multiplication register where electron multiplication (avalanche multiplication) occurs, then it is presented to the output amplifier for readout.

The HGC utilised an EMCCD (CCD97 BI, e2v Technologies Ltd., Chelmsford, UK), which was first used by the Space Research Centre in astronomical research (Figure 2.10). The CCD was a back illuminated sensor in which the light receiving surface (silicon) at the front was back-thinned to enhance the amount of light captured, thus improving quantum efficiency. The CCD read out was using Correlated Double Sampling and had an extra gain register controlled by the application of a high voltage clock pulse (40-50 V). It had a noise of 8 electron/pixel/frame (at 293 K and 30 Hz). Table 2.1 shows the technical details of the CCD.
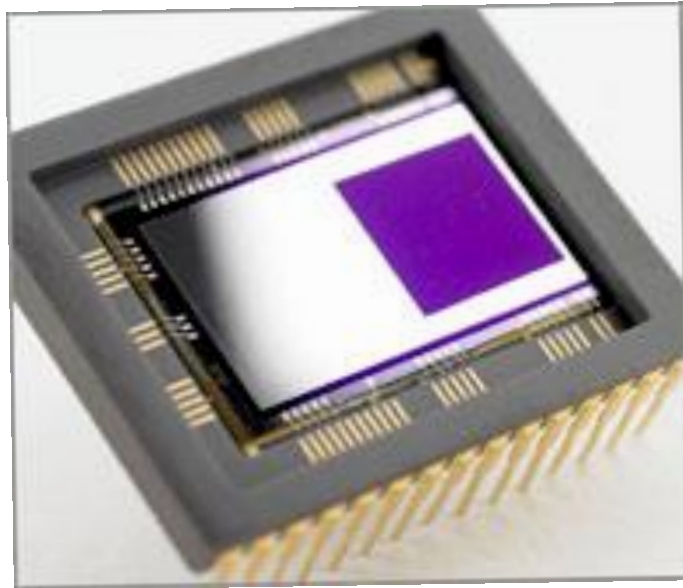
Figure 2.10: Example of the EMCCD chip utilised in the HGC [95].

Table 2.1: Characteristic of the CCD97 BI.

| | |
|---|---|
| Active image area | $8.192 \times 8.192$ mm |
| Image section active pixels | 512(horizontal) $\times$ 512(vertical) * |
| Image pixel size | $16 \times 16\,\mu$m |
| Operating temperature (°C) | -55 to +60 |

*pixels binned to $128 \times 128$ resulting pixel size of $64 \times 64\,\mu$m

### 2.5.1.3  Collimator

Gamma camera collimators are usually made of dense metal and are attached in front of the scintillator detector, allowing the incoming gamma photons to be channelled through the collimator hole(s) to reach the crystal detector. The HGC used a pinhole collimator (having a hole diameter of either 0.5 mm or 1.0 mm) fabricated by Ultimate

Metals Limited (Leighton Buzzard, UK) from tungsten 6 mm in thickness and 45 mm in diameter (Figure 2.11). A pinhole collimator was chosen to:

i.    increase the FOV (as the CCD had a small area);

ii.    ease of construction;

iii.    maintain the compactness of the camera.



Figure 2.11: Bespoke pinhole collimator for HGC with pinhole diameters of 1 mm (left) or 0.5 mm (right).

A 60 degrees acceptance angle was used for each pinhole. This gave a nominal FOV of approximately 40 mm × 40 mm at a distance of 25 mm from the camera surface. Figure 2.12 illustrates the relationship between the source-to-collimator distance (SCD) and the field of view (FOV). Based on the detector size and location within the camera head, the FOV at certain distances was estimated [14]. The images generated were in a square-shape due to the shape of the detector used in this camera.
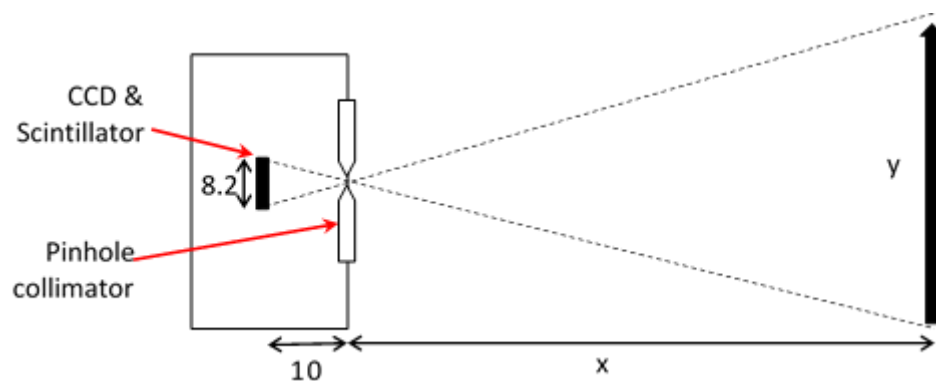


| x (mm) | 50 | 100 | 150 | 200 | 250 | 300 | 350 |
|--------|----|-----|-----|-----|-----|-----|-----|
| y (mm) | 40 | 80  | 120 | 160 | 200 | 240 | 280 |

Figure 2.12: Relationship between the SCD (x) and vertical or horizontal size (y) of the FOV.

#### 2.5.1.4  Shielding and casing

Shielding of the gamma camera blocks all unwanted, background or scattered radiation that would result in image degradation. The sides and back of the detector in the HGC was surrounded by tungsten shielding 3 mm in thickness. The tungsten collimator formed the front surface of the camera. In addition, the detector was surrounded by 4 mm thick aluminium camera housing (except the window which is 1 mm thick) which attenuated most of the lower energy photons. Figure 2.13 illustrates the shielding components of the HGC.
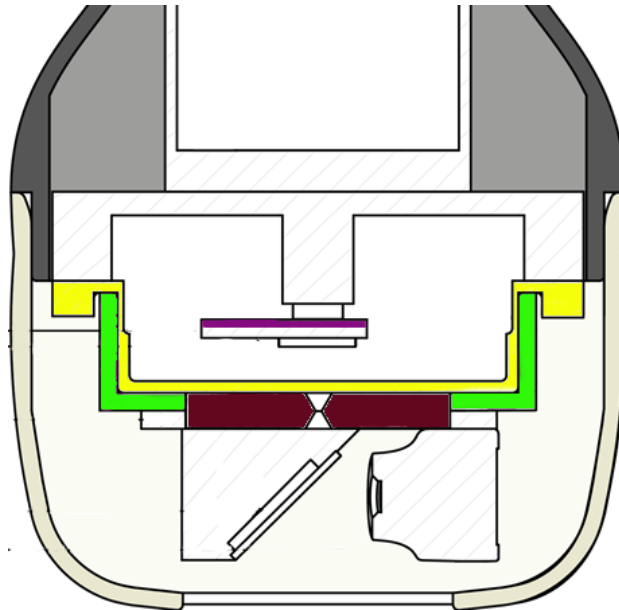


Figure 2.13: Shielding materials surrounded the detector at the tip of the camera head. (Brown: 6 mm tungsten; green: 3 mm tungsten; purple: 1 mm tungsten; yellow: 4 mm aluminium except the window to the pinhole which was 1 mm thick)

The shielding and the detector head were enclosed in 3-D printed plastic enclosure to facilitate both electrical and thermal isolation. The outer surface of the plastic enclosure was produced in a fine textured finish to allow sufficient grip for holding, and also easy to maintain cleanliness and minimise contamination should the camera come into unintentional contact with patients or biological fluids. Customised 3-D printing technology was also applied to the fabrication of the protective nose casing (Figure 2.14) which covered the tip of the camera head. The casing was designed with a transparent window principally to allow optical light to pass through while preventing contamination to the camera detector.

Figure 2.14: Custom made protective casing with the transparent window for HGC.

### 2.5.1.5   Cooling system

The number of electrons known as dark noise to be generated was proportional to the operating temperature of the CCD, which was regulated by a Peltier cooler. The CCD used in this camera was backed with a Peltier cooling package. Thermoelectric coolers operate based on the Peltier effect where heat is extracted or absorbed when an electric current flows through the junctions of two different materials. The Peltier cooler of the CCD was coupled to an organic PCM (PlusICE A-32, PCM Products Limited, Yaxley, Cambridgeshire, UK) with paraffin compounds and it was able to reduce the CCD operating temperature to -10 °C (measured by Fenwal thermistor part number 196-302LAD-002 (Honeywell, Mansfield, TX, USA)) [95].

### 2.5.2   Optical camera components

### 2.5.2.1   Optical camera

To design the HGC small enough to be handheld, the size and weight of the optical camera are major considerations together with the optical camera performance. In the HGC, a lightweight, compact, high quality camera, named uEye XS Industrial Camera (IDS Imaging Development Systems GmbH, Obersulm, Germany) was used to capture the photographic image and video. This camera containing a 5.04 Megapixel complementary metal–oxide–semiconductor (CMOS) sensor to deliver a high quality images with accurate colour reproduction. The camera was integrated with the HGC controlling computer using a USB 2.0 interface and Mini B USB 2.0 connector. Table 2.2 shows the technical details and performance of the camera.

Table 2.2: Technical specifications of uEye XS Industrial Camera used in HGC [97].

| | |
|---|---|
| Optical size | $3.620 \times 2.720$ mm |
| Pixel size | 1.4 µm |
| Resolution | 2592 (Horizontal) $\times$ 1944 (Vertical) pixel |
| Frame rate free-run mode | 15 frame per second |
| Operating temperature | 0 to +55 ℃ |
| Dimensions (Height/Width/Length) | 26.5 mm $\times$ 23.0 mm $\times$ 21.5 mm |
| Weight | 12 g |

#### 2.5.2.2 Mirror

A flat mirror was mounted in front of the collimator at an angle of 45º to reflect light photons to the optical camera assembly. The mirror was 1 mm in thickness and made from soda lime glass. It allowed the incident gamma photons to pass through with minimal absorption (<3%) [40] and scatter while the optical photons are reflected.

#### 2.5.2.3 Optical rig

The optical mount as shown in Figure 2.15 was important in the HGC design in order to provide accurate and fixed positioning of the optical camera and mirror, so that the FOV of each detector was identical and independent of the source-to-detector distance.
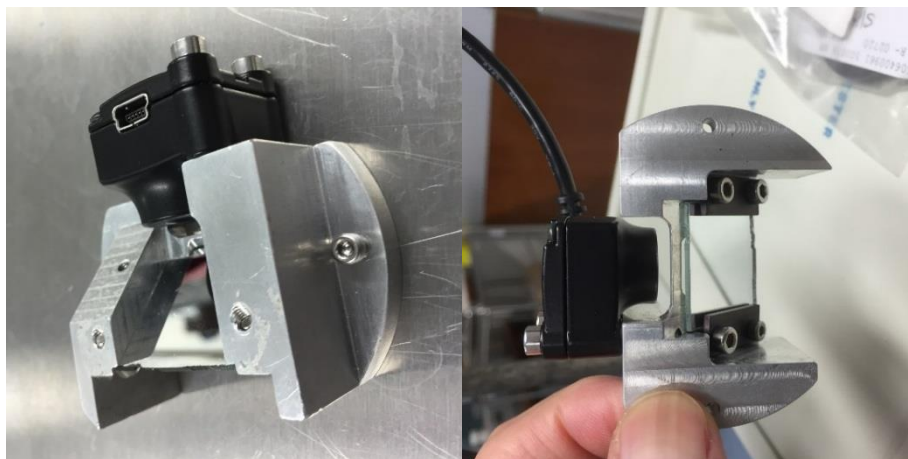


Figure 2.15: Photographs of the optical rig mounted with the mirror and optical camera.

#### 2.5.3 Software and electronics

A bespoke software programme named "University of Leicester Space Research Centre CCD Control and Acquisition (version SVN75-HW2)" (Figure 2.16) was written using

IDL (Exelis Visual Information Solutions, Inc., Boulder, CO, USA) to control the hardware of HGC for image frame acquisition, formation and post-processing. The programme ran on an HP laptop computer in which connected to an electronic control box as shown in Figure 2.17 using a standard USB2 cable. The camera head was connected to the electronics control box via a 25-way insulated cable.
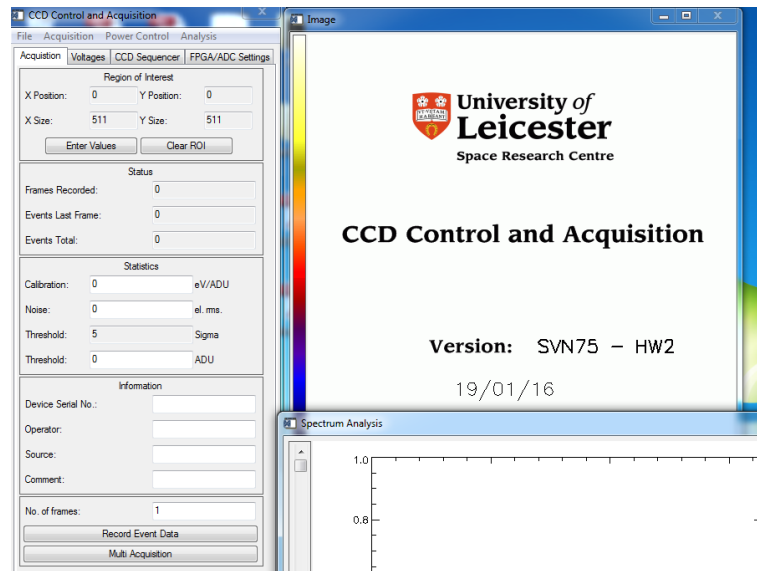


Figure 2.16: CCD Control and Acquisition user interface in the IDL environment.
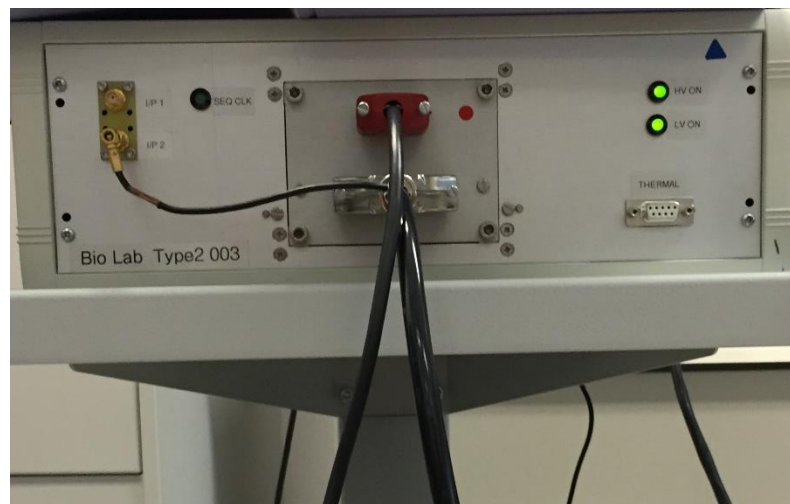


Figure 2.17: Photograph of the electronic control box and cable connections (front view).

### 2.5.4 Image acquisition, processing and storage

#### 2.5.4.1 Gamma image

The HGC acquired the gamma images over a period of time and the raw images were stored in .rec file extension. Subsequently, the images were analysed on a frame by

frame basis using a "blob-detection" algorithm with automatic scale selection, i.e. to find the best fit of a Gaussian distribution to each individual light splash. The scale-space theory [43] allowed the analysis of the two-dimensional (2-D) image. It created a scale-space representation from each frame of the image through the convolution of the image with Gaussian kernels of increasing scale. A scale normalised Hessian matrix (Laplace operator) was applied to each layer of scale-space representation. Local maxima in this 3-D scale space stack corresponded to a "bright blob" (point of interest) with the location of the blob given by the position of the maxima in the original image dimensions, and the scale of the blob given by the position of the maxima in the scale dimension [98].

As the scale produced was limited by the discrete values chosen for creating the scale-space representation, an additional peak fitting algorithm was applied to the scale dimension to interpolate, and therefore improved the accuracy of the result. Stepping through the frames that make up the image, every gamma interaction could be characterised by a representative Gaussian with a peak intensity, A, and a standard deviation, $\sigma$. An energy spectrum histogram was created by taking the product of $\sigma$ and A for all scintillator events [98]. The blobbed image data were then stored in .btx file extension.

The blobbed image can be displayed in either centre point or cumulative modes. Centre point mode image displayed the peak of the Gaussian fit of individual light splash as a single event; while cumulative mode image displayed the whole Gaussian fit of light splashes with a peak amplitude A and a standard deviation $\sigma$. These images were displayed in the IDL software and stored either in Digital Imaging and Communications in Medicine (DICOM), Tagged Image File Format (TIFF) or Joint Photographic Experts Group (JPEG) image format. Gamma image data analysed in this way (in DICOM or TIFF extension), could also be quantified. Customised metadata were also stored however these were incompatible with the standard nuclear medicine workstation.

### 2.5.4.2   Optical image

The current version of the optical camera was embedded with a compact chipset for space-saving and economic reasons. The generated optical images were auto-corrected with parameter of auto gain, exposure, contrast correction, and white balance. Image data was stored in JPEG image format with the colour precision of 32 bits per pixel (RGB). Simple metadata were also stored with the information limited to image size, data precision and file size.

### 2.5.4.3   DICOM image compatibility

Digital Imaging and Communications in Medicine (DICOM) is a harmonised standard in digital medical imaging developed by the American College of Radiology (ACR) and the National Electrical Manufacturers Association (NEMA). It provides necessary tools for diagnostically accurate representation and processing of medical imaging data [99]. These include protocols of data format, storage, transfer and display to encompass all functional aspects of digital imaging. DICOM enables the integration of a group of medical devices, such as workstations, printers and picture archiving and communication systems (PACS) from different manufacturers. Each device is required to state the DICOM classes in which it supported in the DICOM Conformance Statements.

A consistent set of data formats enables interchange of various type of medical imaging information on different media. Any digital image file that compliant with part 10 of DICOM Standard are considered as "DICOM files". The file consists of image data sets and header. Each header generally contains important information related to the image data sets, such as patient demographics, image acquisition parameter and so on. These DICOM attributes are organised in a standardised series of tag, for example acquisition date in the tag of "0008,0022".

The "DICOM gamma images" produced by the current version of HGC were not compatible with the DICOM 3.0 Standard, therefore they were not interchangeable or readable by any clinical workstation within the hospital environment. One requirement of the study was to reproduce these gamma images to a DICOM 3.0 standard. MATLAB® R2015b (The MathWorks, Inc., Natick, Massachusetts, USA) provides the

function of writing a DICOM image. Firstly the attributes of the image header were identified and compared with the header of the image generated by a clinical LFOV gamma camera (Nucline™ X-Ring-R, Mediso, Hungary). Matlab code was developed to edit the image header so that the essential attributes could be added to the gamma image (See Appendix A.1.). The edited DICOM image could then be loaded into and viewed by the clinical nuclear medicine workstation (Hermes Medical Solutions, London UK). This provided an interim solution to enable further analysis on the standard nuclear medicine workstation prior to any further revision of the IDL software as mentioned in Section 2.5.3.

### 2.5.5 Hybrid image

For this version of HGC, the 2-D optical images were captured directly from the optical camera electronics with the aid of bespoke interface software. The gamma camera produced a planar image. As the position of both the optical camera and gamma detector (distance between the CCD and the pinhole collimator was 10 mm) were calibrated, this resulted in a constant scale factor for all distances. However, differences in the alignment of each image required minor spatial corrections. The camera system allowed either single- or dual-modality mode acquisition during operation.

The magnification of the systems depends on the distance between the object being imaged and the collimator. This required the gamma image to be modified to match with the optical image by applying an appropriate scale factor and adjusting the orientation. The gamma image was superimposed on the optical image using the pixel addition method, with co-registration of both the gamma image pixel and optical image pixel. Figure 2.18 shows an example of the optical, gamma and hybrid images. The fused images were saved and displayed in any type of the image formats, which included Tagged Image File Format (TIFF) or Joint Photographic Experts Group (JPEG).
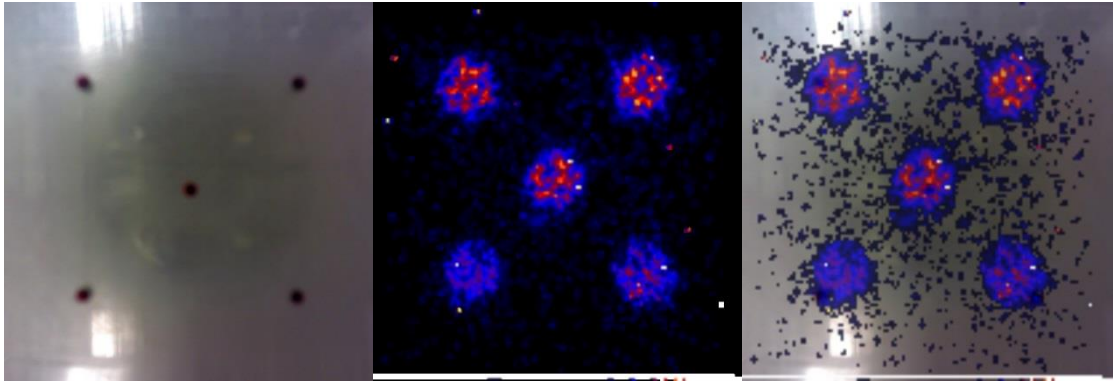
Figure 2.18: Example of the fused images (right) - a combination of the optical image (left) and gamma image (middle) of a phantom filled with red colour radioactive solution in the wells.

## 2.6   NebulEYE Mini Gamma Camera

The Universities of Nottingham and Leicester through their spin-out company Gamma Technologies Limited further developed the prototype HGC, in collaboration with Xstrahl Limited (Surrey, UK). This was intended to translate the laboratory prototype to a standard medical device. The NebulEYE mini Gamma Camera System (Nebuleye) was manufactured by the industrial partners. Figure 2.19 shows a photograph of the pre-commercial prototype Nebuleye at Queen's Medical Centre and the essential components of the camera head (Figure 2.20). The technology of the camera was similar to the HGC with minor modifications and taking ergonomic and manufacturing factors into consideration. Table 2.3 shows the technical details of the Nebuleye.
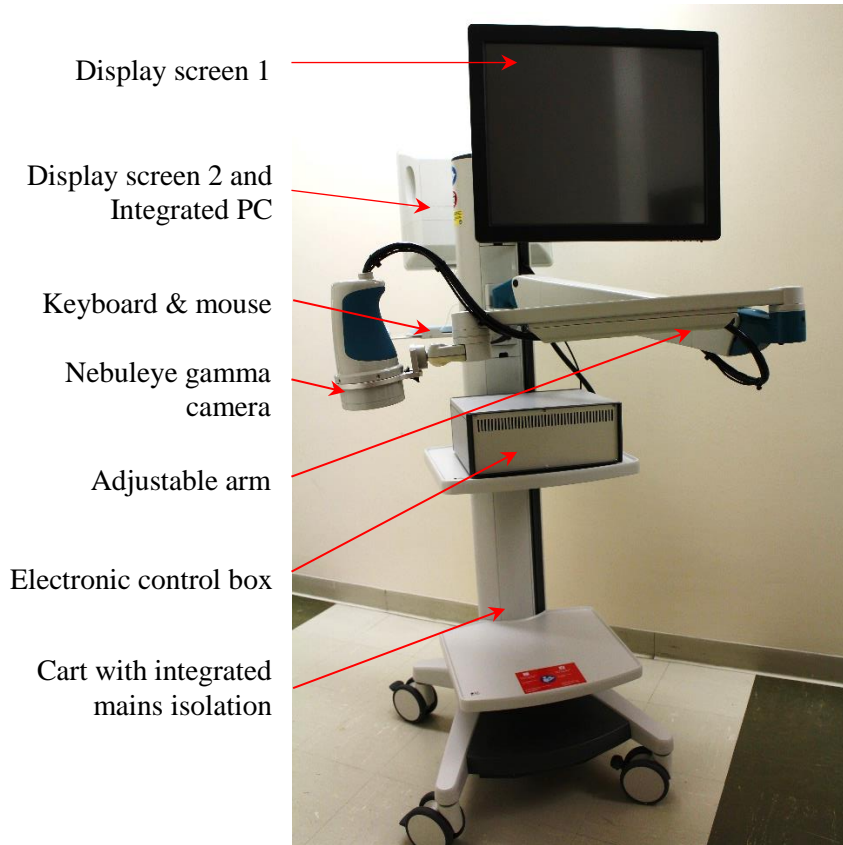
Figure 2.19: Photograph of Nebuleye Mini Gamma Camera System v1.0.
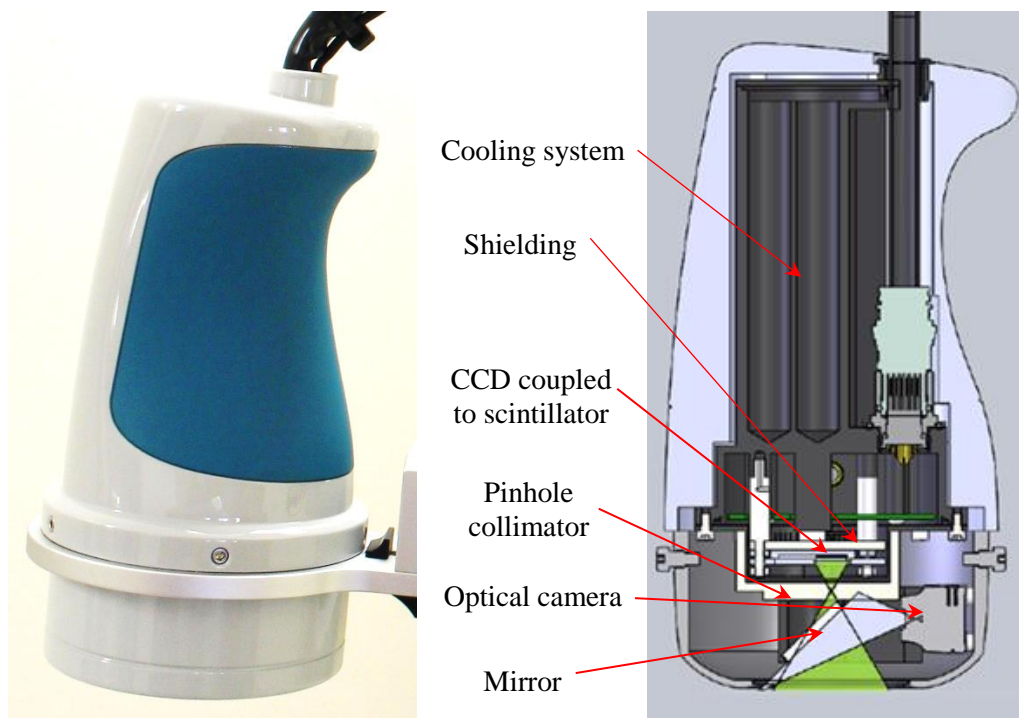


Figure 2.20: (Left) Photograph of the Nebuleye held on an articulated arm. (Right) Cross-sectional schematic diagram of the Nebuleye (Image courtesy of GTL).

Table 2.3: Technical details of the Nebuleye [100].

| | |
|---|---|
| Gamma camera detector | 1.5 mm thick CsI(Tl) coupled to CCD97 |
| Detector Operating Temperature | -10°C to -1°C |
| Energy Range | 30-200 keV |
| Collimator | 1.0 mm diameter pinhole |
| System Weight | 80 kg |
| Height | 1.978 m |
| Width | 1.449 m |

The intended use of the device was for intraoperative and bedside hybrid optical-nuclear imaging. It was mounted onto a positioning arm and trolley to assist with movement and positioning of the camera at patient's bedside and in the operating theatre.

### 2.6.1   Nebuleye Gamma Camera integrates with optical imaging

The Nebuleye gamma camera consisted of 1.5 mm thick CsI(Tl) crystal scintillator coupled to CCD, pinhole collimator, optical camera, mirror and cooling system, encapsulated in a re-designed plastic enclosure made from Acrylonitrile Butadiene Styrene (ABS). It was designed to be compact enough to be handheld by the operator and weighed approximately 1 kg. The Nebuleye utilised a single 1.0 mm diameter pinhole collimator. It was made from tungsten 6 mm thick in a circular shape around the pinhole and 3 mm thick at the sides. The pinhole collimator had a 60 degrees acceptance angle. Figure 2.21 shows the fabricated pinhole collimator removed from the camera head.



Figure 2.21: Pinhole collimator of Nebuleye.

### 2.6.2 PC with Nebuleye software

The camera system was equipped with an integrated, medically approved PC operating in Windows Operating System 7 Professional. A second touch-screen display monitor was provided offering multiple in-theatre user configurations. Bespoke Nebuleye software was developed using C# 4.0 programming language and was provided to control use and calibration of the camera system. Figure 2.22 shows the main page of the beta software providing menu options for various functions and applications.
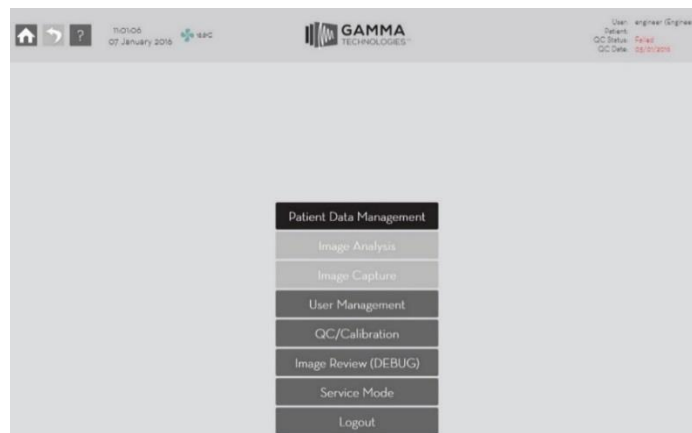


Figure 2.22: User interface of the Nebuleye software.

### 2.6.3 Image acquisition, processing and storage

As with the HGC, Nebuleye acquired the gamma image frame by frame over a period of time and the raw image was stored in .rec file extension. Simultaneously, the optical image was captured in either auto focus or fixed focal distance mode and the image data was kept in JPEG format. Both images were combined to produce a planar hybrid optical-gamma image in the same orientation. The hybrid images were stored and displayed in JPEG format. It is worth noting that at the time of writing DICOM compliance was never available with the current version of software (beta v1.3.320) which was still under development particularly for image post-processing and image storage.

### 2.6.4 Cart

The Nebuleye was supplied as a fully assembled cart based system (Pro-cart, ITD GmbH, Johanniskirchen, Germany) to assist movement in the clinical environment. This was an IEC 60601 Approved Cart with integrated mains isolation. The basic frame of the cart carried a shelf for holding the electronics box, an articulated arm to hold the

camera head, a keyboard holder with mousepad and twin monitor mountings. Brakes on the cart wheels and a push handle eased the control of the system during manoeuver, positioning and storage.

### 2.6.5 Sterile sheath

To maintain the sterility of the camera system during intraoperative procedures, a camera sheath specifically designed for the camera head was used. The sterile drape was manufactured by P3 Medical Limited (Bristol, UK) with a cap to fit into the camera head, and optical window and an adjustable sheath with three acrylic adhesive straps, long enough to cover the articulated arm and the cable (Figure 2.23), permitting the correct connection and operation of the camera. The transparent cap window with removable objective lens cover enabled the incoming light photons to pass through while minimising image degradation caused by the photon attenuation processes. Table 2.4 provides details of the sterile sheath.



Figure 2.23: The sterile drape fitted on the Nebuleye. (Inset) Clear cap window to allow production of the optical image.

Table 2.4: Technical details of the sterile sheath.

| | |
|---|---|
| Size | $150 \times 2500$ mm |
| Method of sterilisation | Ethylene Oxide |
| Cap material | Solid co-polyester sheet |
| Sheath material | Ethylene Butylene Styrene Block Copolymer |

## 2.7   Summary

This chapter has described the development of the compact SFOV gamma camera systems and incorporation of the optical cameras to become the hybrid optical gamma camera systems. Detailed descriptions of the HGC and Nebuleye were provided and this version of the camera systems, unless otherwise stated, were used in subsequent work described in this thesis. Prior to clinical use, characterisation work (as discussed in Chapter 3) and evaluation work using clinically mimicking phantom and test objects (as discussed in Chapter 5) were required to rigorously assess the performances of the camera systems. In addition, ethical and regulatory requirements as well as safety assessments needed to be addressed to ensure the device was safe to be used clinically.

# Chapter 3

# Characterisation of the SFOV Hybrid Optical Gamma Camera

## 3.1 Introduction

Testing the performance of gamma cameras is essential in order to determine if the device meets the manufacturers' specifications and is operating within the set parameter limits throughout its period of clinical use. The testing schemes adopted by the manufacturers have been based on the methods developed by international standards organisations such as National Electrical Manufacturers Association (NEMA) and the International Electrotechnical Commission (IEC). The main internationally harmonised standards relevant to medical gamma camera manufacturing are the NEMA NU 1-2012 Performance Measurements of Gamma Cameras [101] and IEC 61675-2:2015 Radionuclide imaging devices - Characteristics and test conditions - Part 2: Gamma cameras for planar, whole body, and SPECT imaging [102].

User acceptance tests or validation tests are carried out by the user after the camera has been installed in the clinical environment. The user test protocols should be identical, or as near as possible, to those used for the factory testing. This allows the user to assess if the camera complies with the specifications set by the manufacturer. These tests of the camera also provide baseline performance data for comparison with future routine performance tests for quality control purposes. National authorities and organisations such as American Association of Physicists in Medicine (AAPM), United States of America (USA) and Institute of Physics and Engineering in Medicine (IPEM), United Kingdom (UK) have also published detailed test protocols for regular use in the clinical setting. Both the acceptance and reference tests are required to be repeated if there has been a change in camera components, such as due to equipment breakdown or a major service that could affect camera performance.

Routine quality control tests are performed at regular intervals as specified in the local protocols and operating procedures. Some of these are operational checks which should be carried out daily before the camera is used. The results of these tests are then compared with the baseline values to determine if the pre-defined performance limits are met. Details of the routine quality control tests for the SFOV Hybrid Optical Gamma Camera are discussed in Section 6.5. At the time of writing, there was a lack of harmonised protocols for the testing of SFOV gamma cameras. Moreover, the SFOV Hybrid Optical Gamma Camera involves the combination of gamma and optical cameras both of which require individual image quality assessment in addition to checking the alignment of fused images. Figure 3.1 summarises the levels of a gamma camera performance assessments based on the International Atomic Energy Agency (IAEA) publications [103].

**Factory testing**
- by the manufacturer with harmonised protocols in factory settings
- to determine the required specifications are met and compare with other similar device
- NEMA, IEC standards

**Acceptance testing**
- by the user and/or technical specialist after installation or major change of device component(s) with harmonised protocols
- to confirm the manufacturer's specifications are met

**Reference testing**
- by the user before clinically use or major change of device component(s) using national, in house or manufacturer protocol
- to establish the device baseline performance
- IPEM, AAPM, IAEA guidelines

**Routine testing**
- by the user routinely using national, in house or manufacturer protocol in clinical settings
- to confirm the performance limits are met

Figure 3.1: Performance assessments throughout a gamma camera's life cycle (Based on IAEA Human Health Series No. 6 [103])

In this chapter, the tests for characterising the performance of the new prototype Nebuleye camera are described. The camera was assessed using a set of modified characterisation protocols specifically developed for SFOV cameras. The test results were then compared with the prototype HGC.

## 3.2   Performance characterisation of the cameras

The Nebuleye mini gamma camera system is a combined optical and gamma camera system intended for intraoperative and bedside hybrid imaging.  The system provides gamma images to illustrate the physiological information of a living subject administered with a radiopharmaceutical, and optical images to show the anatomical information of the region of interest. The camera head is mounted onto an ergonomic arm and cart to assist the movement and positioning of the device, enabling the camera system to be used at patient's bedside and in the operating theatre.

The performance of the pre-commercial prototype Nebuleye camera was assessed using protocols that had been specifically developed for testing SFOV gamma cameras. These test protocols were modified procedures developed by the Universities of Leicester and Nottingham [104, 105], based on those produced by the Institute of Physics and Engineering in Medicine (IPEM) [106] and the International Atomic Energy Agency (IAEA) [103]. The testing procedures were adjusted to suit the newly designed camera system and were harmonised to make inter-comparison possible between similar imaging systems.  Most of the procedures have two test components, namely an intrinsic and extrinsic measurement. An extrinsic test, which is also known as a system test, includes the effect of the collimator. Bugby et al [105] has reported the performance tests of SFOV gamma cameras which includes intrinsic uniformity, sensitivity, intrinsic and extrinsic spatial resolution, spatial linearity and count rate capability. The system uniformity and sensitivity, detector head shielding leakage, optical-gamma alignment, as well as optical image quality test were carried out experimentally for the first time.

During the experimental period, the software and hardware were in a period of development. The two camera systems used in the characterisation tests were the early pre-commercialised prototype of Nebuleye (Nebuleye 2 and Nebuleye 3) which were

provided by the manufacturer for testing and research purposes. These cameras were almost identical except that the optical rig in Nebuleye 3 was upgraded to provide a more accurate alignment for gamma-optical image fusion. This version of software did not include 'blob detection' feature, hence the software mentioned in Section 2.5.3 was used to analyse the gamma images, enabling further quantification work to be carried out. All radioactivity used in the experiments was obtained from the radiopharmacy unit at Queen's Medical Centre and assayed using a dose calibrator (CRC®-25R, Capintec Inc, NJ, USA).

Image analysis was carried out using IDL software v8.5.1 (Exelis Visual Information Solutions, Inc., Boulder, CO, USA), ImageJ 1.50b (NIH, USA), MATLAB® R2015b (The MathWorks, Inc., Natick, Massachusetts, USA) and GraphPad Prism version 6.07 for Windows (GraphPad Software, La Jolla California, USA). The following parameters were assessed:

    a) Intrinsic spatial resolution (Section 3.2.1)

    b) System spatial resolution (Section 3.2.2)

    c) Intrinsic uniformity (Section 3.2.3)

    d) System uniformity (Section 3.2.4)

    e) Intrinsic sensitivity (Section 3.2.5)

    f) System sensitivity (Section 3.2.6)

    g) Spatial linearity (Section 3.2.7)

    h) Count rate capability (Section 3.2.8)

    i) Detector head shielding leakage (Section 3.2.9)

    j) Optical-gamma alignment (Section 3.2.10)

    k) Optical image quality (Section 3.2.11)

### 3.2.1   Intrinsic spatial resolution

The intrinsic spatial resolution is a measure of the sharpness and detail of a gamma image, without use of the collimator. It is normally reported either as the full width at half maximum (FWHM) of the line spread function (LSF) produced from a thin line source, or point spread function (PSF) obtained from a point source, or as the minimum separation of two sources that can be discriminated from each other.

The testing protocol used for this work was based on the method suggested by Bugby *et al.* [105]. The camera head was turned to face vertically downward. A 10 mm-thick lead mask, containing a machined slit of 2 mm width and 20 mm length in dimension was placed on the face of the un-collimated gamma camera. The position of the slit was carefully aligned with the x and y axes of the camera head. The distance between the mask and scintillator detector was 8.5 mm due to camera design. The camera was irradiated by gamma fluxes originated from a 3 mm-diameter $^{99m}$Tc point source (15.3 MBq) placed 250 mm away from the mask (Figure 3.2). Images were acquired containing 18000 frames (30 minutes). The procedure was repeated with the lead mask rotated through an angle of 90°.



Figure 3.2: Photograph of experiment set up during intrinsic spatial resolution test. A $^{99m}$Tc point source was positioned at a distance of 250mm from the attached slit mask.

In each case the resulting image was a line corresponding to the spatial distribution of detected events resulting from the gamma rays that passed through the slit mask. A line profile was drawn on the image display perpendicular to the slit image and presented as edge response function (ERF). Then the line spread function (LSF) was derived by performing the first differentiation of the ERF. Each peak of the LSF plot was fitted with Gaussian distribution model in order to determine the full width at half maximum (FWHM) and the full width at tenth maximum (FWTM) values.

Figure 3.3 (a) shows an example of the resulting image for the intrinsic resolution test with the slit mask positioned horizontally. Due to the lead mask not being perfectly aligned with the detector array principal axes, the acquired image was rotated to account for the misalignment. Figure 3.3 (b) shows the ERF across the line profile with the summed number of counts at y-axis. The low level signal (5 ± 4 counts) at both sides of the image indicates the background count level while the high count levels (176 ± 12 counts) represents the counts within the slit. Where the number of counts within the slit remains level the graph shows a plateau situated between steeply ascending and descending edges. The derivative of the ERF generates the LSF as shown in Figure 3.3 (c). The two peaks indicate the edges of the slit profile. The results were then presented in absolute values (modulus of negative values) with Gaussian model fitted as shown in Figure 3.3 (d).
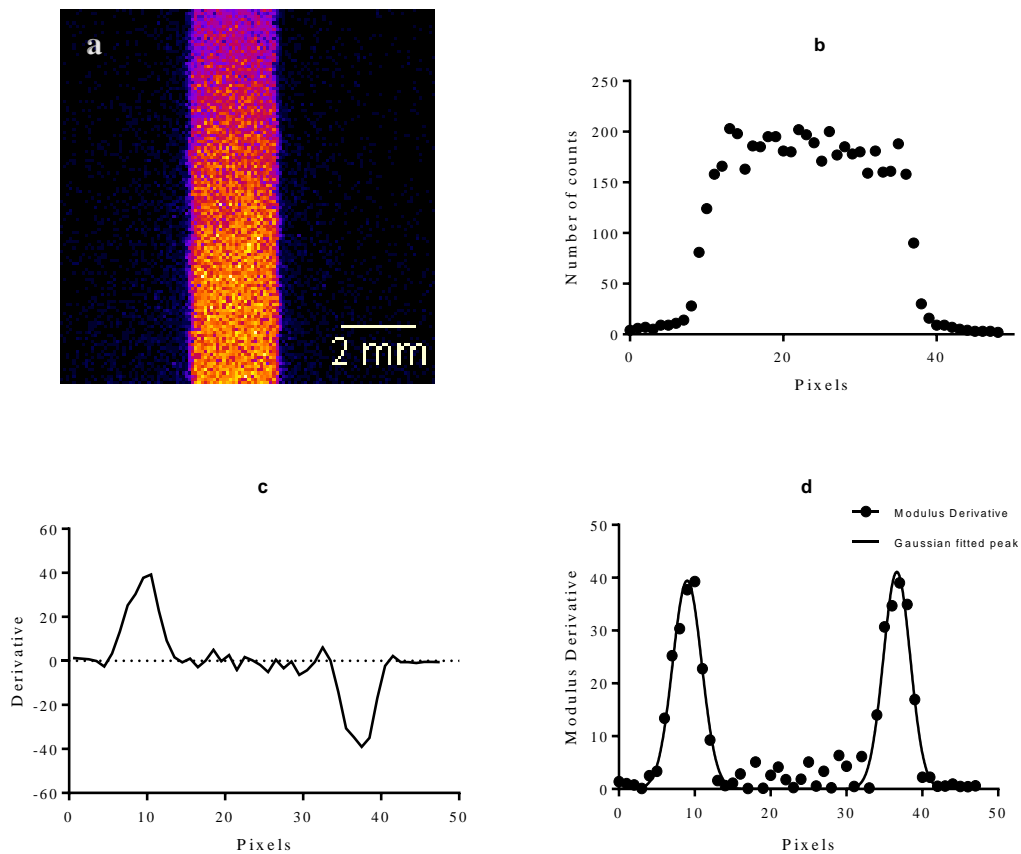


Figure 3.3: (a) Example image of the slit mask (rectangle shaped) taken by the camera with 30 minutes acquisition time was plotted as (b) ERF. (c) LSF was calculated as the first derivative of the ERF and (d) the absolute value of the results were Gaussian fitted.

Table 3.1 tabulates the mean resolution measurements of the camera using both edges of the slit images where the slit was orientated parallel and perpendicular to the detector array's principal axes in respective acquisition. The measured resolution of the camera was approximately 4 to 5 pixels (pixel size 64 µm × 64 µm).

Table 3.1 Intrinsic resolution measurement of Nebuleye.

| Parameter | Measurement |
|---|---|
| **FWHM (mm)** | $0.28 \pm 0.02$ |
| **FWTM (mm)** | $0.52 \pm 0.03$ |

### 3.2.2   System spatial resolution

System spatial resolution ($R_s$) is the measure of the sharpness of the image recorded with a gamma camera, which includes the effect of collimator and can be estimated by:

$$R_s = \sqrt{R_i^2 + R_c^2}$$

3.1

where $R_i$ is the intrinsic resolution and $R_c$ is the collimator resolution. For pinhole collimators, several parameters determine the collimator resolution, these include pinhole diameter, source-to-collimator distance (SCD), the angle between the source and the central axis, the length of the collimator hole, the pinhole acceptance angle and the collimator material (which affects the linear attenuation coefficient) and energy of the radionuclide imaged. This measurement is more clinically relevant in comparison to the intrinsic spatial resolution. As a rule of thumb, the system spatial resolution degrades as the SCD increases. For SFOV gamma cameras mounted with a pinhole collimator, the system spatial resolution is normally reported as the FWHM and FWTM of a LSF or PSF at the non-magnifying point with scattering medium.

The measurement was carried out with the 1 mm diameter pinhole collimator in place and the camera head was turned to face vertically downward. A 1 mm diameter capillary tube (source width identical to the geometric resolution of the pinhole at the non-magnifying point) filled with 39.3 MBq of $^{99m}$Tc (at a concentration of 78.6 MBq ml$^{-1}$) was used as line source. The capillary tube was positioned as a straight line in between two PMMA plate of 5 mm in thickness which placed adjacent to each

other as shown in Figure 3.4. Image acquisition was carried out for 300 s with a PMMA block 10 mm in thickness placed in between the camera head and the line source. Then the procedures were repeated with various PMMA blocks thickness range between 20 mm and 70 mm at 10 mm interval.
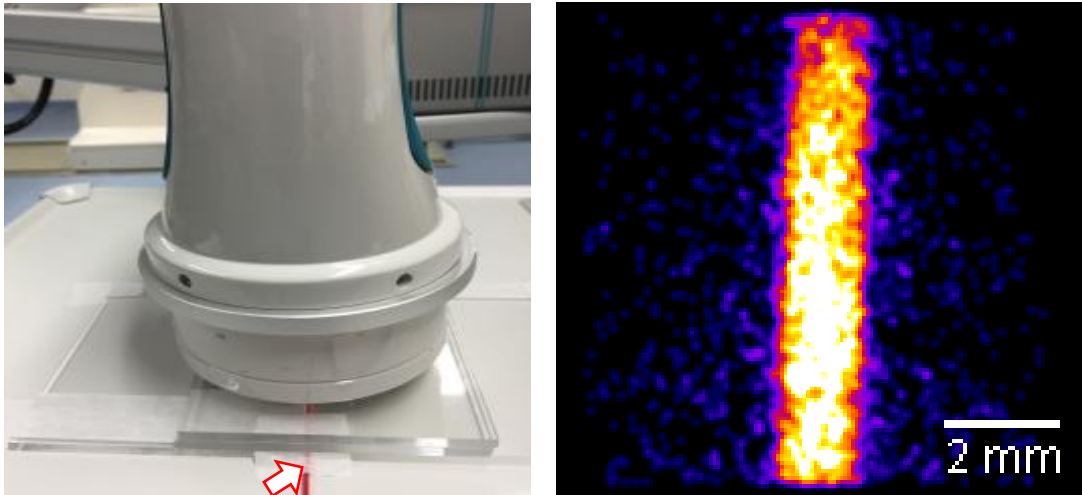


Figure 3.4: (Left) Photograph of equipment set up during system spatial resolution test. A PMMA plate 10 mm in thickness was positioned between a $^{99m}$Tc line source (arrow) and the camera head. (Right) Example image of the line source with 10 mm PMMA as the scattering medium, taken by the camera with 5 minutes acquisition time. Image was post-processed with the multiplication of 100 and smoothing filter of 1 pixel was applied. Magnification factor was incorporated on the image scale bar.

Figure 3.4 (right) shows the resulting image of the test with a line corresponding to the shape of a line source. A line profile was drawn perpendicular to the line source and the data was Gaussian fitted. The FWHM and FWTM values were calculated. The magnification factor was taken into consideration during the calculation of the values based on the SCD. These values were then plotted against the thickness of PMMA and the graph was fitted by linear regression. From the linear equations, the FWHM and FWTM at the non-magnifying position (SCD at 10 mm) were extrapolated since the experimental measurement was not possible at this position due to the occupancy of the optical rig in front of the collimator.

Figure 3.5 shows a graph of the computed resolutions against the PMMA thickness. Resolution degrades with the increase in the PMMA thickness. The linear relationship between distance, $d$ (scattering material) and resolution for the camera are tabulated in Table 3.2. The FWTM values increase more rapidly than the FWHM values due to the decrease in signal-to-noise ratio (as a result of reducing sensitivity) with increasing

thickness of the PMMA as discussed in 3.2.5. The FWHM resolution at the non-magnifying distance (10 mm) and at the camera head window surface (28 mm) were found to be $1.84 \pm 0.69$ mm and $3.08 \pm 0.71$ mm respectively.
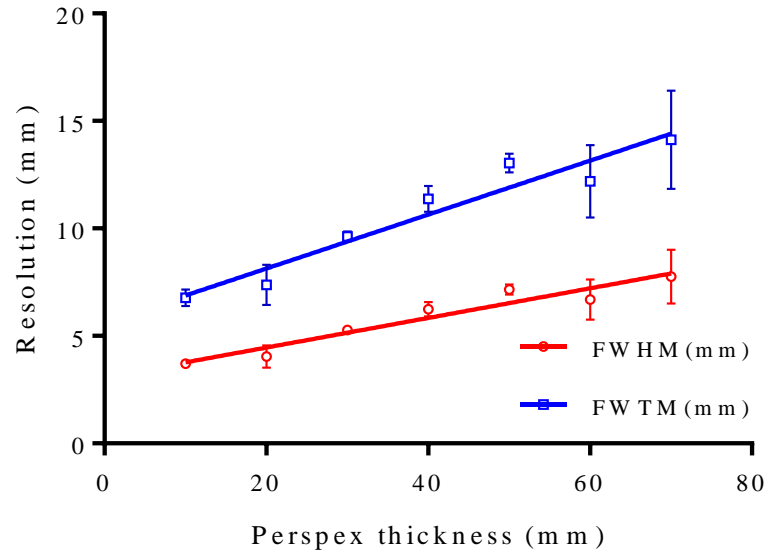


Figure 3.5: System spatial resolution measurements for Nebuleye using 1.0 mm diameter pinhole collimators. FWHM (red circles) and FWTM (blue squares) values with the best fitted lines for a range of PMMA thickness are plotted (n=3).

Table 3.2: Linear relationship between depth of scattering material and resolution of the camera with gradient m and y-intercept c calculated using GraphPad Prism software.

| Resolution | Fitted parameters | | $R^2$ |
|---|---|---|---|
| | **m** | **c** | |
| FWHM | $0.069 \pm 0.009$ | $3.081 \pm 0.387$ | 0.927 |
| FWTM | $0.126 \pm 0.016$ | $5.624 \pm 0.706$ | 0.927 |

### 3.2.3   Intrinsic uniformity

The intrinsic uniformity is a measure of the degree of uniformity of count density across the detector. It is measured by irradiating the camera detector with a uniform flux of incident photons, without a collimator in place. The variations of the count density within the image indicate changes of camera performance caused by spatial non-linearity and inaccuracy of energy response. Intrinsic uniformity may be quantified either by the changes in uniformity over an entire image or variation in count density over a specified distance. In general, a lower value indicates a higher uniformity.

A 3 mm diameter point source containing 26.4 MBq of $^{99m}$Tc was placed 350 mm away from the detector face to provide a uniform gamma irradition across the detector (Figure 3.6). At least two flood images were acquired with 30 minutes acquisition time. Dark image, or known as background image were taken with 600 s acquisition time, without the presence of radioactive source. Matlab code was developed to analyse the image (See Appendix A.3.).



Figure 3.6: Experimental set up for the intrinsic uniformity test. A $^{99m}$Tc point source (arrow) was placed underneath of the Nebuleye with the collimator removed.

Figure 3.7 (a) shows an example of the resulting flood field image. Higher count densities were found in the middle of the image (count densities gradient gradually decreased from bottom to top of image). This could be due to the dark signal gradient of the CCD with the increase of detector temperature over image acquisition. Several pixels of outliers were noticeable particularly a cold spot indicating lower detection efficiency regions. For the flat field correction, a flood mask image was created by subtracting the dark image from flood field image followed by normalising the resulting image to its maximum pixel value, to create a correction map with consistent dynamic range. For uniformity quantification, a flood field image was subtracted with dark image and divided by the flood mask image to correct the non-uniformity of the image. A median filter was applied to the resulting image and it was subsequently quantified

by obtaining the maximum, minimum, mean and standard deviation of counts per pixel of the image (Figure 3.7(b)). In this test, the overall and regional changes in the image uniformity is reported as integral uniformity, coefficient of variation (CoV) and differential uniformity (DU) respectively [106]. Integral uniformity (IU) is a measure of the overall uniformity of the whole field of view. It is defined as:

$$IU = \frac{C_{max} - C_{min}}{C_{max} + C_{min}} \times 100\%$$

<div align="right">3.2</div>

where $C_{max}$ and $C_{min}$ are the maximum and minimum counts per pixel of the image. CoV is a measure of the overall variation of count density in the image and is defined as a percentage (%):

$$CoV = \frac{\sigma}{M} \times 100$$

<div align="right">3.3</div>

where $\sigma$ is the standard deviation of counts per pixel and M is the mean counts per pixel. DU can be calculated by Equation 3.4. The mean differential uniformity was then computed with 10 times of repeated DU quantification.

$$DU = \frac{C_{max} - C_{min}}{C_{max} + C_{min}} \times 100$$

<div align="right">3.4</div>

where $C_{max}$ and $C_{min}$ are the maximum and minimum counts per pixel of the image.
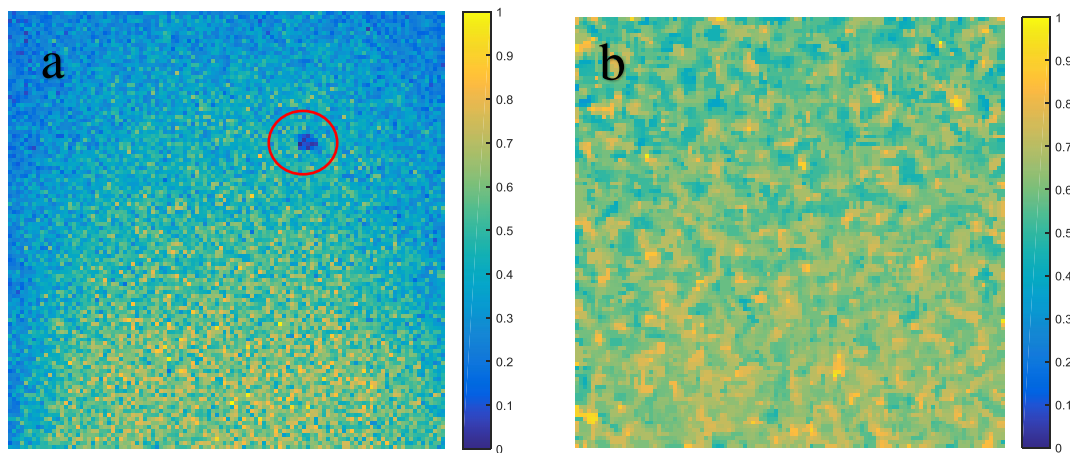


Figure 3.7: (a) Example of a raw flood field image obtained by Nebuleye 2 and (b) the resulting image after flat field corrections were applied. A cold spot (red circle) was observed in the raw flood field image indicating lower detection efficiency regions.

Table 3.3 tabulates the calculated uniformity measurements of the camera. Integral uniformity was more than 50 % indicating poor intrinsic uniformity across the entire FOV. Similarly, CoV was higher than DU indicating big difference in count densities with pixels of very high or low counts within the FOV. This is further confirmed by examining the pixel intensity profile (variation of count densities) across representative row of the uniformity-corrected image (Figure 3.8). These values were normalised to the mean intensity of the pixels within the selected row. The number of counts were range from 49 to 89 counts per pixel (67 ± 9 mean counts per pixel).

Table 3.3: Intrinsic uniformity measurements of Nebuleye.

| Uniformity Measurement | Measurement (%) |
|---|---|
| Integral uniformity | 51.72 |
| Coefficient of variation | 13.54 |
| Differential uniformity | 8.34 |
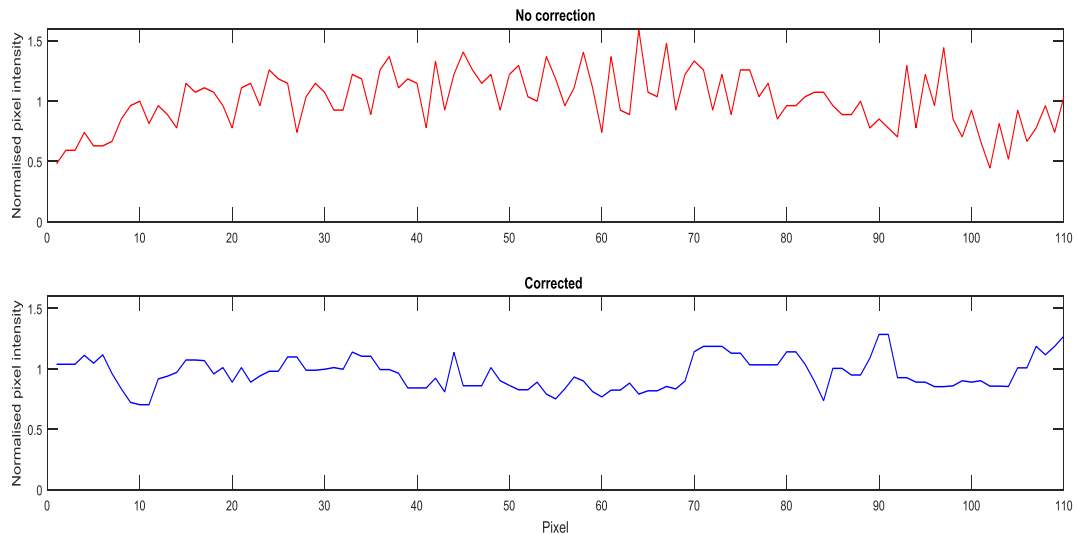


Figure 3.8: Normalised pixel intensity of the flood image without correction (top) and with correction (below) for intrinsic uniformity test.

### 3.2.4 System uniformity

Similar to the intrinsic uniformity test, system uniformity is a measure of deviation of count densities in an image, which includes the effect of any irregularities in the collimator. In this test, the overall and regional changes of an image uniformity are reported as the integral uniformity, coefficient of variation (CoV) and differential uniformity (DU) respectively. This test was newly introduced to examine the

performance of the SFOV gamma camera, as it is a more realistic and clinically relevant way of assessing the camera's performance. It may serve as a daily quality control check because it can be performed without removing the collimator. The system uniformity test is a measurement recommended by IPEM [106]. For LFOV gamma cameras, the test is carried out using a thin flood source of $^{99m}$Tc (approximately 64 × 45.5 cm in dimension) placed against the collimator to irradiate the entire FOV with uniform flux of photons.

For this measurement, a 40 ml Greiner standard cell culture flask (nominal size (mm): 70 (L) × 35 (W) × 24 (H)) was filled with 15 ml of mixed coloured water and $^{99m}$Tc pertechnetate solution (TcO$_4^-$) in a concentration of 2.2 MBq/ml. The cell culture flask is made of high-grade polystyrene with standard screw cap to avoid the radioactive source causing contamination. The camera, fitted with 1 mm diameter pinhole collimator, was turned to face vertically downward. The flood source was positioned with a source to camera surface distance of approximately 13 mm to provide a uniform gamma illumination across the detector. Figure 3.9 shows the experiment set up for the system uniformity test. At least two flood images were acquired with acquisition time of 30 minutes respectively. A dark image, also known as a background image, was taken without the presence of radioactive source with a 200 s acquisition time.
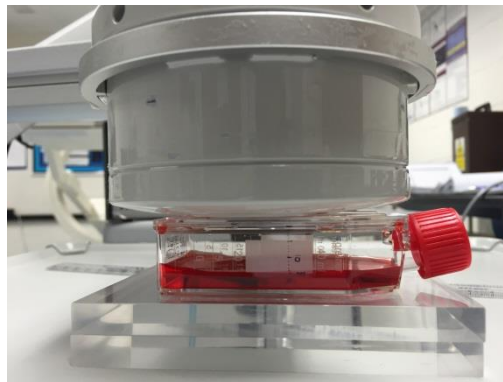


Figure 3.9: The flood source placed within field of view of the camera.

Figure 3.10 (a) illustrates an example of the resulting flood field image. Higher count densities were found in the middle of the image (count densities gradient gradually decreased from bottom to top of image). As discussed earlier, this might due to the dark signal gradient of the CCD with the increase of detector temperature over image

acquisition. Flat field correction method was identical in Section 3.2.3 where a flood mask image was created by subtracting the dark image from flood field image followed by normalising the resulting image to its maximum pixel value. Subsequently, a flood field image was subtracted with dark image and divided by the flood mask image to correct the non-uniformity of the image. Then a median filter was applied to the resulting image prior further quantification (Figure 3.10 (b)).
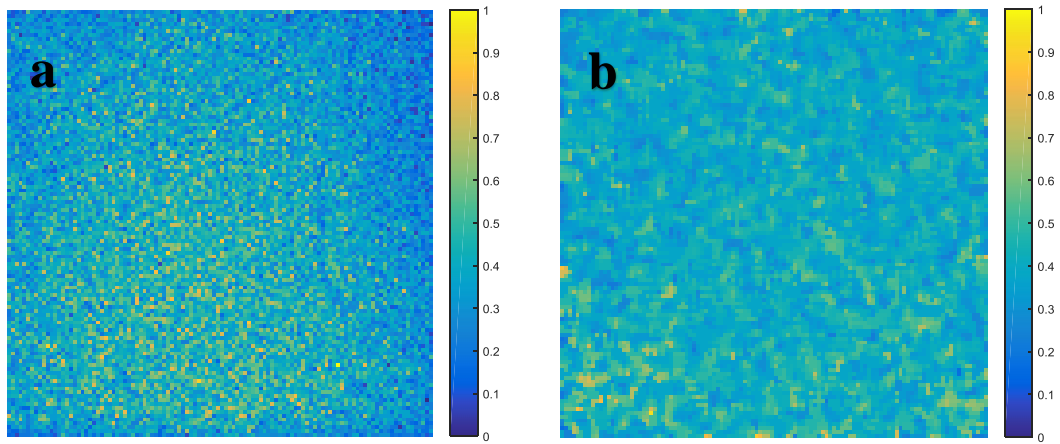


Figure 3.10: (a) Example of flood field image and (b) corrected flood image obtained by Nebuleye 3.

Table 3.4 tabulates the calculated uniformity measurements of the camera. The CoV value for original image and uniformity corrected image was 35% and 20% respectively, where it shows a significant improvement after the correction applied. The IU was higher than DU indicating big difference in count densities with pixels of very high or low counts within the field of view. It was also higher than the IU quantified in intrinsic uniformity test. One of the reasons was due to the spatial non-uniformity caused by the pinhole collimator [16]. Figure 3.11 illustrates the pixel intensity profile (variation of count densities) across representative row of the uniformity-corrected image. These values were normalised to the mean intensity of the pixels within the selected row. The number of counts were across a range from 21 to 48 counts ($32 \pm 5$ mean counts per pixel).

Table 3.4: NebulEYE mini gamma camera system uniformity measurements with uniformity correction applied.

| Uniformity Measurement | Measurement (%) |
|---|---|
| Integral uniformity | 70.73 |
| Coefficient of variation | 19.58 |
| Differential uniformity | 16.55 |
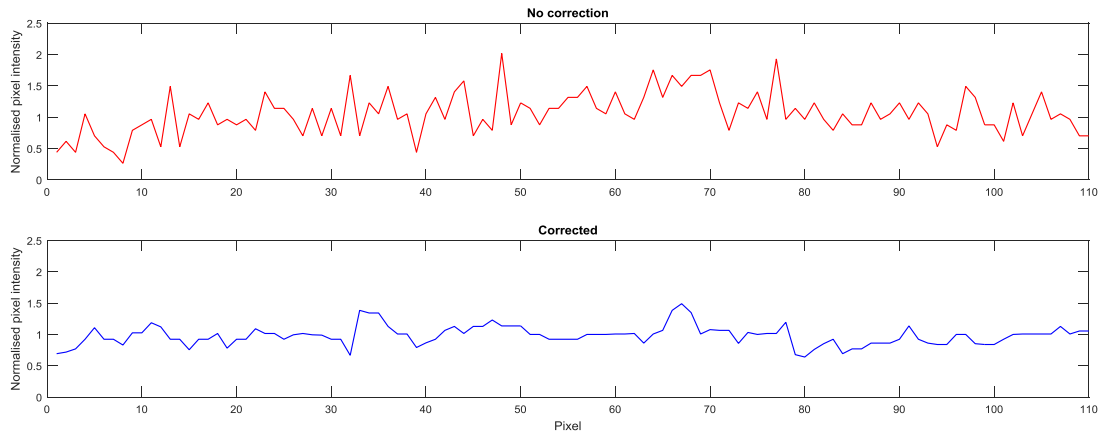
Figure 3.11: Normalised pixel intensity of the flood image without correction (top) and with correction (below) for the system uniformity test.

### 3.2.5 Intrinsic sensitivity

The intrinsic sensitivity is a measure of the proportion of the detected gamma rays emitted from a known activity of radionuclide by a gamma camera without collimator in place. It is usually reported as the ratio of the count rate per unit activity measured in units of cps MBq$^{-1}$ at a defined distance from the source to the detector surface. Several factors influence the sensitivity of the camera, such as type of radionuclide and thickness of scintillation crystal. The sensitivity of the camera is proportional to the thickness of the crystal and inversely proportion to the radionuclide energy and the thickness of the scattering medium.

A 3 mm-diameter hole was filled with 16 MBq $^{99m}$Tc to act as point source and was placed 250 mm away from the detector surface. The strength of the radioactivity was assayed and the exact time of the measurement was also recorded. A flood image was acquired with acquisition time of 500 s. The image acquisition was repeated with the addition of scattering medium (PMMA range from 10 mm to 70 mm at 10 mm interval) in between the source and the camera. The time for each acquisition was recorded. Raw images were post-processed (without applying a correction map) and the number of counts were quantified. The counts in the region of interest (ROI) of the image was used to determine the count rate and the activity was corrected based on the time of the measurement and standard decay calculations.

Figure 3.12 shows the relationship between the intrinsic sensitivity of the camera and the thickness of the scattering medium. At these experimental settings, the thickness of

PMMA required to reduce the sensitivity to half was 67 mm ($r^2$=0.99). The intrinsic sensitivity was 12.4 cps MBq$^{-1}$ with the source positioned at 250 mm away from the detector surface, which is approximately 15% of the estimated incident photons calculated from the solid angle formulae (Equation 3.5).

$$\Omega = 4\tan^{-1} \frac{\alpha\beta}{2h\sqrt{4h^2+\alpha^2+\beta^2}}$$

3.5

where *h* is the distance of a source placed at the centre of a rectangular detector of dimensions $\alpha \times \beta$. The incident photons on the detector from an isotropic point source is the proportion of photons $\frac{\Omega}{4\pi}$. In contrast, the theoretical sensitivity of the camera with a thickness of 1.5 mm CsI(Tl) crystal is 43.6% at 141 keV [107]. In general, the decrease of SFOV gamma camera sensitivity might due to the following reasons:

    a) inefficiency in the detector coupling between the crystal and the EMCCD

    b) losses of count due to the smaller size of detector and the position of the source

    c) attenuation within the source holder

    d) attenuation by the aluminium lid (as the vacuum lid positioned in front of the detector) (HVL for aluminium at 140 keV ~18 mm)
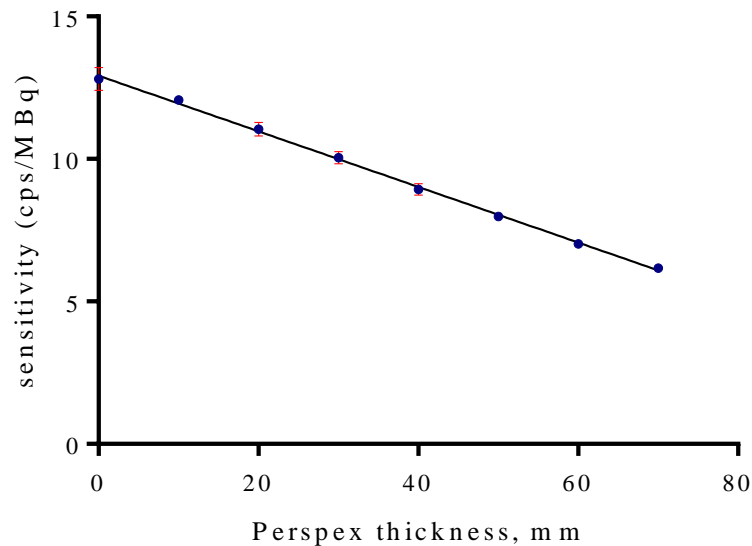


Figure 3.12: Relationship between intrinsic sensitivity and the depth of scattering medium (n=3).

### 3.2.6   System sensitivity

The system sensitivity is a test of the count rate response of a collimated scintillation camera to a radionuclide source of known radioactivity. It is reported as the ratio of the count rate per unit activity measured in units of cps MBq[-1] at a defined distance from the source to the detector surface (usually at the non-magnifying point). This parameter is mainly influenced by the intrinsic sensitivity of the detector and the collimator efficiency, *g*. Therefore, it needs to be measured individually for each collimator. For a pinhole collimator, collimator efficiency [14] is given by

$$g \approx \frac{d_{eff}\cos^3\theta}{16b^2} \qquad\qquad 3.6$$

where $d_{eff} = \sqrt{d\left[d + 2\mu^{-1}tan\frac{\alpha}{2}\right]}$. Based on Equation 3.6, the collimator efficiency is directly related to the effective pinhole diameter and decreases with increasing SCD.

In the experiment, approximately 20 MBq of ^{99m}Tc-pertechnetate solution was held in a 3-mm diameter well. Then the activity of the source was assayed in the radionuclide dose calibrator and the time was recorded. Figure 3.13 shows the experimental setup during the test. A 1.0 mm diameter pinhole collimator was fitted in this version of camera. A 200 s planar image was acquired, with and without the presence of scattering medium. The acquisition was repeated at the source to camera surface distance between 10 and 70 mm (PMMA range from 10 mm to 70 mm at 10 mm interval). The time for each acquisition was recorded. Raw images were post-processed (without applying a correction map) and the number of counts were quantified in order to compute the decay corrected count rate in the ROI selected in the image.
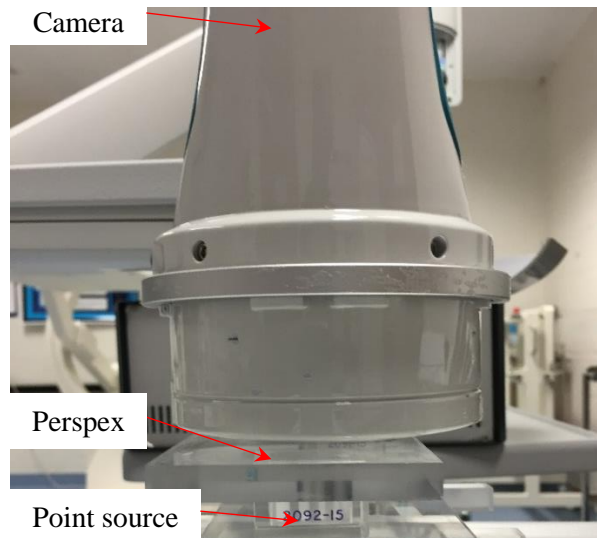
Figure 3.13: Experimental set up for system sensitivity test.

In this test, a series of measurements using the same point source (with or without scatter in between source and the camera) at different SCD were taken to measure the system sensitivity. Figure 3.14 shows the relationship between the system sensitivity and the SCD in comparison with the calculated collimator efficiency. The measured system sensitivity and the calculated collimator efficiency decreased with the increase of the SCD. By extrapolating the measurements, the system sensitivity was 8.86 cps MBq$^{-1}$ at the non-magnifying distance and 3.82 cps MBq$^{-1}$ at 50 mm away from the collimator without the presence of the scatter. With the presence of the scattering medium, the system sensitivity was lower in comparison with the data acquired without the scattering medium.
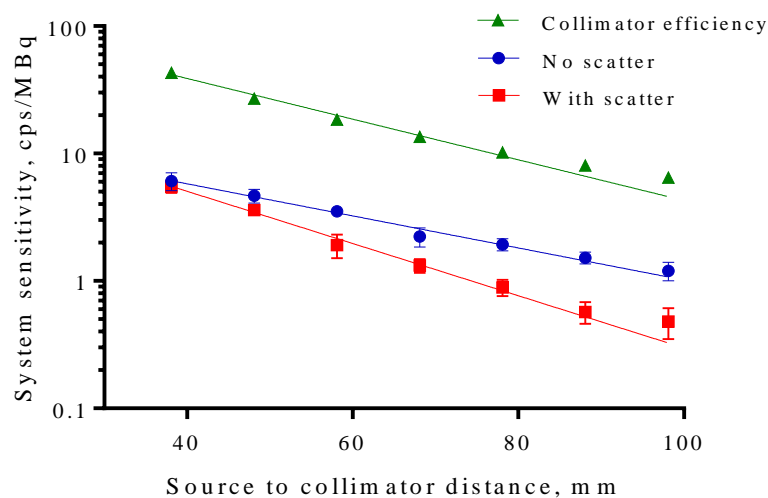


Figure 3.14: Relationship of the collimator efficiency and system sensitivity (blue line-without scatter; red line-with scatter) of the camera with the depth of scattering medium (n=3).

### 3.2.7 Spatial linearity

Spatial linearity is a measure of the spatial distortion calculated by assessing an image of a line produced by a slit mask. It is carried out intrinsically therefore excludes the effects of collimator. It is reported as the absolute linearity (maximum deviation from best-fit line) and the differential linearity (standard deviation of the best-fit line) in the unit of mm. As this is an SFOV gamma camera, a slit mask was used to create a line in gamma image. The experimental set up was identical to the intrinsic spatial resolution test, enabling the images generated from the test were used for this purpose. The same experimental procedures were repeated with the lead mask rotated through 90°. This is to examine the non-linearity of the line image in both x and y direction.

Figure 3.15 shows the resulting image of the slit mask irradiated by the uniform gamma flux in both the horizontal and the vertical orientation. Ideally the line in the image should appear straight. Due to the lead mask not being perfectly aligned to the x and y axes of the detector arrays, the acquired image was rotated to account for the misalignment. For both images, pixel intensity profiles of the ROI within the slit image were obtained and the profiles were fitted with Gaussian function. The peak value of the Gaussian distribution was determined and considered as the estimated center point of the slit profile. Then the difference between each center point and its mean value was calculated in term of mean, maximum and standard deviations. Then all measurements were converted to the unit of µm. During the analysis, 120 of 132 rows across the slit were included in the calculations. Those excluded rows were out of the ROI or due to low signal-to-noise ratios.

Table 3.5 tabulates the results of the linearity measurements for the camera.
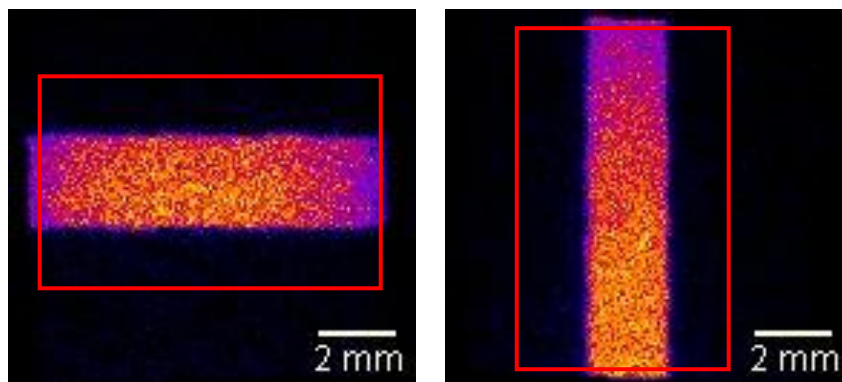


Figure 3.15: Horizontal and vertical slit images with the regions of interest (red rectangle).

Table 3.5: Linearity measurements of Nebuleye.

| Linearity Measurement | Measurement (µm) | | |
|---|---|---|---|
| | **Vertical** | **Horizontal** | **Average** |
| Mean deviation | 50.3 | 108.0 | 79.2 |
| Absolute linearity | 198.0 | 288.0 | 243.0 |
| Differential linearity | 38.0 | 66.0 | 52.0 |

### 3.2.8 Count rate capability

The count rate capability of a scintillation camera is a measure of the relationship between the recorded count rate and the intensity of incident gamma photons. Ideally the recorded count rate is directly proportional to the incident count rate, however the performance does deteriorate at high count rates. As the count rate increases, there is a chance of recording two events at the same time, resulting in counting losses. This causes the recorded count rate to deviate from the incident count rate especially when high count rates can result in signal losses where the camera detection process may be paralysed or part-paralysed. IPEM [106] and Bugby *et al.* [105] suggested that this parameter should be reported in term of the input count rate, in cps units at which there is a 20% difference between the recorded and input count rate. In contrast, NEMA [101] and Cherry *et al.* [14] have recommended that the observed count rate at 20% loss should be reported. The maximum recorded count rate is also typically stated [101, 103, 106].

This test was carried out intrinsically without the presence of scattering medium. The decaying source method was used to determine the recorded count rate at each specific time interval, until the activity of the source was negligible. In this experiment, a series of nine point sources containing $^{99m}$Tc pertechnetate solution with known activities range from 2 to 550 MBq was filled in a vial. The activity of the source was measured in the radionuclide dose calibrator and the time of day was recorded. Figure 3.16 shows a vial filled with radioactive source placed at 350 mm away from the detector surface during the test. Each source was imaged with 10 s acquisition. The acquisition was repeated at 1 hour intervals over 6 hours to ensure that a range of input count rates were included.

The exact time of each acquisition was recorded. Raw images were post-processed (without applying a correction map) and the number of counts were quantified in order to compute the background and decay corrected count rate. The incident counts were calculated based on the activity of the source at the time the image was taken using the solid angle formulae (Equation 3.5). Recorded count rate versus incident count rate was plotted and a line of best fit calculated for the linear region was generated in order to calculate the relationship between the measured count rate and the incident count rate.
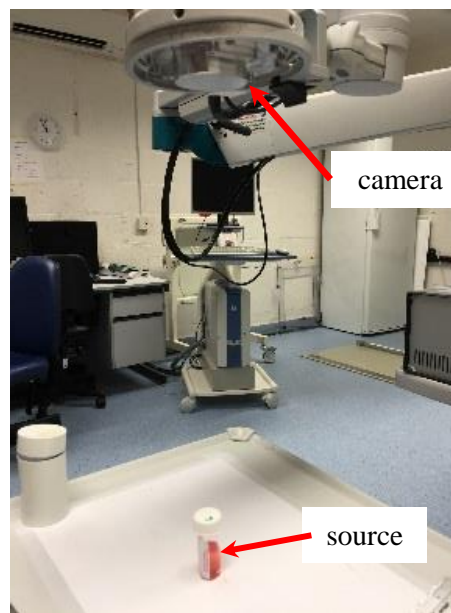


Figure 3.16: The radioactive source was placed 350 mm away from the uncollimated Nebuleye.

Figure 3.17 shows the count rate response curve obtained for the Nebuleye. It illustrates that the camera was paralysable. The linear region of the curve occurred at low count rates ($r^2$=0.993) suggesting that the detection efficiency of the camera was almost linear for incident count rate up to 11 kcps. The input count rate and recorded count rate at which there is a 20% loss was 15.71 kcps and 2537 cps respectively. The maximum recorded count rate was 2845 cps. As described in Section 3.2.5, the detection efficiency of the camera without the collimator was approximately 15% of the incident photons. This has resulted in the measured count rate being lower in comparison with a typical LFOV gamma camera. The maximum recorded count rate for a clinically used LFOV gamma camera [13, 108] is 350 kcps. To standardise the comparison between the SFOV and LFOV gamma camera, the recorded count rate at 20% loss and maximum recorded count rate was reported in our study. One of the limitations was that the test

was performed without the presence of scattering material, consequentially irrelevant to real clinical scenario where scattered radiation arising from the patient. This may underestimate the count rate capability of the camera and the recorded count rate may significantly decrease in clinical situation.
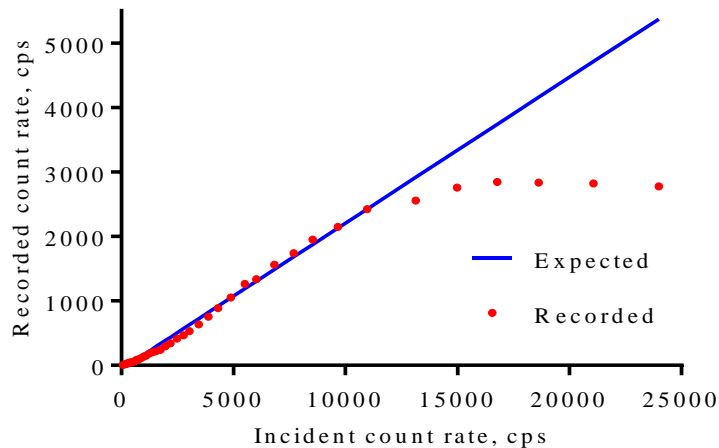


Figure 3.17: Recorded count rate versus incident count rate curve of Nebuleye.

### 3.2.9 Detector head shielding leakage

The sides and back of a gamma camera's detector head are surrounded by shielding material to eliminate any unwanted radiation from being detected by the camera. These radiation sources might originate from within the patient, or from cosmic rays and background radiation. Detector head shielding leakage is a measure of the sufficiency of the shielding material within the camera head. The test is usually carried out using a $^{99m}$Tc source, and along with another radionuclide which produces gamma energy at the highest end of the range of those used clinically.

IAEA [103] has also recommended a measurement of the count rate of a 4 MBq $^{99m}$Tc source positioned at twelve sites around the detector head as well as other potential leaking points such as any cable outlets. Each acquisition takes about 100 s. Then all measurements are divided by the reference count rate acquired using the same source positioned 10 cm in front of the collimated camera head to calculate the percentage of leakage at each point. All readings should be background corrected. Additional tests should be carried out using a radionuclide corresponds to the maximum design energy of the camera. The maximum percentage of shielding leakage is reported. If the

shielding is insufficient, the percentage value obtained could therefore exceed a value of 100%.

For a typical LFOV gamma camera, NEMA [101] has suggested that two types of measurement should be carried out. Firstly, the count rate of a test source placed at different distances on top of the patient couch but outside the FOV is obtained. Each measurement is then compared with the reference count rate measured using the same source positioned 20 cm away from and directly in front of the camera collimator. Secondly, two sets of count rate measurements are required with a source placed at 2 m away from the detector, at the side and in front of the system.

The shielding leakage test for the SFOV gamma camera was modified from the IAEA protocol [103] to accommodate the specific requirements of the SFOV gamma camera design. As the camera head was a compact shielded enclosure accommodating all components it was necessary to check if there were any weak points that potentially lead to the unwanted radiation to reach the detector. Twelve check points were determined with particular consideration of the exit point of the cable and the joints in the shielding. A 4 MBq $^{99m}$Tc solution in a volume of 0.1 ml was filled in a syringe to act as point source.

The collimated camera head was positioned with the detector window facing downward. The measurements were carried out with the source placed next to the camera head at respective designated positions (Figure 3.18). Then the source was located on the central axis of the collimator at SCD of 10 cm (position 12) to obtain the reference count rate. Each data was performed with 100 s acquisition. The radioactive source was subsequently removed and the background count rate was measured. The procedures were repeated using a 4 MBq $^{111}$In source in 0.1 ml of the same type of syringe. The shielding leakage at each position measured was expressed as a percentage of the reference count rate according to IAEA recommendations [103].
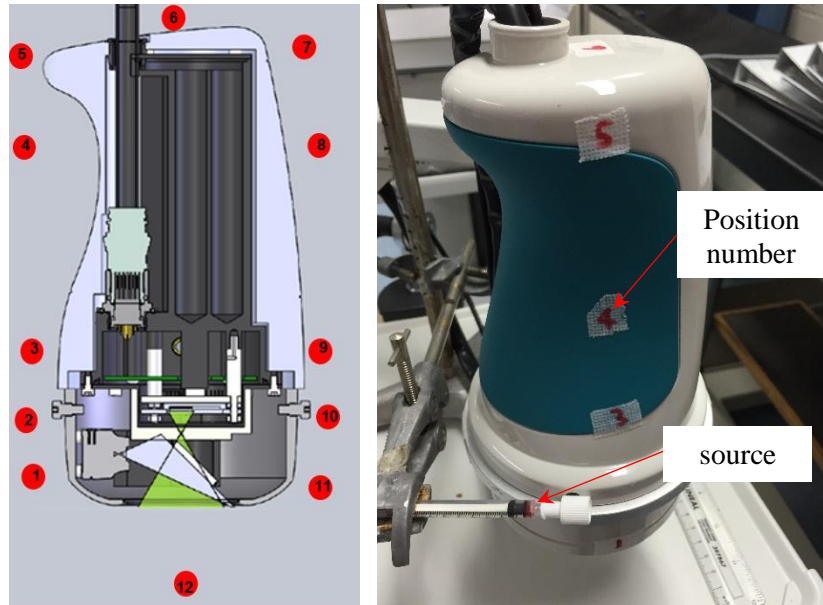
Figure 3.18: (Left) Schematic diagram of the camera head showing the position of the source during the shielding leakage test. Position number 12 is the reference point where the source was placed 10 cm in front of the collimator. (Right) Photograph of the experiment set up illustrating the camera head mounted on an articulated arm and the source held by a clamp on a retort stand placed adjacent to the camera head.

Figure 3.19 and Table 3.6 shows the shielding leakage at designated positions of the camera head as the percentage of the on axis reference value using different radionuclides. This ranged from 3.1 % to 135.7 % and 8.1% to 175.1 % for $^{99m}$Tc and $^{111}$In respectively. The magnitude of the shielding leakage measured using $^{111}$In is relatively higher than those measurements performed using $^{99m}$Tc. Both of the polar plots are in a butterfly pattern, suggesting that the highest leaking points are at positions numbered 2, 3, 9 and 10. With reference to the camera diagram, these might be due to the weak joints between the shielding material and the nearest distance from the source to the detector. The straight line at the collimator axis was the reference count rate at 100 %.

Table 3.6: Mean count rate as a percentage of the reference count rate at various positions of the camera head.

| Position | Percentage of the reference count rate (%) | |
|:---:|:---:|:---:|
| | $^{99m}$Tc | $^{111}$In |
| 1 | 6.1 ± 2.5 | 26.6 ± 4.5 |
| 2 | 135.7 ± 218.8* | 155.7 ± 7.8 |
| 3 | 76.8 ± 12.1 | 175.1 ± 35.4 |
| 4 | 17.4 ± 11.8 | 86.6 ± 3.3 |
| 5 | 5.3 ± 1.8 | 20.6 ± 2.7 |
| 6 | 3.1 ± 0.8 | 8.1 ± 0.2 |
| 7 | 6.2 ± 4.2 | 21.2 ± 1.8 |
| 8 | 13.5 ± 4.6 | 69.4 ± 3.4 |
| 9 | 59.7 ± 39.1 | 156.8 ± 16.1 |
| 10 | 30.1 ± 29.4 | 147.5 ± 3.8 |
| 11 | 8.4 ± 2.5 | 20.8 ± 16.2 |

*Large standard deviation due to high leakage value in one of the measurement.
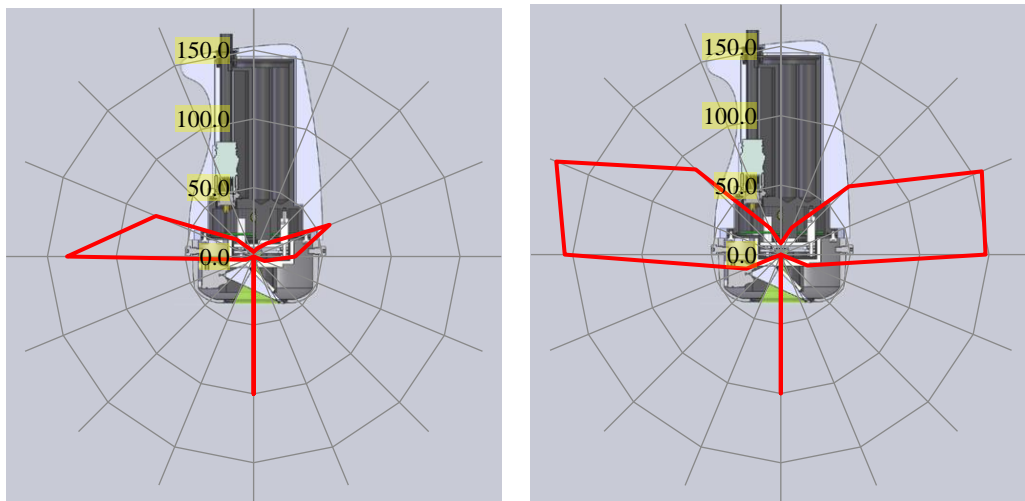


Figure 3.19: Polar plots of the shielding leakage (%) corresponds to the position around the camera head using $^{99m}$Tc (left) and $^{111}$In sources (right).

Detailed investigations were carried out around the region of the highest radiation leaking points. Sixteen points were equally distributed over a 360º cross section of the camera head (Figure 3.20). From this experiment, the shielding leakage as the percentage of the reference count rate at each position was between 11.6 % and 644.7 %. The polar plot shows the distribution of the radiation leakage pattern where

three distinct regions were to be poorly shielded. The unwanted photons that reach the detector may cause the deterioration of the image quality and accuracy where more noises will present in the image as shown in the Figure 3.20 (inset). The maximum percentage of shielding leakage for the camera was 644.7 ± 18.4 %.
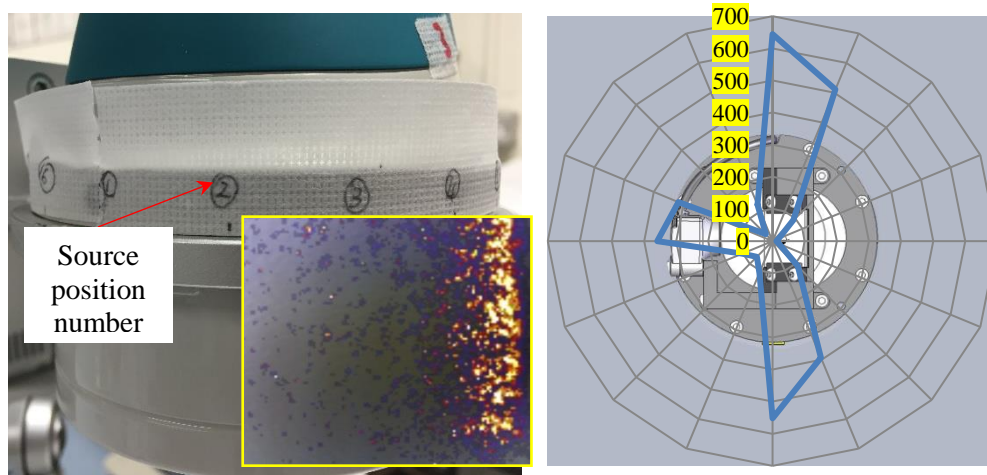


Figure 3.20: (Left) Photograph of the camera head showing the source position number during the shielding leakage test. (Inset) Hybrid image acquired with the source placed at the suspected leaking site of the camera head showing insufficient shielding of the camera head. (Right) Polar plot of the percentage shielding leakage (%) corresponds to the position around the cross sectional diagram of the camera head.

### 3.2.10 Optical-gamma image alignment

The SFOV hybrid optical gamma camera consisted of both a gamma camera and an optical camera. The accuracy of alignment of both modalities mainly depends on the position of the optical camera, mirror and the pinhole collimator. It is desirable to achieve as close alignment of the two cameras as possible but this will depend on the design and construction of the system. In practice software corrections are necessary to ensure the image of the same structure on the gamma image and on the optical image will be accurately superimposed. An optical-gamma alignment test is a measure to assess the alignment accuracy of the optical and gamma images. It is expressed as the deviation of the centre of mass of a landmark between the gamma image and optical image.

Alignment accuracy tests for an inter-modality superimposed images are a unique aspect of the performance testing for a hybrid camera, such as SPECT-CT and PET-CT. In the context of PET-CT scanner, the typical method used to assess the alignment accuracy of this modality is to image a test object which has structures that are visible

on both PET and CT [109]. Capillary tubes or syringes filled with F-18 solution can be used as a source and placed at different locations in the FOV of the scanner. The gamma images show the radiation distributions within the test object and the boundaries are clearly shown in the CT imaging. The resulting fused image is then used to evaluate the alignment accuracy using the software provided by the manufacturer.

The Nebuleye 3 was used in this test as the optical mount had been previously modified by the manufacturer. Before performing the alignment accuracy test, the scale factor and the x-y axes shift values of each camera system were determined and subsequently applied to each image set. The alignment accuracy test was carried out using a hot spot phantom with several holes at a separation distance (Figure 3.21). Five holes were filled with a solution of approximately 1 MBq of $^{99m}$Tc in total mixed with red liquid dye. Image acquisition was carried out over a 120 s with the phantom positioned at SCD between 45 and 150 mm. Resulting images were post-processed and analysed using ImageJ 1.47v (National Institute of Health, US).
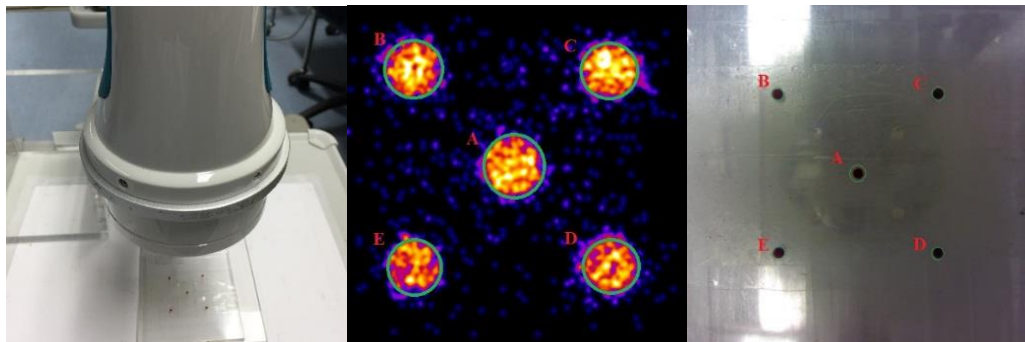


Figure 3.21: (Left) Photograph of the experiment setup during the alignment test using hot spot phantom. Circular ROIs were drawn on the spots within the post-processed gamma (middle) and optical (right) images.

To determine the scale factor, the ratio between the distance of centre-to-peripheral spots of the optical image and gamma image were calculated using images acquired at different SCDs. The distances between centre of mass (COM) of the centre spot and the peripheral spot in each case were measured. Five circular ROIs were drawn on the hot spots within the gamma images, and on the visible well within the optical images respectively (Figure 3.21 centre and right images). The average scale factor of the camera was $4.55 \pm 0.12$. This scale factor was then applied to the gamma image and the image size was resized to $512 \times 512$ to match with the optical image size.

To calculate the x- and y-axes shift, the difference between the COM of hot spots in the scale factor corrected gamma images and the COM of the corresponding ROIs in the optical image in x-y directions were quantified. The average shift was 2.3 ± 1.3 pixel for the x-axis and 15.5 ± 1.7 pixel for the y-axis. After applying the scale factor and x-y axes shift correction, the centre and peripheral deviation (in mm with magnification factor applied) of the COM between the optical image and the gamma image were calculated. For the Nebuleye, the deviation of the COM between gamma and optical images was 0.31 ± 0.32 mm at centre and 0.65 ± 0.36 mm at peripheral.

### 3.2.11 Optical image quality

The optical camera (uEye XS Industrial Camera, IDS Imaging Development Systems GmbH, Obersulm, Germany) of the Nebuleye mini gamma camera system utilised a 5.04 Megapixels CMOS sensor, an integrated autofocus lens and a digital signal processing (DSP). To assess the image quality performance, it involves the measurement of the characteristics such as dynamic ranges, speed, resolution and noise using objective and reproducible methods [110]. International Organisation for Standardisation (ISO) has developed a harmonised framework of standard test charts measuring these parameter on digital still optical cameras [111]. These extensive performance tests can be performed using a commercially available program such as Imatest [112]. However, the software is relatively expensive and complicated.

Bob Atkins [113] has suggested a robust but simpler method to assess the image quality. A modified test chart (Figure 3.22) printed on a 4" × 6" glossy paper is used as the lens testing target which featured the following test patterns:

a) Resolution: resolution patterns, Siemens star pattern, sine wave logarithmic horizontal resolution target, concentric circle patterns

b) chromatic aberration: black border

c) lens focusing: checkerboard pattern

d) image noise: grey patches

e) visual assessment of image quality: text blocks

f) calibration: 100 mm long line, grey scale test strip

To assess the lens of a typical digital camera, three or more test charts are attached to a sheet of pegboard (top left, centre, bottom right). The centres of the camera and the test chart are aligned. The camera is fitted on a tripod while for indoor testing, light conditions should be uniform and no reflections from the test targets. The lens testing chart image is subsequently being analysed.
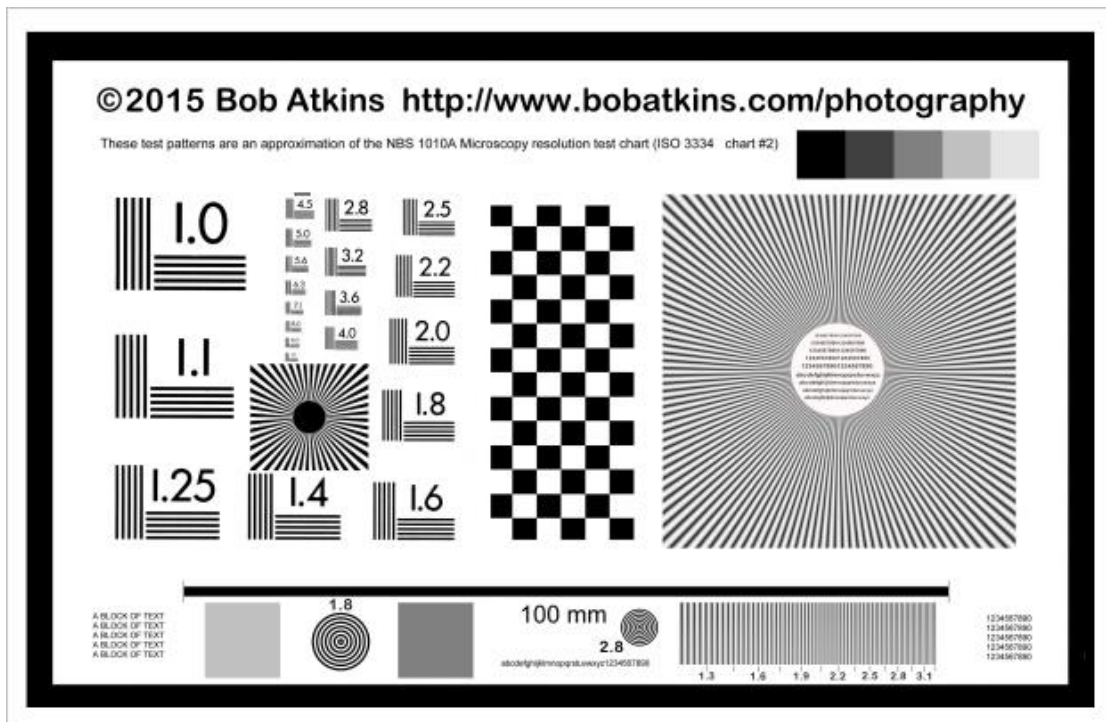


Figure 3.22: The resolution test chart suggested by Bob Atkins [113].

Part of methodologies suggested by Bob Atkins was adopted to examine the performance of the optical component of the hybrid optical gamma camera due to its simplicity and user friendly reason. It was a quick and simple test aimed to understand the basic performance of the optical camera particularly the resolution. The test chart was printed on a glossy photo paper and attached on the flat table in the clinical environment. The alignment between the camera and the test chart was adjusted to the right angle in two steps. Firstly, a leveller was used to establish a horizontal plane of the camera mounted on the articulated arm. Then a thumbtack or nail with straight and thin rod was placed in the centre of the chart at right angle where only the tip of the rod was visible.

This model of camera enables the end-user to select appropriate fixed focal distance (FFD) based on clinical scenario. Multiple optical images of the specified test pattern (e.g. resolution patterns and Siemens star pattern) were acquired with different FFD and camera-source distance (CSD) settings. The FFD was set within the range from 120 to 180 (manufacturer arbitrary units) and SSD was between 40 mm and 120 mm. The resultant image was showed on the display screen of the camera system. Visual assessment was carried out in the same clinical environment by an assessor standing approximately 50 cm away with the observer's eye level parallel to the display screen.

The resolution pattern was observed to determine the minimum line set that could be resolved in the image. Table 3.7 tabulates the visual assessment results of the resolution test pattern on the selected images. The data can be served as baseline performance for the camera. The highest spatial frequency (3.2 lp/mm) was observed with the settings of FFD 120 and CSD at 60 mm. The best resolution was achieved at the CSD of 60 mm, which was approximately 100 mm for the object distance. This was the minimum object distance for this model of the optical camera to achieve its optimum performance. With the FFD set at 180, no line set was able to be resolved.

Table 3.7: The smallest group of line set (lp/mm) which can be observed in images acquired with different FFD and CSD settings.

| CSD (mm) | FFD | | | | | |
|---|---|---|---|---|---|---|
| | 120 | 130 | 140 | 150 | 160 | 170 |
| 40 | 2.5 | 2 | 1.6 | 1.25 | 1.1 | 1 |
| 60 | 3.2 | 2.5 | 2.2 | 1.6 | 1.1 | 1 |
| 80 | 2.5 | 2.2 | 2.2 | 1.8 | 1.1 | 1 |
| 100 | 2.2 | 2 | 2 | 1.8 | 1.25 | 1.1 |
| 120 | 1.6 | 1.6 | 1.6 | 1.6 | 1.25 | 1 |

To further understand the resolution on the sensor, the magnification factors at various CSD are needed. The magnification factor is the ratio of the height of image and the height of the object. The Siemens star pattern was used for the calibration purposes and the magnification factor was tabulated in Table 3.8. Then the resolution on sensor corresponded to the line set resolved at difference CSD was calculated. The resolutions on sensor were range between 71 and 291 lp/mm.

Table 3.8: Magnification factor and the calculated resolution on sensor (lp/mm) at different SSD.

| SSD (mm) | Magnification | FFD | | | | | |
|:---:|:---:|:---:|:---:|:---:|:---:|:---:|:---:|
| | | **120** | **130** | **140** | **150** | **160** | **170** |
| 40 | 1/71 | 178 | 142 | 114 | 89 | 78 | 71 |
| 60 | 1/91 | 291 | 228 | 200 | 146 | 100 | 91 |
| 80 | 1/112 | 280 | 246 | 246 | 202 | 123 | 112 |
| 100 | 1/130 | 286 | 260 | 260 | 234 | 163 | 143 |
| 120 | 1/151 | 242 | 242 | 242 | 242 | 189 | 151 |

Another test pattern used for the analysis was the Siemens star pattern. The diameter of the centre of the star pattern to merge or blur was measured in four different angles. The average diameter was subsequently computed in considering the magnification factor. Figure 3.23 shows the results the diameter of the centre corresponded to the CSD (left) and FFD (right) values. The error bars indicates the standard deviation of the repeated measurements. The smaller the diameter of the star pattern starting to merge, the higher the resolution of the camera system. The left graph illustrates that the lowest resolution of the star pattern occurred with the CSD at 40 mm. This was due to the CSD setting below the minimum object distance causing the focus shift.
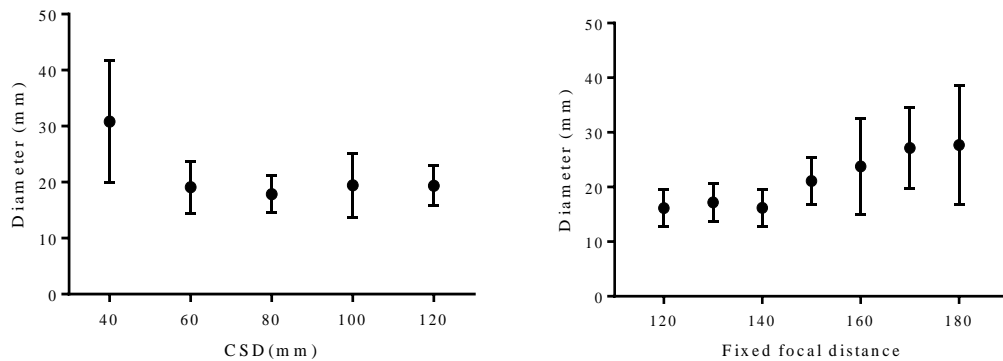


Figure 3.23: Relationship between the diameters of the centre of the star pattern to merge and (left) the CSD and (right) FFD (n=4).

Generally, the results were consistent for the CSD settings range from 60 to 120 mm and the FFD settings range from 120 to 140. It was increased gradually with the FFD setting at 150 onwards. Figure 3.24 demonstrates the examples of the Siemens star pattern taken with different CSD and FFD settings. Rings of apparent sharpness in the star pattern image (alternate appearance of blurred ring and ring of sharpness) were

observed in most of the images acquired at CSD 40 mm. This was due to the CSD setting below the minimum object distance causing the focus shift.
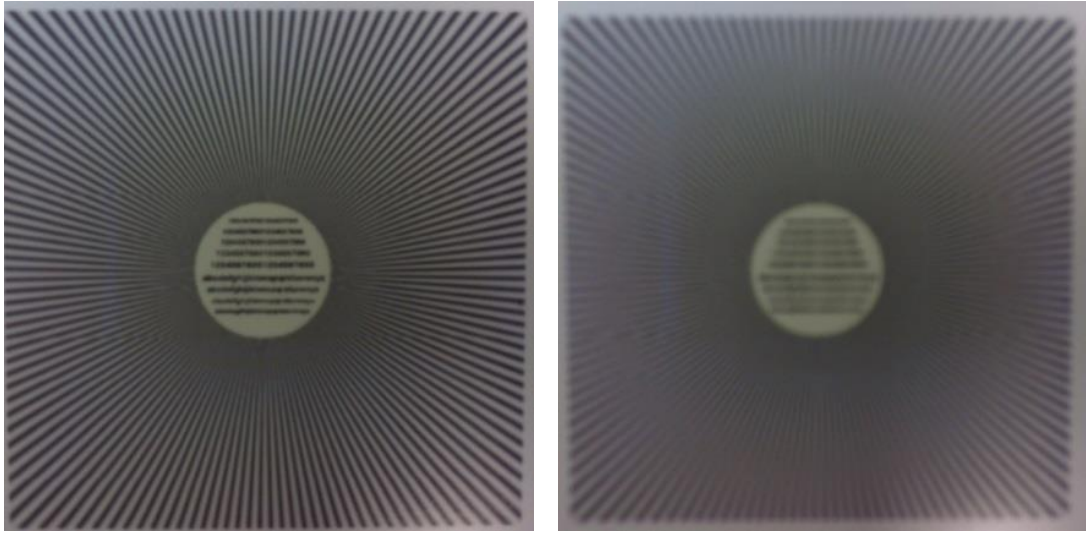


Figure 3.24: Siemens star pattern acquired using uEye XS optical camera at CSD 40mm and FFD 120 (left) or 160 (right). The diameter of the centre of the star pattern to merge or blur for image acquired using FFD 120 was bigger than image with FFD 160.

## 3.3 Comparison of the performance characteristic between HGC and Nebuleye

As described in Chapter 2, the technology used in manufacturing the camera head of HGC and Nebuleye were identical. Theoretically the performance of these two cameras were comparable and correlated well with each other. However, due to different manufacturer, software, electronics and design features of the camera heads, certain performance characteristics may differ between the two cameras. Newly developed testing protocol and analysis method had incorporated these differences to make the characterisation works feasible to the Nebuleye and HGC. Performance of a standard LFOV gamma camera (Brightview X, Philips Healthcare, Milpitas, CA, USA) [108] was also compared with the SFOV gamma cameras. Table 3.9 summarises the performance of the HGC, Nebuleye and LFOV camera system.

Table 3.9: Comparison of the technical performances of the HGC, Nebuleye and standard LFOV clinical camera system.

| Parameter | HGC | Nebuleye | BrightViewX[a] |
|---|---|---|---|
| Intrinsic spatial resolution | | | |
| FWHM (mm) | $0.32 \pm 0.05$ | $0.28 \pm 0.02$ | 3.3 |
| FWTM (mm) | $0.58 \pm 0.05$ | $0.52 \pm 0.03$ | 6.3 |
| System spatial resolution | | | (LEHR) |
| FWHM (mm) | $2.43 \pm 0.25$ | $1.84 \pm 0.39$ | 7.4 |
| FWTM (mm) | $4.36 \pm 0.43$ | $3.37 \pm 0.71$ | 14.0 |
| Intrinsic Uniformity | | | |
| CoV (%) | 16.39 | 13.54 | NA |
| Integral Uniformity (%) | 72.30 | 51.72 | 2.5 |
| Differential Uniformity (%) | 11.58 | 8.34 | 2.0 |
| System uniformity | | | |
| CoV (%) | 24.53 | 19.58 | NA |
| Integral Uniformity (%) | 86.21 | 70.73 | NA |
| Differential Uniformity (%) | 21.86 | 16.55 | NA |
| Intrinsic sensitivity (cps/MBq) | 17.0 | 12.4 | NA |
| | at 250mm | at 250mm | |
| System sensitivity | 14.68 | 8.86 | 124.78 |
| (cps/MBq) | at 10mm | at 10mm | (LEGP) |
| | 6.60 | 3.82 | |
| | at 50mm | at 50mm | |
| Spatial linearity | | | |
| Absolute (mm) | 0.10 | 0.24 | 0.50 |
| Differential (mm) | 0.02 | 0.05 | 0.10 |
| Count rate capability | | | |
| Input count rate at 20% loss (cps) | 18620 | 15710 | NA |
| Recorded count rate at 20% loss (cps) | 2432 | 2537 | 300000 |
| Maximum recorded count rate (cps) | 2937 | 2845 | 350000 |
| Detector head shield leakage | 547.9 | 644.7 | NA |
| (max leakage % at 141 keV) | | | |

[a] Equipped with NaI(Tl) detector in a dimension of 406 $\times$ 539 $\times$ 9.5 mm;
NA- Not available

Most of the characterisation test results of HGC were based on the experimental data provided by the University of Leicester [107]. These raw data were then processed using the same data analysis method as the Nebuleye. Another part of the tests were newly introduced or modified specifically for SFOV gamma cameras. They were carried out in the identical settings for both of the cameras. These included the following tests:

a) Intrinsic uniformity (analysed using Matlab with median filter applied)

b) System uniformity (new experimental and analysis method)

c) System sensitivity (quantified using experimental data)

d) Count rate capability (observation using higher activity)

e) Detector head shield leakage (new experimental and analysis method)

For comparison purposes, intra-class correlation coefficient (ICC) test was performed on suitable testing results to assess the reliability of the measurements. The ICC (single measures), 95 % confidence interval (CI) and p-value was reported.

Both the SFOV gamma cameras utilised similar CsI(Tl) having a thickness of 1.5 mm and EMCCD as the photon detector. The intrinsic spatial resolution was $0.28 \pm 0.02$ mm and $0.32 \pm 0.05$ mm at FWHM for Nebuleye and HGC respectively. The difference of the resolution in term of FWHM between the cameras was less than a pixel's width, i.e. $0.04 \pm 0.05$ mm. Similarly, the difference of the system spatial resolution between the two cameras was $0.59 \pm 0.46$ mm at FWHM and $0.99 \pm 0.83$ mm at FWTM where the effect of the collimator was took into consideration. The system spatial resolution of a standard LFOV gamma camera mounted with low energy high resolution (LEHR) collimator was 7.4 mm at FWHM which was about threefold higher than the SFOV gamma camera. This indicates that the SFOV gamma camera with a pinhole collimator could offer higher resolution images without the involvement of any sophisticated image processing.

The intrinsic uniformity of the SFOV gamma cameras was 13.54 % and 16.39 % for the CoV of the uniformity image produced by Nebuleye and HGC respectively. With the collimator included, the system uniformity increased to 19.58 % and 24.53 %. Figure 3.25 shows the corrected uniformity image acquired using Nebuleye (left) and

HGC (right). The CoV values for HGC was slightly higher as there were several hot pixels appeared on the original flood image possibly due to the manufacturer defect of the CCD. In general, the uniformity results are relatively higher than the performance of a standard clinical gamma camera. These posed a limitation in the camera performance and may need further improvement in future camera development.
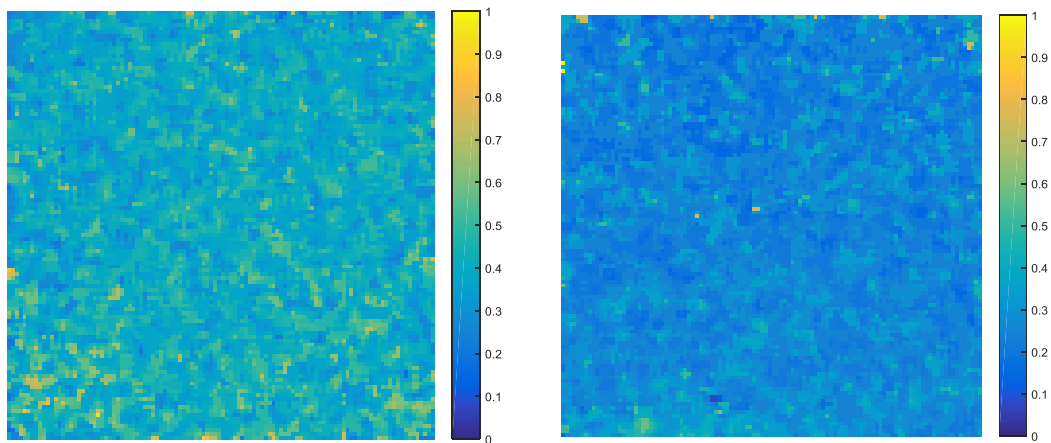


Figure 3.25: The corrected uniformity image acquired using Nebuleye (left) and HGC (right).

The sensitivity of both the Nebuleye and HGC was studied intrinsically and extrinsically. With a point source placed at 250 mm away without the presence of a scattering medium, the intrinsic sensitivity was 17.0 cps/MBq for HGC and 12.4 cps/MBq for Nebuleye. For the system sensitivity, it was 14.68 cps/MBq and 8.86 cps/MBq for HGC and Nebuleye respectively with the SCD at 10 mm (ICC 0.936, 95% CI 0.676 to 0.989, $p < 0.001$). For the count rate capability test, the recorded count rate at 20% loss was 2432 cps and 2537 cps for HGC and Nebuleye respectively (ICC 0.998, 95% CI 0.996 to 0.999, $p < 0.001$). Based on the ICC test, both sets of test results were in strong agreement ($p < 0.001$).

For the shielding leakage test, the maximum percentage of leakage at 141 keV was 547.9 % and 644.7 % for HGC and Nebuleye respectively. These values were above the reference value, indicating that the unwanted or background radiation may be detected and form as part of the image produced. The position of the maximum percentage of leakage was measured at similar height of camera head (position 2-3 or 9-10) suggested that the current shielding may not be sufficient. For the spatial linearity test, the absolute linearity for both HGC and Nebuleye were 0.10 mm and 0.24 mm respectively. These were significantly smaller than a standard LFOV gamma camera.

## 3.4  Summary

This chapter has described the performance testing of the new prototype Nebuleye camera. This work has further extended the scope of testing and was successfully applied to characterise an SFOV hybrid gamma camera for medical use. The newly introduced tests enabled the system uniformity, system sensitivity, detector head shielding leakage, optical-gamma image alignment and optical image quality of the hybrid camera to be assessed objectively. These tests, combining with the characterisation protocol developed by Bhatia *et al.* [104] and Bugby *et al.* [105], formed a complete and rigorous testing scheme to assess SFOV hybrid optical gamma cameras and to compare with other similar SFOV gamma cameras.

Overall the performance of the SFOV gamma cameras was found to be comparable when assessed using the same testing protocol. The SFOV gamma cameras have superiority in term of resolution and linearity in comparison with the standard LFOV gamma camera. With the better understanding of the characteristics of the camera, it provides the basis of the experimental work to further evaluate the performances of the camera in preclinical and clinical arenas as discussed in Chapter 4, 5 and 8.

# Chapter 4

# Preclinical imaging using the SFOV Hybrid Optical Gamma Cameras

## 4.1 Introduction

*In vivo* small animal imaging is highly valuable for biomedical research as it has the capabilities for the non-invasive study of dynamic biological processes in a preclinical model of disease at the molecular and cellular level. Over the years, this approach has been widely used in evaluating the therapeutic effectiveness of new treatment regimens, assisting in the identification of new disease biomarkers, new tracer development and drug design [114]. It provides important information in bridging from *in vitro* studies of diseases and explaining the pharmacological mechanisms of pharmaceuticals prior to their translation into clinical use.

Dedicated preclinical imaging modalities such as optical, fluorescence, SPECT, PET, CT and MRI are commercially available and can produce high quality images. Each modality has its own advantages and limitations with regards to resolution, sensitivity, signal penetration capability and cost. Immense efforts have been made to complement the weaknesses of individual imaging modalities through the innovation of multimodal imaging methods, for instance the combined radionuclide and CT imaging.

In nuclear and optical imaging the recent development of multimodal imaging probes have propelled non-invasive imaging into a new generation of advanced applications [115]. Most of the probes are still in the developmental stage and are yet to be translated into clinical use. This advancement is believed to enhance the performance of *in vivo* imaging and may be of benefit to some clinical procedures, in particular in radioguided surgery [116]. The combination of two modalities are currently being investigated using dual signals emitted from the same probe.

Given the current interest in hybrid tracers [117] the development of the HGC to become a hybrid gamma-fluorescence camera was considered. Preclinical radionuclide-fluorescence imaging may provide added values in this research area. This chapter describes the initial assessment of the SFOV hybrid optical gamma cameras for use in small animal radionuclide imaging. Part I of the chapter explains the performance assessments using bespoke mouse phantoms. Part II describes the use of the SFOV gamma cameras in imaging newly developed near infrared fluorescent-radioactive hybrid probes.

## 4.2 Small animal imaging

The ability to investigate *in vivo*, anatomical and functional details of experimental disease models provides detailed information on pharmaceutical uptake, retention and metabolism. The hybrid image, now commonly used fusion of functional and anatomical images, can be obtained without having to move the experimental subject from one camera to another. Figure 4.1 shows examples of the range of multimodal imaging for preclinical animal studies.
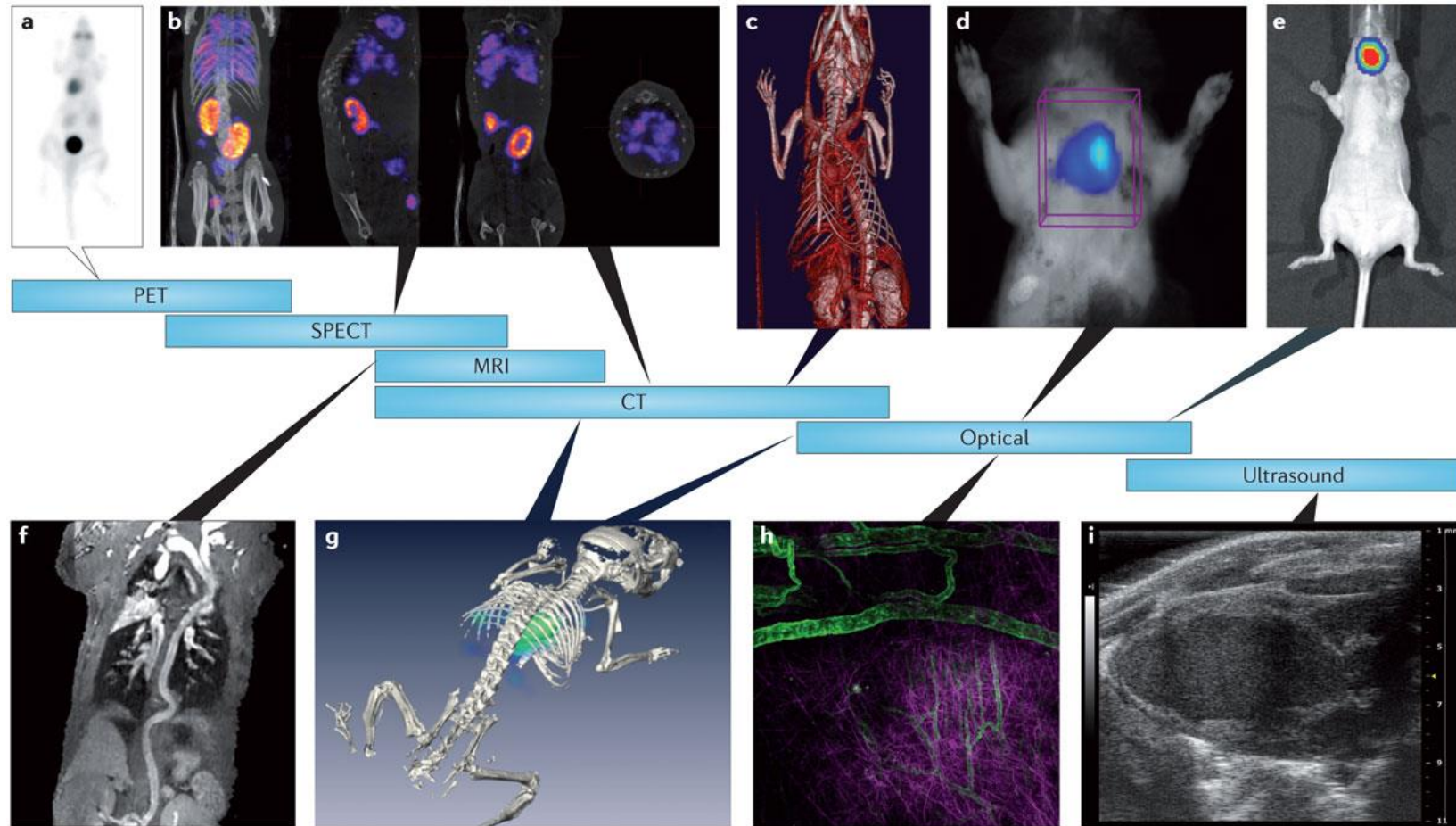
Figure 4.1: Examples of the commercially available multimodal imaging systems and its applications in animal studies. (a) PET image of $^{18}$F-FDG distribution in mice; (b) SPECT-CT images of $^{111}$In-DTPA-octreotide in mice; (c) Contrast-enhanced whole-body microCT angiogram; (d) Fluorescence-mediated tomography-derived matrix metalloproteinase activity in a mouse aorta; (e) Bioluminescence imaging of mouse with orthotopic hypopharynx tumour model; (f) Contrast-enhanced whole-body MR angiogram; (g) Fluorescence-mediated tomography-CT image; (h) Multiphoton laser scanning microscope image of a melanoma-bearing mouse expressing vascular green fluorescent protein (GFP), using second harmonics generation to detect collagen; (i) Ultrasound image (B-mode) of left ventricle of a mouse. Image taken from [118].

Amongst these modalities, preclinical SPECT-CT and PET-CT scanners are widely used for research purposes in biomedical and life sciences. Figure 4.2 shows example of preclinical SPECT-CT and PET-CT imaging systems used in the SPECT PET and Optical animal imaging facility (SPOT), at the University of Nottingham. Spatial resolution and sensitivity are the main performance parameter in determining good quality images in small animals such as mice and rats. For small animal SPECT imaging, the imaging systems must have adequately high spatial resolution ($\leq 1$ mm [114]) and sensitivity to provide a high quality and accurate visualisation of the molecular distribution and concentration of the tracer under investigation [119]. Figure 4.3 shows examples of high quality SPECT-CT (top) and PET-CT (bottom) images of mice administered with radiotracers.
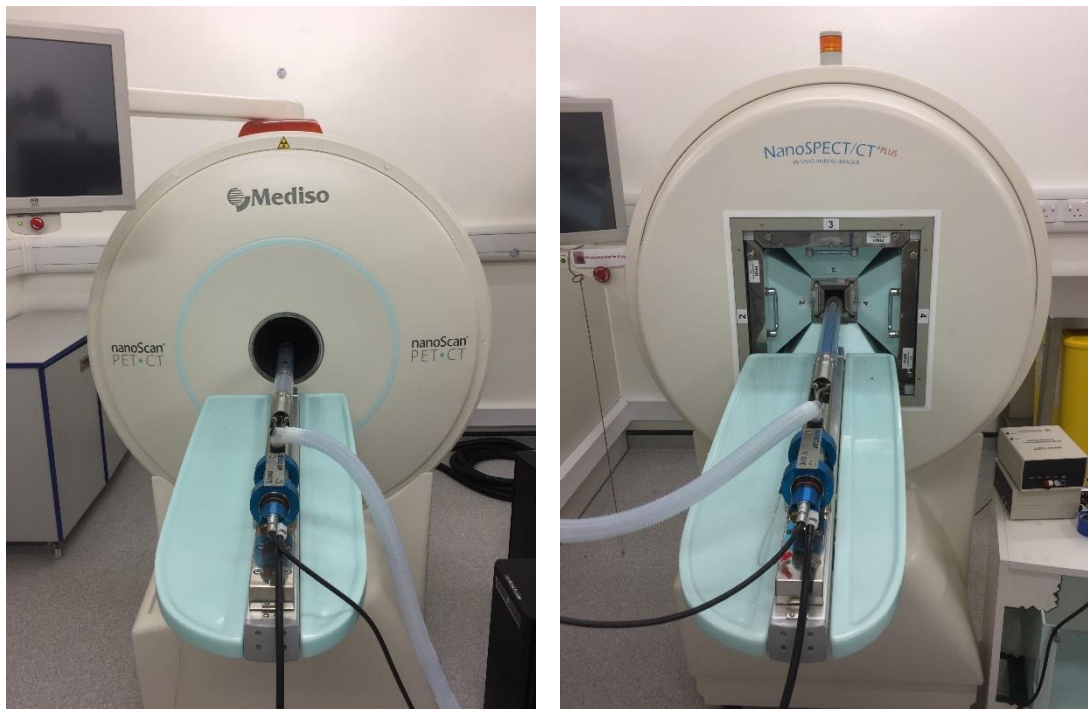


Figure 4.2: Photograph of (left) nanoScan PET-CT and (right) nanoScan SPECT-CT (Mediso Medical Imaging Systems, Budapest, Hungary) in the University of Nottingham preclinical imaging facility (SPOT).
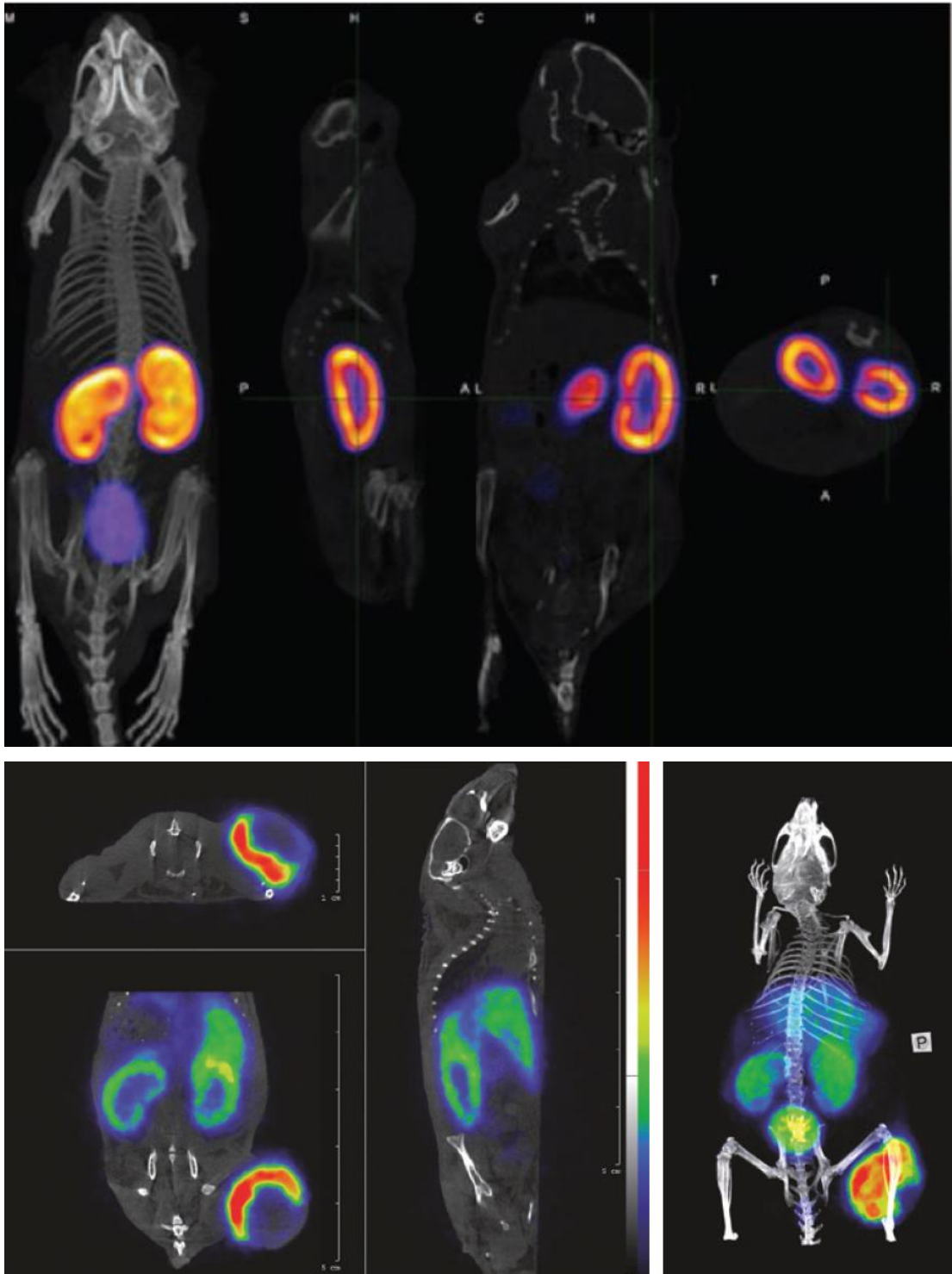
Figure 4.3: (Top) SPECT-CT images of mouse with kidney excretion of ^{99m}Tc-Exendin-4 [120]. (Bottom) PET-CT images of nude mouse bearing a tumour on the right leg after administered with 34 MBq ^{64}Cu-labelled tumour associated antibody [121].

High spatial resolution SPECT camera design was attained by using a pinhole collimator with an aperture diameter in sub-millimetres range and increasing camera sensitivity by using multiple pinholes, for example 75 pinholes within U-SPECT II

scanner collimator [122]. This camera configuration with the aid of post-processing software, enabled the acquisition of high quality small animal SPECT images [114]. Table 4.1 summarises performance characteristics of the preclinical SPECT and PET scanners at Nottingham for comparison with the HGC.

Table 4.1: Comparison of the SPECT, PET and HGC characteristics.

| | NanoScan PET Mediso (122S) [121] | NanoScan SPECT Mediso [120, 123] | HGC [107] |
|---|---|---|---|
| Detector material | LYSO | NaI(Tl) | CsI(Tl) |
| Crystal dimension (mm) | $1.12 \times 1.12 \times 13$ | $280 \times 280 \times 9.5$ | $8.19 \times 8.19 \times 1.50$ |
| Collimator | NA | $M^3$ pinhole | 1 mm pinhole |
| FOV (mm) | 100 (axial) | $270 \times 270$ | $40 \times 40$** |
| Energy window (keV) | 250 - 750 | 200 - 600 | 30 - 265 |
| Spatial resolution (FWHM, mm) | 0.7* | 0.3 | 1.8 |
| Sensitivity | 8 % | 13000 cps/MBq | 6.6 cps/MBq** |

*With 3D OSEM image reconstruction
** Based on SCD at 50 mm
NA-not available
$M^3$-multifocus, multisize, multi-pinhole (16, 25, 36 pinhole per aperture)

At the time of investigation SFOV gamma cameras were not widely used for imaging preclinical animal models. Celentano *et al.* [124] and Autiero *et al.* [125] have reported the use of a prototype fluorescence and radionuclide planar imaging system in mice studies. Scintigraphic images were acquired using a semiconductor pixelated detector (Silicon or CdTe detector) with a 1 mm diameter pinhole collimator. Other reports have described the preliminary assessment of a portable gamma camera in sentinel node localisation in pigs and mice [126, 127].

## 4.3 Phantom imaging

The performance of the SFOV gamma camera systems used in this work has been fully characterised as discussed in Chapter 3. With the introduction of these camera systems into preclinical imaging it is crucial that there are systematic methods to evaluate the

performance and limitations of SFOV gamma cameras used in animal studies. A number of phantoms have been designed and fabricated to assess the performance of SFOV gamma camera systems such as the sentinel node phantom (Section 5.3.1) and head and neck phantom [128], however the design of these anthropomorphic phantoms was not relevant to animal studies.

With this in view, there was a need for the systematic assessment of the SFOV gamma cameras using phantoms specifically designed to simulate preclinical imaging, such as in mice imaging. The commercially available phantoms such as NEMA NU4 Micro-PET Image Quality Mouse Phantom (QRM Quality Assurance in Radiology and Medicine GmbH, Moehrendorf, Germany) [129] and Micro Hollow Sphere Phantom™ (Data Spectrum Corporation, Durham, NC, USA) [130] have mainly been used for the quality control testing of preclinical PET or SPECT scanners. However, there is still a challenge in the complete filling of small cavities with radioactive solutions without bubbles. In addition these commercial phantom can be relatively expensive.

It was envisaged that low cost, simple and versatile phantoms simulating the preclinical situation was needed. It is important to examine the performance of the SFOV gamma cameras prior to use in animal imaging. The aim of these studies was to assess the imaging performance of the SFOV gamma cameras using bespoke mouse phantoms.

### 4.3.1   Phantom descriptions

Phantoms simulating the anatomy of a mouse were designed and developed at the University of Leicester. They were used to assess the imaging performance of SFOV gamma cameras in the research laboratory of the nuclear medicine clinic at Queen's Medical Centre, Nottingham University Hospitals NHS Trust and the SPOT preclinical imaging facility at the University of Nottingham.

#### 4.3.1.1   Mouse skeletal phantom

The mouse skeletal phantom (Figure 4.4) was designed to simulate the skeleton of a typical mouse for use in bone scintigraphy. The phantom was fabricated using a PMMA plate of dimensions 130 mm (L) × 70 mm (W) × 5 (H) mm. Shallow pits or holes

simulating the mouse skeletal anatomy were created on the PMMA plate allowing radioactive solution to be filled within the predefined holes.
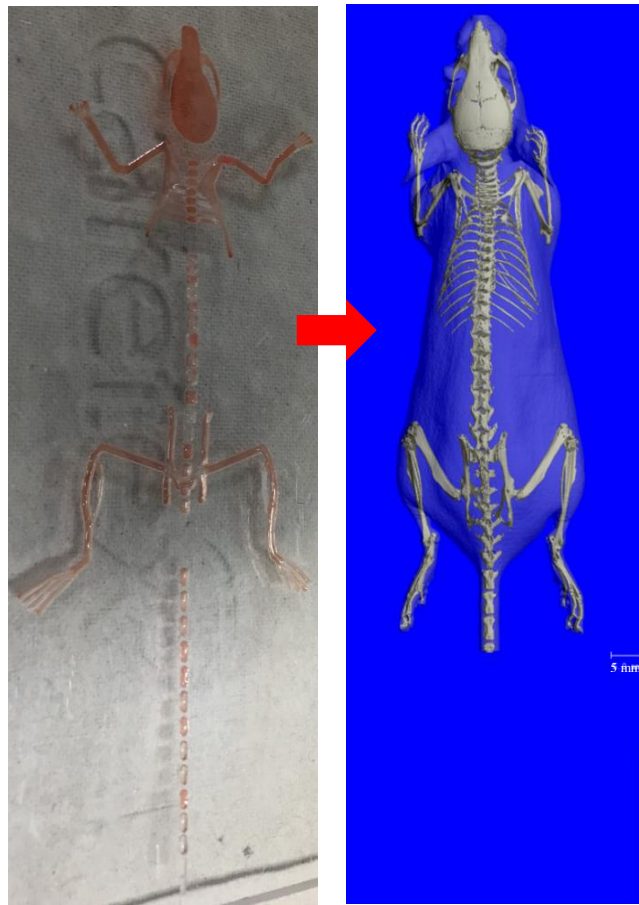


Figure 4.4: (Left) Photograph of mouse skeletal phantom filled with red-colour liquid within the skeletal cavities. (Right) Example x-ray Micro-CT Scans of a mouse. (Image taken from Micro CT Laboratory, University of Calgary) [131].

### 4.3.1.2   3-D printed mouse phantoms

3-D printed mouse phantoms were designed from high resolution 3-D magnetic resonance microscopy animal data, as described in [132]. Two mouse phantoms with different organ cavities and sizes were fabricated at the Space Research Centre 3-D printing centre, University of Leicester. Table 4.2 summarises the technical details of the phantoms. The organ cavities were anatomically correct fillable volumes with two outlet holes to ease the filling and draining process. These provided a realistic and flexible method to test any reporter (radionuclide or contrast agent) for use in small animal SPECT-CT, PET-CT or fluorescence cameras, and were considered useful for imaging with the SFOV gamma cameras.
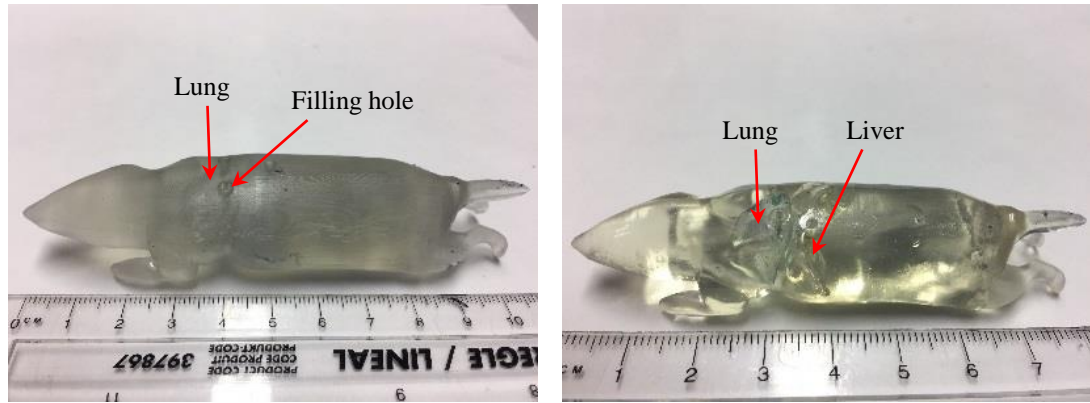
Figure 4.5: Photograph of 3-D printed mouse phantoms, (left) Phantom A and (right) Phantom B.

Table 4.2: Technical specifications of the 3-D printed mouse phantoms.

|  | **Phantom A** | **Phantom B** |
|---|---|---|
| **Descriptions** | Adult mouse with lung cavity | Baby mouse with lung and liver cavities, transparent surface |
| **Organ volume (mm³)** | 0.6 | 0.25 (lung) / 0.45 (liver) |
| **Length (nose to tail) (mm)*** | 105.57 ± 0.12 | 79.33 ± 0.12 |
| **Width (mm)*** | 26.52 ± 0.72 | 20.27 ± 0.12 |
| **CT number (body)*** | 150.99 ± 51.52 | -57.31 ± 37.54 |

*Measurements were performed on CT images using VivoQuant$^{TM}$ 2.50 software (Invicro, Boston, MA, USA).

### 4.3.2  Mouse skeletal phantom imaging assessment

The phantom was used to assess the imaging capabilities of the HGC and Nebuleye SFOV hybrid gamma cameras in the research laboratory. Initial imaging was focussed on regional scintigraphy where 10.7 MBq of $^{99m}$Tc solution (activity concentration of 107 MBq/ml) was filled in the pelvis and hind limb regions of the phantom as shown in Figure 4.6 (within the yellow dashed line). Images were taken with acquisition time of 60 s and the cameras were positioned at SSD of between 0 and 40 mm. Figure 4.7 shows the resulting scintigraphic images acquired using Nebuleye positioned at different SSDs. With these acquisition settings, the fine details within the pelvic region were not resolved, however the radionuclide source pattern within the limb regions could be clearly seen.
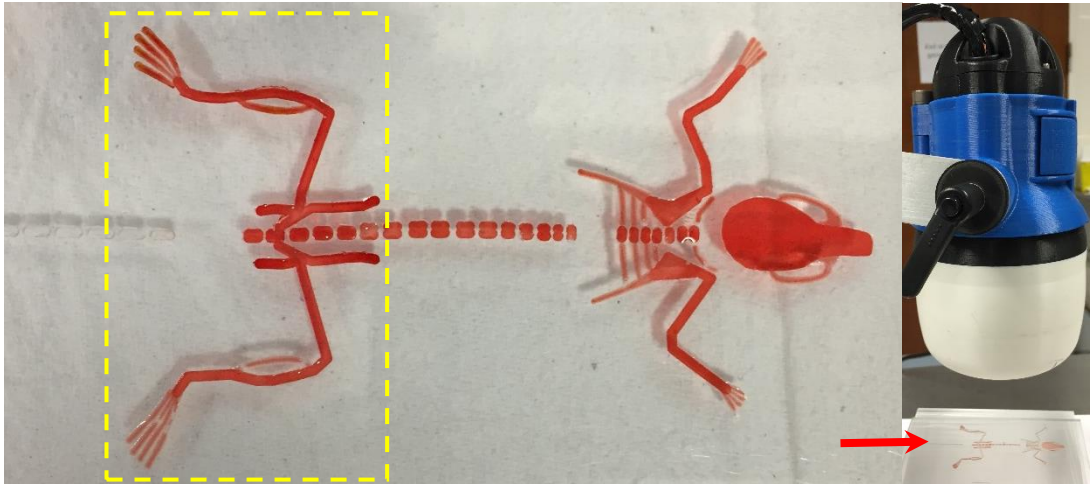
Figure 4.6: (Left) Mouse skeletal phantom filled with red-coloured $^{99m}$Tc solution. Only pelvis and hind limbs regions were filled up with the radioactive source during initial regional scan (region marked with yellow dashed line). (Right) Photograph of the experiment set up using HGC.
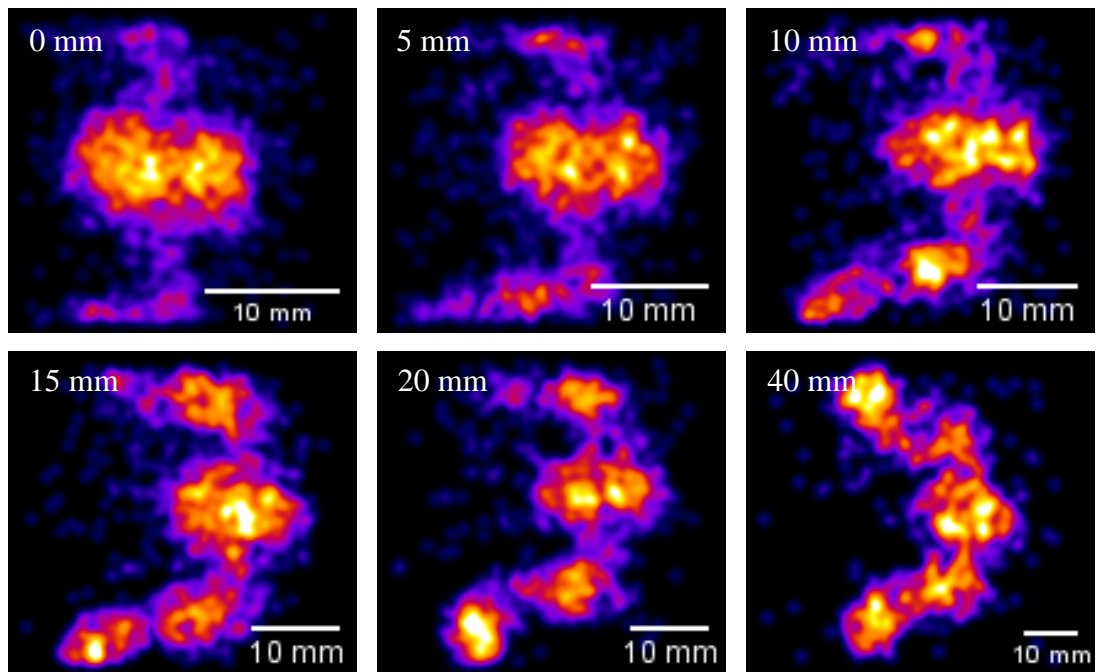


Figure 4.7: Regional scintigraphy of the phantom filled with $^{99m}$Tc solution at pelvis and hind limbs regions. The images were acquired using Nebuleye positioned at different SSDs (as indicated in the images) with imaging time of 60 s.

Further imaging assessment was undertaken of whole body imaging where the simulated skeletal system (excluding the tail) was filled with the $^{99m}$Tc solution at an activity concentration of 48 MBq/ml. A series of images was undertaken with the camera placed at SSD of 50 mm and 100 mm, and imaging time varied between 1 and 5 minutes. Figure 4.8 shows example planar images of the phantom acquired using Nebuleye positioned at SSD of 50 and 100 mm with imaging time of 1, 3 and 5 minutes.

The hind limbs region were not within the FOV of the camera positioned at SSD of 50 mm. With the increase of imaging time, the visibility of the pattern of the skeletal system was increased, however not at the high resolution expected.

| 60 s | 180s | 300 s |
|---|---|---|
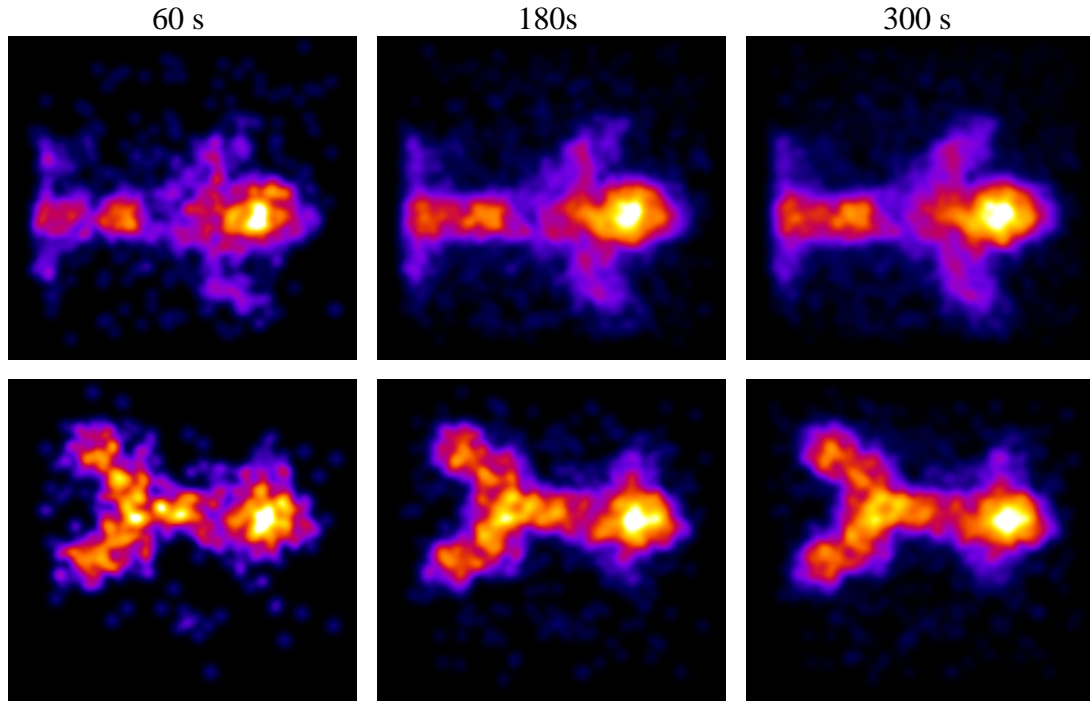


Figure 4.8: Whole body skeletal phantom imaging acquired using Nebuleye positioned at SSD of 50 mm (top row) and 100 mm (bottom row) with the different acquisition times as indicated.

### 4.3.3   3-D printed mouse phantom imaging

Two 3-D printed mouse phantoms described in 4.3.1.2 were used to assess the imaging performance of the SFOV hybrid optical gamma cameras using 0.5 mm and 1 mm pinhole collimators. The lung and liver cavities of Phantom A and Phantom B were filled with 38 MBq and 43 MBq of $^{99m}$Tc solution respectively. Special care were taken to prevent any air bubbles trapped within the cavities. After filling the hole outlets were sealed using self-adhesive tape to prevent any surface radioactive contamination.

Imaging was undertaken with the Nebuleye fitted with 1 mm diameter pinhole collimator, positioned above and posterior to Phantom A at SSD of 10 mm and Phantom B at SSD of 100 mm respectively. The imaging duration time for both image acquisitions was 30 minutes. Figure 4.9 illustrated the optical and hybrid images obtained from both image acquisitions. The hybrid images provide the location of the lung and liver cavities within the mouse phantom. However, it was disappointing that

the gamma images failed to show the discrete separation between the right and left lobes of lung or the lung and liver cavities for these camera configurations.

| Optical | Hybrid |
|---------|--------|
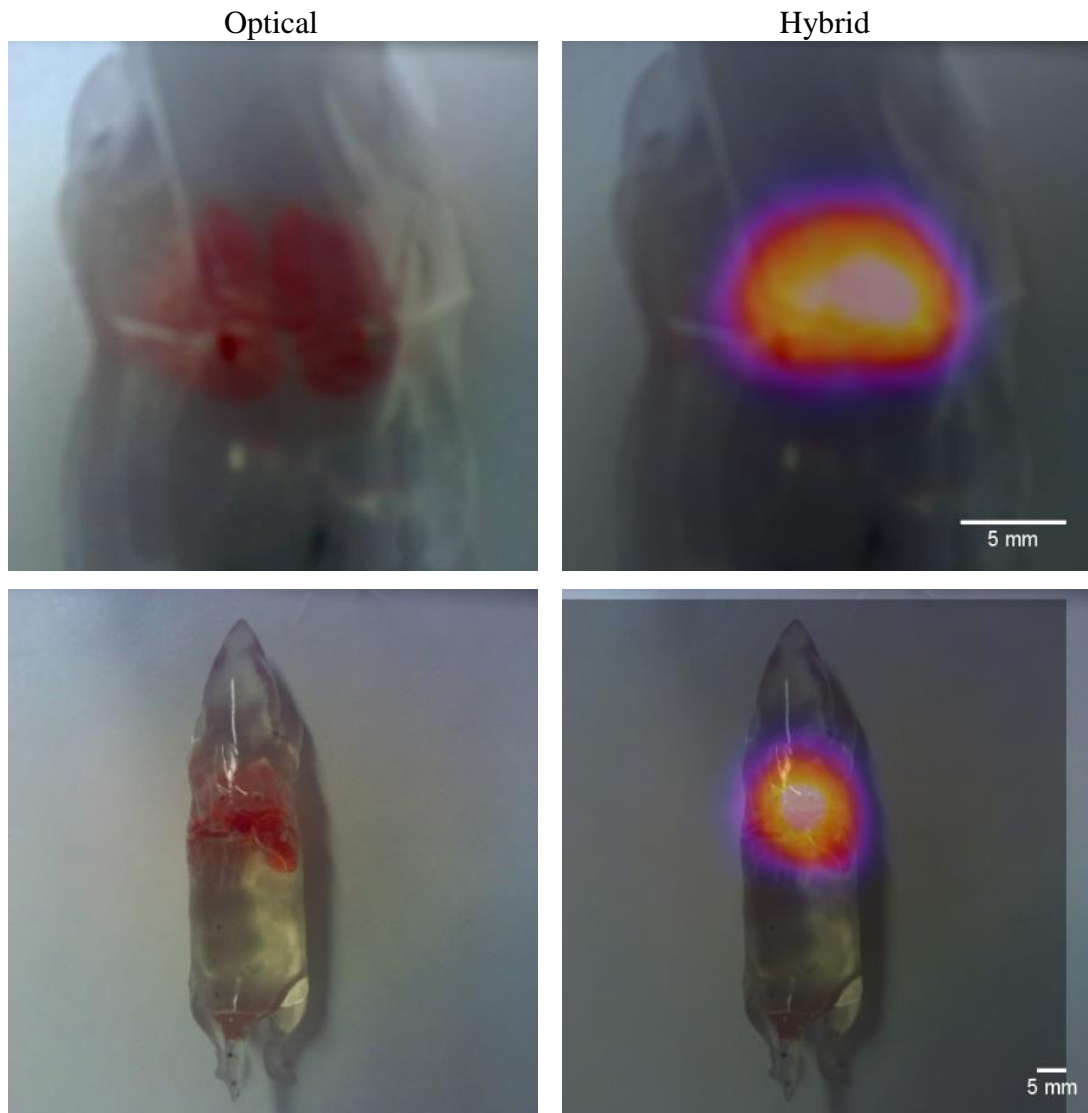


Figure 4.9: (Top row) Resulted images of the Phantom A filled with red-colour $^{99m}$Tc solution in the lung cavities. (Bottom row) Images of the Phantom B filled with the same radioactive source in the lung and liver cavities. Both images were acquired using Nebuleye fitted with 1 mm pinhole diameter positioned at 10 and 100 mm away from the camera.

Further imaging were performed using HGC fitted with 0.5 mm pinhole collimator and imaging time of 30 minutes. Oblique views were acquired with the HGC positioned 15° tilted from the central axis. The view from this angle was selected due to the apparent separation between lungs and liver cavities as shown in Figure 4.10 (red arrow). Figure 4.11 shows the optical and hybrid oblique views obtained. With this camera

configuration, the images obtained partially show the separation of the lung and liver cavities.
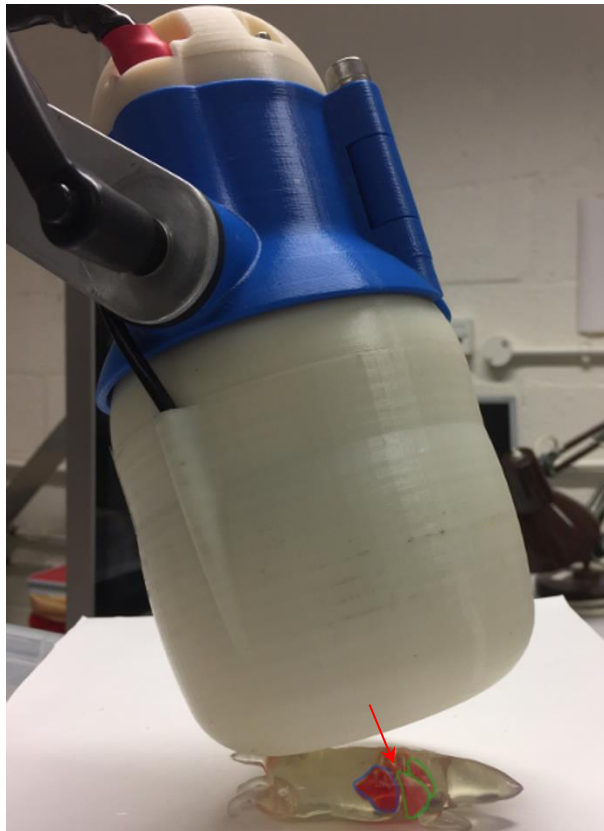


Figure 4.10: Photograph of the 3-D mouse phantom experiment set up. The HGC was positioned above Phantom B (oblique ~15° from central axis). The green line indicates the border of the lung cavities while blue line indicates the liver cavities.
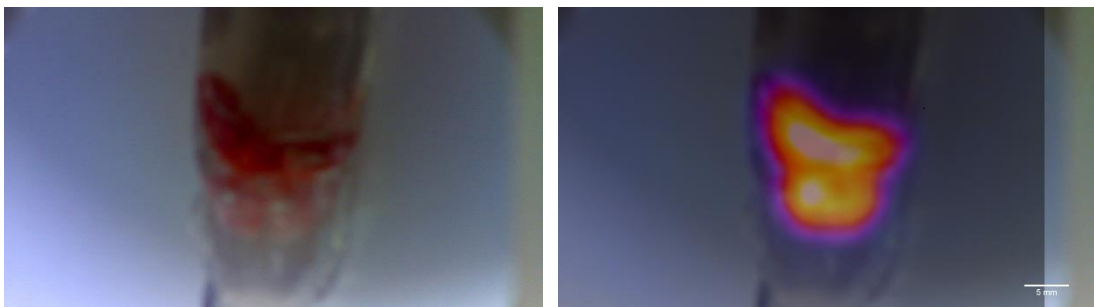


Figure 4.11: Optical and hybrid images of Phantom B acquired using HGC fitted with 0.5 mm pinhole collimator.

For comparison purposes, imaging of Phantom B with a standard preclinical SPECT-CT scanner (NanoSPECT/CT®PLUS, Mediso Medical Imaging Systems, Budapest, Hungary) in the SPOT preclinical imaging facility was performed. The images were viewed using VivoQuant™ 2.50 multi-modal image processing software (inviCRO,

Boston, USA). Figure 4.12 shows the SPECT-CT images of different plane of views in which there was a distinct demarcation between the lung and liver cavities.
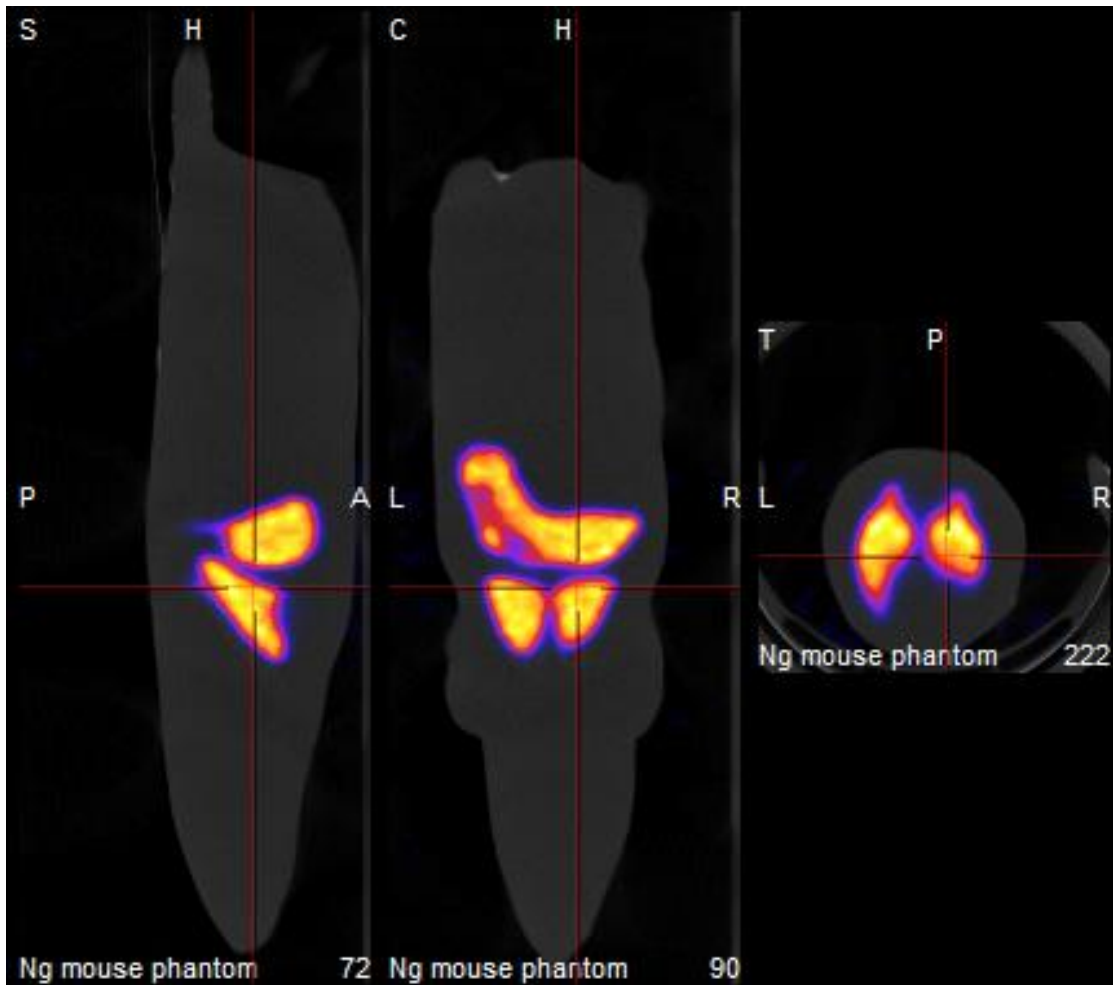


Figure 4.12: Sagittal (left), coronal (middle) and transverse (right) view of SPECT-CT image of Phantom B (CT acquisition: 45 kVp, 500 ms; SPECT acquisition: 240 projections)

### 4.3.4   Discussion

Imaging with the mouse phantoms using the SFOV gamma cameras has demonstrated the challenges in imaging the relatively small sizes of tissues or organs in these models. The mouse skeletal phantom provided a simple method to assess SFOV gamma cameras in bone scintigraphy. It was however found that the planar images obtained from the camera could not resolved the fine details of the small bone structure where the separation of the active regions was of the order of 1 mm, however the overall pattern of the radioactive source within the phantom could be clearly visualised. One disadvantage is that filling of the radioactive solution was time consuming due to the fine structure of the phantom. Since it was not possible to seal the activity in the

phantom there was a risk of contamination during use. In addition, the radioactive solution was found to evaporate over a period of time resulting in non-uniform distribution of the radionuclide during the experiments.

The 3-D printed phantom offered a novel method for assessing imaging capabilities. Over the range of SCD used, the separation between the organs (lung and liver) was not resolved. The 3-D printed mouse phantom featured selected organs to provide a robust and realistic test object not only for assessing the SFOV gamma cameras, but also for SPECT and PET imaging. These phantoms can be filled with radioactive sources of different activity concentrations, and could possibly to be used for routine testing of dual-modality radio and near-infrared fluorescent (NIRF) probes in future.

## 4.4 Evaluation of a hybrid near infrared fluorescent-radioactive probe for tumour necrosis imaging

### 4.4.1 Introduction

Tissue necrosis is a form of cell death caused by external factors or disease, such as radiation, and loss of blood supply and is an important factor in tumour growth and cancer progression. It is characterised by cell swelling, irreversible plasma membrane damage, and organelle breakdown. The detailed processes are discussed elsewhere [133]. Since each necrotic dying cell releases pro-inflammatory signals, the amount of tissue necrosis can be used as a prognostic factor or predictor of various cancer diseases [134]. As a rule of thumb, a higher amount of necrosis represents more aggressive tumour cell growth and is usually associated with poor patient prognosis.

Xie *et al.* [115] have reported the use of near infrared fluorescent (NIRF) carboxylated cyanines, namely HQ5 and IRDye 800CW (800CW), which shows significant necrotic avidity to quantify tumour necrosis, through optical imaging. This NIRF imaging technique provides promise for whole body imaging of small animals as well as imaging superficial tissues in human subjects. However, the penetration depth of the emitted lights from NIRF agents coupled to biomolecules in living subjects is limited to 1-2 cm [135], resulting in the  insufficient detection of light signal from deep seated tissues when viewed externally.

Nuclear medicine imaging has been used clinically over the decades to image various diseases including deep seated tumours due to its high photon penetrative capabilities. At the time of this study the Leiden University Medical Center (Leiden, the Netherlands) had newly developed cyanine-based radioactive probes for multimodal tumour necrosis imaging. NIRF and SPECT imaging were being carried out to evaluate the efficacy of the probe in animal tumour models. The aim of this study was to explore the feasibility of the SFOV hybrid optical gamma cameras for preclinical imaging, particularly to evaluate the *in vivo* imaging performance of an ^{111}In-labelled probe.

### 4.4.2   Method

#### 4.4.2.1   Animal and probe

The Leiden University Medical Center (Leiden, the Netherlands) prepared the animal models and probes for this study. Two female athymic nude mice (BALB/c nu/nu, 6 weeks old) (Charles River Laboratories, L'Arbresle Cedex, France) were implanted with bilateral and subcutaneous 4T1-luc2 tumour cells (PerkinElmer, Waltham, MA, USA) onto the lower back region. The mice were identified as M1 and M2 in this experiment. Tumours were allowed to grow for approximately 1.5 - 2 weeks after tumour implantation until they reached a size of 6 - 7 mm in diameter. Figure 4.13 shows a photograph of the tumour bearing mouse with two lumps in the lower back.
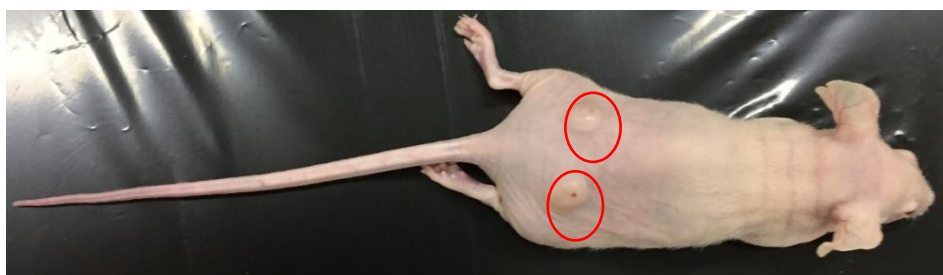


Figure 4.13: Photograph of the 4T1-luc2 tumour bearing mouse. Two bilateral and subcutaneous tumours (red circles) can be clearly seen in the lower back of the nude mouse.

The newly developed dual-modality probe (^{111}In-DTPA-RGD-800CW) was prepared in-house and administered intravenously into the tumour bearing mice (32 MBq each). All experimental surgical and analytical procedures were performed under isoflurane gas anesthesia (3% induction, 1.5-2% maintenance) in 70% pressurised air and 30% oxygen gas. Animals were sacrificed by cervical dislocation at the end of the experimental period. All animal experiments were carried out according to local animal

health, ethical requirements and the research was approved by the Animal Welfare Committee of Leiden University Medical Center, the Netherlands.

### 4.4.2.2 Imaging

All imaging was carried out using the Nebuleye and HGC SFOV gamma cameras fitted with a 1 mm diameter pinhole collimator. Prior to administration a sample of the tracer containing approximately 13.8 MBq was placed in an Eppendorf tube and images recorded to test the correct operation of the camera. Following the administration of the radiolabelled probe to the mice, the Nebuleye was used to acquire *in vivo* images of the mice at different time points up to 31 hours 41 minutes after administration. The camera was either held by the operator or placed on top of a foam or plastic stand during image acquisition. Figure 4.14 shows a photograph of the Nebuleye in use during animal imaging. After the final imaging the M2 mouse was sacrificed and several tissues were excised. Further *ex vivo* imaging was then carried out. The hybrid planar images of the mice were presented in a fused optical-gamma display. A standard SPECT image produced by a 3-headed U-SPECT-II gamma camera (MILabs, Utrecht, the Netherlands) was available for comparison.



Figure 4.14: Photograph of the animal imaging setup at Leiden University Medical Centre using Nebuleye. The camera was positioned on an ad-hoc foam stand to minimise motion effect during image acquisition.

### 4.4.3 Results

Figure 4.15 shows an example of the optical, gamma and fused image of an ^{111}In-labelled probe in the Eppendorf tube, acquired by Nebuleye during the control testing of the camera system. This was the first use of the camera for *in vivo* radionuclide imaging studies in experimental animals in this case nude mice bearing 4T1-luc2 tumour cells. Figure 4.16 shows the optical, gamma and the fused images of the mouse, 105 minutes following the administration of ^{111}In-labelled probe. Based on the gamma image, these radiotracers could be clearly seen to be accumulated within the central part of the body (possibly liver, kidney) and the bladder (excretion).
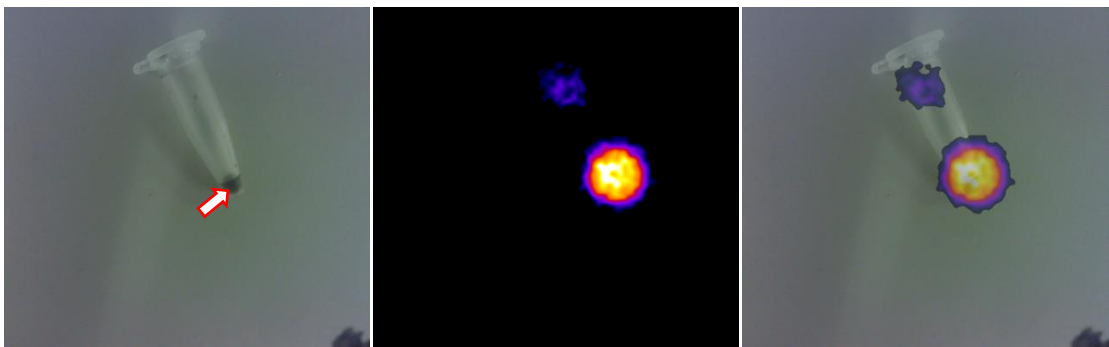


Figure 4.15: (Left) Optical, (middle) gamma and (hybrid) images of Eppendorf tube filled with ^{111}In-labelled probe (arrow), acquired using Nebuleye positioned on a plastic stand 7 cm away from the source and with a 500 s of imaging time. The gamma image also indicated that there was a small amount of ^{111}In source contaminated on top part of the tube.
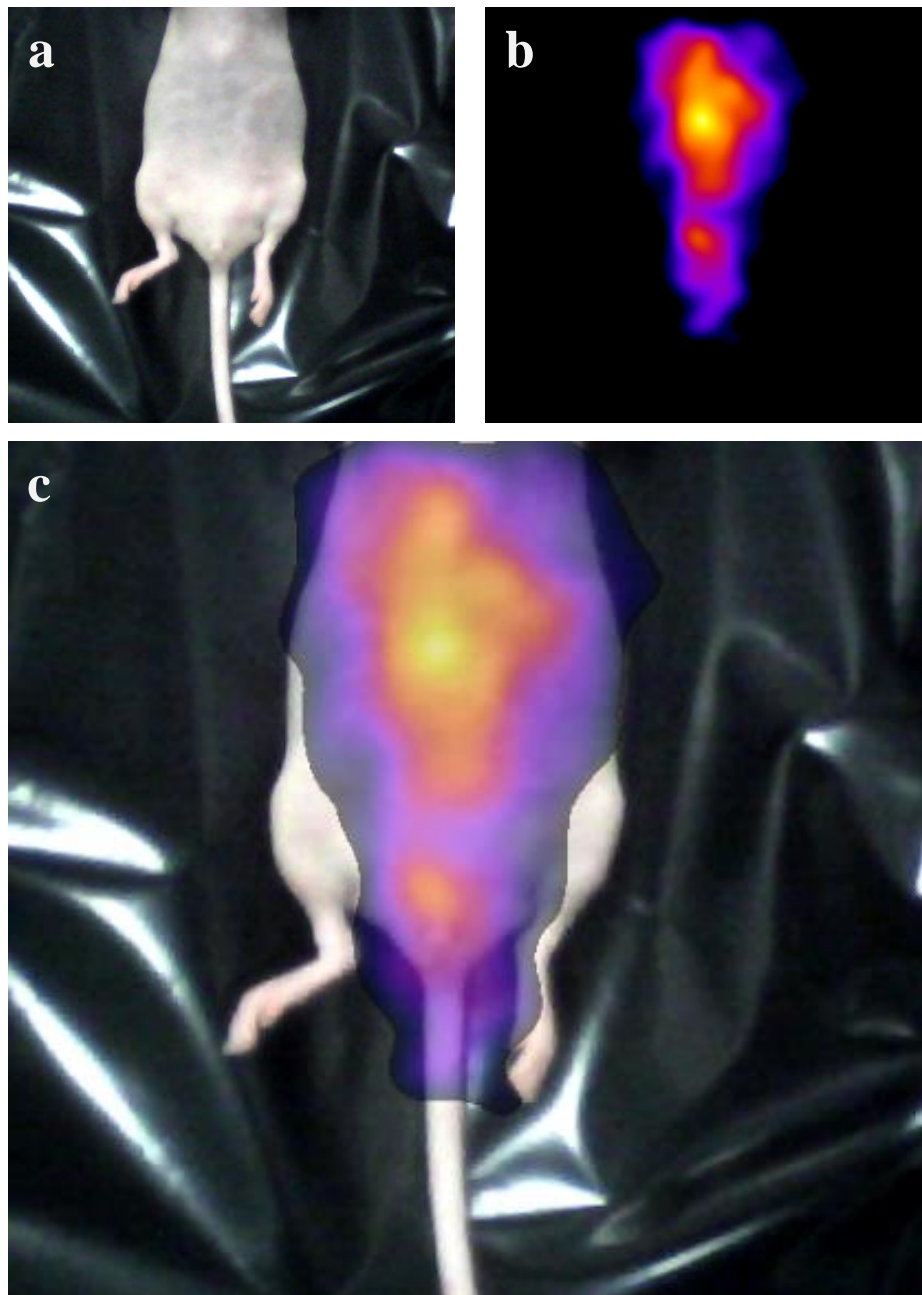
Figure 4.16: Example image of mouse in supine position, acquired by HGC at 105 minutes post-administration of 32 MBq ^{111}In-labelled probe, placed at SCD of 12 cm for a 30 s acquisition time: (a) optical (b) gamma (c) hybrid images. Images were cropped and post-processed.

Further imaging was performed using the Nebuleye at different distances and imaging times, with the mice in a prone position. Figure 4.17 (top) shows the images of mouse M1 26 hours 42 minutes following administration of radiolabelled probe (SSD 12.5 cm; 10 minutes acquisition) while Figure 4.17 (bottom) shows the image of mouse M2 at 30 hours 52 minutes post-administration of the probe (SSD 7 cm; 20 minutes acquisition). Even though the acquisitions were carried out at nearer imaging distance and with longer imaging times, both sets of data only showed a single bright blob within

the central part of the body and did not identify activity within the tumour masses implanted on the back of the mice.

| **Gamma** | **Optical** | **Hybrid** |
|:---:|:---:|:---:|
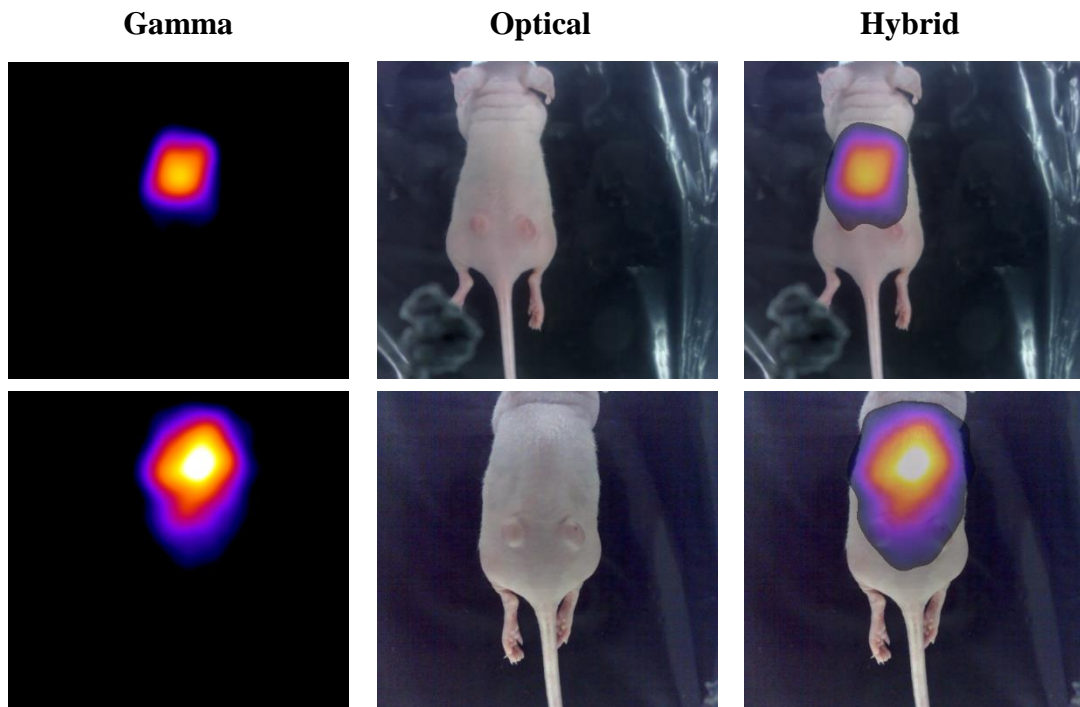


Figure 4.17: Gamma, optical and hybrid images of the (top) mouse M1 acquired using Nebuleye positioned at SSD of 12.5 cm (on top of a plastic stand) with 10 minutes acquisition time and (bottom) mouse M2 acquired at SSD of 7 cm and 20 minutes imaging time.

At this time point, mouse M2 was sacrificed as planned in the study protocol and additional images were taken using Nebuleye at a closer distance, focusing on the central region of the body. Figure 4.18 shows the images acquired by Nebuleye with mouse M2 placed directly on top of the imaging window (~SCD 30 mm). Two bright blobs shown in gamma image (Figure 4.18 (a)) were detected with this camera settings, representing the radiotracer distribution within the kidneys. As the camera distance setting was too close to the mouse, the optical image produced did not show any specific anatomical landmarks that could be identified. Figure 4.19 shows series of gamma image from the same study acquired using different lengths of acquisition time. Subjective visual assessment found that the shape of the kidneys could be clearly defined within a minute acquisition time and that there was no advantage by imaging over times greater than 100 s.
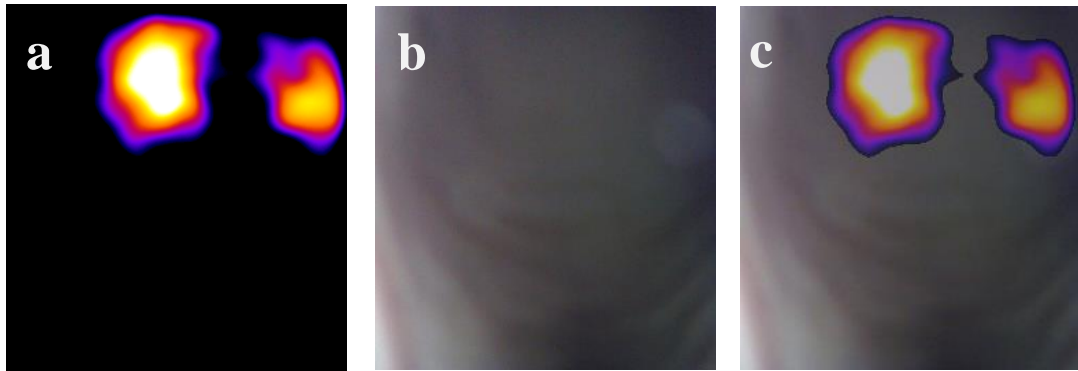
Figure 4.18: The (a) gamma (b) optical (c) hybrid images showing activity distribution in the right and left kidneys, acquired 31 hours 41 minutes following administration of 32 MBq $^{111}$In to the mouse M2. The gamma image was acquired by Nebuleye facing upward and the mouse M2 was placed supinely on the top of the camera imaging window, with 200 s acquisition time.
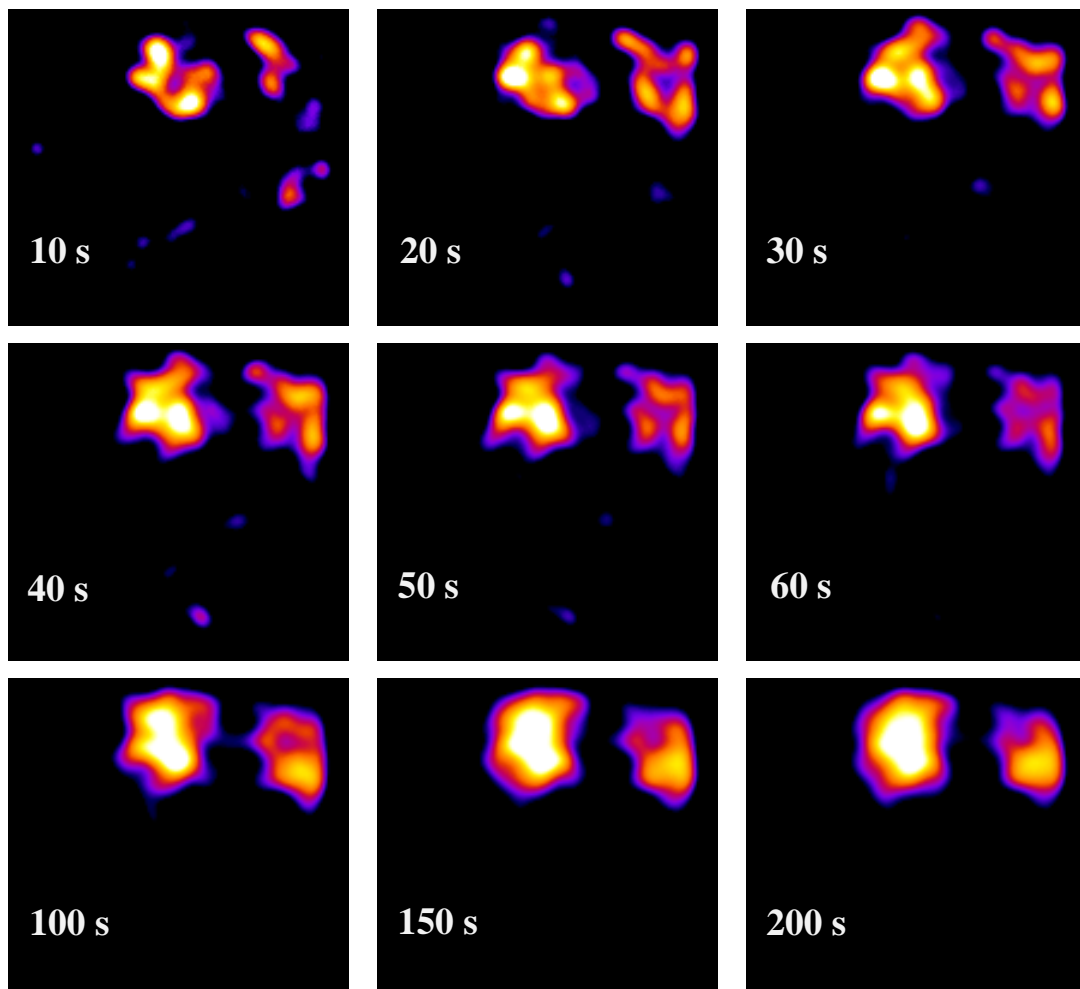


Figure 4.19: Gamma images of the same mouse imaging setup displayed in cumulative time series (from 10 s to 200 s as indicated in the images). Gaussian blur filter (4 pixel) was applied.

*Ex vivo* imaging were performed with the excised kidney, tumour and muscle tissues (control) from mouse M2 using the HGC. Figure 4.20 shows the image of radiotracer distribution in the excised tissues. The hybrid image confirmed accumulation of the

radiotracer in the kidneys whereas there was no uptake seen in the tumour and muscle tissues. For comparison the coronal SPECT image of the same mouse acquired using the preclinical SPECT camera system (shown in Figure 4.21), show that the distribution of the radiotracer was similar and radiotracer uptake within the kidneys can be clearly seen.
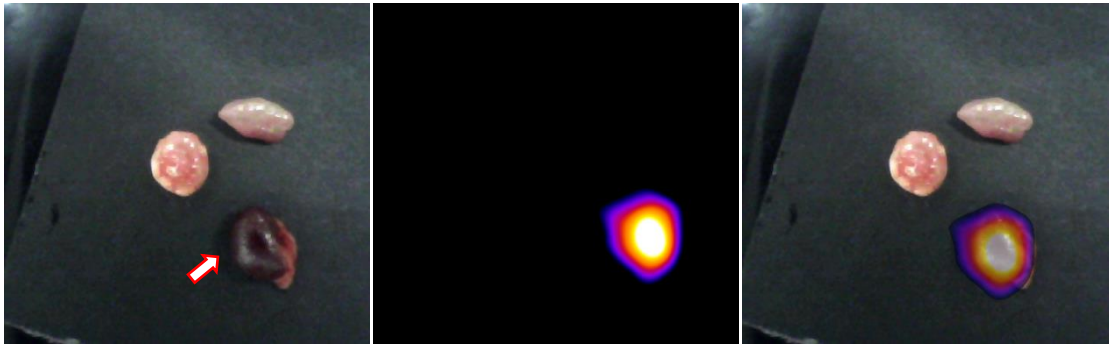


Figure 4.20: (Left) Optical, (middle) gamma and (right) hybrid images of the excised tissues (kidney (red arrow), tumour and muscle), acquired using HGC handheld by operator with camera at 3 cm away from the tissues and with a 300 s of imaging time.
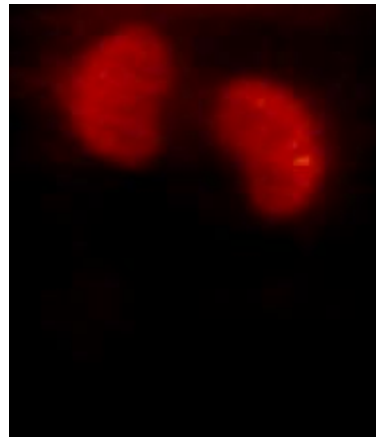


Figure 4.21: 2-D coronal plane gamma image generated from SPECT of mouse M2, taken approximately 36 hours after administration of 32 MBq $^{111}$In probe. The image was acquired using a 0.6 mm mouse pinhole collimated, 3-headed U-SPECT-II gamma camera (MILabs, Utrecht, the Netherlands) with energy settings at 171 and 245 keV and a window of 20%. Subsequently, the image was reconstructed using 20 Pixel-based subsets for rapid multi-pinhole (POSEM) iterations with 4 subsets, 3-D gauss 0 mm (FWHM) filtering and a 0.2-mm voxel size, and with decay and scatter corrections integrated into the reconstruction (image provided by LUMC).

### 4.4.4 Discussion

This was an exploratory experiment carried out at Leiden University Medical Centre to assess the imaging performance of the SFOV gamma cameras (Nebuleye and HGC) in experimental animal tumour models. During this work, additional modifications were made to the HGC to explore the proof of concept of NIRF imaging. A bandpass filter

with nominal center wavelength of 850 nm (FWHM 100 nm) was fitted to the existing optical camera. Even though exploratory NIRF imaging was carried out concurrently in this study, using the modified HGC, the pilot results were not discussed in this thesis until more promising results have been obtained. An example image (Figure 9.2) is shown in the general discussion in Chapter 9. There was limited access to the mice for radionuclide and fluorescence imaging since the imaging was performed sequentially on an individual mouse, and it was necessary to minimise unnecessarily prolonged periods of anaesthesia to reduce any adverse effects on respiration, cardiovascular disruption or thermoregulation caused by prolonged anaesthesia [136].

The probe developed in this study was intended for HT29 tumour cell necrosis imaging, however following dissection it was shown that the cells did not grow as expected. Alternatively, 4T1-luc2 tumour cells were introduced to the nude mice to complement the study. No specific uptake of the probe was expected in the 4T1-luc2 tumour cells, and this was confirmed from the gamma imaging results. The images show that the sensitivity and spatial resolution of the SFOV gamma cameras require further improvements for the animal studies especially when imaging a mouse in which the sizes of the organ are relatively small.

## 4.5 Summary

Preliminary phantom assessments were undertaken using bespoke phantoms to examine the performance of the SFOV gamma cameras for use in preclinical imaging. The results of the animal study obtained for the first time have demonstrated the feasibility of using SFOV hybrid optical gamma cameras for imaging mice injected with newly developed $^{111}$In labelled tracers. As expected the hybrid cameras do not have the superior imaging capability equivalent to SPECT imaging due to the relative lower sensitivity and resolution of planar imaging, however they may have a role in planar imaging of experimental animal models in a similar way to bioluminescence imaging where the fluorescent image is fused with a standard optical image. The relatively low cost in manufacturing the SFOV gamma cameras could offer a quick look solution for screening large numbers preclinical imaging studies. Further investigation is needed to improve the system sensitivity and resolution and to develop camera systems for combined gamma-NIRF imaging in future.

# Chapter 5

# Assessment of the potential use of the SFOV Hybrid Optical Gamma Cameras for Breast Cancer Surgery

## 5.1 Introduction

Breast cancer is the most common cancer diagnosed in women worldwide. In 2014, Cancer Research UK estimated that there were 55,222 new cases of breast cancer and 11,433 deaths in the UK [137]. The disease is mainly divided into two categories, namely invasive and non-invasive breast cancer (carcinoma in-situ). Invasive breast cancer has the potential to spread from the primary tumour site to other parts of the body, through the bloodstream or the axillary lymphatic system, resulting in secondary or metastatic breast cancer. The findings using diagnostic imaging modalities provide important information for the staging of the disease.

The treatment of the breast cancer may vary depending on the stage of the disease. In general it involves surgery or radiotherapy to treat local disease in combination with chemotherapy, endocrine therapy or biological therapy to treat systemic disease. The axillary node status is a major prognostic factor and is used for tailoring patient-specific treatment [138]. The conventional approach to determine the node status was axillary lymph node dissection. However this approach carries risks of both acute and late morbidities for the patient, with complications such as lymphedema [139].

Sentinel lymph node biopsy (SLNB) is a less invasive method to assess nodal involvement in breast carcinoma [140]. This is currently performed with the aid of radioguided gamma probe detection. With the current development of high resolution SFOV gamma cameras and the increasing interest in the intraoperative applications

[54], it was considered that the hybrid gamma cameras may offer potential in the localisation of the sentinel node as well as the primary tumour in the breast conserving surgery (BCS). This chapter describes the pre-surgical assessment of the SFOV hybrid optical gamma cameras for use in intraoperative imaging of patient with breast cancer. The cameras were assessed objectively and subjectively using phantom simulations and test objects. The test results were then compared with images produced by a clinical LFOV gamma camera and a commercially available SFOV gamma camera system.

## 5.2   Intraoperative imaging in Breast Cancer Surgery

Povoski *et al.* [141] has summarised the use of a gamma probe for the intraoperative detection of radionuclides. In radioguided breast cancer surgery, the applications include sentinel lymph node biopsy (SLNB), radioguided occult lesion localisation (ROLL), sentinel node and occult lesion localisation (SNOLL) and radioactive seed localisation (RSL) procedures. Gamma probes provide an audible signal that indicates the level of radiotracer uptake in breast tissues allowing the surgeon to harvest the suspicious nodes or tissues in the same way as surveying an area of ground with a metal detector.

With the current technological developments it is apparent that SFOV handheld gamma cameras may offer potential clinical utility in any of the aforementioned areas of investigation currently carried out using gamma probes. In addition, high resolution portable gamma cameras may provide added values in SLNB procedure when no standard LFOV gamma camera is available, in cases of difficult drainage or extra-axillary drainage, where there is low radiopharmaceutical uptake within the target tissues, when sentinel lymph nodes (SLNs) are located close to the injection site or where there is radiation scatter caused by high activity at the injection site [142].

### 5.2.1   Sentinel lymph node biopsy (SLNB)

Sentinel Lymph Node Biopsy (SLNB) is regarded as the standard method to determine the likelihood of cancer spreading from a primary breast tumour and becoming metastatic throughout the lymphatic system in cases of early-stage breast cancer with clinically negative nodes [140]. It is based on the assumption that invasion of malignant cells at the sentinel node triggers potential metastatic growth. Figure 5.1 illustrates the

human lymphatic networks and shows an example of cancerous cells migration from the primary site to the SLNs.
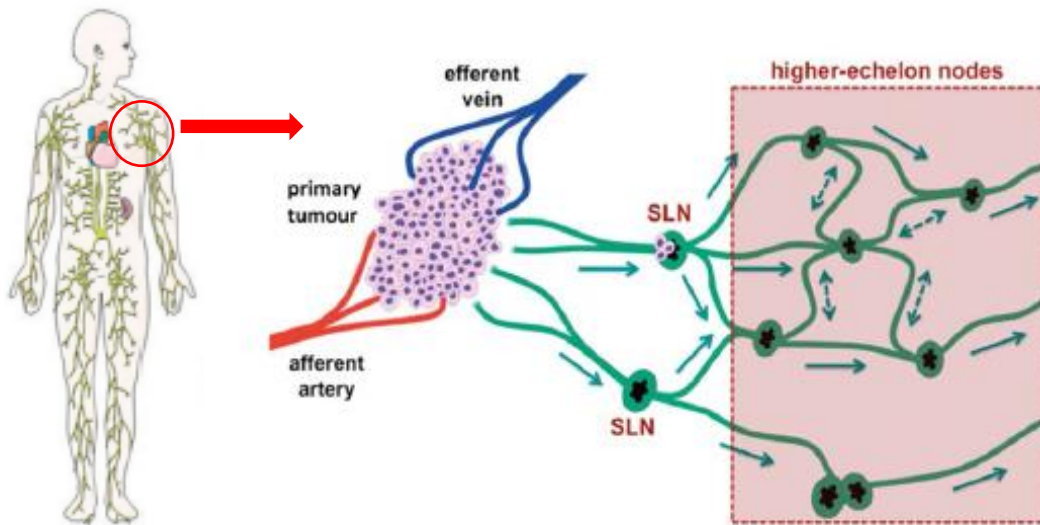


Figure 5.1: Schematic drawing of the lymphatic network (left) and the migration of cancerous cells from primary tumour to SLNs through lymphatic vessel. Images taken from [143].

The standard protocol for the SLNB procedure involves the administration of a $^{99m}$Tc-labelled radiotracer (Table 5.1) such as $^{99m}$Tc-nanocolloid albumin and a blue dye (Patent Blue V, Laboratoire Guerbet, Aulnay-sous-Bois, France) to identify the location of the sentinel node. A handheld gamma probe is used during surgery to identify the uptake of the radiotracer in the node [141]. This gives an audible signal or a visible display shown as a count rate. In some centres, lymphoscintigraphy is performed using a standard gamma camera or SPECT-CT scanner to image the distribution of the tracer prior to surgery (Figure 5.2), however this is not usually carried out in UK departments, because most surgeons are now proficient in using the gamma probe alone.

Table 5.1: $^{99m}$Tc-based radiopharmaceutical used in SLNB procedures taken from [143].

| Colloid composition | Size range (nm) | Notes |
|---|---|---|
| Human serum albumin | 3–600 | Registered in different countries in Europe; not approved in USA |
| Stannous/stannic hydroxide | 30–200 | Approved in some European countries |
| Rhenium sulphide | 8–68 | Registered in different countries in Europe |
| Sulphur colloid | 50–1000 | Registered in USA |
| 0.1 µm filtered sulphur colloid | 30–50 | |
| Antimony trisulphide | 2–16 | Registered in Australia |
| | 17–23 | |
| Calcium phytate | 150–200 | Mainly used in Japan; size depends on Ca$^{2+}$ concentration |
| | 150–1500 | |
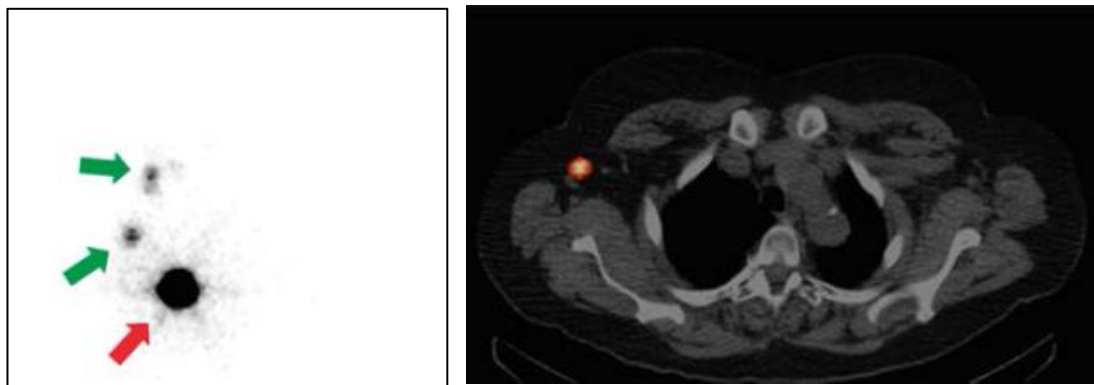


Figure 5.2: Example of lymphoscintigraphy (left) and axial plane of SPECT-CT imaging (right) performed using clinical camera systems prior SLNB procedure, taken from [143]. Red arrow indicates the injection site and the green arrows show the sentinel nodes.

The amount of administered radioactivity typically varies between 3.7 MBq and 370 MBq depending on the study protocol and patient morphology [144-146]. Only a small fraction of the injected radiopharmaceutical clears from the injection site to accumulate in the SLN (typically ranging between 0.1 % [147] and 1.0 % [148] of the injected dose per lymph node). One of the major factors to determine the efficiency of the nodal uptake is the size of the particulate with smaller nanoparticles (<10 nm) generally being more suitable for lymphoscintigraphy or rapid SLNB and larger particles (>100 nm) being retained longer in the first encountered lymph node [143].

Recent developments in SFOV gamma camera technologies offer real time intraoperative imaging in SLNB procedures [46, 47, 58, 64, 81, 88, 149-152]. This can provide additional information to surgeons in localising the sentinel node, in guiding the direction and margin of the dissection and in reducing the potential to miss the involved nodes. It is thought that these gamma cameras may also allow monitoring of the clearance of the radioactive sentinel node within the lymph basin and localisation of deeply seated nodes or nodes adjacent to another source of radioactive uptake which cannot be detected by the non-imaging probe.

### 5.2.2 Radioguided occult lesion localisation (ROLL) / Sentinel node and occult lesion localisation (SNOLL)

Due to the advances in mammographic imaging and the widespread use of breast screening programmes, about 25-35 % of breast cancer detected are non-palpable at diagnosis [153, 154]. The accurate identification of the non-palpable lesions pre- and intraoperatively as well as the precise localisation of the tumour with its adequate resection margin are crucial in the quality of surgical care as these factors affect the oncological and cosmetic outcomes [155]. Previously wire guided localisation (WGL) has been the standard technique used in guiding the surgical resection of non-palpable breast tumours where a guide wire is placed *in situ* under ultrasonographic or radiographic control.

Radioguided occult lesion localisation (ROLL) is an increasingly popular technique, which was first reported by Luini *et al.* in 1998 [156]. The ROLL technique involves the injection of $^{99m}$Tc-labelled macro-aggregates of human serum albumin to the breast tumour under the guidance of ultrasonography or mammography. The amount of injected activity typically ranges from 3.7 MBq [156] to 90 MBq [157]. A gamma probe is used intraoperatively to identify the site of the tumour and to determine the resection margins.

This procedure can be combined with the SLNB procedure to harvest SLN, which is also known as the combined sentinel node and occult lesion localisation (SNOLL). It may involve the additional injection of radioactive source $^{99m}$Tc-nanocolloid using subdermal technique. Several research groups have reported the first use of the SFOV

gamma cameras in ROLL and SNOLL procedures [48, 158, 159]. These studies showed that the cameras provided intraoperative imaging to guide the localisation of tumour and may predict tumour dissection margins. It was also stated that the use of the camera may shorten the surgical time in comparison with use of the gamma probe [158].

### 5.2.3 Radioactive seed localisation (RSL)

In 2001, Gray *et al.* reported a seed localisation technique in the biopsy or lumpectomy of non-palpable breast lesions [160]. Radioactive seed localisation (RSL) is another radioguided surgical technique to identify occult breast tumours by using the insertion of a sealed radioactive $^{125}$I seed in the breast tissue to be excised, under ultrasonographic or mammographic guidance (Figure 5.3). The gamma probe is then used to locate the radioactive seed in order to guide the surgeon to the suspicious opacity or lesion during the surgical procedure. Other research groups also proposed the use of a dual-head gamma camera system equipped with a parallel-hole low energy collimator to localise the radioactive seed [161]. The RSL procedure was found to be simpler than the ROLL technique and due to the longer physical half-life of the $^{125}$I seed, it could be inserted prior to surgery without causing discomfort to the patient [162].



Figure 5.3: Example showing the use of mammographic X-ray imaging to reconfirm that the seed has been accurately inserted within an invasive ductal carcinoma of the left breast. Taken from [163].

Similar to ROLL procedure, the use of SFOV gamma cameras in RSL could be beneficial. The camera used should be sensitive enough to detect lower energy gamma rays (~35 keV) emitted from $^{125}$I and should have the spatial resolution to resolve a radioactive seed of small physical size (~1 mm in diameter). Pouw *et al.* [164, 165] reported the feasibility of the application of a freehand SPECT, a unique combination of conventional gamma probe with an optical tracking system in RSL. The imaging system provided continuous real time 3-D gamma images with information about depth and location of the radioactive seeds, thus enabling accurate and adequate excision of the tumour. In addition, it was suggested that the RSL technique may improve daily clinical logistics and reduce the workload of the radiology department.

## 5.3 Assessment of the performances of SFOV gamma cameras in SLNB

With the introduction of SFOV gamma camera systems into surgical practice it is essential that there are rigorous methods for testing, evaluation and quality control as discussed in Chapter 3. Further understanding of the performance and limitations of SFOV gamma cameras in SLNB procedure is important to ensure a high quality surgical care. There has to date been limited systematic assessment of SFOV gamma cameras, particularly with phantoms designed to simulate the specific intended area of use, such as SLNB in breast cancer. The commercially available phantoms have mainly been used as training devices for simulation of the sentinel node detection process [166-168]. In addition, special features of the phantom such as the presence of high activity at the injection site, the different node depths (ND), the node-to-injection site separation (NS) and the node-to-injection site activity ratio (NIR) which mimic clinical scenario are necessary.

Some investigators have reported the use of simple bespoke phantoms in evaluating the performance of SFOV gamma cameras. Krohn *et al.* [169] performed a thorough assessment of mobile intraoperative imaging systems using a modified Jaszczak phantom. This phantom was commercially available and relatively expensive. Lees *et al.* reported the fabrication of a mini Williams Phantom with four wells in different diameters adjacent to each other specifically to assess the spatial resolution of SFOV gamma cameras [170]. Ferretti *et al.* has also described the use of four small spheres

for image quality testing [59]. These phantoms offer an inexpensive and simple method for the performance testing, however both phantoms must be filled with radioactive solution before use and the difficulty in doing this can be a major limitation due to the small cavities to be filled.

For any given SLN procedure differences in patient morphology may result in the accumulation of high activity at the injection site or low radioactivity uptakes of the node. These may cause radiation scatter effects if there are nodes located adjacent to each other, subsequently reducing the chances in detecting the true sentinel node [54]. There remains a need for a low cost, simple, versatile and reproducible phantom that simulates the clinical situation to investigate these issues and to assess and compare the new generation of camera systems entering surgical use. The aims of the study were to design a phantom and methods for assessing the specific imaging performance of SFOV gamma cameras for sentinel node imaging and to the compare performance with a standard LFOV gamma camera.

### 5.3.1   Design and construction of the sentinel node phantom

The phantom was designed to simulate the presence of a SLN and the injection site (IS) in a volume similar to that of the human breast, using movable radionuclide sources contained in syringes of different sizes. This allowed for the use of liquid sources with minimal risk of contamination (as used in a previous design of Perkins *et al.* [171]) and allowed the phantom to be safely and easily reconfigured during use. This modular concept phantom consisted of a series of PMMA plates with a layer of bars to provide flexibility in positioning the sources accurately within the phantom, allowing node depth and node-to-injection site separation to be varied. The use of syringes provided a convenient way to load the designated activity concentration of radionuclide.

The phantom was fabricated in the Department of Medical Physics and Clinical Engineering, Queen's Medical Centre, Nottingham University Hospitals NHS Trust from Polymethyl-Methacrylate (PMMA), commonly known as acrylic glass. The base structure of the phantom was a cube-shaped PMMA support frame, in a dimension of 120 mm (W) × 130 mm (D) × 110 (H) mm. It was assembled with four 10 mm thick plates. This offered pre-determined spaces to accommodate other components of the

phantom with variable configurations. Figure 5.4 illustrates the photograph of the sentinel node phantom assembly.
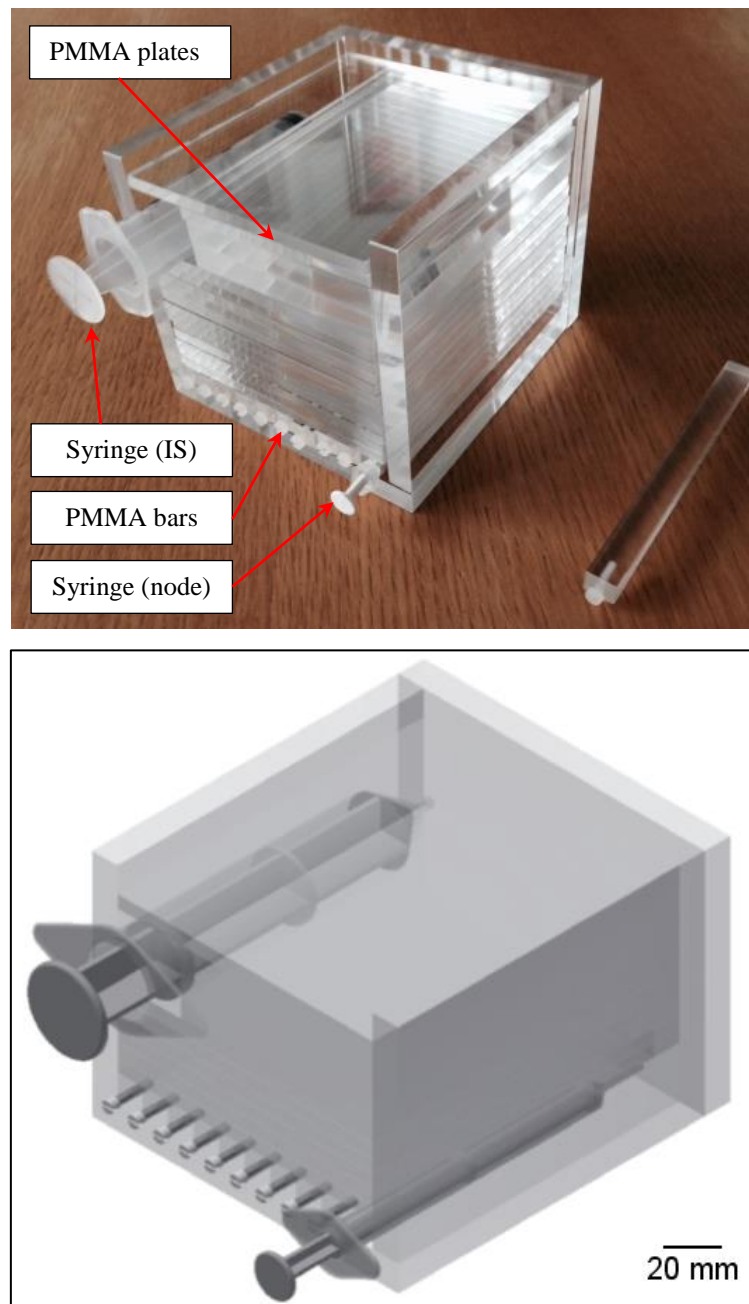


Figure 5.4: (Top) Photograph of the sentinel node phantom assembled with PMMA plates and bars within the cube-shaped support frame. Bigger syringe on the top left of phantom represented the injection site and the smaller syringe simulated the node. (Bottom) 3-D representation of the sentinel node phantom assembly.

Sixteen independent plates and nine bars were stacked within the PMMA support frame. A plastic screw was fastened at the end of each PMMA bar to aid insertion or removal of the bar during use. The upper surface of the phantom was covered with a

5 mm thick PMMA plate mimicking the skin surface. BD Plastipak® syringes (Becton, Dickinson and Company, Ireland) with maximum volumes of 20 ml and 1 ml were used as cavities representing the injection site and node respectively. The syringes were partly filled with radioactive solution and sealed with a blind hub to create discrete regions of radioactivity at the node-to-injection site activity ratio required.

This phantom design allowed for node depths of between 15 mm and 95 mm and node-to-injection site separations ranging between 25 mm and 95 mm (centre-to-centre distances). This dimensional configuration was based on previously published data where the size and depth of breast tumour and node were reported as having a mean node depth of 35 mm [172], tumour size of $17 \pm 9.4$ mm [173] and node size of 7 mm [174], with the mean distances from primary tumour to nodes varying between 65 and 125 mm [175]. Additional syringes could be added to simulate the presence of multiple node uptakes should that be required. Table 5.2 summarises the technical specifications of the phantom.

Table 5.2: Technical specifications of the sentinel node phantom.

| Features | Dimensions (mm) | Quantity |
|---|---|---|
| PMMA bars with plastic screw | $10 \times 120 \times 10$ | 9 |
| PMMA plates | $100 \times 120 \times 5$ | 13 |
| | $75 \times 120 \times 5$ | 1 |
| | $75 \times 120 \times 10$ | 2 |
| PMMA syringe stopper | $10 \times 20 \times 10$ | 1 |

Construction of the phantom was straight forward and could be easily undertaken by most clinical engineering workshops. The prototype was constructed at a cost of £360 including materials and labour. Syringes are readily available in all Nuclear Medicine Departments and this allows the flexibility for calibration in a standard radionuclide activity calibrator and filling with any radioactive liquid at various activity concentrations or volumes.

### 5.3.2    Phantom assessment methods

### 5.3.2.1    Performance of SFOV gamma cameras

The sentinel node phantom was used to assess the HGC in the research laboratory of the nuclear medicine clinic at Queen's Medical Centre, Nottingham University Hospitals NHS Trust and the Bioimaging laboratory at the Space Research Centre, University of Leicester. The performance tests involved the investigation of the detectability of a hot spot (node) in the acquired gamma images. During the tests, the phantom was used with two syringes filled with radioactive solution. Syringe 1 (injection site) and Syringe 2 (sentinel node) were filled with 3.0 ml and 0.1 ml of $^{99m}$Tc-pertechnetate solution respectively, with node-to-injection site activity ratios between 1:100 and 10:100. Figure 5.5 illustrates the experimental set up of the phantom imaging tests.
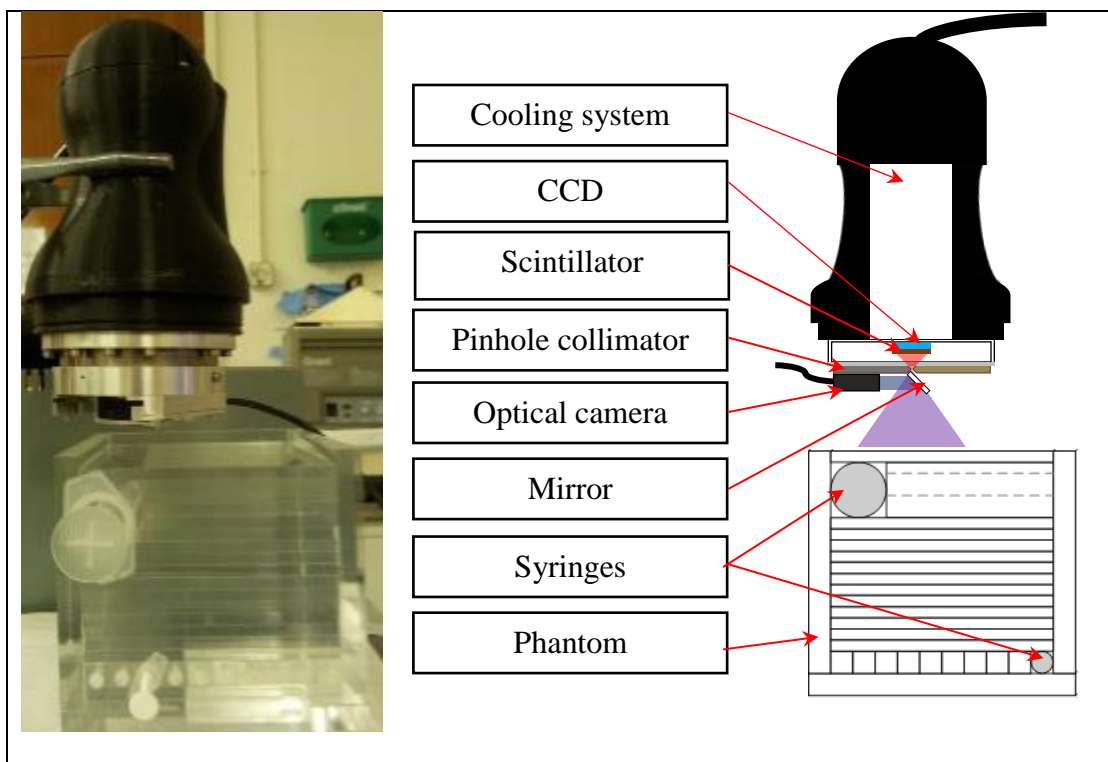


Figure 5.5: (Left) Photograph and (right) schematic diagram of the phantom imaging tests set up.

Syringe 1 was placed at the top left of the phantom, underneath the 5 mm thick square PMMA plate to simulate the injection site. Syringe 2 was positioned at different ND (between 15 and 95 mm from surface) and NS (between 25 and 95 mm) to simulate the node. Series of planar image were acquired with 60 seconds acquisition time. The optical camera was used to verify the position of the phantom during the experiments.

Resultant images were post-processed and analysed by using ImageJ 1.47v (National Institute of Health, US). Any outlier pixel(s) (bright spots) were removed and the image was filtered and enhanced by improving image contrast. Cumulative detection mode was chosen to present all images in this study while centre-point detection mode images were used for quantification purposes.

Figure 5.6 gives an example scintigraphic image of the phantom for a NIR 10:100, positioned at SCD of 180 mm. The node was positioned at 35 mm beneath the phantom surface and 65 mm (centre-to-centre) away from the injection site, which reflected the average position as mentioned in Section 5.3.1. Multiple images were acquired with different ND, NIR, SCD, NS settings, with the presence of high activity from the injection site. Figure 5.7 shows the example of the gamma images acquired at different NS and ND. The detectability of the sentinel node was assessed by quantifying the contrast-to-noise ratio (CNR) of the node (Section 5.3.2.3) and by the visual examination of images (Section 5.3.2.4).
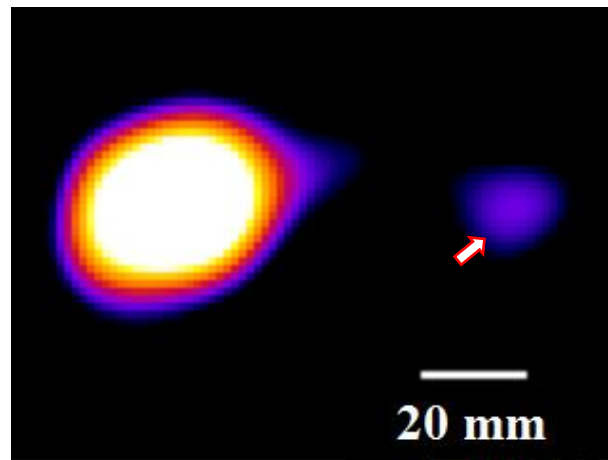


Figure 5.6: Gamma image of the simulated IS and node (arrow) (ND:35mm; NS: 65mm) filled with 20.2 MBq and 2.27 MBq $^{99m}$Tc-pertechnetate respectively placed at SCD 180 mm. Image was taken using 0.5 mm diameter pinhole collimator HGC with acquisition time of 60 seconds, subsequently applied with a 6.0 pixel Gaussian smoothing filter and cropped.
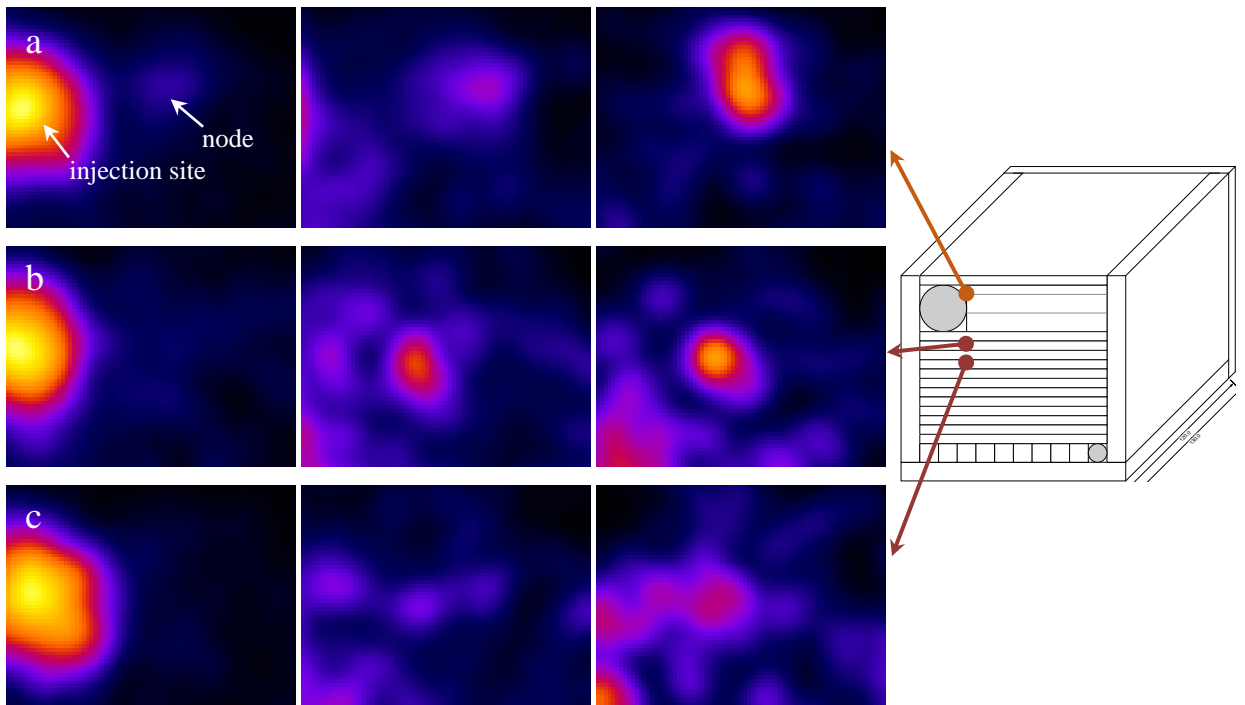
Figure 5.7: Image of the phantom with the presence of high activity at injection site acquired using HGC. The node containing 0.2 MBq $^{99m}$Tc (NIR 1:100), at the depth of 15 mm (row a), 45 mm (row b), 55 mm (row c) and NS of 25 mm (left column), 35 mm (middle column) and 45 mm (right column). Acquisition time for each image was 60 s. Images on row c do not show the node, the apparent features in both these images are due to scattered events from the injection site.

The phantom imaging acquired by the HGC gave a good indication of the potential of the sentinel node phantom in assessing different types of gamma camera. In light of this, the phantom was used with a second SFOV gamma camera - CrystalCam CXC-CT40A Gamma Camera (Crystal Photonics GmbH, Germany). Figure 5.8 shows the experimental set up during the imaging test with the camera system. This camera is equipped with changeable parallel-hole collimators (either low energy high sensitivity (LEHS) or low energy high resolution (LEHR)), having limited FOV but higher sensitivity compared to HGC, resulted shorter image acquisition time.
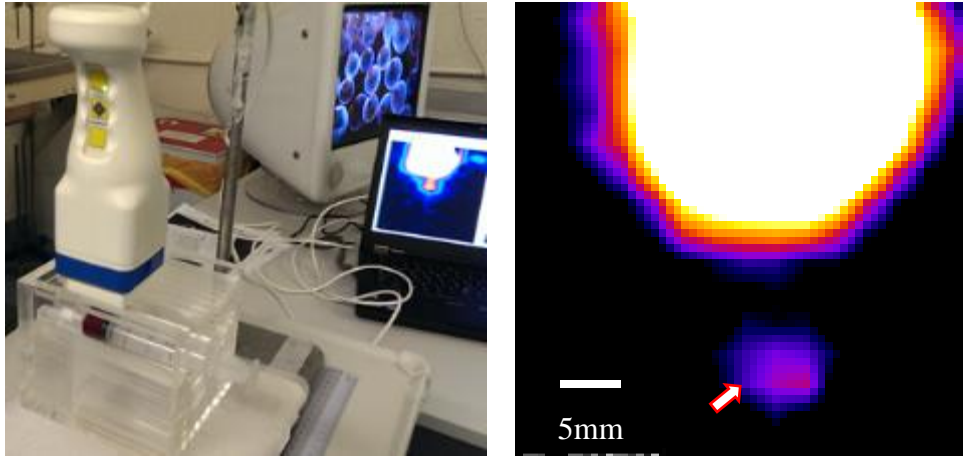
Figure 5.8: (Left) Photograph of the experimental set up during the detectability test. (Right) Gamma image of the simulated IS and node (arrow) (ND:15mm; NS: 35mm) filled with 20 MBq and 0.2 MBq $^{99m}$Tc-pertechnetate respectively placed at SCD 20 mm. Image were taken using CrystalCam gamma camera mounted with LEHS collimator with acquisition time of 5 seconds. The displayed image was post-processed with the change of pixel size from 2.5 mm/pixel to 0.625 mm/pixel to smooth the image.

### 5.3.2.2 Performance comparison with standard LFOV gamma camera

For comparison purposes, imaging with a conventional LFOV gamma camera (Nucline™ X-Ring-R, Mediso, Hungary) was performed at nuclear medicine clinic, Queen's Medical Centre, Nottingham University Hospitals NHS Trust. Scintigraphic images were acquired using the LFOV gamma camera fitted with a LEHR parallel-hole collimator for 60 s in a $128 \times 128$ matrix. The SCD was set similarly to the performance test carried out with the HGC. Images were viewed using a dedicated nuclear medicine workstation (Hermes Medical Solutions, London UK). Figure 5.9 shows the comparison of the images acquired using LFOV and SFOV gamma cameras in which the node at NS 25 mm could not be resolved by the LFOV gamma camera.
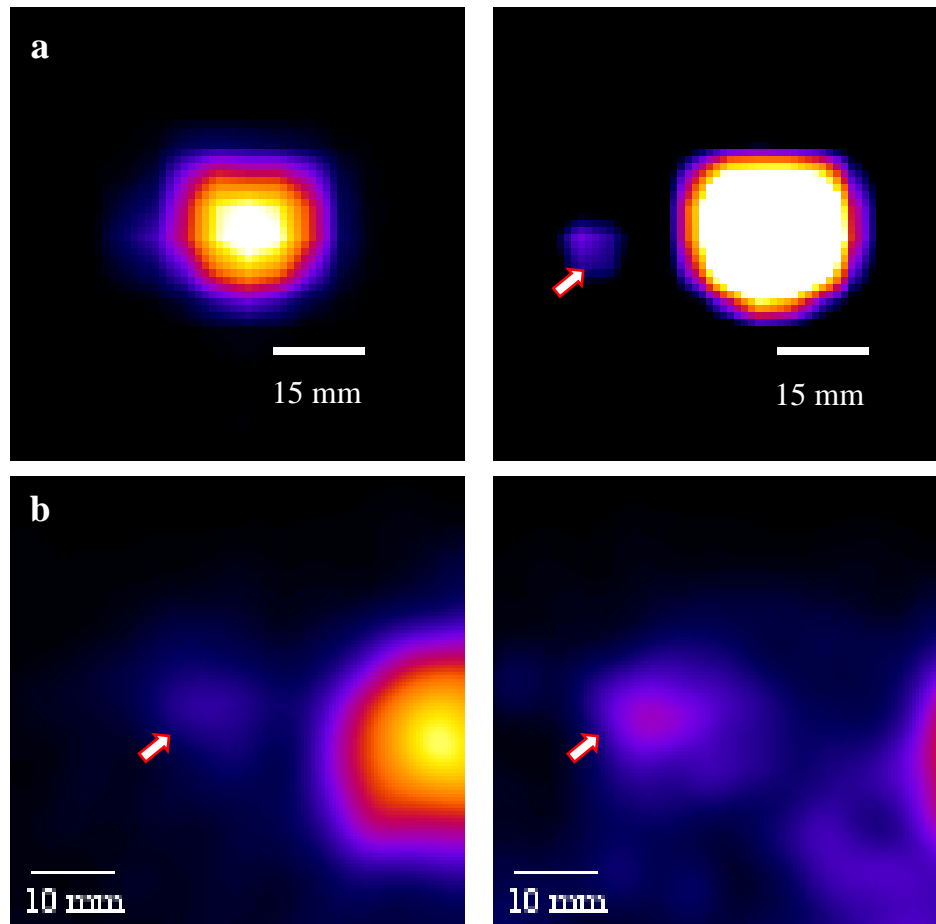
Figure 5.9: Comparison of images acquired using the (row a) LFOV and (row b) SFOV gamma cameras with NS of 25 mm (left) and 35 mm (right) at ND of 15 mm. The image acquisition was performed with 60 s acquisition time at SCD of 50 mm. The arrow indicates the simulated node.

Initial use of the sentinel node phantom for the assessment of Brightview XCT SPECT-CT camera systems (Philips Healthcare, Milpitas, CA, USA) was also explored. SPECT-CT system is one of the standard imaging modality used in pre-operative lymphoscintigram. The SPECT-CT images shows both anatomical and nuclear information which may guide the surgeon during SLN localisation procedure. Figure 5.10 illustrate the experiment setup and an image acquired by this camera system. With the aid of the CT image, the coronal view of the phantom image shows excellent demarcation between the simulated IS and node.
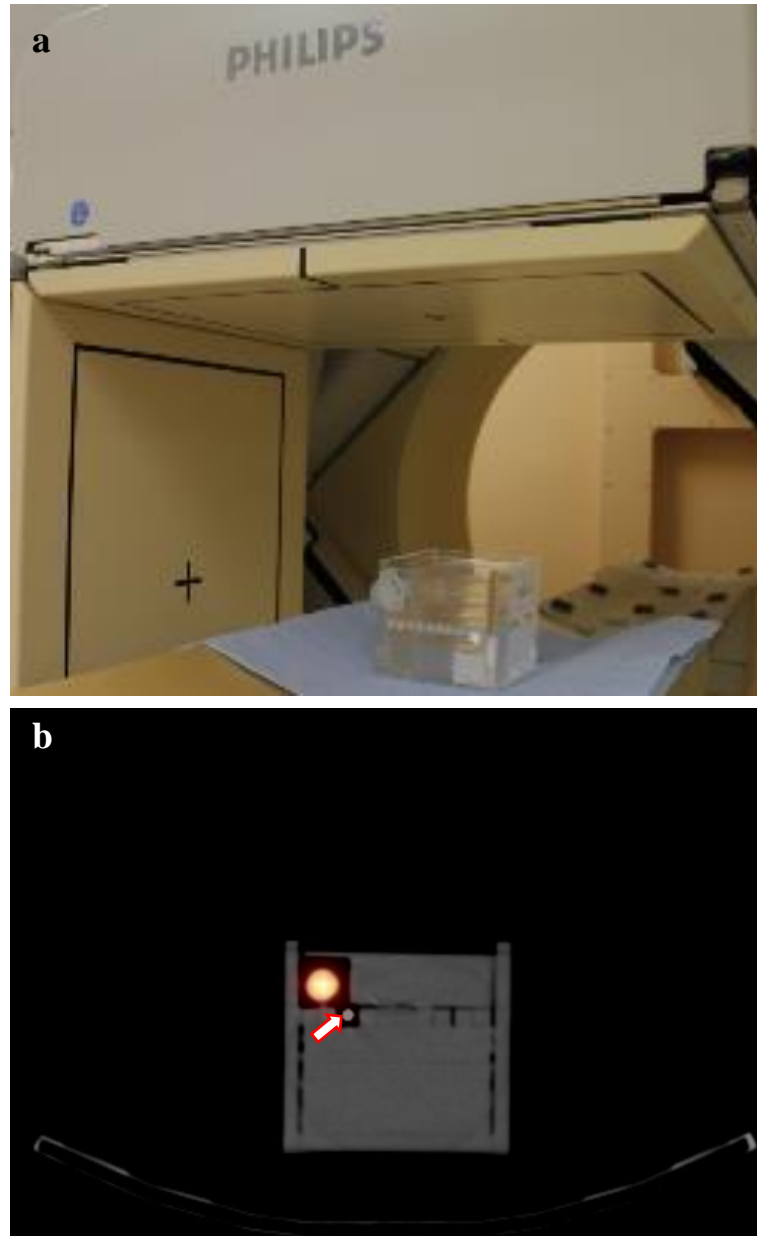
Figure 5.10: (Top) Photograph of the phantom imaging set up in the SPECT-CT camera. (Bottom) Example of hybrid SPECT-CT image at ND of 35 mm, NS of 25 mm centre-to-centre and acquired using the camera (LEHR collimator) with 1800 s acquisition time. The arrow indicates the simulated node.

### 5.3.2.3 Quantitative assessment (CNR)

Quantitative assessment was carried out by measuring the contrast-to-noise ratio of the node ($CNR_n$) using the equation 5.1.

$$CNR_n = \frac{N_n - N_0}{\sigma_0}$$

5.1

where $N_n$ is the value of pixels in a node area, $N_0$ is the value of pixels in the background area and $\sigma_0$ is the standard deviation of pixel values in background areas. The detectability of a node was correlated with the threshold CNR of the hot spot in the image. It was evaluated following Rose criterion [14, 176] where any hot spot with CNR value exceeding 3-5, considered to be detectable. The quantification was carried out using ImageJ 1.47v (National Institute of Health, US) and the measurements were performed three times in order to calculate the standard deviation.

CNR measurements were carried out with the phantom images of nodes located at depths between 15 mm and 55 mm with NS of 25 mm and different NIR (1:100 and 10:100), acquired by the HGC. The $CNR_n$ values were ranged between 3 and 62 as shown in Figure 5.11. The graph shows that higher radioactivity uptake by the node (higher NIR) increases the CNR values. However, the relationship between CNR and ND are inversely proportional. In particular, the phantom image assessment showed the detectability limits of node seated at depths below 45 mm with NS of 25 mm and NIR of 1:100. This indicates that the HGC will be capable to detect sentinel node which normally situated at mean depth of 35 mm.
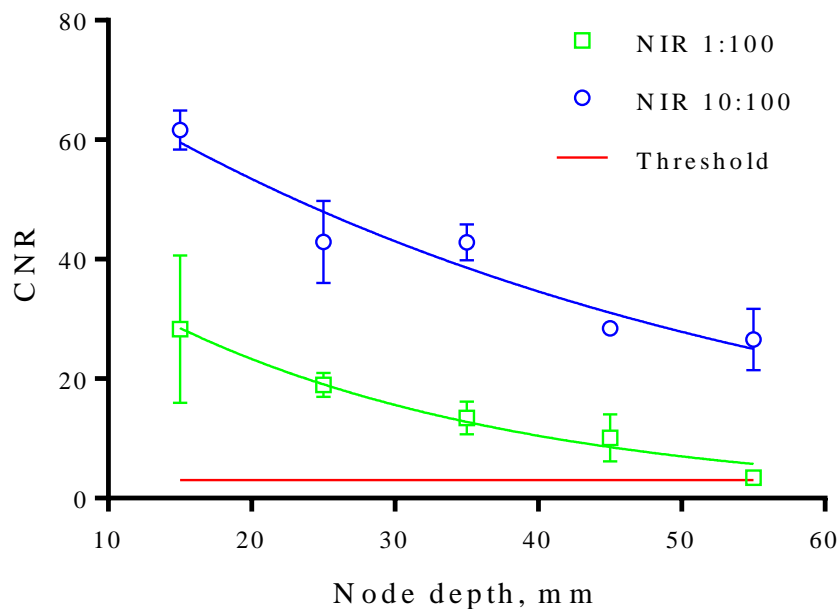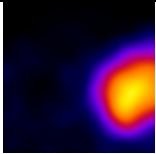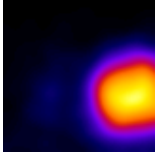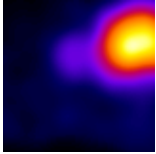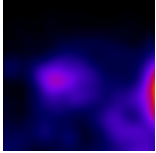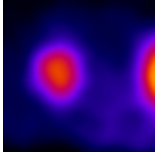


Figure 5.11: $CNR_n$ values (NS of 25 mm) as a function of ND and NIR (1:100 and 10:100). The images were acquired with 1 minute acquisition time using HGC mounted with 1 mm diameter pinhole collimator placed at SCD of 50 mm (n=3).

#### 5.3.2.4 Qualitative assessment

Two subjective types of visual assessment were performed to determine whether a node was detectable in an image acquired by either SFOV or LFOV gamma camera. The first assessment was carried out by a medical physics postgraduate researcher to visually assess the images followed by categorising them as visible (V), partially visible (P) and not visible (N). The second examination was performed by three independent assessors, two nuclear medicine professionals and a medical physics postgraduate researcher. After randomisation, anonymised gamma images were reviewed on a 24" flat-screen LCD nuclear medicine workstation. Each image was assessed and graded according to a standard grading scale in Table 5.3.

Table 5.3: Grading scores for detectability assessment of gamma image

| Grade | Descriptions | Examples |
|-------|-------------|----------|
| 1 | Node not detected. |  |
| 2 | Node partially detected (very faint or partially hidden by injection site). |  |
| 3 | Overall node detected without discrete border between node and injection site/background (node not clear). |  |
| 4 | Overall node detected with discrete border between node and injection site/background, but not excellent image quality. |  |
| 5 | Excellent node detectability with good image quality. |  |

Note: Example gamma images obtained using HGC from the phantom studies.

Table 5.4 summarised the results of the visual assessment of the node detectability. It was noticeable that the detectability of radioactivity distributions in the node degraded with the increasing depth of the node position. The phantom simulation tests revealed that, by visual examination of the images, the LFOV gamma camera could not detect

low-activity (0.2 MBq) in nodes with a NS of 25 mm at any depth whereas the HGC could detect the node up to the depth of 45 mm, i.e. images are impaired beyond that depth. Results from the independent visual assessment scores also suggested that the SFOV gamma camera had superior detectability for nodes at NS of 25 mm in comparison to the LFOV gamma camera for the same conditions (Table 5.5).

Table 5.4: Node detectability of the phantom images acquired with NIR 1:100, different ND and NS. Images were acquired in 60 s using conventional LFOV gamma camera mounted with LEHR parallel-hole collimator and HGC fitted with 1 mm diameter pinhole collimator.

| | SFOV | | LFOV | |
|:---:|:---:|:---:|:---:|:---:|
| **Node depth (mm)** | **Node-to-injection site separation (mm)** | | | |
| | **25** | **35** | **25** | **35** |
| 15 | V | V | N | V |
| 25 | V | V | N | V |
| 35 | P | V | N | V |
| 45 | P | V | N | V |
| 55 | N | P | N | V |
| 65 | N | P | N | P |
| 75 | N | P | N | P |
| 85 | N | P | N | P |
| 95 | N | P | N | P |

V, visible; P, partially visible; N, not visible.

Table 5.5: Average scores of detectability of node by three evaluators.

| Node depth | SFOV | | LFOV | |
|---|---|---|---|---|
| | NS (mm) | | | |
| | **25** | **35** | **25** | **35** |
| 15 | 4.67 | 4.67 | 1.00 | 4.33 |
| 25 | 3.67 | 2.33 | 1.67 | 5.00 |
| 35 | 2.33 | 3.00 | 1.33 | 5.00 |
| 45 | 2.67 | 2.33 | 1.67 | 4.33 |
| 55 | 2.00 | 2.00 | 2.33 | 3.33 |
| 65 | 1.67 | 2.00 | 1.33 | 2.67 |
| 75 | 4.00 | 3.00 | 1.00 | 2.33 |
| 85 | 2.67 | 3.67 | 1.00 | 2.67 |
| 95 | 4.33 | 3.00 | 2.00 | 2.67 |
| **Average** | 3.11±1.02 | 2.89±0.82 | 1.48±0.45 | 3.59±1.02 |

### 5.3.3 Discussion

The sentinel node phantom was found to be robust and straight forward to construct and simple to use. It was used with syringes that are readily available in any hospital setting and would be a useful device for any nuclear medicine department or surgical unit with appropriate technical or physics support. Preparation of the syringes with the radioactive solution was relatively simple and could easily be performed by nuclear medicine or physics staff familiar with drawing up radioactivity in syringes. The phantom could also be used in quantifying the performances of various camera and detector systems, including LFOV planar and SPECT camera systems as well as non-imaging gamma probes.

With the modular phantom design, the performances and limitations of a camera system may be tested with different configurations (varying ND, NS, NIR and activity). The simulations in this study did not include any active background activity given that the transportation of radionuclide to the sentinel node is within the lymphatic channels and does not contribute significantly to systematic background activity. In future use the amounts of radioactivity and experimental methods used may be varied depending on the individual practices of different centres (such as one or two-day protocols).

One of the challenges in the SLNB procedure was the radiation cross talk at the node due to the presence of the high activity at the injection site. Visual assessment in the phantom studies have shown that the high resolution HGC could resolve the radioactivity uptake in the node even though the simulated NS was 25 mm centre-to-centre from the injection site. Some nodes were not detected during visual assessment, for example the node at a depth beyond 45 mm, even though the tabulated $CNR_n$ values were above the threshold CNR value. To improve the visibility of the node in display, image thresholding, masking the high activity injection site and applying appropriate filters during post-processing may be used.

The impairment of node detection with the increasing depth is believed to be due to the photon scattering and attenuation. Based on the known mass attenuation coefficient of PMMA ($0.1497$ $cm^2$/g at 140 keV), only 50% of the gamma photons will be transmitted through 40 mm depth of material. Furthermore, the sensitivity of the HGC is also strongly dependent on SCD as previously assessed by Bugby *et al.* [105]. Here the camera performance testing showed that the SFOV gamma cameras can be a useful tool for SLNB procedure in BCS. It is also suggested that the camera system may be used in other radioguided SLNB procedures such as in melanoma, head and neck, gastrointestinal, penile and vulvar cancer surgeries.

## 5.4 *In vitro* assessment of the use in radioactive seed localisation

Iodine-125 labelled titanium seeds are internal markers which are now becoming standard clinical practice to mark the location of the breast tumours in a number of hospitals worldwide [177]. In the UK, this surgical technique was first introduced in September 2014 to replace the wire guided localisation (WGL) technique [178]. This technique involves the implantation of the ^{125}I seed with a nominal activity of between 3 and 10.7 MBq at the centre of the tumour under the mammographic or ultrasonographic guidance [165, 177]. A gamma probe is used to transdermally localise the seed prior to incision and subsequently to guide the resection of the tumour and verify the clearance of the radioactive source from the breast tissues. The probe is also utilised to localise the ^{125}I seed in the excised specimen.

The application of gamma probes in localising the seed intraoperatively was further improved by the use of freehand-SPECT system [165] and dual-head gamma camera systems fitted with parallel hole collimators [161]. This localisation techniques were able to provide accurate information about depth and location of the seed. In particular, the 3-D navigation system of the freehand-SPECT was able to intraoperatively provide images in the operating theatre. However, this system still required further optimisation in term of spatial resolution (5 mm) and accuracy in localisation especially with the deep seated small lesions and lower activity ^{125}I seeds [164]. When undertaking this work it was considered that the hybrid optical gamma cameras could potentially offer added values to the RSL technique due to its high spatial resolution and ability to provide hybrid optical-gamma images. The aim of the study was to examine the imaging performances of the SFOV gamma cameras with ^{125}I seed.

### 5.4.1 Performance assessments

Two ^{125}I-seeds (OncoSeed™ model 6711C, Oncura, GE Healthcare, Arlington Heights, IL, USA) was used in this work. The initial activity of the seeds was 8.36 MBq (Seed A) and 8.33 MBq (Seed B) respectively which decayed over time during the experimental work took place between December 2016 and May 2017. The activity of the seeds was calculated and summarised in Table 5.6.

Table 5.6: Calculated activity of the ^{125}I seed over the period of the experimental work.

| Days | Decayed activity (MBq) | |
|---|---|---|
| | Seed A | Seed B |
| 0 | 8.36 | 8.33 |
| 30 | 5.89 | 5.87 |
| 60 | 4.15 | 4.13 |
| 90 | 2.93 | 2.91 |
| 120 | 2.06 | 2.05 |
| 150 | 1.45 | 1.45 |

Figure 5.12 shows the photograph and the schematic diagram of the OncoSeed™. It consists of a 0.05 mm-thick welded titanium capsule with the ends sealed by arc welding. The ^{125}I is adsorbed into a silver rod with dimension 0.5 mm in diameter and

3 mm long, which acts as x-ray marker. The seeds were considered as sealed radioactive sources and handled according to the national regulatory requirements. Imaging assessments were undertaken with HGC and Nebuleye in the research gamma camera facility in Medical Physics, Queen's Medical Centre, Nottingham University Hospitals NHS Trust.
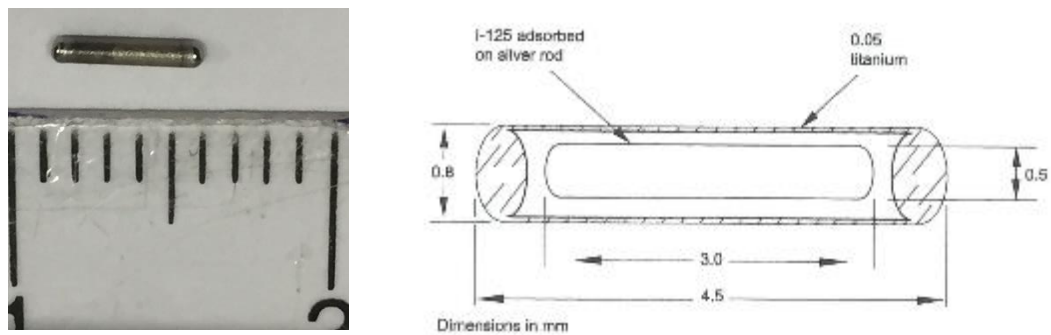


Figure 5.12: Photograph showing scale in mm (left) and a schematic representation (right) of an $^{125}$I-seed.

Feasibility of the source detection using the SFOV gamma camera was described in Section 7.4.4. Sensitivity and spatial resolution of the SFOV gamma cameras using the $^{125}$I seeds were assessed, based on the performance test protocol as detailed in Chapter 3. The system spatial resolution test was carried out by the imaging the $^{125}$I seed in place of a line source due to the diameter of the seed being small enough for the purpose of quantification. Table 5.7 tabulates the characteristics of the SFOV gamma cameras for both HGC and Nebuleye. Further performance assessments were carried out mimicking the clinical scenario, which taking into considerations of different source depths, source to surface distances (SSD), activity levels and source separations, utilising bespoke phantoms to simulate patient anatomy and position. The hybrid optical-gamma images were obtained and assessed. Comparisons were made with a standard gamma probe and LFOV gamma camera.

Table 5.7: Sensitivity and spatial resolution of the SFOV and LFOV gamma cameras using $^{125}$I source.

| Parameter | HGC | | Nebuleye | Nucline™ X-Ring-R | Gamma probe** |
|---|---|---|---|---|---|
| | 0.5 mm pinhole | 1 mm pinhole | 1 mm pinhole | | |
| System spatial resolution FWHM (mm) at 10 mm | 0.75 ± 0.07 | 1.99 ± 0.23 | 1.53 ± 0.23 | 7.3 (LEHR) * | 14.47 ± 0.08 |
| Intrinsic Sensitivity (cps/MBq) | 0.25 at 250 mm | | 0.22 at 250 mm | 45438 at 25 mm | 68.38 at 250 mm |
| System sensitivity (cps/MBq) | 0.02 at 48 mm | 1.69 at 48 mm | 0.41 at 48 mm | 14.14 at 20 mm (LEGP) | Not applicable |

*Data taken from [13] using $^{99m}$Tc source.
** Navigator GPS$^{TM}$ with 12 mm angled probe (RMD Instruments Corp., Watertown, MA, USA)

### 5.4.1.1 Seed Depth

The bespoke phantom described in Section 5.3.1 was used to simulate the breast with the seed placed at different depths. Imaging assessments were undertaken with Nebuleye and 2.43 MBq of $^{125}$I seed placed underneath the PMMA of different thicknesses within the phantom (Figure 5.13). The camera was position at SCD of 63 mm using an image acquisition time of 5 minutes. This camera positioning gave a nominal FOV of $52 \times 52$ mm. These experiments were carried out to measure the CNR of the acquired gamma images with seed at depths between 0 mm and 25 mm. CNR was quantified using the method as described in Section 5.3.2.3.
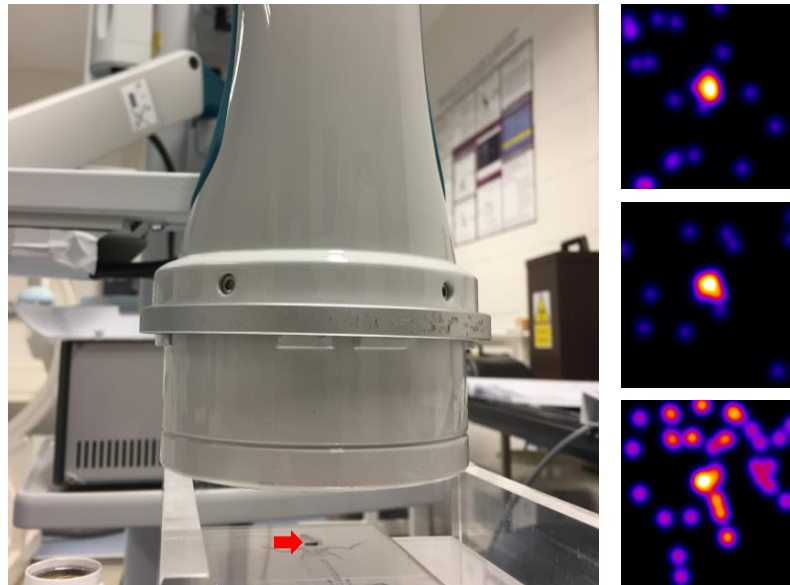
Figure 5.13: (Left) Photograph of the Nebuleye camera positioned above the ^{125}I seed (arrow) placed on top of a PMMA plate to simulate the seed on the skin surface. (Right) Images of the seed acquired at a depth of 0, 10 and 20 mm PMMA (top to bottom).

Figure 5.14 illustrates the CNR values ranged from 1 to 22, quantified using the acquired images. As expected the graph shows that the relationship between CNR and ND are inversely proportional, with the deeper seed depths producing lower CNR values. The results illustrate that the seed detectability limits of above 20 mm using an amount of activity (2.43 MBq) which was typically lower than that used clinically (3-10 MBq).
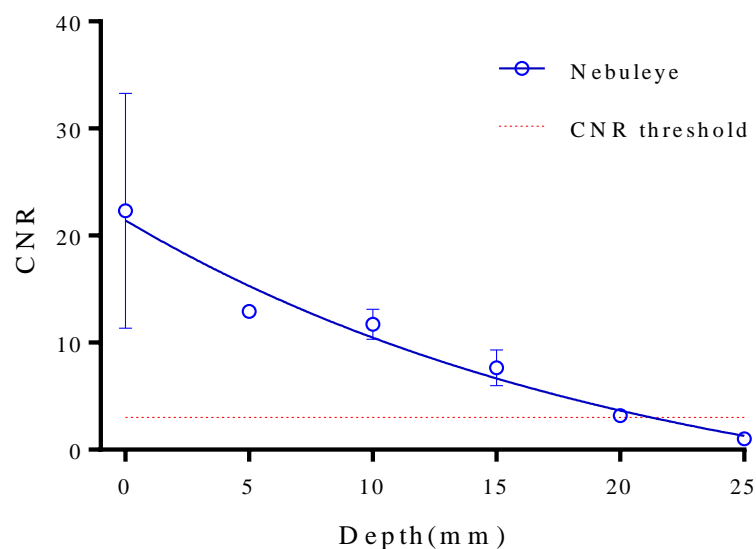


Figure 5.14: Relationship of CNR values and depths for the ^{125}I seed images acquired using Nebuleye mounted with 1 mm diameter pinhole collimator placed at SCD of 63 mm (n=3).

[125]I decays with the emission of the characteristic X-ray of energies 27.4 keV and 31.4 keV and a 35.5 keV gamma photon. When the low energy photons interact with the scattering medium such as PMMA or water attenuation occurs reducing the number of photons which could penetrate through the medium to reach the detector. Figure 5.15 illustrated the percentages of the photon attenuation when interacting with PMMA and water, which was calculated based on the National Institute of Standards and Technology (Maryland, USA) data for X-ray interaction cross sections and material densities [179]. The half value layer (HVL) of PMMA and water for the ^{125}I was derived from the attenuation graph by interpolation, these being 15 mm and 19 mm respectively. This gives an indication of the depth of the 50 % loss in tissues.
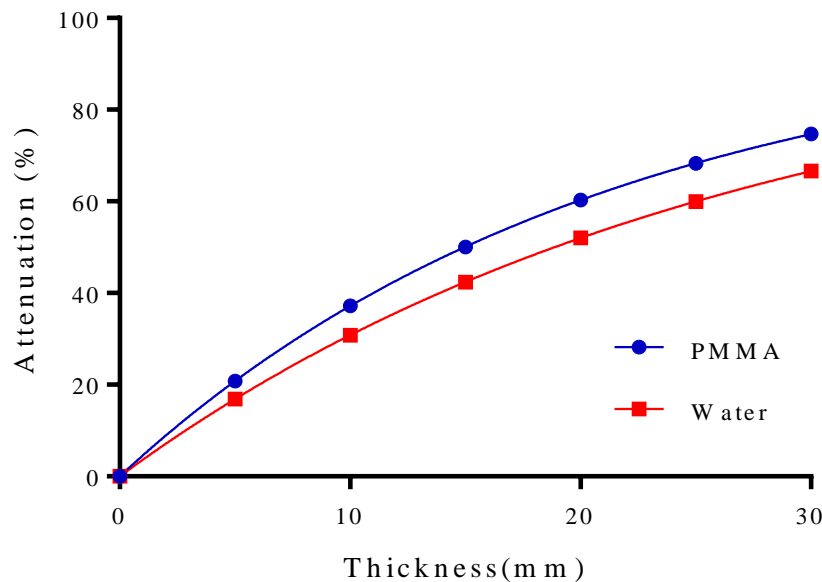


Figure 5.15: Calculated percentage of the photons attenuation when passing through different thicknesses of PMMA and water.

### 5.4.1.2 Source to collimator distance

Similar imaging assessments were also undertaken with Nebuleye and the 2.4 MBq ^{125}I seed, without the presence of scattering medium. CNR measurements were made with the gamma images of seed placed at SCD between 20 mm and 100 mm. The CNR values were ranged between 6 and 224 as shown in Figure 5.16. The detectability of the seed is decreased with the increase of the SCD. The ^{125}I seed positioned at these settings can be visible, however with the presence of scattering medium, the detectability degraded with the increase of the thickness of the scatter as discussed in

Section 5.4.1.1. Figure 5.16 (right) illustrates the gamma images acquired at SCD of 100 mm, with and without the presence of the PMMA.
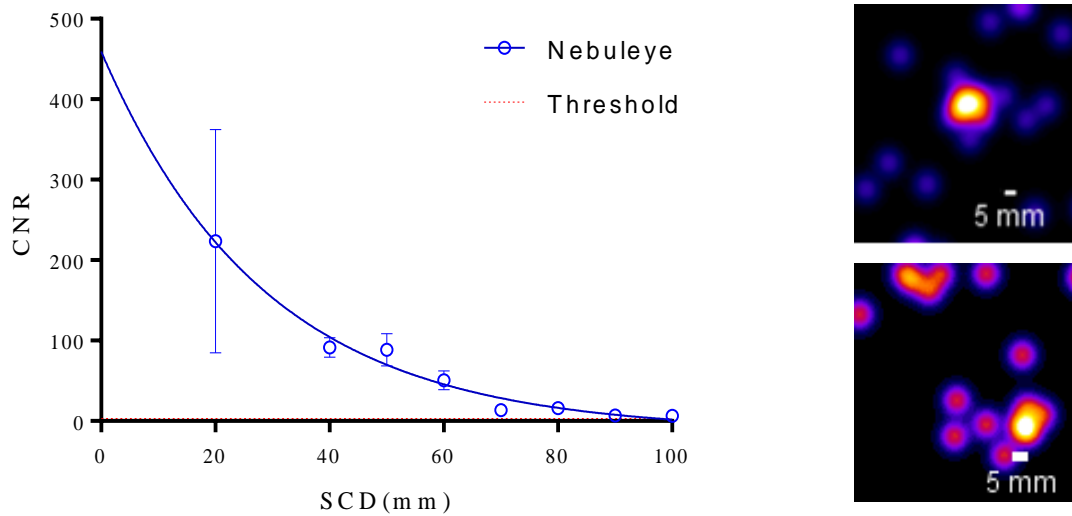


Figure 5.16: (Left) Relationship of CNR values and SCDs for the ^{125}I seed (2.4 MBq) images acquired using Nebuleye mounted with 1 mm diameter pinhole collimator. Image acquisition time was 5 minutes respectively (n=3). (Right) Gamma images acquired at SCD of 100 mm without scatter (top) and with the presence of 60 mm of PMMA (bottom).

### 5.4.1.3 Acquisition time

Images acquired with different length of acquisition time were also evaluated. The Nebuleye was positioned at SCD of 63 mm to take gamma images of ^{125}I seed with low (2.9 MBq) and high (6.4 MBq) amounts of activity. CNR measurements were performed with the gamma images of the seed taken with acquisition times between 1 and 30 minutes. The CNR values were ranged between 4 and 40 for seed at lower activity level; between 5 and 127 at higher activity level as shown in Figure 5.17. The camera was able to detect the seed in all images acquired with this experiment set up. The seed was visually identified in all resulted gamma images. Both CNR values increased with the increase of acquisition time. However, the graph shows that the increase of the CNR values for the images of seed with higher activity level is steeper than those with lower activity level.
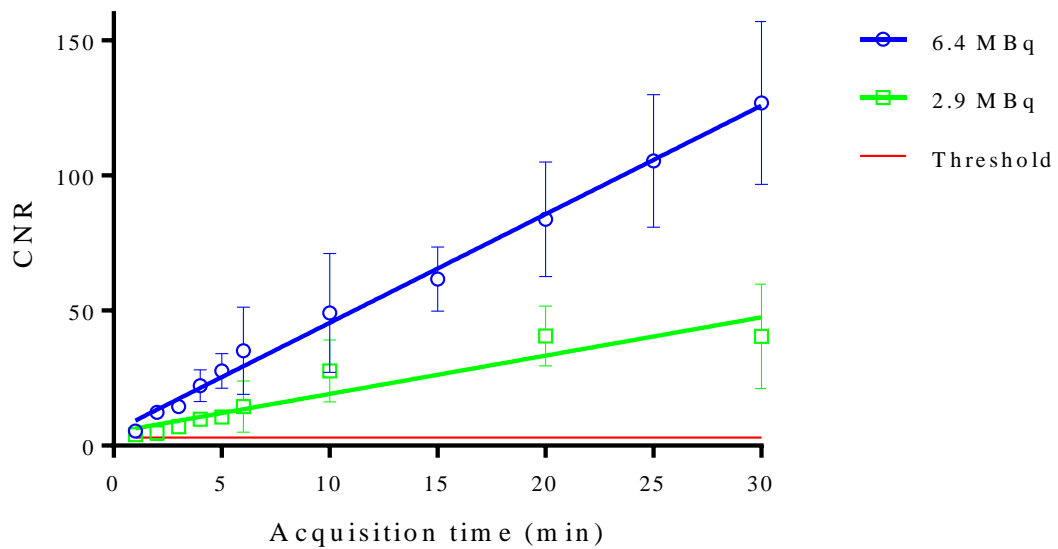
Figure 5.17: Relationship of CNR values and acquisition time for the ^{125}I seed at low (2.9 MBq) and high (6.4 MBq) activity levels. Images were acquired using Nebuleye mounted with 1 mm diameter pinhole collimator at SCD of 63 mm (n=3).

### 5.4.1.4 Pinhole diameter

It was considered of interest to assess the effect of the diameter of pinhole collimator used in the SFOV gamma camera. Since the pinhole collimator could not be changed in the Nebuleye camera this work was carried out using the HGC. Images were taken using HGC mounted with either 0.5 mm diameter pinhole collimator or 1 mm diameter pinhole collimator. The seed (2.9 MBq) was position at SCD between 20 mm and 100 mm and the imaging time was 5 minutes. The CNR values of each of the images were quantified. They were ranged between 1 and 67 for images of the seed placed at the SCDs from 20 mm to 100 mm as shown in Figure 5.18. In general, the CNR values decreased with the increase of SCDs. Higher CNR values were obtained for images acquired using the HGC with 1 mm pinhole collimator, due to higher sensitivity. Most of the images were above the CNR threshold, however the imaging assessing showed the detectability limit for seed placed at SCD beyond 60 mm, acquired using HGC fitted with 0.5 mm pinhole collimator.

| SCD 40 mm | SCD 60 mm | SCD 100 mm |
|:---:|:---:|:---:|
| 2278 counts | 646 counts | 56 counts |
| 18 counts | 6 counts | 2 counts |
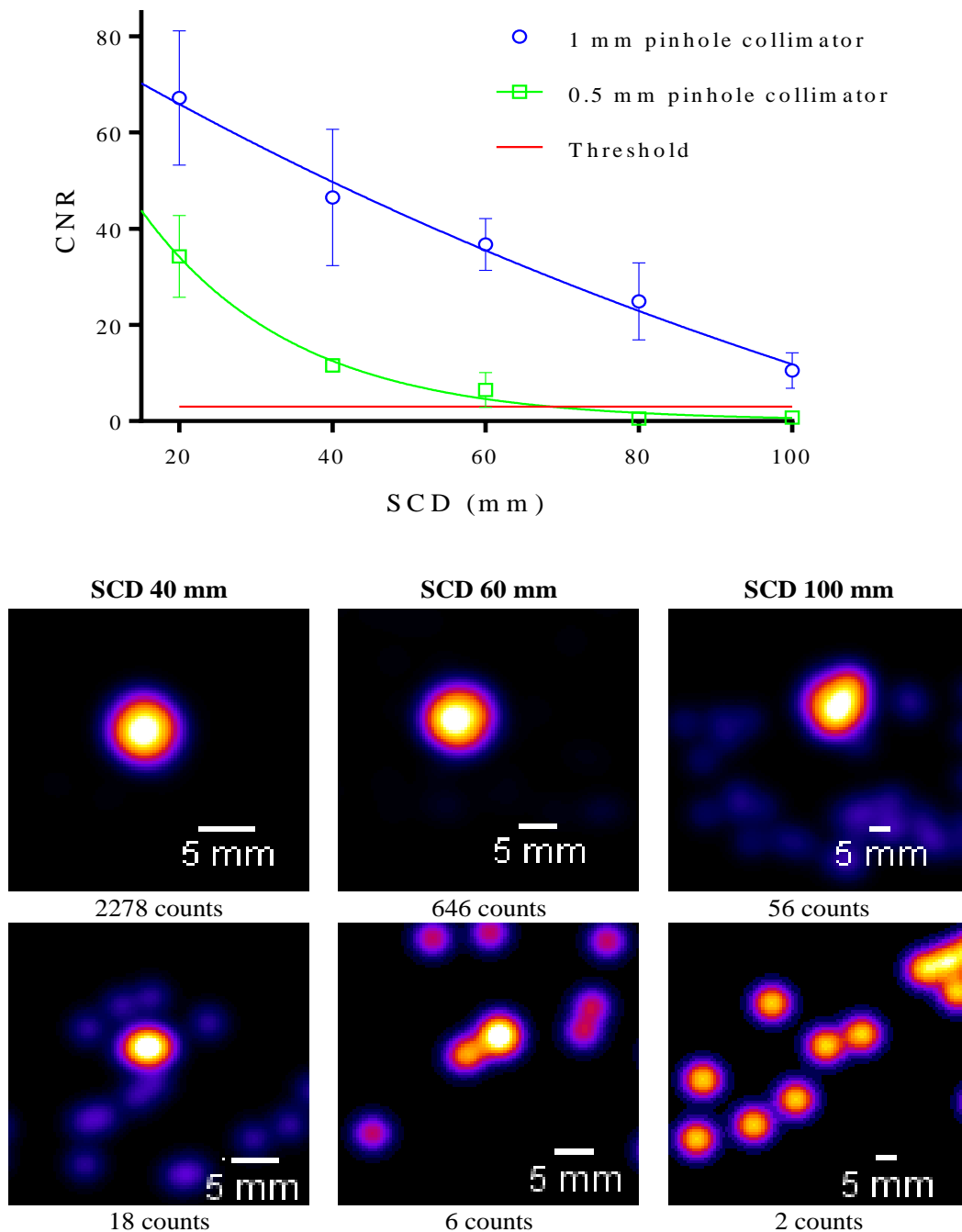
Figure 5.18: Relationship between CNR and SCDs for images acquired using 1 mm (top row) and 0.5 mm (bottom row) pinhole collimators. The number of counts within the ROI of the seed were indicated underneath of each images (n=3).

Further imaging assessment were carried out to examine the visualisation of two $^{125}$I seeds (~1 MBq each) positioned in parallel to each other separated at a distance between 1, 2 and 3 mm at SCD of 30 mm. Images were acquired with 600 s using hybrid optical gamma cameras fitted with either 0.5 mm or 1 mm diameter pinhole collimator. Figure 5.19 shows the gamma, optical and fused images of the two $^{125}$I seeds with a separation

of 3 mm (edge-to-edge), taken using Nebuleye fitted with 1 mm diameter pinhole collimator. This is the minimum separation of two seeds which could be resolved by this camera configuration. The quantified system spatial resolution (FWHM) at SCD of 30 mm was $3.54 \pm 0.23$ mm.



Figure 5.19: Gamma (left), optical (middle) and hybrid (right) images of the $^{125}$I seeds placed with a separation distance of 3 mm, taken by Nebuleye mounted with 1 mm diameter pinhole collimator with SCD of 30 mm and 10 minutes acquisition time.

With the smaller diameter pinhole collimator (0.5 mm) fitted in the HGC, the system spatial resolution (FWHM) at SCD of 30 mm was improved to $2.08 \pm 0.07$ mm. This camera configurations enabled us to resolve the two $^{125}$I seeds with a separation of 2 mm. Figure 5.20 illustrates the line profiles of the gamma images. Two peaks can be clearly identified in the Gaussian fitted profile generated from gamma image acquired with the seeds placed at 2 mm apart, however a single peak was shown with the seeds placed closer (1 mm apart).
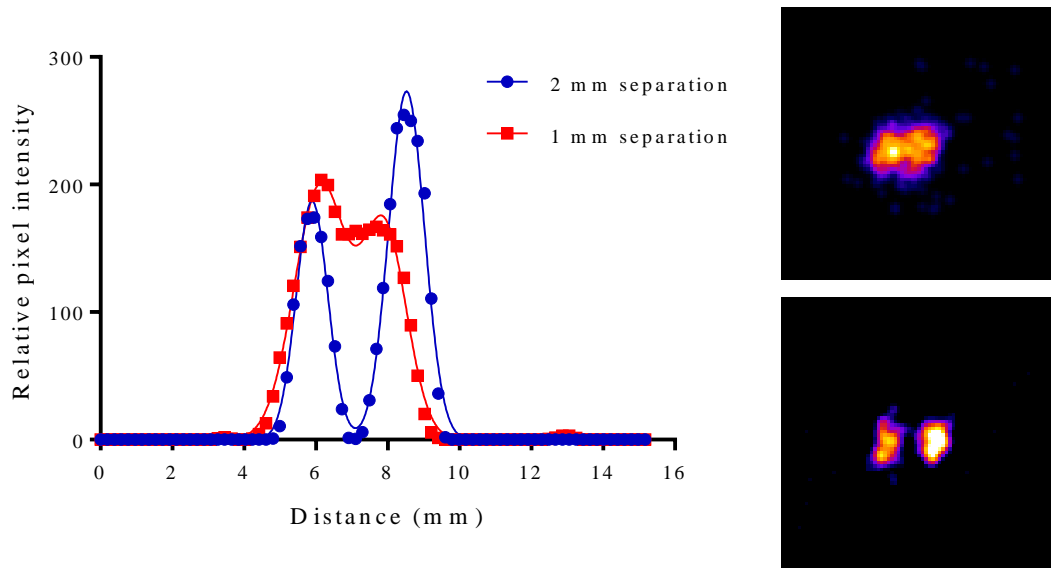
Figure 5.20: (Left) Line profiles (5 pixel width) drawn across the centre of the hot spot(s) in the gamma images (right) with seeds placed 1 mm (top) and 2 mm (bottom) apart. The connecting lines were the profiles fitted with Gaussian function.

### 5.4.1.5 Clinical simulation

Pilot subjective assessment were performed to determine the ability of the SFOV gamma cameras in localising the seed in clinical simulation. $^{125}$I seed (~6 MBq) was placed beneath the skin of breast region of an adult cardiopulmonary resuscitation (CPR) training manikin. Four designated positions were marked with letters on the skin surface (A to D) as shown in Figure 5.21. The number and position of the located seed was blinded to the assessors. Six independent participants (nuclear medicine staff) were informed of the study objectives and procedure. Imaging was undertaken using Nebuleye positioned at SSD of 100 mm using a 2 minute acquisition time. Images were processed and displayed on the beta version of Nebuleye software. The participants were asked to visually assess the resulted image subsequently determine the position and number of seed involved. If the first image was not satisfactory, a second image acquisition was taken with a shorter SSD focusing on the 'suspected area' as determined by the assessor.
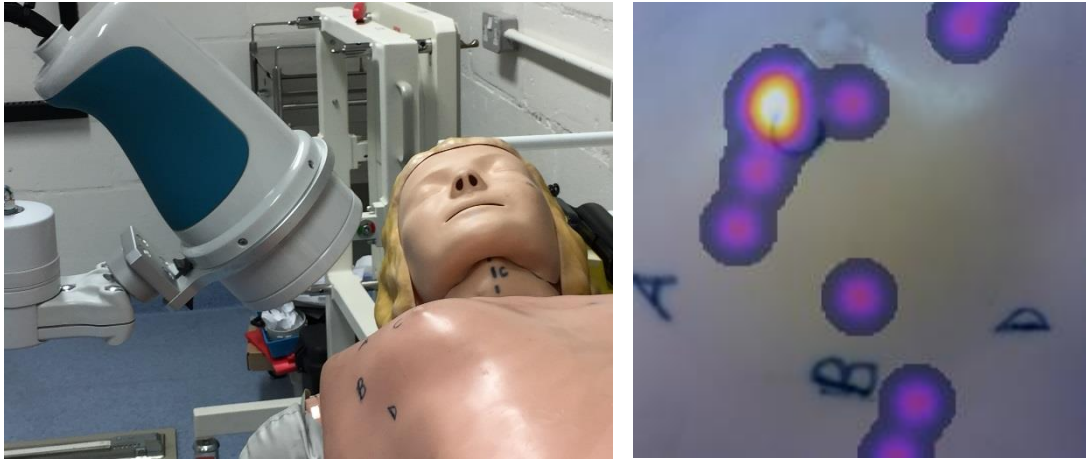
Figure 5.21: (Left) Photograph of the clinical simulation. (Right) Post-processed hybrid image illustrated a bright blob at the position of "C" surrounded with background radiations.

Table 5.8 summarised the details of the clinical simulation assessment undertaken using Nebuleye. All assessors were able to determine the correct number of seeds located at the designated sites by visual assessment of the resulted hybrid image. Four of the 6 assessors required second imaging at a nearer SSD in order to confirm the number and location of the seeds.

Table 5.8: List of assessments undertaken using the Nebuleye.

| Assessor | Number of seeds | Number of seeds determined (at correct position) | Number of images taken |
|---|---|---|---|
| 1 | 2 | 2 | 2 |
| 2 | 1 | 1 | 1 |
| 3 | 0 | 0 | 2 |
| 4 | 1 | 1 | 1 |
| 5 | 1 | 1 | 2 |
| 6 | 1 | 1 | 2 |

### 5.4.2 Simultaneous detection of dual radionuclides

Pouw *et al.* [180] have reported the use of standard gamma probes for the simultaneous detection of dual radionuclides in a combined RSL and SLNB procedures for non-palpable BCS. These involved the implantation of $^{125}$I seeds to guide the excision of primary tumours and the administration of $^{99m}$Tc-nanocolloid for SLNB. To assess the potential of the HGC for the combined procedures of RSL and SLNB a pilot laboratory study was carried out in an anthropomorphic breast phantom.

An $^{125}$I seed (6.25 MBq) and $^{99m}$Tc solution (0.16 MBq) contained in an eppendorf tube were inserted into a bespoke anthropomorphic breast phantom developed at the University of Leicester [37]. These were placed 2 cm apart (centre-to-centre), 5.5 cm away from the dome apex and 2 cm underneath of simulated skin surface of the phantom. Imaging was undertaken using the HGC fitted with a 1 mm pinhole collimator positioned 5 cm away from the phantom to record an oblique view as shown in Figure 5.22. Image acquisition time varied between 30 s and 600 s.
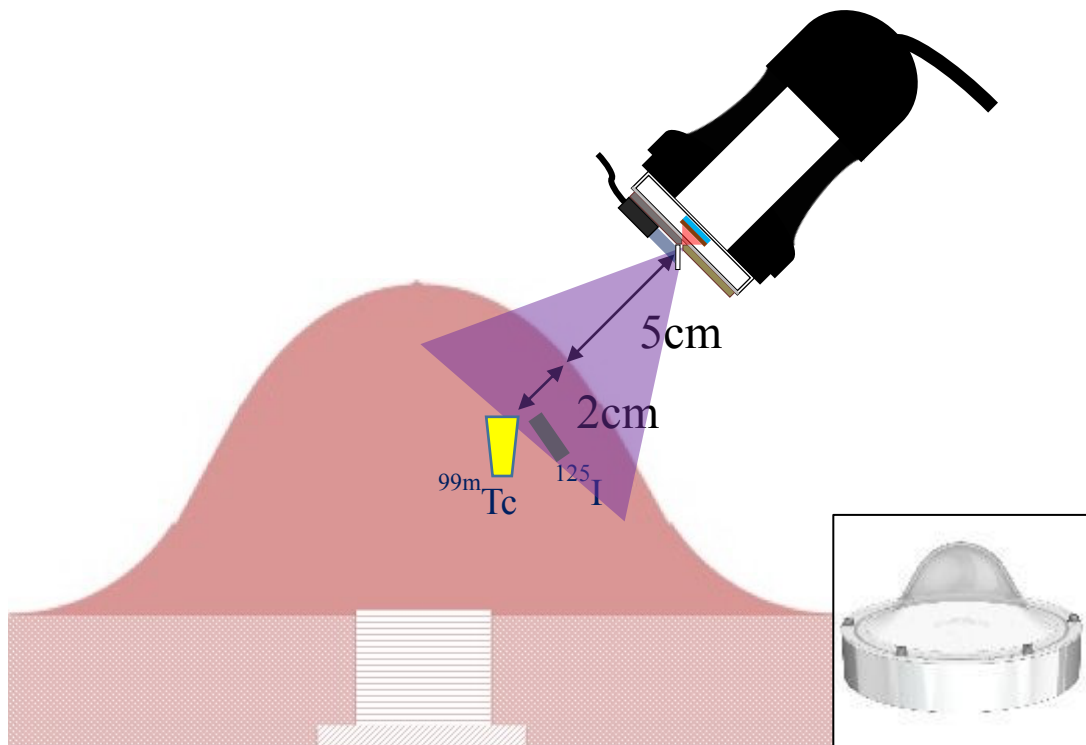


Figure 5.22: Schematic diagram of the experimental set up and (inset) breast phantom. Image courtesy of University of Leicester.

For comparison purposes, imaging with a conventional LFOV gamma camera (Nucline™ X-Ring-R, Mediso, Hungary) and an SPECT-CT camera system (Brightview XCT, Philips Healthcare, Milpitas, CA, USA) was performed at nuclear medicine clinic, Queen's Medical Centre, Nottingham University Hospitals NHS Trust. The energy window width of 20% centered on the photopeaks of the respective radionuclides (30 and 140 keV) were set at both camera systems for simultaneous acquisition. Images were viewed using a dedicated nuclear medicine workstation (Hermes Medical Solutions, London UK). For SPECT-CT image registration, it was

performed using ImageJ 1.47v (National Institute of Health, US) due to the local Hermes workstation was limited to fuse two sets of image data.

Figure 5.23 shows the gamma images of $^{125}$I seed taken with HGC for various acquisition times between 30 and 600 s. In this experiment, both radionuclide sources could be detected within a 30 s of acquisition time. Although both sources could be seen it was not possible to discriminate between the different gamma emission energies. With the increase of acquisition time, the demarcation of the individual source was found to be more distinct by subjective visual assessment.

Figure 5.24 shows the phantom images acquired using LFOV gamma camera and SPECT-CT camera system with the conditions and sources in place as described above. Two hot spots can be clearly seen in both images. With the aid of the CT image, the SPECT images were fused and displayed in different colour scales (green: $^{125}$I; hot metal: $^{99m}$Tc) to ease identification two different radionuclides accumulate within the target tissues (simulating activity in the sentinel node and the seed in primary tumour).
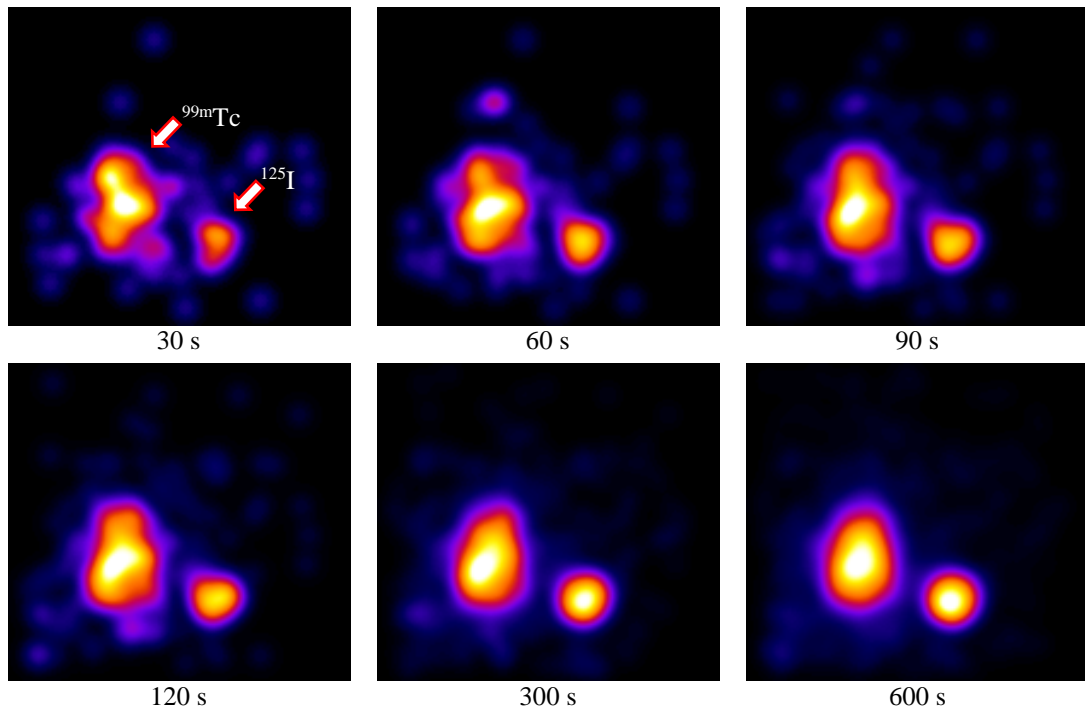


Figure 5.23: Gamma images (oblique view) of the dual isotopes acquired using HGC with different acquisition times.
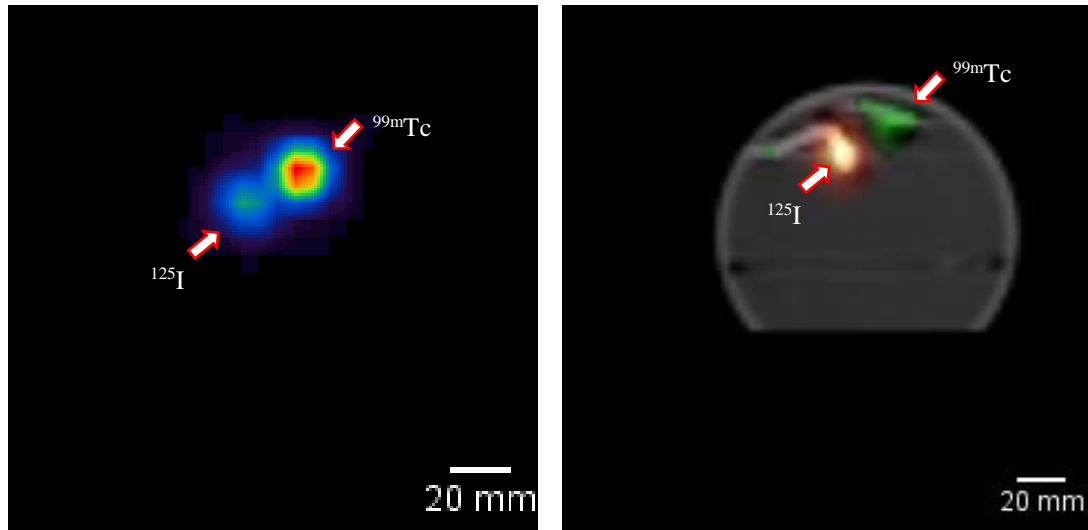
Figure 5.24: (Left) Scintigraphic image acquired using LFOVgamma camera with 20 minutes acquisition time, phantom placed at SCD of 2 cm and matrix size of $128 \times 128$. (Right) Fused SPECT and CT images obtained using SPECT-CT with matrix size of $128 \times 128$, 120 projections over a 180° rotation in which 20 s per projection for each detector. Two separate SPECT images of $^{125}$I and $^{99m}$Tc were generated simultaneously in addition to the CT image (3 sets of image data) during the imaging session.

### 5.4.3 Discussion

This chapter describes the first results of the use of the SFOV gamma cameras (HGC and Nebuleye) in the detection and imaging of $^{125}$I seed sources. The camera systems have presented the ability for detecting the lower energy (35.5 keV) of gamma photons emitted by the $^{125}$I as well as simultaneous detection of $^{99m}$Tc. This would be particularly useful in RSL for non-palpable breast tumours and other soft tissue masses [181], as a compliment to the current standard procedure using gamma probe. The hybrid images could aid the surgeon in localising the seed thereafter confirming the position without additional mammography intraoperatively. This may also be a useful tool in assessing clearance of radioactivity around the breast tissues and lymphatic basin following surgery and localising the seed *ex vivo* during removal from the excised specimen.

A limitation at the time of the investigation was that the energy window setting was not possible in current version of hybrid optical gamma cameras, resulting the same colour scale image display of photons detected. This limits the potential of the camera to segregate tissue masses when dual radionuclides are used simultaneously for example during the combined RSL and SLNB procedures. In addition, the 2-D images do not provide any estimation of depth of the radionuclide uptake, which would be crucial

information for the more accurate excision and harvesting of the sentinel node and tumour masses.

Preliminary camera testing have revealed that SFOV gamma cameras were able to detect $^{125}$I with activity levels typically used in surgery within an acceptable acquisition time. In particular the camera was able to detect the $^{125}$I seed at SCD of 63 mm (with no scattering material in place) within a one-minute acquisition time. In contrast, the camera has a detection limit for deep seated tumours to depths less than 20 mm beneath the skin surface with the SCD of 63 mm and 5 minutes imaging time. These limitations can be improved by prolonging the image acquisition time and shortening SCD to increase system sensitivity and spatial resolution, but the decrease in the FOV and longer surgery times may be a problem.

The detectability of $^{125}$I seeds can also be enhanced by using larger pinhole collimator (i.e. 1 mm in diameter). The camera fitted with 0.5 mm pinhole collimator exhibits lower sensitivity but higher spatial resolution. It could resolve two seeds placed at a distance of 2 mm with the SCD of 30 mm and 10 minutes acquisition time. With the increase of the pinhole diameter (1 mm), the camera was able to resolve seeds at a separation distance of 3 mm. These images could be useful for localising multiple seeds in the same breast which are embedded under mammographic guidance in the case of larger lesions (tumour bracketing) or multiple lesions, in order to aid determination of surgical dissection margins.

## 5.5 Summary

This chapter describes systematic methods for the assessment of hybrid SFOV gamma cameras intended for use in breast cancer surgery. A phantom assessment method has been established to examine the performance of SFOV gamma cameras in imaging sentinel nodes. The qualitative and quantitative assessments performed in these studies could be considered as part of the systematic performance tests of SFOV gamma cameras carried out prior to clinical use and the results could serve as baseline data for future references. This assessment method examines the detection performance of the SFOV gamma camera in detecting SLNs at various ND, NS, NIR and activity, exhibits the feasibility of its imaging capability in radioguided surgery or other clinical

applications. The methods described may also be used for the further objective comparison of the detectability of SFOV gamma cameras, LFOV gamma camera and SPECT camera systems as well as intraoperative gamma probes.

In addition, this study also demonstrates the feasibility and capabilities of SFOV gamma cameras in the detection of $^{125}$I seeds and could be a useful tool in RSL with the added benefit of providing hybrid optical gamma images for guiding the surgical procedure intraoperatively. The tests show the detectability of the $^{125}$I seed at different depth, SCDs, acquisition time and diameter of pinhole collimator as well as the simultaneous detection of multiple radionuclides. This work adds technical information to support the future applications of the SFOV gamma cameras for clinical investigations as described in Chapter 8.

# Chapter 6

# Preparatory studies of the pre-production prototype SFOV Hybrid Optical Gamma Camera prior to surgical use

## 6.1 Introduction

Since initial conception, the HGC technology had been developed to enhance the operation, stability and performance for hybrid gamma-optical imaging. The potential clinical applications were considered to examine new areas such as sentinel lymph node biopsy, radioactive seed localisation and theragnostic procedures. As a result of the novel design of the camera and the intellectual property (IP) held by the Universities of Nottingham and Leicester, a spin out company called Gamma Technologies Limited (GTL) was formed in 2013. A Biomedical Catalyst Fund from the UK Technology Strategy Board (Innovate UK) was awarded in 2014 to support preclinical prototyping of the device for use in clinical and surgical settings. GTL further developed the prototype design together with the industrial partner, Xstrahl Limited (Surrey, UK) to transform the HGC into a new medical device, known as Nebuleye. The pre-commercial prototype, Nebuleye was fabricated and sent to Queen's Medical Centre, Nottingham for initial physical evaluation.

*In vitro* imaging assessment as described in Chapter 5 evaluated the performance of the camera in a clinical environment by using bespoke phantoms and test objects. Further preparatory work was undertaken to take the Nebuleye to the stage where it was acceptable for use in the operating theatre. For use as a medical device in the clinical

setting, the camera design and construction was required to meet the UK regulatory and ethnical requirements as required by The Medicines and Healthcare products Regulatory Agency (MHRA). This chapter describes the preparatory work undertaken in order to meet all requirements for a clinical trial of the Nebuleye in the surgical department. It outlines the clinical trial study design for use in SLNB in patients with breast cancer, the regulatory requirements and the routine quality control scheme for calibration prior to surgical use. Ultimately the clinical trial did not go ahead due to the commercial partner not obtaining CE marking of the Nebuleye device, however the trial protocol has been developed for future use along with the routine quality control testing procedures.

## 6.2    Regulatory requirements

### 6.2.1    CE marking

All medical devices must be complied with regulatory requirements as stipulated by relevant authorities, for example, CE marking in the European Union Directive (Council Directive 93/42/EEC on Medical Devices) [182] and the Premarket Notification 510(k) under the Subpart E 21CFR807.92 Federal Food Drug & Cosmetic Act [183] before commercialisation. The regulatory processes cover thorough assessments which include electrical safety and electromagnetic compatibility, quality system management and risk management. In the United Kingdom, all medical devices must meet the requirements as specified in the Medical Devices Regulations 2002 [184] by carrying out a conformity assessment. Part of the assessments are described in the harmonised international standards such as family standards of EN 60601 Medical Electrical Equipment and Systems [185], BS EN ISO 14971:2012 Medical devices-Application of risk management to medical devices [186] and BS EN ISO 13485:2016 Medical devices-Quality management systems (QMS)-Requirements for regulatory purposes [187].

At time of the assessments carried out in this thesis, the Nebuleye camera was undergoing the process of documentary filing for CE marking in order to be certified as a medical device. Based on the Annex IX of the Council Directive 93/42/EEC on Medical Devices, the Nebuleye was classified as Class IIa medical device. Figure 6.1 illustrates the potential pathways to obtain the CE mark for the camera, under the

auspices of the Medicines and Healthcare products Regulatory Agency (MHRA), UK. The CE mark application filing was carried out by the manufacturer as part of the device development, while the contributions of the work undertaken in this study at the University of Nottingham were to carry out device characterisation, preliminary human factor analysis, *in vitro* testing and ultimately a clinical study. This provided opportunities to identify any major use issues, so that they could be addressed before submitting for final regulatory approval.
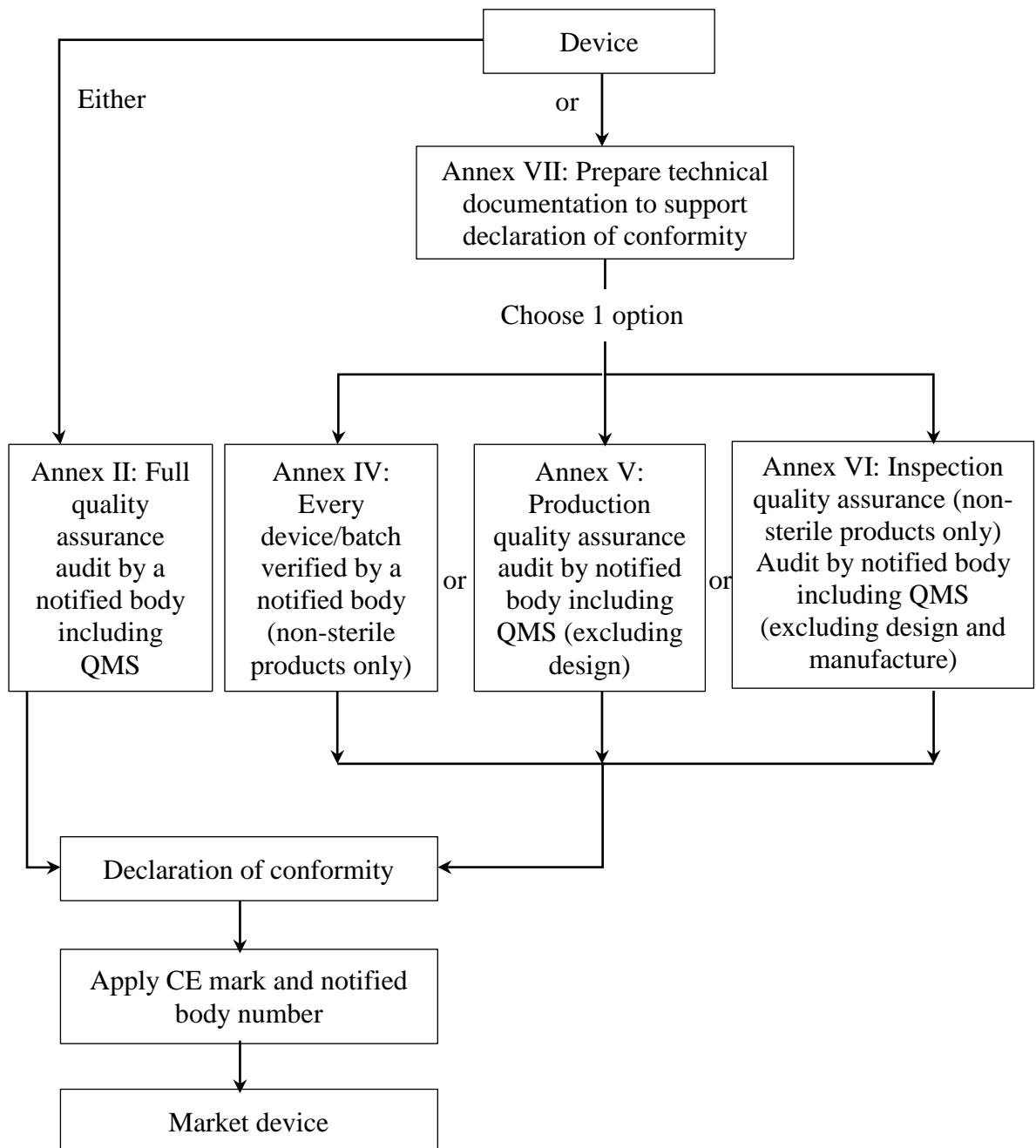
Figure 6.1: Flowchart of the Class IIa medical devices routes to CE marking taken from [188].

### 6.2.2   Clinical trial

The first use of the SFOV Hybrid Optical Gamma Camera for SLN localisation in patients undergoing surgery for primary breast cancer was planned as part of this work. It was classified as an investigational medical device study and relevant regulatory compliance applications were made through the University of Nottingham as the study sponsor. The study was granted with a favourable ethic opinion by the UK National Research Ethics Committee (Reference Number: 16/YH/0008) and registered in the *Clinicaltrials.gov* database (NCT02621099).

## 6.3   Study design

This was a pilot trial of the use of the pre-production Nebuleye in the operating theatre. The primary objective of the study was to assess the validity and agreement between the camera and standard gamma probe in sentinel lymph node detection during surgery by comparing the performance of the camera with the gamma probe, blue dye and with the dual techniques (combined gamma probe and blue dye-guided techniques), in terms of overall sentinel node detection rate. In addition, the secondary objectives of the study were:

a) subjective assessment of the intraoperative incremental value of the camera compared to the conventional gamma probe;

b) to assess if the additional information obtained by optical imaging aids sentinel lymph node localisation and obtain surgeon feedback on use of the camera; and

c) to determine if the camera could offer additional information on the detection of sentinel lymph nodes in the internal mammary chain.

This non-randomised, non-blinded sequential single centre feasibility study was to be carried out at the Breast Surgery Clinic, Royal Derby Hospital Centre, Derby. The following text describes the study protocol. Figure 6.2 summarises the sequences for this study.

PIS and consent form to be given to the potential participant and signed consent obtained

Radiopharmaceutical administration at the Nuclear Medicine Clinic

Record patient information in CRF

Blue dye administration

Draw external skin mark at sternal notch

Parasternal image acquisition to localise any uptake in internal mammary node(1st image) using the camera

Baseline image (axilla) acquisition prior to surgery (2nd image) using the camera

Assessment of baseline image and record number of node(s) in CRF

Apply sterile sheath to detector head and arm of the camera

Drape the patient

Incision at the site of suspicous node

Sentinel lymph node localisation using gamma probe

Sentinel lymph node localisation using the camera (3rd image)

Removal and confirmation of sentinel lymph node activity using gamma probe with 10s count and visually inspection of blue dye. Record number of counts at node and background

Residual survey using gamma probe, back to previous step (3rd image with camera) if additional node is found

Image acquisition of axillary region for residual check (4th image) using the camera

Record number of node detected by gamma probe, blue dye and dual techniques in the CRF

Specimen image acquisition (5th image) using the camera

Specimen delivered to histopathology lab

**Legends:**  ☐ Standard SLNB  ▇ Research procedure

Figure 6.2: Study flow-chart.

### 6.3.1   Patient recruitment

#### 6.3.1.1   Patient selection

The initial approach will be from a member of the patient's usual care team or the senior research nurse who has permission to access patient data. They will screen the patient details for their eligibility according to the criteria as tabulated in Table 6.1. Once patients express interest they will be given the patient information sheets (PIS) and consent documents before the study takes place.

Table 6.1: Patient selection criteria for this study.

| **Inclusion criteria** |
| --- |
| 1. Female |
| 2. Age > 18 years |
| 3. Scheduled for a Sentinel Lymph Node Biopsy procedure for breast cancer |
| 4. Has capacity to provide written 'informed consent' |
| **Exclusion criteria** |
| 1. Patients who have had a nuclear medicine procedure with administration of a radiopharmaceutical within 72 hours prior to the procedure |
| 2. Patients who have had prior systemic therapy for the breast cancer being scheduled for sentinel node biopsy (e.g. neoadjuvant chemotherapy and primary endocrine therapy) |
| 3. Non-English speaking patient |

#### 6.3.1.2   Informed consent

Arrangement will be made for the potential participants to meet with the senior research nurse (or the breast surgeons who are the chief or co-investigators) who will obtain written consent as appropriate. The investigator will explain the details of the trial while ensuring that the participant has sufficient time to consider participating or not. The investigator will answer any questions that the participant has concerning study participation. It will be explained to the potential participant that entry into the trial is entirely voluntary and that their treatment and care will not be affected by their decision. It will also be explained that they can withdraw at any time. Informed consent will be signed and dated by the participants before they undergo any interventions (including physical examination and history taking) related to the study. One copy of this will be

kept by the participant, one will be kept by the investigator, and a third copy will be retained in the patient's hospital records.

### 6.3.2 Surgical and imaging procedures

This study will not alter the standard SLNB procedures provided by NHS treatment. Once the patient has given written consent to take part in this study, a participant trial identity code number will be provided. Following administration of the radiopharmaceutical, the participants will come to the operating theatre for the preparation of the breast surgery. Immediately prior to surgery, the investigator will review the participant's consent before proceeding with the study in the operating theatre.

Daily quality control tests will be carried out on the camera prior to use in the operating theatre to ensure the device is functioning correctly. Before each SLNB procedure, the researcher will record the patient information in the case report form (CRF) that will be limited to details of radiopharmaceutical administered (radiopharmaceutical, activity administered (MBq), date and time of administration), breast cancer details (symptomatic or screening, stage of cancer and type such as ductal carcinoma in situ or invasive carcinoma) and type of surgery. Subsequently, the surgical and imaging procedures will be carried out according to the procedures as listed below:

a) After injection of blue dye, the surgeon will draw a mark on the skin at the position of the sternal notch. The researcher will acquire images using the camera focusing on the parasternal region (covering the $2^{nd} - 4^{th}$ intercostal spaces on the side of the primary tumour) aiming to localise any uptake of the radiotracer within the internal mammary nodes ($1^{st}$ imaging sequence).

b) Subsequently, the researcher will use the camera to acquire images covering the axillary area as a baseline ($2^{nd}$ imaging sequence). The number of visualised sentinel lymph node will be documented in CRF.

c) The surgical team will apply a sterile sheath to the detector head and arm of the camera to maintain its sterility. The operating area of the patient will be prepared as for the routine procedure.

d) The incision will then be carried out once the patient has been prepared according to standard surgical theatre procedures. Sentinel node detection will be performed using the gamma probe.

e) Following incision a further image using the camera will be acquired after the surgeon has each positive node confirmed with the gamma probe ($3^{rd}$ imaging sequence).

f) Removal of the nodes will be carried out by the breast surgeon according to the normal procedure. The surgeon will assess the excised node by the gamma probe with a 10 s count and visual inspection of blue dye (dual techniques). The number of counts from the node and background will be recorded in the CRF.

g) After the removal of all sentinel nodes, the surgeon will perform a residual check using the gamma probe, followed by the camera ($4^{th}$ imaging sequence).

h) The number of sentinel lymph nodes located with gamma probe, blue dye technique and dual techniques will be documented in the CRF.

i) After the surgical procedures are completed, the researcher will acquire an image of each excised node with the camera positioned away from the patient ($5^{th}$ imaging sequence).

For the imaging steps, further descriptions are illustrated in Table 6.2.

Table 6.2: Descriptions of the imaging plan in this study.

| Imaging sequence | Imaging location (ROI) | Description | Operator |
|---|---|---|---|
| 1 | parasternal region (rectangle) | Camera positions at distance of 3 cm from patient | researcher |
| 2 | axillary region (oval) | Camera positions at distance of 3 cm from patient | researcher |
| 3 | individual positive node(s) detected (oval) | Image each node being detected. Camera positions as near as possible to the node by surgeon and image taken by research team. | researcher and surgeon |

| Imaging sequence | Imaging location (ROI) | Description | Operator |
|---|---|---|---|
| 4 | repeat axillary region (oval) | Camera positions at distance of 3 cm from patient. | researcher and surgeon |
| 5 | excised positive node(s) | Image each node being excised. Camera positions at distance of 2 cm from the specimen. | researcher |

**Region of interests (ROI):**
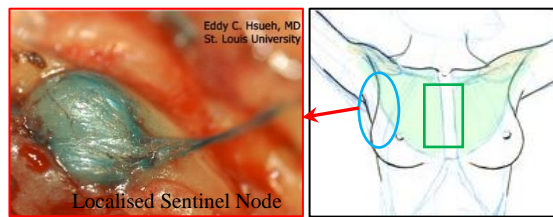


Notes: Approximately an addition of 20 minutes (including 12 minutes of average image acquisition time and 8 minutes of camera system positioning time) are required for each patient investigation in this study.

Images obtained using the camera in this study will include gamma, optical and fused gamma-optical images in each acquisition. Settings and protocols (SCD, acquisition time, acquisition starting time and anonymised image file name) used will be recorded in the CRF. In additional to the intraoperative imaging study using the camera system, a subjective assessment using questionnaire method will be carried out amongst the surgeons to obtain their feedback. No patient information or clinical data will be required as part of this survey.

### 6.3.3 Data analysis and statistical test

Demographic and other prognostic information of patients will be tabulated and summarised as appropriate. The following data will also be captured:

a) Detection rate (binary) by gamma probe, blue dye technique, dual technique and the camera

b) Number of node(s) detected by gamma probe, blue dye technique, dual technique and the camera

For the quantitative analysis, the distribution of continuous variables will be summarised using mean and standard deviation (if normally distributed) or median and

range (if not normally distributed); distribution of categorical variables will be summarised by presenting the number and percentages that falling into each categories.

The primary performance endpoints are the validity and agreement between the camera and the standard gamma probe in sentinel lymph node detection. The detection rate of both detection methods (camera versus dual techniques) will be tabulated as binary data (yes/no). Validity analysis will be computed for sensitivity, specificity, positive predictive value and negative predictive value. Also Kappa (categorical data) statistical method will be used to examine the agreement between two methods. Good agreement will be claimed if the value of kappa between 0.81 and 1.00.

The secondary endpoints will be assessed according to the following methods:

a) McNemar-Bowker method will be used to test the symmetry of detection rate between both methods (camera versus dual techniques).

b) Kappa statistics will be used to assess the extent of reproducibility of the camera between different observers in sentinel lymph node detection.

Statistical significance will be achieved if the computed p-value is equal to or less than 0.05. The results of the user scores from the questionnaire will be assessed to determine the level of confidence and additional value evident when using the camera during the sentinel node biopsy procedure.

## 6.4 Equipment acceptance tests

User acceptance tests are important to ensure the camera system complies with the specifications set by the manufacturer. These tests may be performed by a competent medical physicist or senior technologist acting on behalf of the purchaser, in addition to the tests undertaken by the installing vendor. As the Nebuleye was a newly developed pre-production prototype camera there were no acceptance test protocols in place. Therefore a user acceptance testing protocol needed to be developed specifically for this purpose.

The characterisation tests described in Chapter 3 were considered suitable for the examination of the essential performance. These tests should be carried out on site after

assembling the camera. In additional to the essential performance test, additional tests are also necessary in order to provide a comprehensive assessment of the individual components of an instrument [189]. It was also considered important to assess the software component of the system at this stage to ensure correct functionality. The tests described in the subsequent sections were the additional tests carried out following the assembly of the Nebuleye camera system in the research laboratory, nuclear medicine clinic, Queen's Medical Centre. These included CCD temperature stability, imaging functionality and software testing.

## 6.4.1 CCD temperature stability

The EMCCD used in the Nebuleye camera head required a Peltier cooling system to enhance the detector performance. The manufacturer recommended that the working temperature of the CCD in the clinical environment should be within -10 °C and -3 °C. During use the imaging system was operating in a typical clinical area with the ambient room temperature of 20.2°C. The aim of the test was to examine the ability of the cooling system to regulate the CCD temperature within the target temperature (between -10 and -3°C) over typical time of use in the clinical area.

After powered on the system, the camera was used intermediately (50:50 cycle imaging:standby time) for 5 hours. The temperature of the CCD was measured by thermistor attached to the EMCCD and the readings were recorded at 60 minutes interval (n=3). For comparison purposes, the test was repeated after four months of usage. Figure 6.3 shows the relationship of CCD temperature and time. The CCD temperature during initial use was capable of maintaining the target temperature up to 4 hours of the testing time. This indicated that this camera would have to be shut down for cooling after the CCD temperature exceeded the target temperature. Subsequently the CCD temperature increased beyond -3°C after 2 hours use during the test performed 4 months later, indicating that the efficiency of the cooling system had deteriorated and required manufacturer attention.
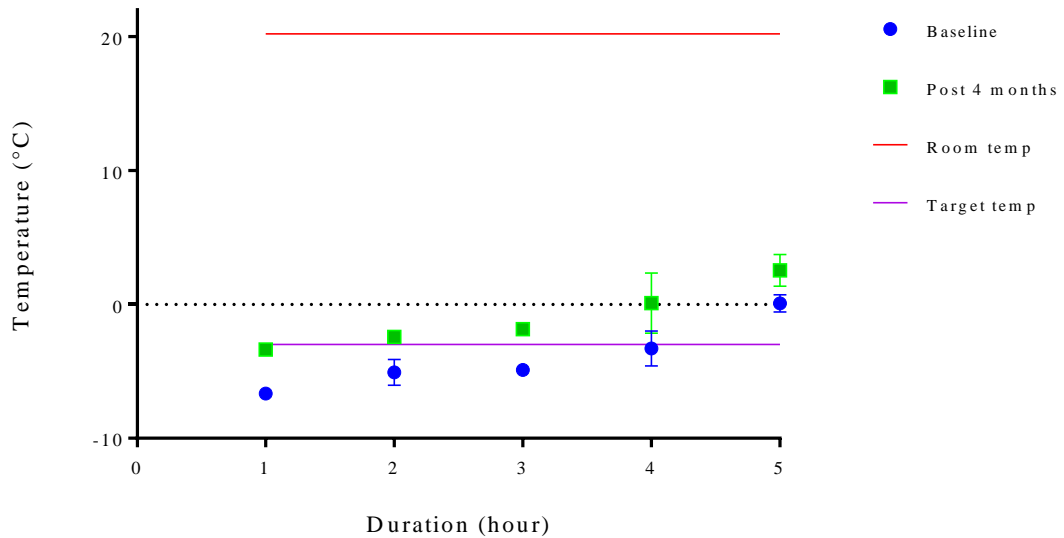
Figure 6.3: CCD temperature over 5 hours of use measured at initial stage (blue dots) and after 4 months use (green dots) (n=3).

### 6.4.2 Imaging functionality

Tests were carried out to assess the ability of the imaging system to provide high resolution optical and gamma images. A bespoke mini Williams Phantom (Figure 6.4) developed by the University of Leicester was used [170]. The phantom was filled with 37.2 MBq of $^{99m}$Tc solution (red colour) in all the wells. Image acquisition was performed with the Nebuleye camera head positioned 1 cm away from the phantom and 600 s imaging time using the acquisition protocol tabulated in Table 6.3.
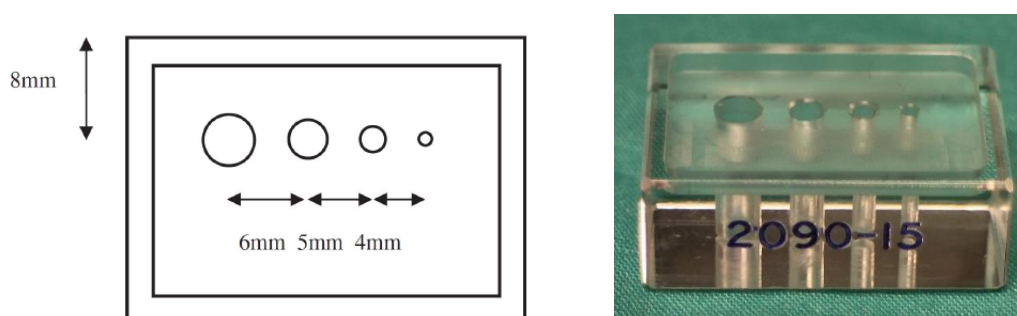


Figure 6.4: Schematic drawing and photograph of the mini Williams Phantom. The diameters of the wells were 4, 3, 2 and 1 mm.

Table 6.3: Image acquisition protocol for imaging functionality test.

| Parameter | Settings |
|---|---|
| ***Gamma camera*** | |
| Background subtraction | 3800 (checked "integrate") |
| Background threshold | 290 |
| ***Optical camera*** | |
| Orientation | Rotate 270 FlipX |
| Fixed focal distance | 150 |

Figure 6.5 shows the images of the phantom acquired using Nebuleye. No artefact as shown in image (c) was observed on the optical image of the phantom (a) however the edge of the phantom was slightly blurred at this camera setting. The gamma image (b) was a raw image generated from the integration of photon events detected in all frames, resulting a big bright blob. For this version of software, blob detection feature was not available, where this post-processing algorithm allows Gaussian distribution to be fitted to each light 'splash' produced in order to enhance the image quality (as shown in image d). No saturation or thresholding was applied during the image display.
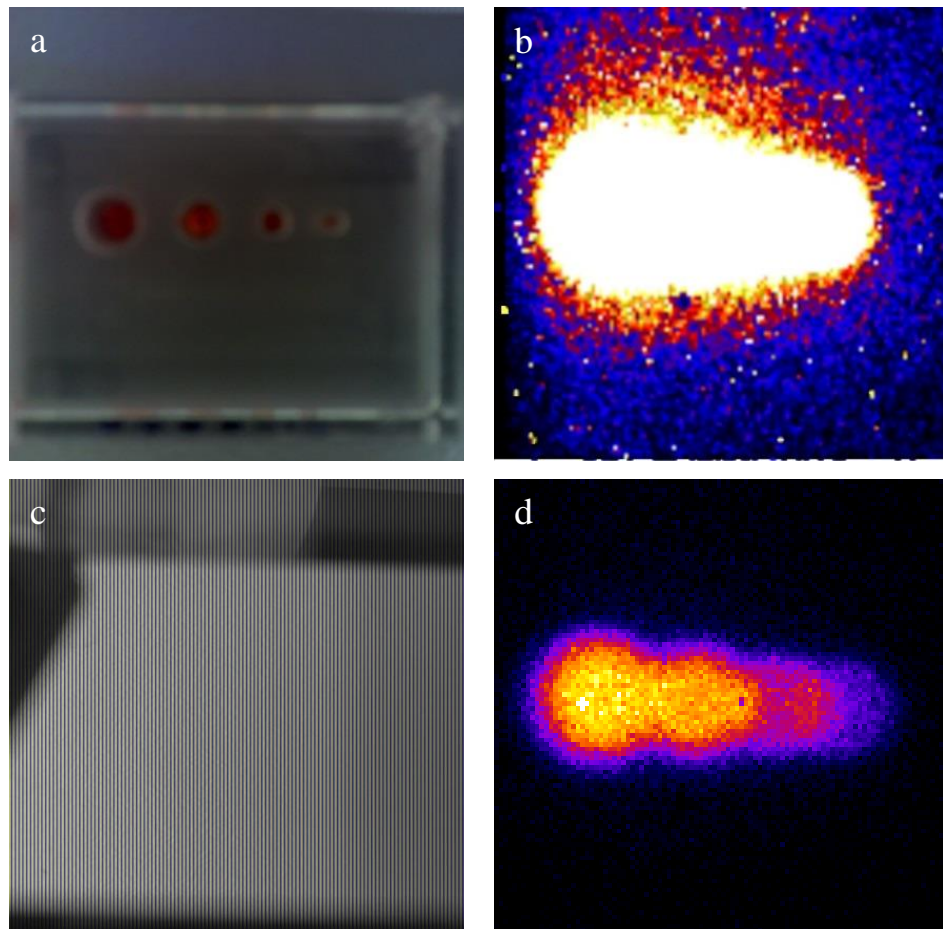
Figure 6.5: (a) Optical and (b) gamma images of the mini Williams Phantom acquired by the Nebuleye gamma camera system. (c) Example of optical image with artefact acquired by Nebuleye; (d) Post-processed gamma image of the mini Williams Phantom from the same test.

### 6.4.3   Software Testing

During the time of testing, the Nebuleye software was still under development. Each version of software as tabulated in

Table 6.4 was installed in the Nebuleye system for user acceptance test. The aim of the test was to assess the functionality and accuracy of the software features. The testing scope included all the features in the software:

   a) Main menu

   b) Patient Data Management

   c) Image Analysis

   d) Image Capture

   e) User Management

   f) Quality Control/Calibration

   g) Image Review

h) Service Mode

i) Log out

The detected software errors/bugs were sent to the software developer via an online reporting system (DoneDone, Chicago, IL, USA). Once the errors had been rectified, a new version of software was installed in the Nebuleye system for further evaluation. During the testing period, essential features which considered to be crucial for surgical application were also proposed for future inclusion in the software. These were included but not limited to:

a) routine quality control module

b) colour scale feature for image display

c) increase the acquisition time limit from 40 s to longer acquisition time

d) clinical grade image format

e) post-processing features including blob detection algorithm

f) concurrent process of image saving and acquisition

g) optical-gamma image orientation and scale

h) CCD temperature warning sign

Table 6.4: List of Nebuleye software released for testing.

| Version | Date of released/installed |
|---------|----------------------------|
| 1.3.49 | 3 August 2015 |
| 1.3.122 | 25 August 2015 |
| 1.3.143 | 18 September 2015 |
| 1.3.145 | 23 September 2015 |
| 1.3.138 | 24 September 2015 |
| 1.3.202 | 7 October 2015 |
| 1.3.222 | 14 October 2015 |
| 1.3.253 | 23 October 2015 |
| 1.3.320 | 14 December 2015 |
| 1.3.322 | 10 March 2016 |

## 6.5   Routine quality control tests

Following the acceptance and commissioning tests, routine testing on a camera system is essential to ensure adequate performance for ongoing clinical use. The limits of acceptability for the results and course of action to be taken if these limits are exceeded should be specified [103]. The tests should be simple and easy to be performed by any trained end user within a reasonably short time. In the UK, The Ionising Radiations Regulations 1999 through Regulation 32 requires every employer to ensure appropriate quality assurance programmes are in place including adequate testing of the performance of the equipment at appropriate intervals and after any major maintenance procedure or change to that equipment [190]. These tests should be carried out using standard protocols, so that the results will be comparable.

The full testing protocols to characterise SFOV gamma cameras described in Chapter 3 were comprehensive and time consuming and required specialist expertise and so would be difficult to carry out in a busy surgical department. Moreover, some surgical departments may not have regular medical physics and clinical engineering service support. Therefore it was necessary to develop routine quality control tests that were simple and practical for routine use.

The aim of the work was to develop a scheme suitable for evaluating the performance of the Nebuleye in routine basis prior to a clinical trial of first use. These included daily checks that were to be carried out on the day the camera was used and the additional tests that were to be performed at specified intervals. For this instrument the camera head casing was fixed and the collimator could not be removed by the user, therefore only extrinsic tests were possible. This section will discuss those suggested daily and monthly tests which were carried out on Nebuleye in order to form the baseline data.

### 6.5.1   Visual inspection

Visual inspection aims to ensure that the camera head has no sign of physical damage, that the articulated arm has the correct range of motion, the trolley system is functioning properly and the cables and plugs are properly connected and have not been damaged during use or storage. Each component of the imaging system that needed to be visually

checked is detailed in Table 6.5. This inspection was performed prior to switching on the system to check that all components were in satisfactory condition.

Table 6.5: Visual inspection checks on the Nebuleye.

**Camera head**

a) The plastic casing surrounding the camera head was inspected for signs of damage or puncture.

b) The camera head was moved through all possible motions.

c) The camera head interlocking system was checked.

**Cart based system**

a) The articulated arms were moved through all possible motions and to the fullest extent of travel.

b) Wheel locks were applied.

c) The main cable was checked, noting any insecure or lose cable which could create a potential trip hazard.

d) The cart handle was checked.

**Display screen(s) and keyboard & mouse**

a) The display screens were inspected for scratches, fingerprints, dust or other debris.

b) The image monitors were inspected for any interference patterns, rolling, lines or other signs of improper operation or electrical interference.

c) Computer keyboards and accessories were checked for proper operation.

**Control box**

a) The cable connection with the control box was inspected.

b) The control box surrounding was inspected for signs of indentation or puncture.
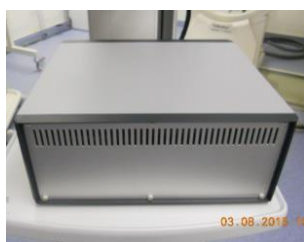
**Sterile sheath**

a) The packaging was checked to ensure it was intact. The plastic sheath was inspected for signs of tears or dirt.



**Main power switch**

a) The main power switch was turned on to check correct operation and power input.

### 6.5.2 System uniformity

System uniformity testing aims to test the system flood field response of the scintillation camera including the effect of any irregularities in the collimator. If available a uniform flood source containing Cobalt-57 can be used. However since this was not available a uniformly mixed solution containing 30 MBq of $^{99m}$Tc in 60 ml of water sealed in a 200 ml Corning Tissue culture flask was considered suitable. The culture flask provided a sealed container of small size suitable for the assessing the camera uniformity. The activity and concentration was determined to be sufficient to create a uniformity image within a pre-determined acquisition time of 10 minutes.

In this test, the collimated detector was irradiated by a thin flood source placed adjacent to the transparent window of the protective casing for 10 minutes. Figure 6.6 shows the experimental setup for the test. Gamma images were processed and analysed as described in Section 3.2.4. Subjective visual assessment was undertaken to investigate any non-uniformity of the image count densities (refer Figure 3.10 (b)). No detectable change of uniformity across FOV was observed in the image. The value of CoV was calculated by computing the mean and standard deviation of counts per pixel over the image recorded to identify any changes or trends of the value.

Figure 6.6: Experimental set up of the system uniformity and sensitivity tests. The camera head was positioned above the flask containing the flood source (mixture of $^{99m}$Tc solution and red coloured dye).

### 6.5.3   System spatial resolution

The system spatial resolution test aims to assess the sharpness of the image produced by the camera with the collimator in place. For routine test, a qualitative approach was used for a quick assessment of resolution. This approach was easier to perform than the quantitative method and involved the entire imaging process including the image display. It may be carried out using a test patterns, phantoms showing artificial lesions in a suitable anatomical structure or a transmission mask with areas transparent to gamma rays. Subsequently assessment was made to determine the capability of the camera in resolving the test pattern detail [106].

For spatial resolution assessment, IPEM [106] have suggested that the width of a line on the acquired image represents the spatial resolution of the camera, on condition that the width of the line or point source is much smaller than the camera's resolution. For LFOV gamma cameras resolution measurement are commonly made using a suitable line or point source of the order of 0.5 mm in size. For SFOV gamma camera the sizes should be of the order of 1 mm (where the system spatial resolution at the camera surface is of the order of 3.08 mm). Filling small holes or cavities with radioactive solution can be difficult and poses the possibility of contamination. Hence, a transmission mask was considered to be a relatively practical solution.

For the Nebuleye, a lead transmission mask having dimensions 90 × 124 mm was designed and manufactured in house with 5 holes of diameter 1.0, 1.5, 2.0, 3.0 and 4.0 mm aligned in a straight line. This was fabricated using 4 mm thick lead plate which has a thickness that was sufficient to attenuate 99% of 140 keV gamma photons. All

holes were within the FOV of the camera at the SSD of 1 cm. A uniformly mixed radioactive solution as mentioned in Section 6.5.2 was used to irradiate the detector for 10 minutes. The transmission mask was laid on top of the flask containing activity and the collimated camera positioned above the mask as shown in Figure 6.7.
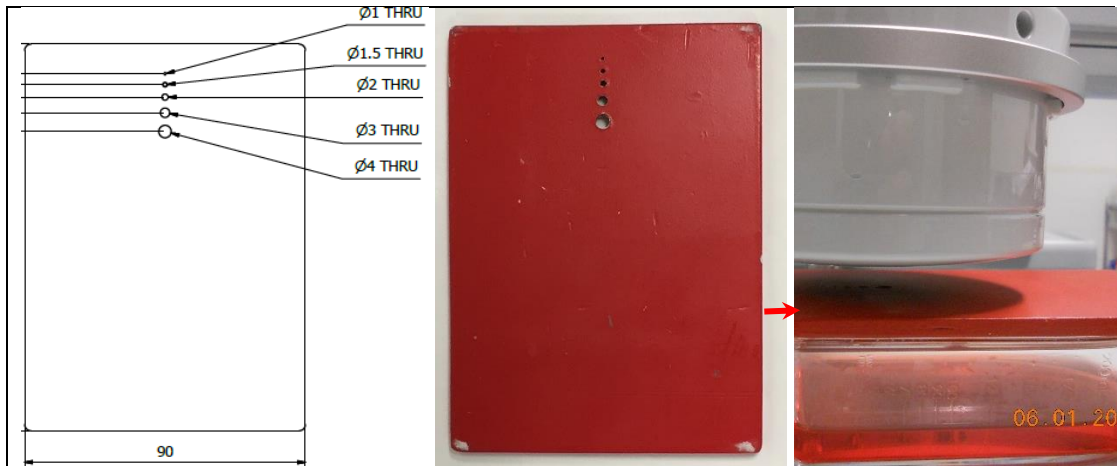


Figure 6.7: (Left) Schematic diagram and (middle) photograph of lead mask with holes (in the unit of mm). (Right) Photograph of the experiment setup during the routine system spatial resolution where the lead mask was placed in between the camera head and the flood source.

Figure 6.8 shows the resulting scintigraphic image of the resolution test pattern. The hot spots indicated the hole sizes of the transmission mask which were visualised by the camera and provided a quick assessment of the system spatial resolution [106]. The image was used as the baseline image for future image comparison.
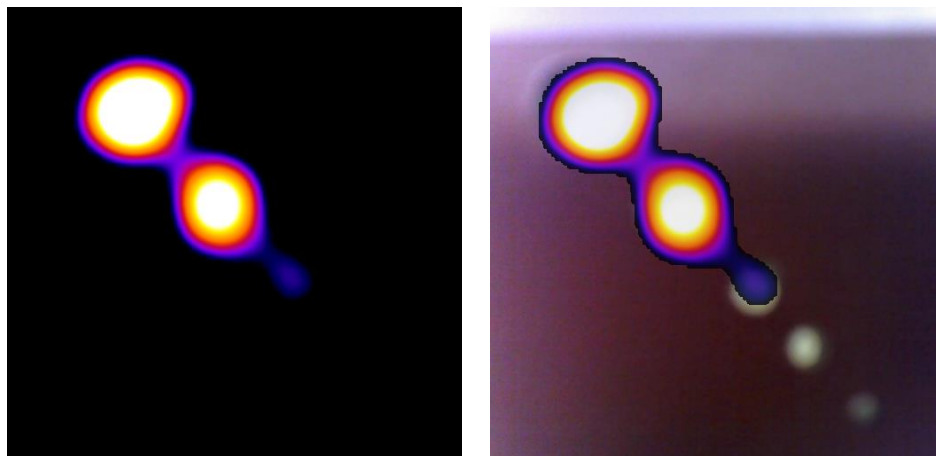


Figure 6.8: Example images of the system spatial resolution test displays: gamma image (left), hybrid image (right). These images show three hot spots, corresponding to the minimum hole size of 2 mm.

### 6.5.4  System sensitivity

System sensitivity is a measure of the count rate response of a collimated scintillation camera to a radionuclide source of known activity. The experimental setup for measuring this was similar to the system uniformity test as discussed in Section 6.5.2. System sensitivity depends on the collimator sensitivity. Due to the pinhole collimator configuration of the SFOV gamma camera, the collimator sensitivity was inversely proportional to the SCD. Therefore, the measurement should be reported in terms of cps/MBq at a specified SCD. The physical size of the flood source and the wall thickness of the container should be minimal (about 3 mm) to reduce the effects of any source self-attenuation [106].

For consistency of the routine testing, radioactive solution contained in the flask as described in Section 6.5.2 was used for all procedures. The image acquisition time of 100 s was required and the activity of the radionuclide and the time of day were recorded. The resulting image was post-processed and the number of counts for each image was recorded. Subsequently measured count rate (C) was calculated, corrected for background count rate. The decayed activity in the source (A) was also calculated. The system sensitivity (cps/MBq) was then computed using the Equation 6.1.

$$\text{Sensitivity} = \frac{C}{A} \qquad\qquad 6.1$$

Since the dimension of the flood source was larger than the FOV of the camera, IPEM [106] has suggested that the calculation needs to consider the loss of the photons due to the inadequacy of the detector area by using Equation 6.2.

$$\text{Sensitivity} = \frac{C}{A} \times \frac{D_s}{D_c} \qquad\qquad 6.2$$

where $D_c$ is the area of the field of view of camera and $D_s$ was the area of the source both at the specified SCD. The system sensitivity for Nebuleye was $1.34 \pm 0.15$ cps/MBq at SCD of 10 cm.

### 6.5.5 Cooling test

The cooling test aimed to assess the ability of Peltier cooler to cool down the CCD from ambient room temperature to the target temperature within a pre-determined cooling period. It should be performed daily before the camera is used. Experimental work was carried out to examine the time taken for the CCD to reach the target temperature after the initiation of the system. The ambient temperature of the room was recorded using a therma-hygrometer. After powering up the system, the temperature of the CCD measured by the thermistor in the CCD package was recorded at 2 minutes interval over a period of 10 minutes.

Figure 6.9 shows an example where the temperature of CCD decreased over time during use. It was able to reach the target temperature of -3°C at approximately 3 minutes after the software initiation (n=6). The readings of the temperature measurement remained stable at the lowest temperature within 5 minutes of powering up. Therefore, the cooling duration for the CCD to reach the target temperature was considered to be within 5 minutes and thereafter this was used as baseline data for future reference.
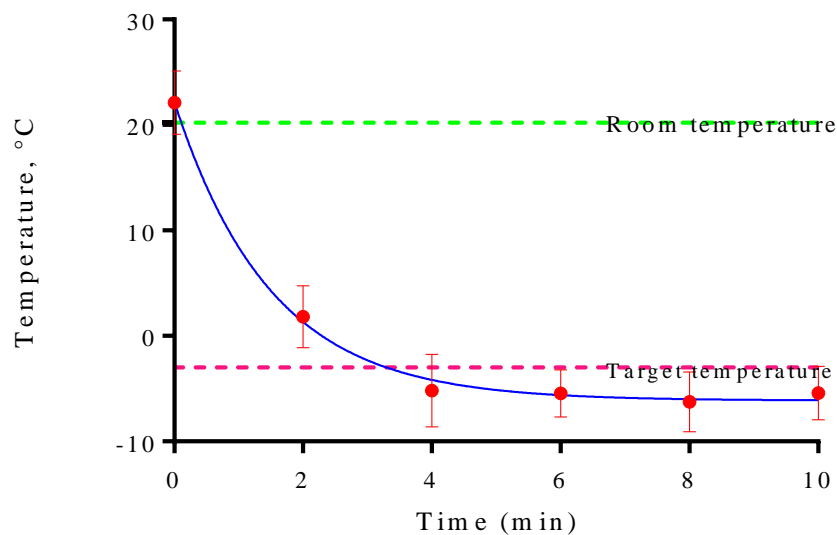


Figure 6.9: CCD temperature after system initiation (n=6).

### 6.5.6 Imaging functionality

The functionality of both the optical and gamma cameras was required to be checked prior to daily use. This test examined the ability of the gamma and optical cameras to produce fused images as expected. The images should have no artefacts or deviation

from expected quality. Any artefact or suspicious noise that appeared in the image, required further investigation. For clinical use, since the availability of radioactive sources may be limited in some surgical departments, it was suggested that the most readily available point source would be a small amount of $^{99m}$Tc placed in the tip of a one ml syringe preferably capped with a blind hub. For this measurement, the tip of the syringe was placed 5 cm underneath the camera head. Image acquisition was performed using a 100 s imaging time. Examples of the gamma and optical images produced are shown in Figure 6.10. Such images could be used as reference images.
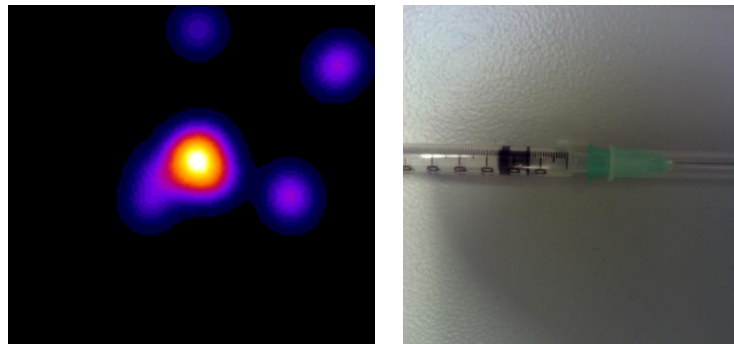


Figure 6.10: Gamma (left) and optical (right) images acquired by the Nebuleye with 100 s acquisition time. There were three hot spots at the peripheral area due to scattered events or background radiation and these can be eliminated by adjusting the threshold and saturation level at image display. The gamma image was post-processed with 6.0 pixel Gaussian smoothing filter.

### 6.5.7  Background radiation level

This test aims to check the background count rate of a scintillation camera in the clinical environment. The background count rate value is recorded over a period of time to illustrate any trends of the values. Significant change of background count rate may indicate that there is an increase in environmental radiation from local sources (patient administrated with radiopharmaceutical), radioactive contamination of the instruments or its surroundings or random noise caused by the device itself or that the detector sensitivity has been impaired. For this measurement, the camera head was positioned with the detector facing downward using an image acquisition time of 100 s. The image was post-processed and the number of counts in each image was quantified. The background count rate of the Nebuleye in the research laboratory, nuclear medicine clinic, QMC was $0.03 \pm 0.03$ cps (ranged between 0.01 to 0.18 cps).

### 6.5.8 Proposed routine quality control scheme and calibration jig design

Based on the initial physical evaluations of Nebuleye, the previously described harmonised routine quality control scheme and the limits of acceptability were proposed. These tests were considered as a simple and robust scheme to be carried out by the end users, which should be possible in department with limited resources. Table 6.6 summaries the recommended tests and the acceptance limits for the Nebuleye camera.

Table 6.6: Reporting parameter and the limit of acceptance for the routine quality control tests.

| Tests | Parameter | Tolerance |
| --- | --- | --- |
| Physical inspection | Visual inspection | No physical damage, all parts functioning. |
| System spatial resolution | Visual inspection: minimum detectable size of hole (actual diameter) | No significant deviation with reference image |
| System uniformity | Qualitative: Visual inspection Quantitative: CoV | No significant non-uniformity <10% manufacturer specification [103] |
| System sensitivity | Counts/s/MBq | <10% manufacturer specification [103] |
| Cooling test | Cooling time | < 5 minutes to reach target temperature |
| Imaging functionality | Visual inspection | No artefact or significant deviation with expected image |
| Background count rate | Counts/s | <20% of the reference value [103] |

The routine quality control tests discussed above required a flood source and transmission mask, positioned in a fixed distance away from the detector during the image acquisition. The experimental work described in the previous sections has demonstrated the feasibility of the proposed methodology. For future use it would be necessary to simplify the testing procedure. Therefore a calibration jig suitable for use

with the Nebuleye SFOV gamma camera has been proposed. This should be capable of accommodating the required tests in a reproducible manner on a routine tests.

A bespoke calibration jig designed for this purposes was proposed. This was a cylindrical shape with a small stand designed to fit in the camera head at a fixed distance. This included a sealed cylindrical shaped flat tank of height approximately 5 mm which could be filled with radioactive solution to act as flood source. The side wall of the flat tank is intended to be fabricated using PMMA and it should be thin enough to reduce the possibility of the gamma ray self-absorption. Sealable ports should be included for easy filling and draining of the radioactive solution which can be secured using plastic screws. This is to ensure that the flood source may be sealed during use and to minimise any bubble trapping during the flood source preparation.

The jig was designed so that the resolution transmission mask could be slotted in between the flood source and the camera. The resolution transmission mask was to be fabricated using 4 mm thick lead with holes of different diameter (1, 1.5, 2, 3 and 4 mm) as previously described. This mask should be easy to insert and remove from the jig whenever necessary. Figure 6.11 illustrates the design concept of the calibration jig. An interlock system was designed to fit the camera head. A flat base would keep the camera standing upright with the flood source in a level position during the test. A spirit level could be included in the design to enable the user to check for horizontal placement of the liquid source.
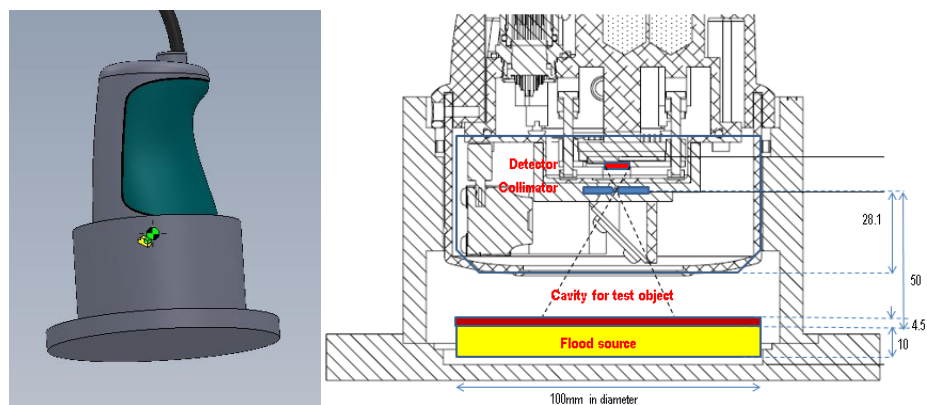


Figure 6.11: (Left) Design concept and (right) schematic diagram of the calibration jig attached to the camera. (Image courtesy of GTL)

## 6.6   Summary

This chapter has described the documentation and protocol required for a pilot clinical trial of a hybrid optical-gamma camera for use in sentinel node localisation procedure during breast cancer surgery.

Although the trial was terminated before it began the protocol and quality control testing procedures have been established and are suitable for future use once CE marking of the system has been achieved. The initial physical evaluation of the camera using the proposed quality control scheme has established the baseline data for Nebuleye. These data may be valuable in the initial stage of device development in order to monitor the performance of the camera over a period of time during initial clinical use.

# Chapter 7

# Assessing the capabilities of the pre-production prototype SFOV Hybrid Optical Gamma Camera

## 7.1 Introduction

Although the clinical trial described in Chapter 6 did not go ahead as planned, the camera offered potential in other areas of nuclear imaging. Further work was undertaken to explore the use of the camera as a handheld device and to assess the capabilities of the system for a range of clinical applications. The Nebuleye camera utilised similar detection technology to the HGC which had been calibrated with $^{99m}$Tc (140 keV), $^{109}$Cd (22.16 keV and 24.94 keV X-ray) and $^{241}$Am (59.5 keV) [43]. It had not previously been tested with other radionuclides commonly used in nuclear medicine such as $^{123}$I (159 keV) and $^{111}$In (171 and 245 keV).

Due to the compact nature of the SFOV gamma camera, it allows the device to be handheld when in use hence increasing access to procedures which are inaccessible when using other larger size gamma cameras. However, the voluntary and involuntary movement of the operator may cause deterioration of image quality subsequently affect diagnosis accuracy. Experimental work was carried out for the first time to examine the operator motion effects when imaging with the SFOV gamma camera. In addition, a qualitative survey of the end user feedback pertaining to the ergonomics of the Nebuleye design was undertaken as part of the device improvement process during the pre-production stage. This chapter examines the imaging consequences of operator motion effects and provides user feedback on the system ergonomics, as well as the first results of imaging a range of radionuclides including $^{99m}$Tc, $^{111}$In, $^{123}$I, $^{125}$I and $^{75}$Se.

## 7.2   Ergonomics

Ergonomics, also known as human factors, are crucial considerations in the design and manufacture of a medical device which is intended to be used by operators in the clinical setting. It can be defined as "the application of knowledge about human capabilities (physical, sensory, emotional, and intellectual) and limitations to the design and development of tools, devices, systems, environments, and organisations" [191]. As with any medical device, the incorporation of human factors in the design and construction of the SFOV gamma camera are important if these systems are to be used routinely in the clinical settings. As described in Chapter 2 the camera began in the laboratory with a rectangle shaped casing surrounded by crude lead covering with sharp edges, then gradually progressing through different stages of development until it was suitable for use in a clinical environment. Figure 7.1 shows the transformation of the final experimental prototype HGC to the current design of Nebuleye.



Figure 7.1: Translation of prototype HGC (left) to become Nebuleye (right). Image courtesy of GTL.

All medical devices must demonstrate appropriate safety and performance compliances prior to clinical use. Even though the Nebuleye camera head is not intended to be used in direct contact with patients, it was still required to demonstrate that the camera was electrically safe and electromagnetically compatible. The camera design should be robust with solid construction and the surfaces should be easy to clean to maintain cleanliness and to prevent any cross infection. The camera was designed for use in the

clinic, at the patient bedside and also for use in the operating theatre where the camera head and the articulated arm would be required to be placed in a sterile sheath or drape to ensure sterility. This is an important consideration to enable repeated use with consecutive surgical cases.

The design of the camera head should be compact with flexibility of movement so that it may be placed firmly in position over the patient. The user interface should also be user-friendly and simple to operate for acquiring and recording good quality images within a reasonably short acquisition time. Acquiring standard gamma images often takes a few minutes, although most surgeons would prefer to see images available within seconds rather than minutes to complete surgical procedures in the minimum time possible. It has been suggested that a FOV of approximately 50 mm × 50 mm is optimal for surgical application [54]. These factors had been carefully considered during the early stage of the Nebuleye design. The following sections describe user evaluation of the first pre-production prototype Nebuleye, which was sent to Queen's Medical Centre in 2015.

### 7.2.1 Qualitative user assessment

Patient safety and performance of the medical device are the main factors to be considered when introducing new equipment into clinical use. The National Patient Safety Agency (NPSA) (now part of NHS England) [192] has published a guidance document describing methods of user testing in the pathway of medical device development. This document suggests various research methods that may be used at different stages of device development, for example ethnography, task analysis and focus groups, interviews and questionnaires. These methods are complementary to those formal approaches such as Failure Modes and Effects Analysis (FMEA) and do not replace the regulatory requirements.

Preliminary human factor analysis with the involvement of a small group of healthcare professionals was carried out during the early stage of development of the pre-production prototype Nebuleye. A questionnaire was designed and used as a quick and inexpensive way of collecting the opinions of a small group of potential end users. The aim of the evaluation was to assess the system functionality in order to optimise its

performance and safety in the clinical environment, particularly in the operating theatre during surgical procedures. The data from this survey was needed for further device development before finalising the system design and configurations.

Healthcare professionals who were potential users of the camera system were included. Nine participants (3 surgeons, 4 clinical scientists, 1 nuclear medicine technologist and 1 clinical engineer) were invited to the nuclear medicine clinic at Queen's Medical Centre to take part in this pilot study. The camera system was set up in a clinical research room, using an adult cardiopulmonary resuscitation (CPR) training manikin in a supine position on the patient couch, to simulate the situation in the operating theatre. A questionnaire (see Appendix B) containing 19 questions (5-point Likert scale, polar, multiple choices or open questions) was distributed and brief introduction of the camera system was provided to each individual participant in the study. The participants were given the opportunity to ask questions and to use the camera (without any radioactive sources), before completing the questionnaire. Feedback on some of the expertise-related questions were not provided by all respondents hence the sum of responses do not equal 9 for all questions.

### 7.2.2   Results

Table 7.1 shows the summary of the selected responses regarding the first impression and the added value in intraoperative procedures. On first impression all 9 participants agreed that this camera system was suitable for use in the operating theatre and visually attractive. Eight participants agreed that it had good surface finishing and 7 were agreed that it had appropriate functionality for clinical use. One participant disagreed due to the stiffness of the articulated arm and camera head holder joint when moving the camera into position. With regards to the the hybrid optical-gamma camera providing added value in patient management during intraoperative procedures, when compared to a gamma probe, most of the participants agreed that it could ease the localisation of uptake (7/8), useful in re-examination of any radioactive residue (8/8), provide images for medical-legal purposes (6/8) and potentially assist with dissection of tissue margins (5/8).

Table 7.1: Responses on the first impression and the added value in intraoperative procedures.

| First impression (n=9) | Disagree | Unsure | Agree |
|---|---|---|---|
| Suitable for use in the operating theatre | 0 | 0 | 9 |
| Visually attractive | 0 | 0 | 9 |
| Good surface finishing | 0 | 1 | 8 |
| Appropriate functionality | 1 | 1 | 7 |
| **Added value in intraoperative procedures** | | | |
| Easier for localisation of uptake | 1 | 0 | 7 |
| Assists with dissection of tissue margins | 0 | 3 | 5 |
| Re-examination of any radioactive residue | 0 | 0 | 8 |
| Provide images for medical-legal purposes | 0 | 2 | 6 |

Note: The sum of responses do not all equal 9 depending on the feedback provided.

Most participants (8/9) had no safety concerns regarding use of this device in the operating theatre and were satisfied with the size and the weight of the camera head (6/9), articulated arm (9/9) and trolley system (9/9). The participants also showed that they felt comfortable when holding the camera head (7/9), with the trolley near the patient couch (9/9) and moving the articulated arm (7/9). However, four participants thought that the camera system may present difficulties for maintaining sterility in the operating theatre while all of them considered the use of a sterile cover to maintain its sterility would be practical (9/9).

It is worth noting that there were suggestions to reduce the size of camera holder to suit the users with smaller hand size. The average female hand size (length) is 172 mm [193]. The current camera holder circumference is 240 mm (~76 mm in diameter) so it may be possible to reduce this to 160 mm (or 50 mm in diameter [194]) in future designs.

During the survey, most of the participants suggested that the best position for the system trolley and the image display in the operating theatre was on the opposite side of the surgical couch to the surgeon, allowing the surgeon to view and control the system without interrupting the procedures. Of the 7 participants (two participants chose not to provide feedback), 6 suggested that an acceptable image acquisition time for a single image to localise radioactivity uptake should be 60 s or less. An image

acquisition duration is important in any surgical procedure and should be as short as possible while providing images of diagnostic quality. In addition, feedback was collected on the necessary applications that should be available on the user interface software (Table 7.2). These provided useful suggestions to the manufacturer for designing applications in future software development.

Table 7.2: Applications in the user interface software.

| **Applications** (n=8) | **Disagree** | **unsure** | **Agree** |
|---|---|---|---|
| Real-time dynamic gamma imaging | 0 | 1 | 7 |
| Real-time optical video | 0 | 0 | 8 |
| Static gamma image | 0 | 0 | 8 |
| Static optical image | 0 | 0 | 8 |
| Static hybrid image (superimposed) | 0 | 0 | 8 |
| Dual-images side by side comparison | 0 | 0 | 8 |
| Masking of high activities at injection site | 0 | 0 | 8 |
| Contrast enhancement | 0 | 1 | 6 |
| Variable colour scales | 0 | 1 | 7 |
| Measurement tools (distance, line profile) | 0 | 1 | 7 |
| Display of counts in hot spot | 0 | 4 | 4 |
| Editing tools/Marker | 1 | 2 | 5 |

## 7.3 Operator motion effects

During the use of a handheld gamma camera it is to be expected that image quality and hence the diagnostic accuracy would be affected by user motion over the period of image acquisition. Both voluntary and involuntary patient movement may also affect the image quality. Such motions will cause blurring of details in the image. These effects could be a real problem as typical static planar nuclear medicine imaging requires relatively long acquisition times of approximately 1 to 5 minutes. This has been recognised in SPECT-CT and PET-CT whole body imaging where the long acquisition times of the PET and SPECT images may result in movement artefacts in the reconstructed images when viewed together with the CT images [195-197].

Image acquisition using an SFOV handheld gamma camera can be performed with the camera head either held by the operator or by a camera holder. Due to the small size of the camera head, it is sometimes preferable to hold the camera by hand to bring the detector as close as possible to the target organ. The severity of motion may potentially be affected by the design of the camera head (e.g. weight and size), the duration of holding the camera head, tremor amplitude of individual operator, involuntary motion, such as sneezing, or due to other external factors.

### 7.3.1 Methods

To our knowledge no data previously existed on the duration that operators could hold such a camera without movement. The aim of this study was to assess the magnitude of the movement of the camera caused by the operator. Six potential users (3 nuclear medicine technologists and 3 medical physicists) were invited to take part in the hand movement study. The Nebuleye was set up in the clinical research room at the nuclear medicine clinic, Queen's Medical Centre. A point source containing approximately 15 MBq $^{99m}$Tc-pertechnetate placed in a 3 mm diameter hole of the mini Williams phantom was positioned at SCD 7 cm in front of the detector. Each operator was requested to hold the camera for 3 minutes at their convenience during image acquisition (Figure 7.2). Image acquisition was repeated with the camera head mounted on the camera holder of the articulated arm and this data was used as a control for comparison purposes.



Figure 7.2: Operator hand movement study set up. Point source was placed underneath of the camera head held by an operator (left) with extended right hand or mounted on an articulated arm (right) at a SCD of approximately 7 cm.

In addition, qualitative assessments were carried out to examine the image quality of the gamma images of mini Williams phantom (as described in Section 6.4.2) filled with 8 MBq of $^{99m}$Tc pertechnetate in 4 wells. The Nebuleye was positioned at SCD 4 cm in front of the camera head, either held by operator or mounted on the camera holder. Each image acquisition time was 3 minutes. The resulted images was post-processed and visually assessed. Line profiles were plotted horizontally across the hot spots.

### 7.3.1.1 Image analysis and software

Each scintigraphic image produced by the Nebuleye was processed and saved as a multi-frames (2 seconds per frame) DICOM image. The image was then assessed using an in house software (MOCO) [198, 199] to determine the magnitude of motion by tracking the centre of mass (COM) of the hot spot. The MOCO software was originally developed to correct organ motion in planar gamma camera acquisitions by tracking the COM of detected gamma photons, and as a consequence could be used to produce coordinates of the motion of the COM of activity over time. During the data processing, the software determined the COM of counts in the first frame of the image and set this as the reference COM (x- and y- coordinates). The COM of each subsequent frame was then determined ($x_n$- and $y_n$- coordinates) and the magnitude of the displacement (distance in respective x- and y-axes) between the COM in each frame and the reference COM was calculated. This information was saved in a text file for further analysis. All data was transformed into an absolute value for the calculation of the displacement in mm.

### 7.3.2 Results

Figure 7.3 shows the gamma images acquired during the study with different ways of holding the camera (either handheld with one or both hands or fixed on the camera holder) and plots of the COM displacement in x- and y- axes against the acquisition time. With the camera mounted on the camera holder a discrete bright spot was seen as shown on the control images (Image name: Control 1 and Control 2). In general the gamma images acquired with the camera held by an operator showed blurring of details when compared to the control image. For the operator motion study, the images from five subjects were included in the data analysis while one had to be excluded due to the movement of the camera completely out of the FOV during the acquisition. User 2, 4

and 6 held the camera with both hands while User 1 and 3 held the camera with either right or left hand. The summary results are tabulated in

Table 7.3. Taking the results together the COM was found to move away from the reference COM by 4.34 ± 2.43 mm and 7.18 ± 3.34 mm in x and y directions respectively.
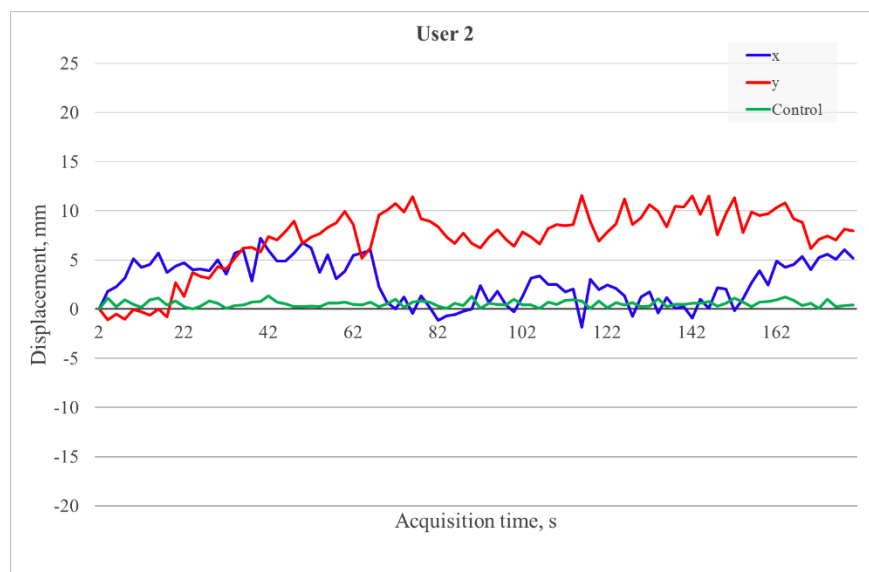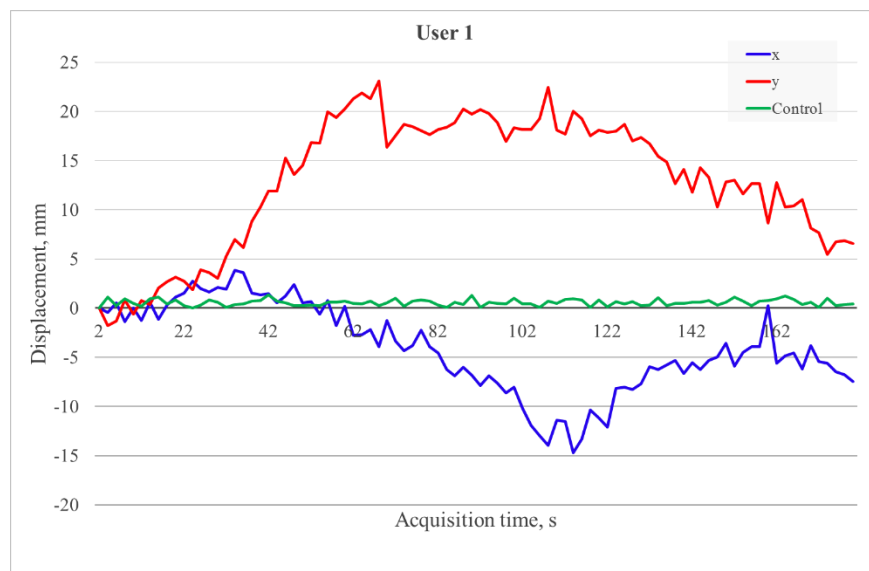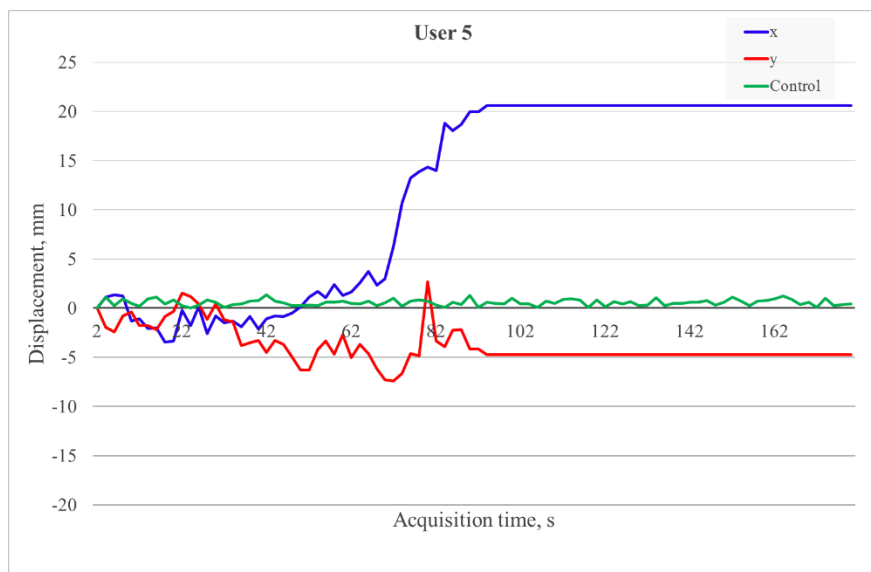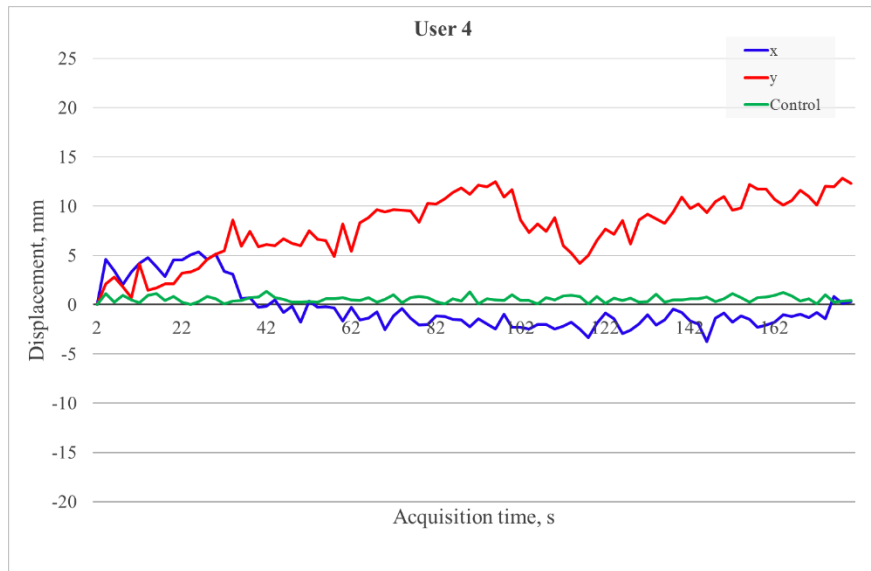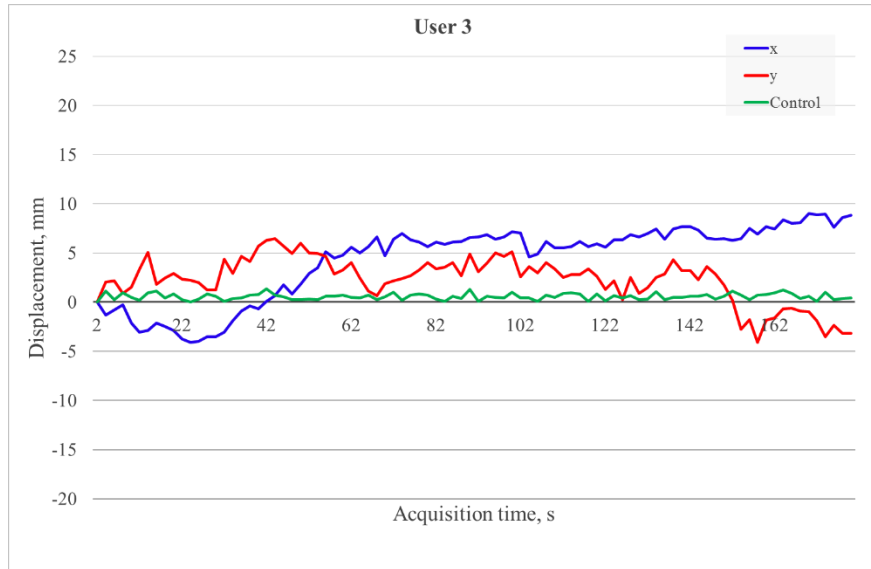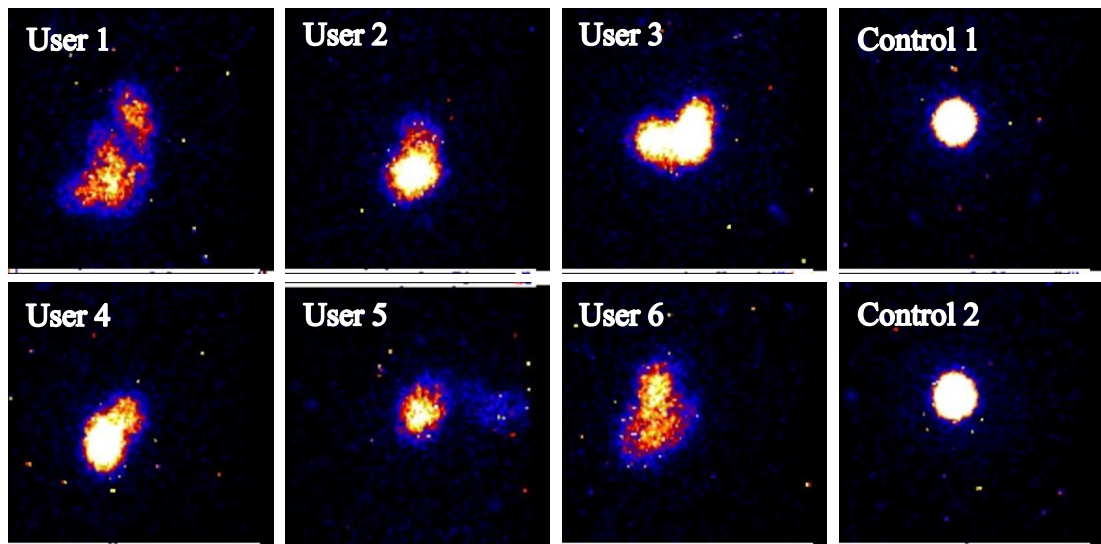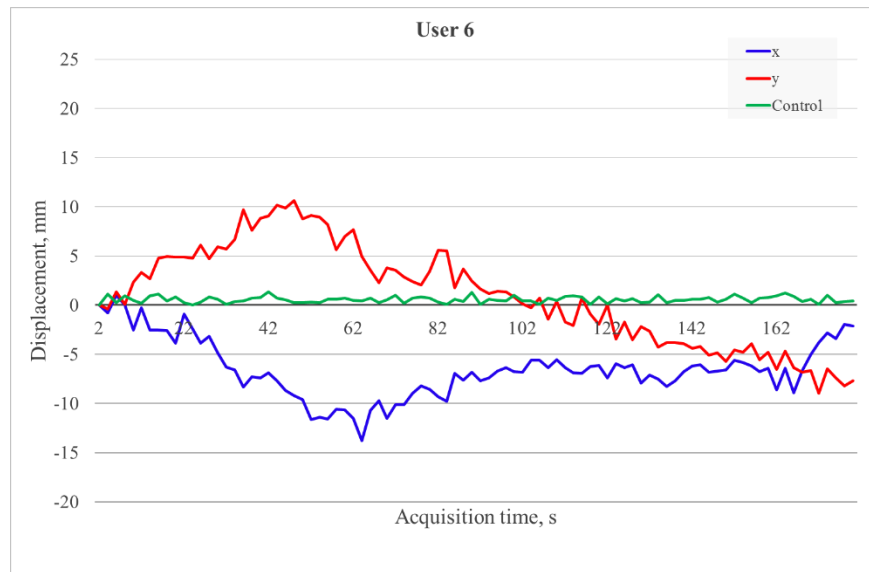
Figure 7.3: (Top) COM displacement plotting over image acquisition time for all users. Blue and red lines show the magnitude of displacement at x- and y-axis respectively and green line shows the average displacement for the control image. (Bottom) Gamma images acquired during the study with the Nebuleye held by individual operator or mounted on the articulated arm as the control image.

Table 7.3: Summary of the COM displacement (mm).

| User | Displacement (mm) | | | | | | Distance |
| | Max | | Min | | Mean ± SD | | |
| | x | y | x | y | x | y | |
|---|---|---|---|---|---|---|---|
| 1 | 14.72 | 23.11 | 0.01 | 0.39 | 4.89 ± 3.66 | 13.14 ± 6.44 | 14.02 ± 10.10 |
| 2 | 7.24 | 11.53 | 0.01 | 0.03 | 2.99 ± 2.01 | 7.33 ± 2.98 | 7.91 ± 4.98 |
| 3 | 9.03 | 6.44 | 0.10 | 0.22 | 5.30 ± 2.35 | 2.97 ± 1.43 | 6.07 ± 3.78 |
| 4 | 5.37 | 12.81 | 0.15 | 0.75 | 1.90 ± 1.31 | 8.00 ± 3.10 | 8.22 ± 4.41 |
| 6 | 13.75 | 10.62 | 0.03 | 0.02 | 6.63 ± 2.84 | 4.46 ± 2.75 | 7.99 ± 5.58 |
| Average | 10.02 | 12.90 | 0.06 | 0.28 | 4.34 ± 2.43 | 7.18 ± 3.34 | 8.84 ± 5.77 |
| Control | 1.89 | 2.09 | 0.00 | 0.03 | 0.59 ± 0.43 | 0.74 ± 0.46 | - |

Figure 7.4 shows the mean COM displacement over the acquisition time. For the first 30 seconds of the image acquisition the magnitude of displacement was less than 5 mm; however it exceeded 5 mm after one minute of acquisition. This suggests that the image acquisition time should preferably be within a minute when the camera is handheld during use. From the visual assessment of the gamma images of mini Williams Phantom filled with $^{99m}$Tc source, the image acquired with the Nebuleye held by the operator showed blurring of detail compared to the image acquired with the camera held by the camera holder. The pixel intensity profiles of both images were generated as shown in Figure 7.5.
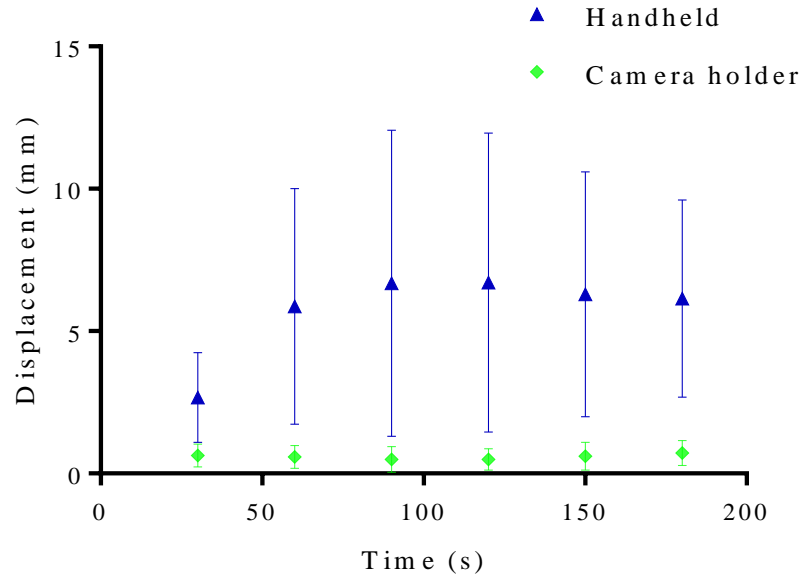
Figure 7.4: Magnitude of COM average displacement over acquisition time (n=75).
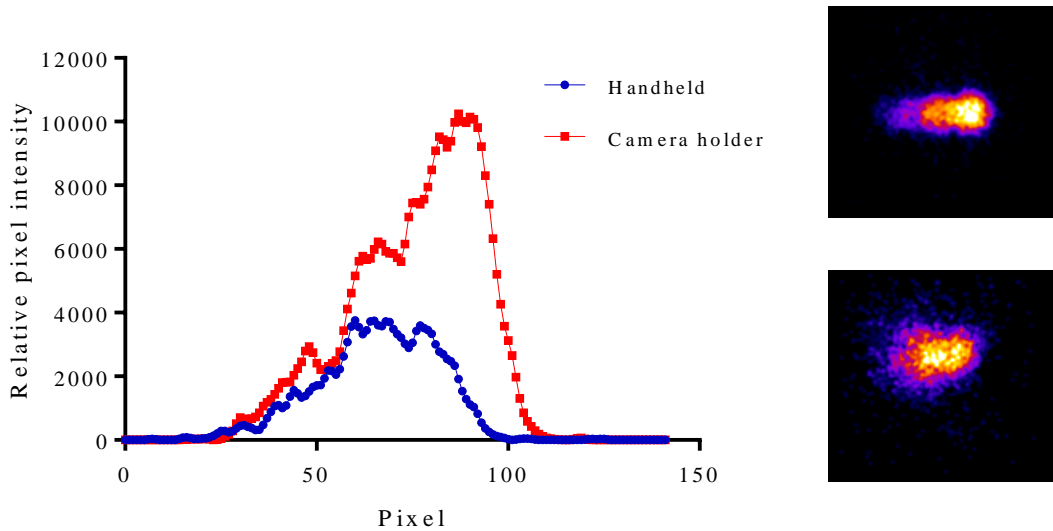


Figure 7.5: (Left) Line profiles of the gamma images of mini Williams phantom filled with $^{99m}$Tc source in the wells, acquired by Nebuleye held by the camera holder (top right image) or by the operator (bottom right image).

## 7.4 Exploratory imaging with clinically relevant radionuclides

As mentioned in Chapter 1 a range of radionuclides is used routinely in diagnostic nuclear imaging, these mainly being $^{99m}$Tc, $^{111}$In and $^{123}$I. These radionuclides emit gamma rays of energies ranging between 80 and 400 keV. The detectors of the SFOV gamma cameras tested in this work consisted of an EMCCD and thin layer of the crystal scintillator. The cameras did not have a pulse height analyser or an energy window setting feature which are typically available in most modern gamma cameras, thus

making energy discrimination impossible. For the detector used in the SFOV gamma camera there was a high possibility that high gamma energy gamma rays could penetrate through the thin layer of the detector undetected, resulting in low detection efficiency. As the detection technology used in Nebuleye is identical to the HGC, the latter camera was used to test the impact of the camera performance with different pinhole diameters and crystal thicknesess due to the current version of Nebuleye was limited to 1 mm pinhole collimator and 1.5 mm crystal thickness configurations.

Lees *et al.* had previously reported the performance testing of the CGC using $^{99m}$Tc, $^{241}$Am and $^{109}$Cd [43]. The gamma rays emitted in the range between 22 keV and 140 keV were successfully detected by the camera. However most previous work had been limited to $^{99m}$Tc. Gamma ray detection using the SFOV gamma camera may be affected by several factors, including the energy and abundance of the emitted gamma rays and optimum activity of the radiopharmaceutical. In addition the settings of the camera including acquisition time, collimator, and SCD play an important role in determining the detection and geometry efficiency.

The prescribed radiopharmaceutical and optimum activity may vary depending on type of procedures, the patient weight and individual metabolic characteristics. The image acquisition settings of the camera may also depend on the clinical use and the standard operating procedures. The aim of the subsequent tests were to explore and examine the detectability of common clinically used radionuclides using the camera. Clinical radiopharmaceuticals readily available in the nuclear medicine clinic, Queen's Medical Centre (Table 7.4) were used in these tests.

Table 7.4: Radiopharmaceuticals used for the detectability test.

| Radionuclide | Gamma Energy (keV) | Physical Half-life | Yield abundance per decay (%) | Physical form |
|---|---|---|---|---|
| $^{125}$I | 35 | 60 days | 7 | Solid (seed) |
| $^{75}$Se | 136 | 120.4 days | 59 | Solid (tablet) |
| $^{99m}$Tc | 140 | 6 hours | 90 | Liquid |
| $^{123}$I | 159 | 13.2 hours | 83 | Liquid |
| $^{111}$In | 171 | 2.8 days | 90 | Liquid |
| $^{111}$In | 245 | 2.8 days | 94 | Liquid |
| $^{75}$Se | 265 | 120.4 days | 60 | Solid (tablet) |

Approximately 4 MBq of the radiopharmaceutical solutions was used to filled the 4 mm diameter well of the mini Williams Phantom. The phantom was positioned at SCD 30 mm and image acquisition was carried out within the restricted FOV for 10 minutes. System sensitivity and resolution of the camera to each radionuclide were quantified using the methodology modified from Section 3.2.2 and 3.2.6.

Further investigations were performed to assess the spatial resolution of the camera using the phantom. The wells (4, 3, 2 and 1 mm diameter) of the mini Williams Phantom were filled with the radioactive solution and placed in front of the camera for imaging. The resulting images were visually assessed and compared with the images generated by a standard LFOV gamma camera (Nucline™ X-Ring-R, Mediso, Hungary).

### 7.4.1 Technetium-99m

Technetium-99m is the most commonly used radionuclide in diagnostic nuclear medicine (principal gamma energy: 140 keV). Typical amounts of activity used in clinical studies ranges from 4 MBq for lacrimal drainage studies up to 900 MBq for parathyroid imaging [200]. Figure 7.6 (left) shows the image formed from a point source of $^{99m}$Tc solution contained in a single well of the phantom. The sensitivity of the camera was measured as $3.58 \pm 0.07$ cps/MBq while the system resolution was $2.82 \pm 0.05$ mm at SCD 30 mm.
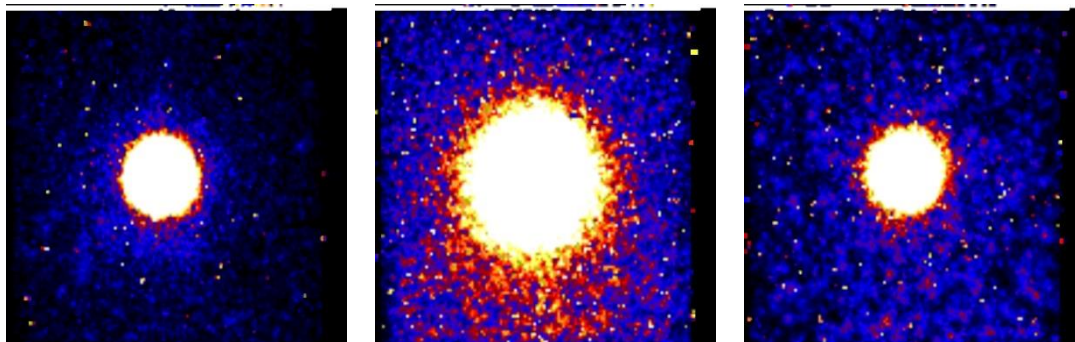
Figure 7.6: Detectability test of (left) $^{99m}$Tc, (middle) $^{111}$In and (right) $^{123}$I point sources performed using the Nebuleye. All images shown using the same image scale.

The geometrical efficiency of the system is proportional to the diameter of the pinhole collimator and this is the reason the 1 mm pinhole was selected for the clinical pre-production prototype camera. For the purpose of comparison further investigation was carried out to show the difference in imaging between using pinhole collimators of 0.5 mm and 1 mm in diameter. As the Nebuleye had only a pinhole collimator with aperture of 1 mm in diameter, the HGC fitted with 0.5 mm pinhole collimator was used to acquire image for comparison purposes. Figure 7.7 shows the mini Williams Phantom images acquired using the SFOV gamma cameras fitted with the different diameter of pinhole collimators. The images showed that with the same acquisition settings, the system spatial resolution of the camera fitted with pinhole collimator of 0.5 mm was significantly higher than that with the 1 mm pinhole where four hot spots could be resolved as shown by the line profiles.
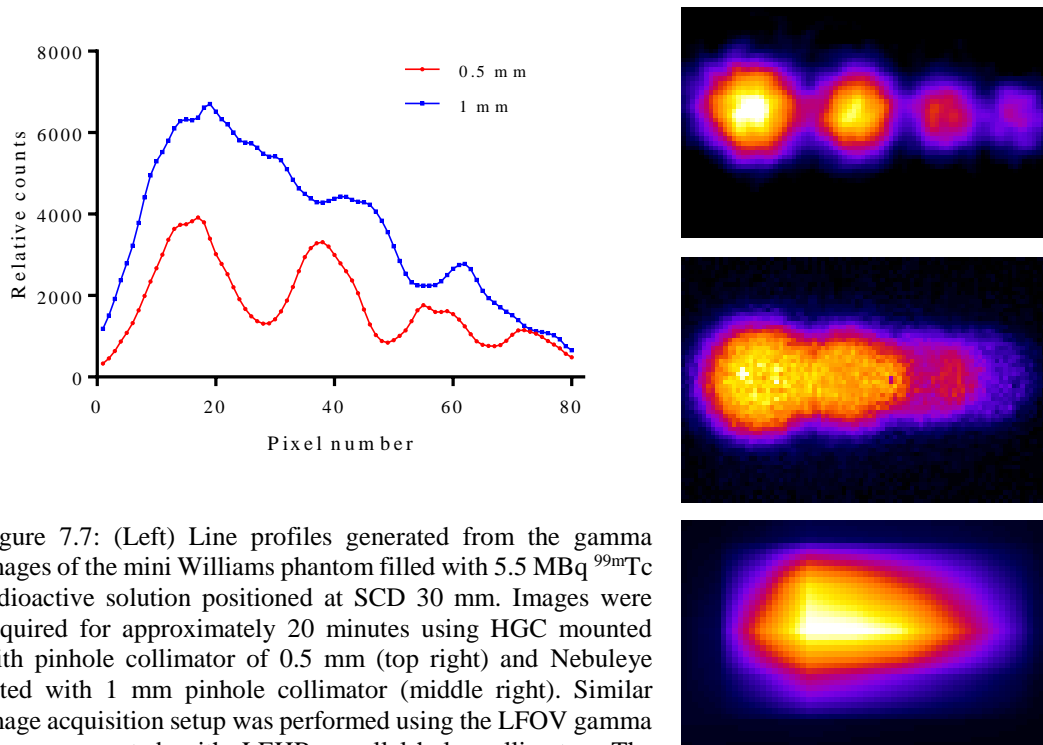
Figure 7.7: (Left) Line profiles generated from the gamma images of the mini Williams phantom filled with 5.5 MBq $^{99m}$Tc radioactive solution positioned at SCD 30 mm. Images were acquired for approximately 20 minutes using HGC mounted with pinhole collimator of 0.5 mm (top right) and Nebuleye fitted with 1 mm pinhole collimator (middle right). Similar image acquisition setup was performed using the LFOV gamma camera mounted with LEHR parallel-hole collimator. The resulted image (bottom right) was cropped to image size identical to the SFOV gamma image.

The phantom images produced by the SFOV gamma cameras and a standard LFOV gamma camera were also compared. Figure 7.7 (bottom right) shows the gamma image acquired using a standard LFOV gamma camera equipped with LEHR collimator. Visually, the spatial resolution of the SFOV gamma camera was superior to the LFOV gamma camera where the hot spots within the mini Williams phantom was not resolved during the same image studies.

### 7.4.2   Indium-111

Indium-111 emits principal gamma rays of 171 and 245 keV. Clinically it is used in radiopharmaceuticals for imaging infection, inflammation and somatostatin receptor imaging and for gastric emptying studies [201]. The amount of activity prescribed for adult clinical studies ranges between $10 - 200$ MBq [200]. Figure 7.6 (middle) shows the gamma image formed from a point source of $^{111}$In solution filled in the mini Williams phantom. A relatively higher noise level was present in the image due to the detection of the higher energy (245 keV) gamma rays and subsequent scattered events. The sensitivity of the camera to $^{111}$In was measured as $5.35 \pm 0.04$ cps/MBq while the resolution was $3.31 \pm 0.04$ mm at SCD 30 mm.

It is widely documented that an increase of SCD results in the degradation of camera geometric efficiency and resolution [14]. This was confirmed by the phantom studies where the Nebuleye camera was used to image mini Williams Phantom placed at SCD of 3, 5 and 8 cm. Figure 7.8 shows the phantom images acquired at different SCDs. With the increase of the SCD, the resolution of the camera decreased where the individual radioactive sources in the respective holes within the phantom merged to become a large bright blob.
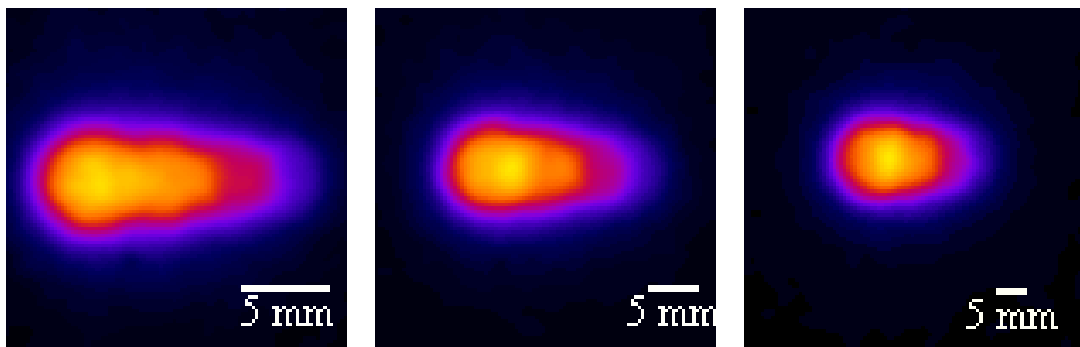


Figure 7.8: Gamma image of the mini Williams Phantom filled with 14.3 MBq ^{111}In radioactive solution placed at SCD of 30 (left), 50 (middle) and 80 mm (right). Images were taken using 1 mm diameter pinhole collimator Nebuleye with acquisition time of 20 minutes. Images were smoothed with a 2.0 pixel Gaussian filter.

### 7.4.3   Iodine-123

Iodine-123 emits gamma rays (159 keV) with the energy relatively similar to that of [99m]Tc. This radionuclide is commonly used for Parkinson's disease imaging (DaTscan) or neuroectodermal tumour imaging (MIBG scintigraphy). Clinical administered activities range between 2 and 400 MBq [200]. Figure 7.6 (right) illustrates the gamma image acquired by the Nebuleye gamma camera and looks similar to the gamma image of [99m]Tc. The sensitivity of the camera to ^{123}I was measured at $2.95 \pm 0.04$ cps/MBq while the resolution was $2.93 \pm 0.05$ mm at SCD 30 mm.

Intrinsic resolution and detection efficiency of gamma cameras depend on the scintillation detector thickness. Thicker crystals result in wider spreading of scintillation light resulting in reduced intrinsic resolution [14]. As the Nebuleye had only a 1.5 mm in thickness CsI(Tl) crystal, it was considered valuable to compare this with the HGC fitted with 0.6 mm thick crystal detector. Mini Williams phantom images captured by the HGC gamma camera revealed that the camera with thinner crystal could

resolve the hot spots better when using the same acquisition settings as shown in Figure 7.9.
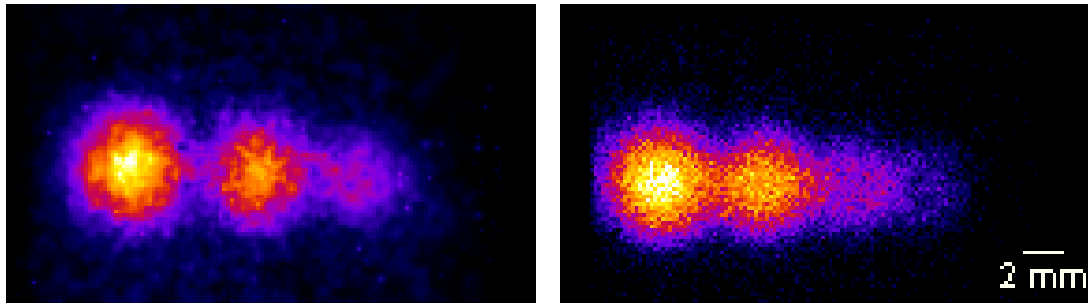


Figure 7.9: Gamma image of the mini Williams phantom filled with ^{123}I radioactive solution placed at SCD 30 mm. Images were taken using HGC equipped with 0.6 mm thick crystal detector (left) and Nebuleye with crystal detector of 1.5 mm in thickness (right). Image acquisition time was approximately 20 minutes.

### 7.4.4 Iodine-125 seeds

Iodine-125 is used as a sealed source seed for permanent radioactive seed implant procedures. It emits relatively low energy gamma rays (35 keV) and for therapy the principle therapeutic action is by Auger-electron emission to treat tumours such as prostate cancer. A more recent application of this source is the radioactive seed localisation technique in breast cancer surgery where an ^{125}I seed with activity ranging between 3 and 8 MBq is implanted within the tumour under ultrasound or radiological control. Figure 7.10 shows the cumulative time series for the images of a seed acquired using the Nebuleye. Visual assessment found that the seed could be detected with an acquisition time within a minute and the bright blob appears clearer with the increase in acquisition time.
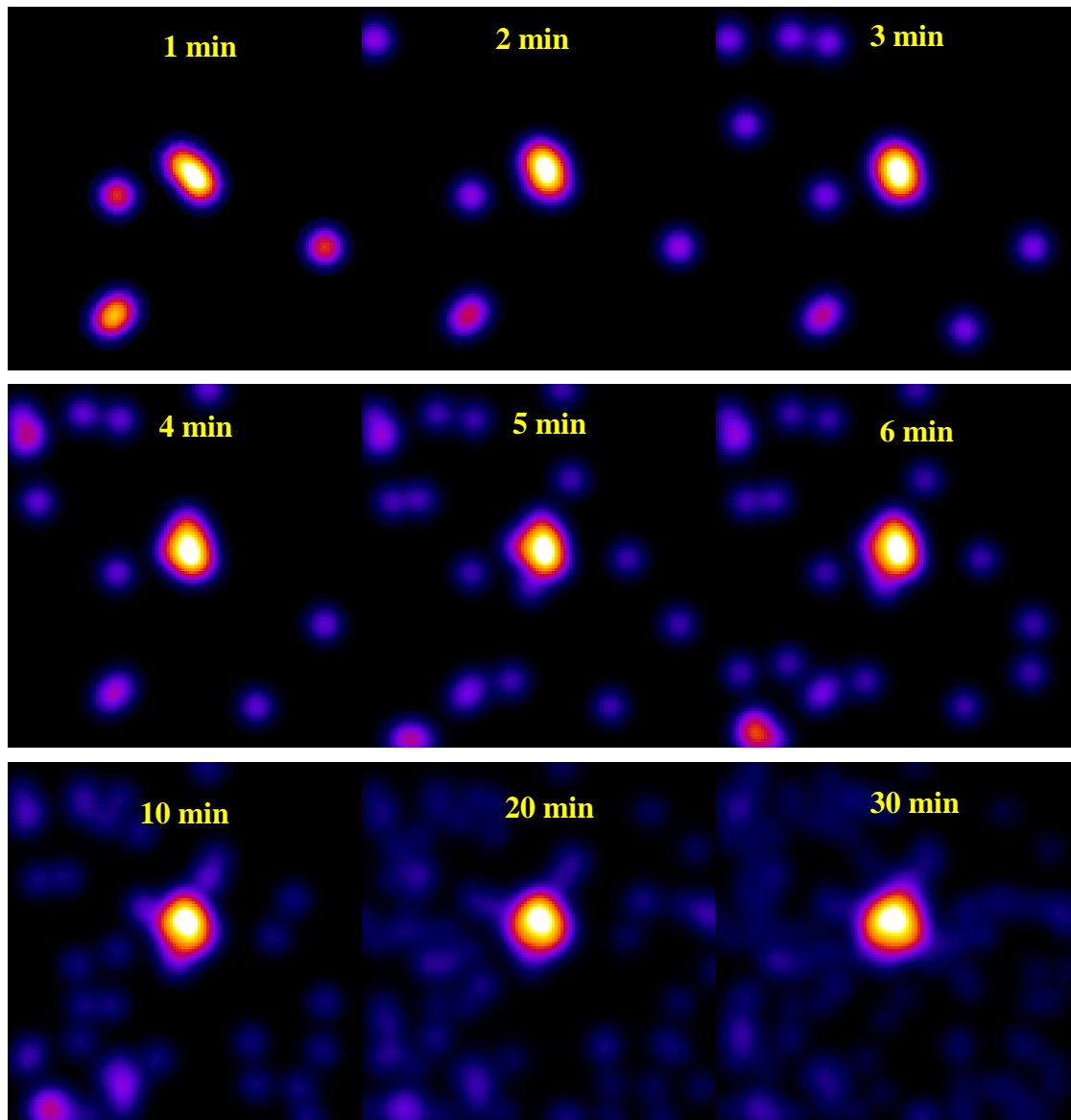
Figure 7.10: Gamma images of the $^{125}$I seed (2.43 MBq) placed at SCD 63 mm, acquired using Nebuleye fitted with 1 mm pinhole collimator. Image acquisition time is indicated on each image. Images were smoothed with a 2.0 pixel Gaussian filter.

### 7.4.5  Selenium-75

Selenium-75 is used as an oral capsule formulation containing Tauroselcholic [$^{75}$Se] acid (SeHCAT) (GE Healthcare, Braunschweig, Germany) and has principal gamma energies of 136 and 265 keV. It is used for measuring bile acid pool loss and in the investigation of bile acid malabsorption [202]. The typical prescribed dose is 0.4 MBq per investigation [200] and the activity retained after 7 days is measured using an uncollimated LFOV gamma camera.

For this investigation the collimated Nebuleye was used to acquire an image of the SeHCAT capsule (~0.35 MBq) placed at SCD 40 mm, using a 38 minute acquisition time. The sensitivity of the camera to $^{75}$Se was measured at $5.69 \pm 0.18$ cps/MBq. Figure 7.11 shows the resulting hybrid image of the SeHCAT capsule. The detected photons may also include the scattered or unwanted radiation that leaked through the camera head shielding due to the higher energy of the gamma rays.
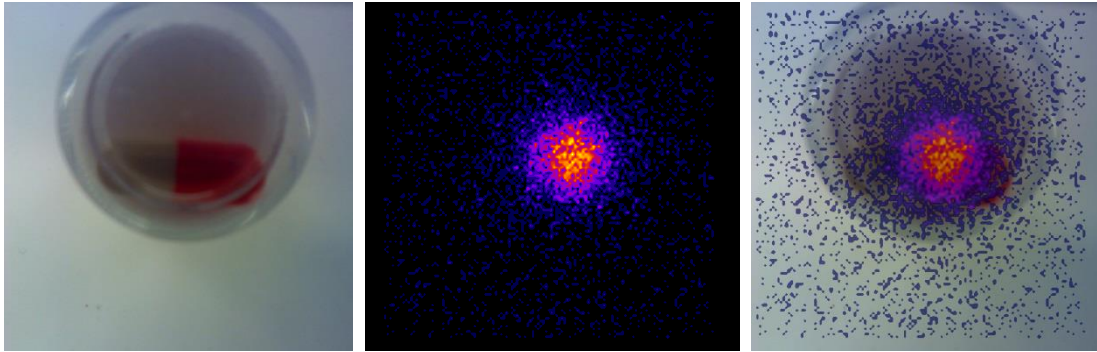


Figure 7.11: (a) Optical, (b) gamma and (c) hybrid images of SeHCAT capsule acquired using Nebuleye positioned at SCD 40 mm.

## 7.5  Summary

The experimental work described in this chapter has provided new and essential information to bridge the gap between laboratory testing and clinical use. It has provided baseline data on user feedback and the imaging consequences on operator motion effects, as well as examining the detectability of a range of radionuclides. In particular the results indicate that users would consider that imaging during surgery should be achieved in the order of 1 minute and user motion limits handheld image acquisition to within 2 minutes.

This is the first time the new pre-commercial device, the Nebuleye has been tested in a clinical environment and provides a better understanding of the camera capabilities for the preclinical imaging described in Chapter 4 and the clinical trial described in Chapter 8.

# Chapter 8

# First Clinical Studies of the SFOV Hybrid Optical Gamma Camera

## 8.1 Introduction

Since the first introduction of the gamma camera in 1958 the basic design and operation of gamma cameras has remained the same over the past 50 years. Recent commercial developments have been based around dual head hybrid systems with integral scanning couches. These systems are bulky and require a dedicated imaging room. The availability of smaller mobile gamma cameras in the 1990s have offered scintigraphic imaging outside of the nuclear medicine department, however, these cameras were still relatively large in size and posed difficulties in close positioning to the organs of interest at the patient bedside or during surgical procedures [203].

As described in Chapter 2, recent technological developments have contributed to the evolution of handheld SFOV gamma cameras which have increased the portability and flexibility of nuclear imaging, creating the possibility of undertaking investigations in the operating theatre, intensive care unit, emergency department or hospital ward [54]. These SFOV gamma cameras may be of value in providing intraoperative imaging where non-imaging gamma probes are currently used [141]. This chapter describes the first clinical results of the use of HGC in the nuclear medicine clinic. The aims of this study were to adopt and evaluate the performance of the prototype HGC for clinical imaging and where possible to undertake the subjective comparison of the images with those from a standard clinical gamma camera. The work in this project was funded by the Science Technology Facilities Council through a joint CLASP Award to the Universities of Nottingham and Leicester.

## 8.2 Methods

### 8.2.1 Hybrid gamma camera

The HGC as described in Section 2.5 was used in this study. For the clinical study the gamma detector was an CsI(Tl) columnar scintillator (either 0.6 mm or 1.5 mm in thickness) (Hamamatsu Photonics UK Ltd., Welwyn Garden City, UK) coupled to an electron-multiplying charge-coupled device (EMCCD) (CCD97 BI, e2v Technologies Ltd., Chelmsford, UK) surrounded by tungsten shielding of 3 mm thickness, to minimise image degradation from scattered photons and background radiation. An interchangeable 6 mm thick tungsten pinhole collimator with a pinhole aperture of either 0.5 mm or 1.0 mm was used for projection of the gamma photons onto the scintillation detector. This gave a nominal field of view (FOV) of approximately $60 \times 60$ mm at a distance of 50 mm from the camera surface.

A thin optical mirror was mounted across the FOV at an angle of 45º to reflect light photons to an optical camera assembly. This provided alignment of the optical images with the same FOV as the gamma camera, allowing fusion of functional and anatomical detail. The weight of the camera head was 1.2 kg. An HP laptop computer (Hewlett-Packard Development Company, Palo Alto, California, USA) was connected to the electronic control unit via a standard USB 2.0 cable and installed with bespoke software (IDL, Exelis Visual Information Solutions, Inc., Boulder, CO, USA) as mentioned in Section 2.5.3. Figure 8.1 shows the assembly of the camera system on a cart based system (ITD GmbH, Johanniskirchen, Germany). The performance of the HGC had been characterised previously as described in Chapter 3 and other publications [105, 204, 205]. Simple quality control check was carried out during the day of the study.
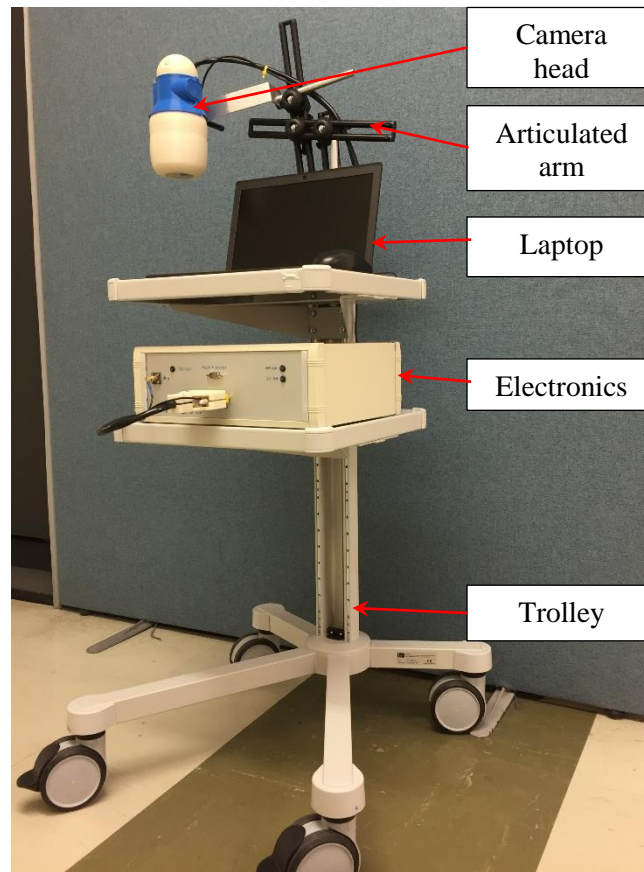
Figure 8.1: A photograph of the HGC mounted on arm and trolley system showing the laptop and electronics interface box.

As part of the assessment of the technology, the HGC went through the regulatory requirements under the special circumstances for medical devices as outlined by the MHRA for clinical research purposes where the device was not intended for subsequent commercialisation. The design and construction of the device had been assessed against the relevant harmonised standards of the Medical Device Directive with the support of the Clinical Engineering Department, NUH NHS Trust. The assessments concluded that the device was compliant with the requirements of BS EN 60601-1:2006 +A12:2014 Medical Electrical Equipment: General requirements for basic safety and essential performance. Subsequently, the approval for use of the device in the Trust was issued by the Chair of the Medical Devices Management Committee at NUH as required by the Trust's Research & Innovation department. This approval was part of the Health Research Authority (HRA) requirements for the clinical trial application.

### 8.2.2 Study design and patients recruitment

This was a non-interventional, non-blinded, single visit study carried out in the nuclear medicine clinic at Queen's Medical Centre, Nottingham University Hospitals NHS Trust. Figure 8.2 summarises the study sequences in this trial. The study was approved by the UK National Research Ethics Committee (Reference Number: 12/EM/0201) and the Research & Innovation Directorate, Nottingham University Hospitals NHS Trust.
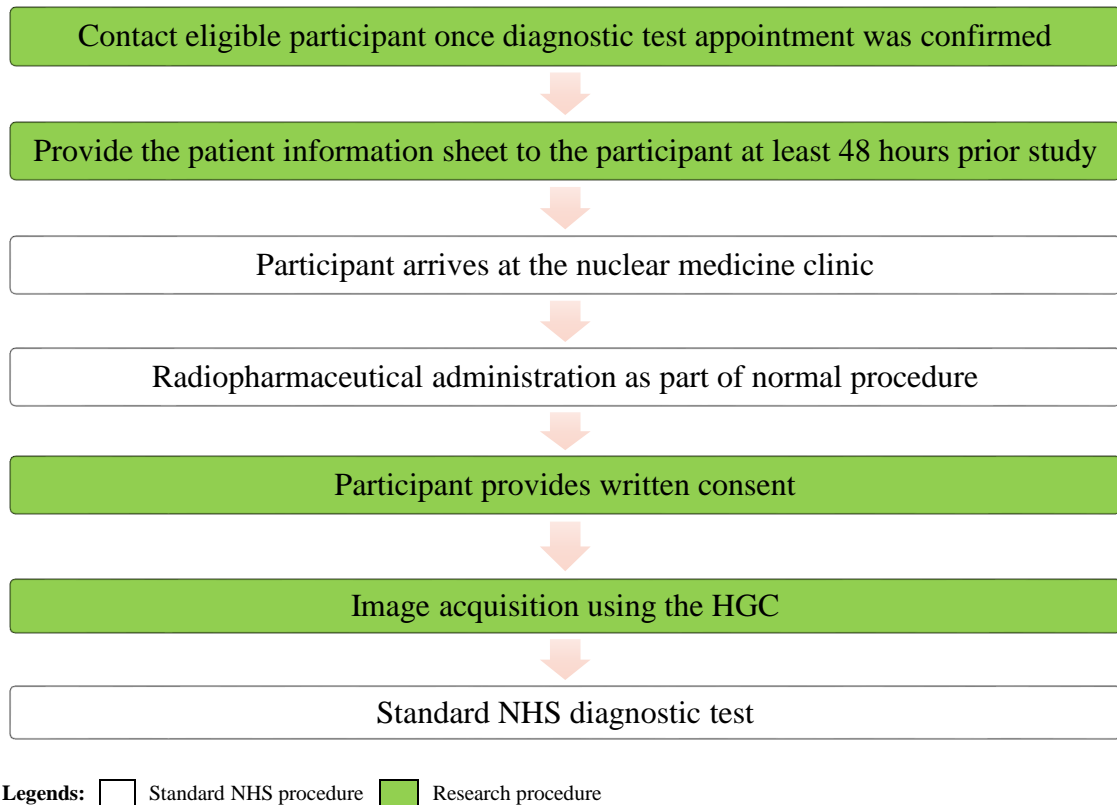


Figure 8.2: Study flow-chart for the clinical trial.

#### 8.2.2.1 Patient selection

Patients who had been referred to the nuclear medicine clinic as part of a standard diagnostic test were invited to take part in this study. An appointment letter was sent through a nuclear medicine clinic to book the standard diagnostic test. Once the diagnostic test appointment was confirmed, the patients were screened for their eligibility by one of the clinical study team. This was done by viewing the clinic on-line appointment system and the patient record. The selection was according the criteria summarised in Table 8.1. Suitable patients were contacted by phone and a brief introduction to the study was given. Prospective participants were asked if they were

interested in participating in this study. If they expressed an interest to participate a copy of the patient information sheet and consent form was sent by mail or e-mail.

Table 8.1: Patient selection criteria for this study.

| **Inclusion criteria** |
|---|
| 1.  Participant must be aged greater than 18 years of age; |
| 2.  Participant must be able to give voluntary informed consent; |
| 3.  Participant must be able to understand the study, willing to co-operate with the study procedures and able to attend the study assessment; |
| 4.  Participant had been administered a radiopharmaceutical as part of a diagnostic test. |
| **Exclusion criteria** |
| 1.  Female participants who were pregnant, lactating or planning pregnancy during the course of the study; |
| 2.  Participants who do not speak or understand English. |

### 8.2.2.2 Informed consent

Patients were given a minimum of 24 hours to carefully consider the participation before formally signing consent at the study site. As this was straight-forward study only requiring a short attendance for imaging the participants were not requested to attend the department to sign consent form before the day of study. On the study day one of the clinical study team met the participant and asked if they were still interested taking part in the study.

A copy of consent form and patient information sheet was provided to the participants. The details of the study were explained by one of the study team. The participants were then given opportunity to ask questions, or to share their concerns. Further explanation was also provided that their participation was entirely voluntary and that their standard treatment would not be influenced by their decision and that they were free to withdraw from the study at any time and for any reason.

Once the participant had agreed and signed to take part in the study, a copy of the form was given to the participant, while another copy was kept by the investigator in the trial master file. A participant study ID number was assigned to maintain participant

anonymity during the study. All study documents were stored securely and only accessible by trial staff and authorised personnel.

### 8.2.3 Imaging

Following administration of the standard diagnostic radiopharmaceutical, the HGC was used to acquire hybrid images of the patient in addition to the routine nuclear medicine imaging procedure. These imaging procedures were performed at a time point when it was convenient for the patient fitting in with the standard diagnostic test schedule in order to minimise unnecessarily interruptions to the normal clinical process.

Each patient participation was approximately 30 minutes and no longer than two hours. Prior to the image acquisition, the participant was asked to either sit or lie down, depending on the type of the procedure. The HGC was either held by the operator or mounted on fixed arm during the imaging. Figure 8.3 shows an example photograph of the HGC use during patient imaging. The imaging settings such as SCD, camera configuration and time of imaging were recorded in the case report form. Image acquisition and processing was undertaken using bespoke software as described in Section 2.5.3 and 2.5.4. Image post-processing and display was carried out using ImageJ 1.47v (National Institute of Health, US) to remove outlier noise, apply the Gaussian smoothing filter and to adjust threshold and saturation levels to improve image display.



Figure 8.3: Photograph of the head of the HGC which was mounted on an articulated arm during imaging of the patient neck area.

All acquired gamma and optical images were anonymised and stored in a University password protected computer. The hybrid planar images of the patient were presented in a fused optical-gamma display. The subjective visual comparison was performed where possible by nuclear medicine professionals, who were experienced in observing scintigraphic images. Standard images produced by a SPECT-CT either Philips Brightview XCT (Philips Healthcare, Milpitas, CA, USA) or General Electric Discovery NM/CT 67 (GE Healthcare, Waukesha, VI, USA) were available for comparison. As this was a pilot study, therefore no statistical test was performed at this stage.

## 8.3  Results

Imaging studies were carried out in 24 patients (age range between 30 and 83 years, mean: 58.6 years) who underwent routine imaging procedures with $^{99m}$Tc and $^{123}$I. These radionuclides were being low energy gamma emitters suitable for use with the HGC. Table 8.2 provides a summary of the number of participants, the administered radiopharmaceutical and the average acquisition time for each procedure. The administration of the radiopharmaceutical was based on the Administration of Radioactive Substances Advisory Committee (ARSAC) guidance notes on good clinical practice for nuclear medicine in the UK [200].

Table 8.2: Summary of the clinical cases, administered radionuclides and activities (MBq) and average imaging time, taken from [45].

| Procedure | Radionuclide | Administrated activity (MBq) | Mean acquisition time ±SD (s) | Number of participants |
|---|---|---|---|---|
| Lymphatic scan | $^{99m}$Tc | 10-20 per injection | 349 ± 105 | 10 (4 excluded) |
| DaTscan | $^{123}$I | 185 | 893 ± 519 | 2 |
| Lacrimal drainage scan | $^{99m}$Tc | 1 per eye | 263 ± 87 | 3 (1 excluded) |
| Thyroid scintigraphy | $^{99m}$Tc | 75-78 | 127 ± 63 | 2 |
| | $^{123}$I | 18.5-20 | 297 ± 98 | 2 |
| Bone scan | $^{99m}$Tc | 600-627 | 266 ± 55 | 3 |
| Leucocyte study | $^{99m}$Tc | 100-225 | 345 ± 200 | 2 (1 excluded) |
| Total | | | | 24 |

SD-Standard deviation

In this pilot study, the patients were chosen based on the criteria where focal uptake of radiotracer within the body may be expected or the SFOV imaging was considered to be of interest or have potential clinical value. These included patients undergoing bone, thyroid, lacrimal drainage and lymphatic imaging as well as DaTscan studies. The resulted images were subjectively assessed. Patient imaging details are given in Table 8.3. Six patients were not included during the final evaluation due to missing information caused by camera malfunction or data errors. There were no safety issues reported during the period of the clinical studies.

Table 8.3: Details of the clinical studies undertaken using the HGC.

| Subject Number | Procedure | Radionuclide | Camera configurations | | Subjective assessment of image quality |
|---|---|---|---|---|---|
| | | | Pinhole diameter (mm) | Crystal thickness (mm) | |
| 001 | LY | $^{99m}$Tc | 0.5 | 0.6 | Good |
| 002 | D | $^{123}$I | 0.5 | 0.6 | Poor |
| 003 | LA | $^{99m}$Tc | 0.5 | 0.6 | NA[a] |
| 004 | LY | $^{99m}$Tc | 0.5 | 0.6 | Good |
| 005 | LY | $^{99m}$Tc | 0.5 | 0.6 | NA[a] |
| 006 | D | $^{123}$I | 0.5 | 0.6 | Poor |
| 007 | LY | $^{99m}$Tc | 0.5 | 0.6 | NA[a] |
| 008 | T | $^{99m}$Tc | 0.5 | 0.6 | Poor |
| 009 | LA | $^{99m}$Tc | 0.5 | 0.6 | Good |
| 010 | T | $^{99m}$Tc | 0.5 | 0.6 | Poor |
| 011 | LA | $^{99m}$Tc | 1.0 | 0.6 | Good |
| 012 | B | $^{99m}$Tc | 1.0 | 0.6 | Poor |
| 013 | B | $^{99m}$Tc | 1.0 | 0.6 | Poor |
| 014 | T | $^{123}$I | 1.0 | 0.6 | Good |
| 015 | LE | $^{99m}$Tc | 1.0 | 1.5 | NA[a] |
| 016 | LE | $^{99m}$Tc | 1.0 | 1.5 | Poor |
| 017 | LY | $^{99m}$Tc | 1.0 | 1.5 | Good |
| 018 | LY | $^{99m}$Tc | 1.0 | 1.5 | Good |
| 019 | LY | $^{99m}$Tc | 1.0 | 1.5 | Good |
| 020 | B | $^{99m}$Tc | 1.0 | 1.5 | Poor |
| 021 | LY | $^{99m}$Tc | 1.0 | 1.5 | Good |
| 022 | T | $^{123}$I | 1.0 | 1.5 | Good |

| Subject Number | Procedure | Radionuclide | Camera configurations | | Subjective assessment of image quality |
|---|---|---|---|---|---|
| | | | Pinhole diameter (mm) | Crystal thickness (mm) | |
| 023 | LY | $^{99m}$Tc | 1.0 | 1.5 | NA[a] |
| 024 | LY | $^{99m}$Tc | 1.0 | 1.5 | NA[a] |

[a]Study terminated due to camera error; NA: Not available; LY: Lymphatic scan; D: DaTscan; LA: Lacrimal drainage scan; T: Thyroid scintigraphy; B: Bone scan; LE: Leucocyte study.

### 8.3.1 DaTscan

During the early stage of the clinical trial, investigations were aimed at high resolution imaging using a 0.6 mm thick crystal and 0.5 mm diameter pinhole collimator. As a trade-off, this resulted in reducing the camera sensitivity, therefore prolonging the acquisition times to over 5 minutes. Two patients undergoing $^{123}$I-ioflupane DaTscan investigations were imaged using this camera configuration. An example of gamma image acquired using HGC shows scattered bright spots within the FOV with no specific photon distributions as compared to a standard DaTscan image (Figure 8.4). Localisation of DaTscan uptake in the striatum was not visualised in these exploratory investigations, thus there was no further investigation on this group of patients.
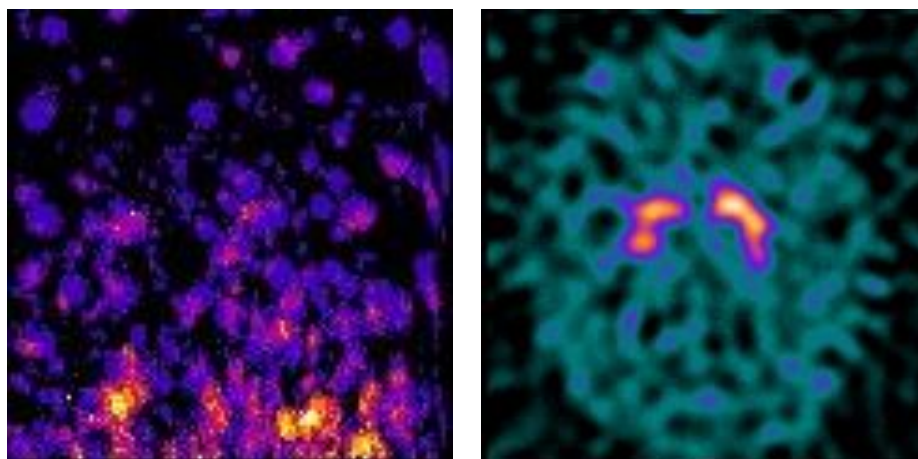


Figure 8.4: (Left) Example of planar image acquired using the HGC positioned at SCD of 8 cm on top of the head (vertex view) of patient 006, 1 hour post-administration of 185 MBq $^{123}$I-Ioflupane, with 100 s acquisition time. (Right) Axial plane (slice 19) of the reconstructed SPECT image of the same patient acquired using SPECT-CT camera system 2.5 hours following administration with 1800 s acquisition time (30 s per projection). The image shows high striatal uptake of the dopamine transporter agent, $^{123}$I-Ioflupane relative to cortex.

### 8.3.2 Thyroid scintigraphy

Thyroid scintigraphy was undertaken in four patients, two who had received $^{99m}$Tc-pertechnetate and two who had received $^{123}$I-sodium iodide (NaI). The initial investigations were using a 0.6 mm thick crystal and 0.5 mm diameter pinhole collimator camera configuration. Figure 8.5 shows an example of hybrid optical-gamma image of thyroid scintigraphy acquired using HGC. No focal uptake within the neck region was observed due to the sensitivity limitations of the camera. The optical images acquired during the start and end of the image acquisition showing significant patient movement which deteriorated the quality of the gamma image formed over the scanning time.
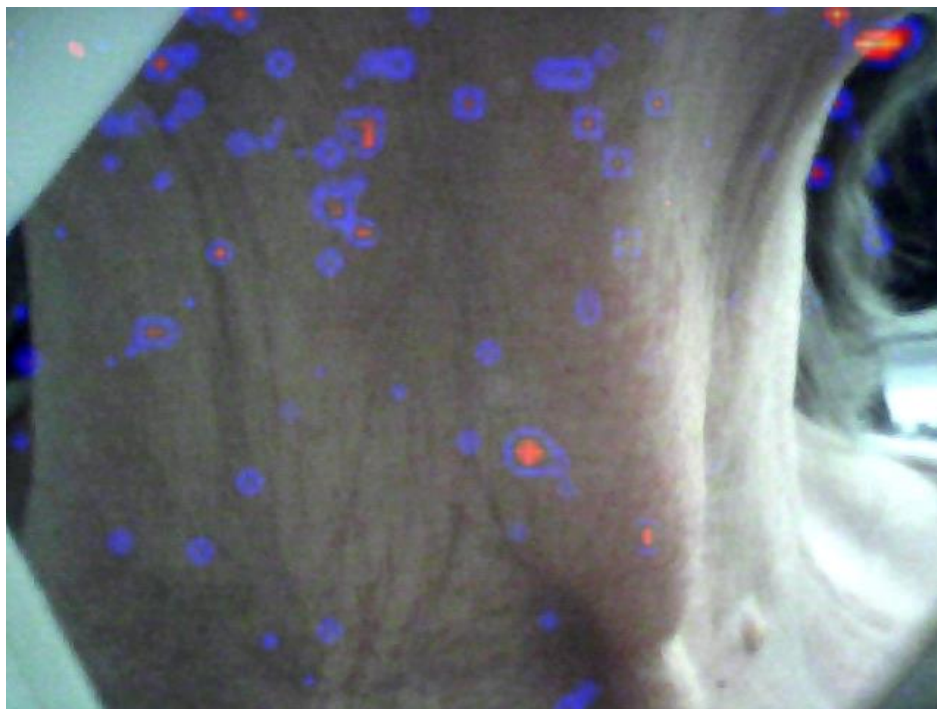


Figure 8.5: Fused optical-gamma image of patient 008 administered with 78 MBq of $^{99m}$Tc-pertechnetate, with an imaging time of 200 s. The number of detected photons was low due to the low sensitivity camera configuration and the camera position (~10 cm away from patient's neck).

Increasing the diameter of the pinhole collimator to 1 mm improved the camera sensitivity. Figure 8.6 shows an example of thyroid imaging where radionuclide uptake can be seen in the right lobe of the thyroid. This uptake was confirmed from the planar gamma image produced by a standard LFOV gamma camera with similar acquisition time. Further camera sensitivity improvement were made with the increasing of the crystal thickness to 1.5 mm. Gamma images were undertaken with 1.5-mm-thick

crystal and 1 mm diameter pinhole collimator camera configuration. Figure 8.7 illustrates an example of thyroid imaging with the presentation of $^{123}$I uptake in both lobes of the thyroid.
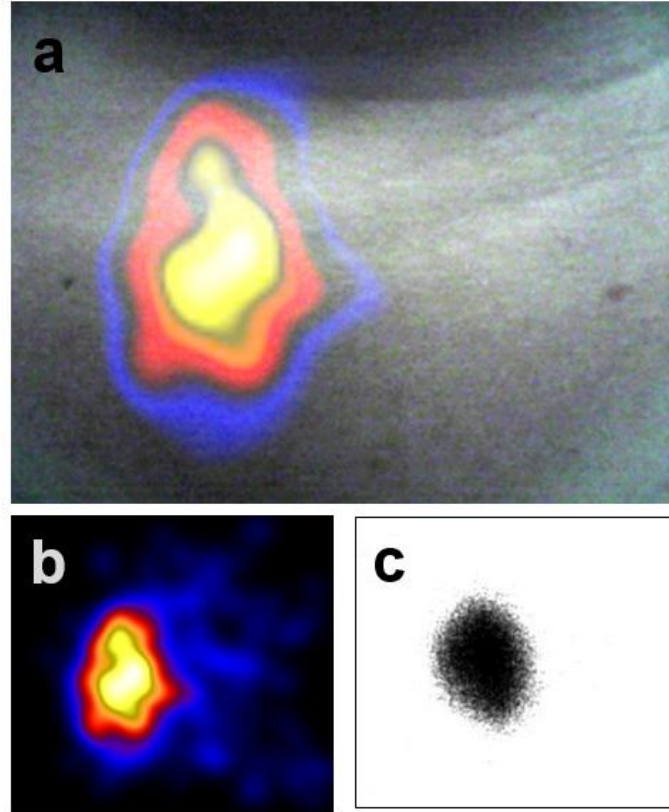


Figure 8.6: (a) Hybrid and (b) gamma image of thyroid scan in patient 014 acquired by HGC 110 minutes following administration of 20 MBq $^{123}$I-NaI, positioned at SCD of 10 cm. (c) LFOV planar gamma image of the same patient. Both gamma images were acquired with an acquisition time of 300 s.

The resulting gamma image provides the functional uptake, while the hybrid image showing the shape, size and position of the thyroid gland with respect to the skin surface. With the increase of nominal FOV (from $112 \times 112$ to $184 \times 184$ mm) at further SCD setting (23 cm), the thyroid image and other anatomical landmarks (e.g. sternal notch) can be clearly seen in the neck region with the aid of the optical image as shown in Figure 8.7 (d). In contrast, the increase of SCD from 14 cm to 23 cm resulted in a decrease of collimator efficiency by 63 % (calculation based on Equation 3.6). This caused a reduction in the photon detection and loss of detail in the gamma image displayed in Figure 8.7 (d). When assessing the images the effects of different image acquisition parameter (SCD, acquisition time) and level of administered activity should be taken into consideration.
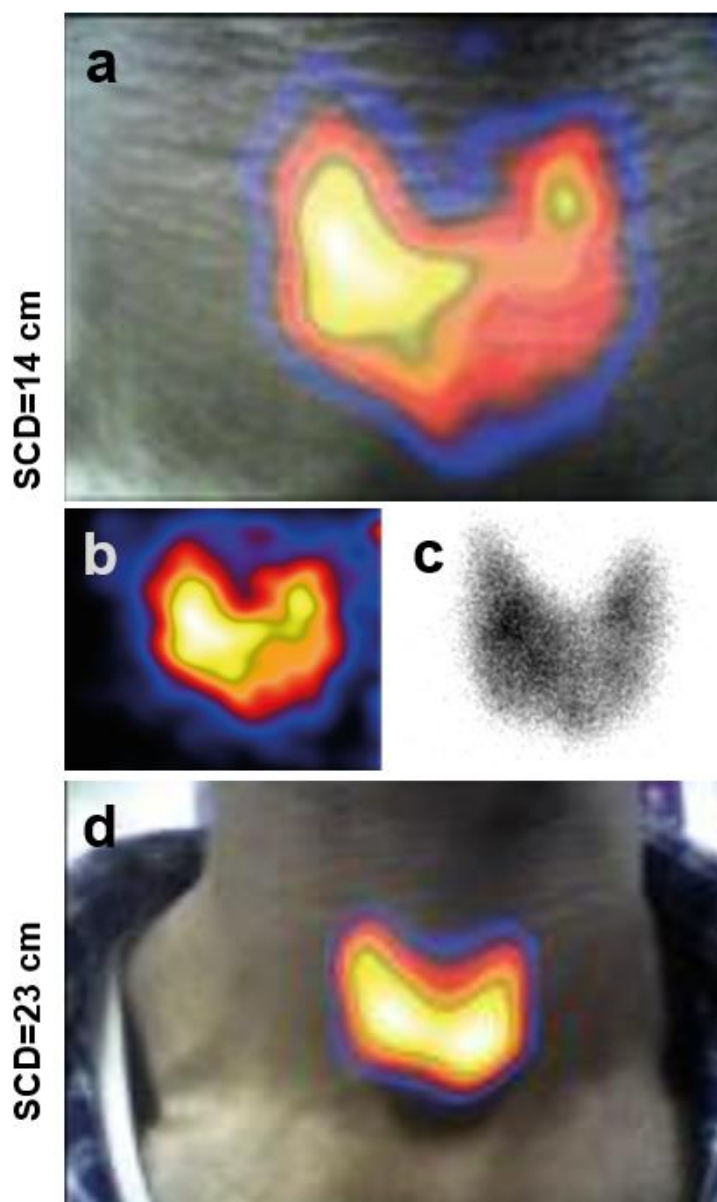
Figure 8.7: Example thyroid scintigraphy in patient 022, acquired by HGC at 149 minutes post-administration of 18.5 MBq $^{123}$I-NaI, positioned at SCD of 14 cm for a 300 s acquisition time: (a) hybrid (b) gamma image (c) LFOV planar gamma image. (d) Hybrid image of the same patient acquired by HGC positioned at an SCD of 23 cm, 142 minutes post-administration of the radiotracer.

Thyroid scintigraphy demonstrates the relative functional activity of the thyroid tissues. The regional abnormality of the organ can be determined by investigating the variation of radiopharmaceutical uptake within the thyroid gland. Clinically further assessments are necessary to confirm the involvement of a thyroid nodule by palpation and carrying out relevant correlation or with the aid of ultrasonography [206]. Example thyroid images taken with the HGC shown in Figure 8.6 (a) and Figure 8.7 (a) illustrate variable regional uptake in two of the patients investigated in this study.

### 8.3.3 Lacrimal drainage scintigraphy

For lacrimal drainage scan, investigations were undertaken using HGC with 0.6-mm thick crystal. Investigation was initiated with the HGC mounted with 0.5 mm pinhole collimator. The hybrid images shown in Figure 8.8 provide clear visualisation of the radiotracer distribution ($^{99m}$Tc-DTPA) with respect to surface anatomy. These images provided good spatial information for identification of regional flow and assisted in the identification of clearance via the nasolacrimal duct. In comparison with the scintigraphic image of the same patient (Figure 8.8 (d)) acquired using a LFOV gamma camera, the distributions of radiopharmaceutical as shown in Figure 8.8(a) are different, due to the lacrimal clearance at different time point.
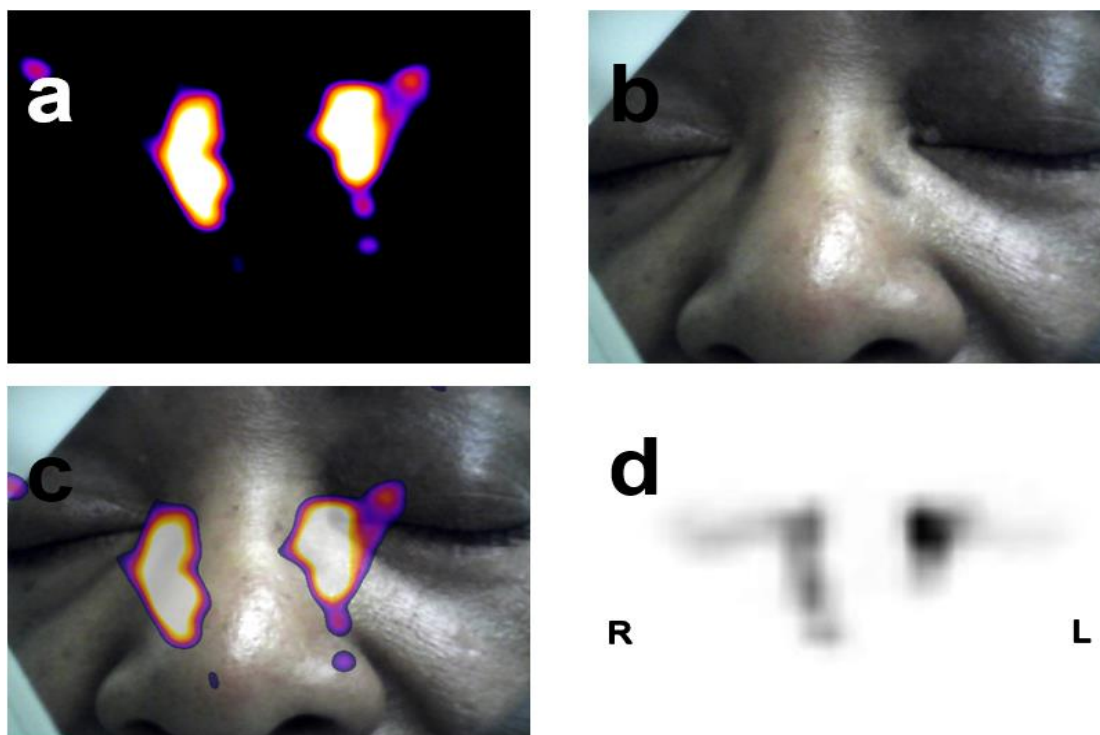


Figure 8.8: The (a) gamma (b) optical (c) hybrid images showing activity distribution in the right and left eyes and nasolacrimal duct in patient 009, acquired 50 minutes following administration of 1 MBq $^{99m}$Tc-DTPA to the surface of each eye. The gamma image was acquired by HGC positioned 10 cm away from the source, with 200 s acquisition time. Image (d) is the anterior planar image produced by a standard LFOV gamma camera recorded at 25 minutes after administration.

Due to the patient movement during image acquisition, a head support and chin rest device was used to minimise the effect while maintaining the SCD constantly throughout the procedure. Figure 8.9 shows another example of the lacrimal drainage image acquired using HGC mounted with 1 mm pinhole collimator. The source-to-

camera distance was 7 cm which gave a nominal FOV of $76 \times 76$ mm, hence the images of the right and left eyes were acquired in a separate acquisition.
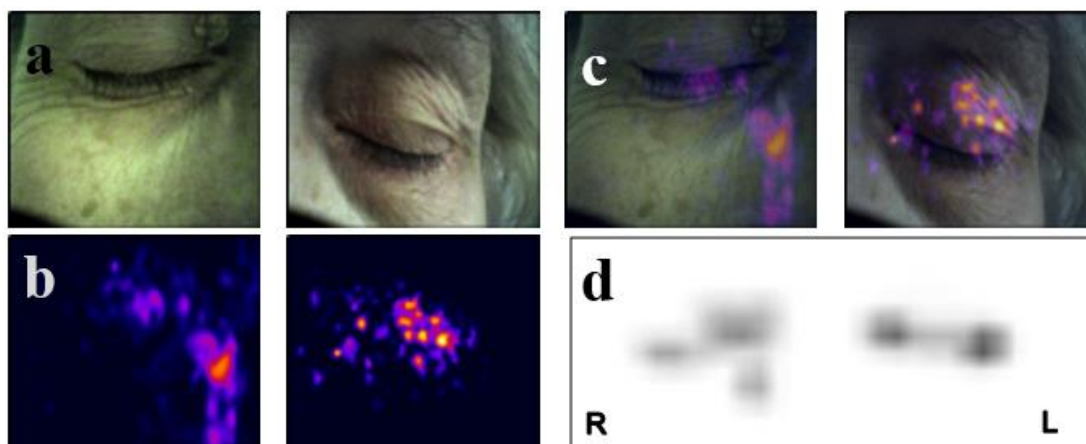


Figure 8.9: The (a) optical (b) gamma (c) hybrid images showing activity distribution in the right and left eyes and nasolacrimal duct in patient 011, acquired 90 min following administration of 1 MBq $^{99m}$Tc-DTPA to the surface of each eye. The gamma image was acquired by HGC positioned at 7 cm from the source, with 300 s acquisition time. Image (d) is the anterior planar image produced by a standard LFOV gamma camera recorded at 20 min after administration.

### 8.3.4   Lymphatic imaging

Six lymphoscintigram investigations in patients with oedema were included in this study. The HGC was positioned at a suitable distance (SCD ranged between 8 and 25 cm) in order to acquire image of the designated FOV while maintaining the camera sensitivity and resolution. Figure 8.10 illustrates an example of the gamma images generated by LFOV gamma camera (a) and HGC at specific regions such as left inguinal (b) and injection sites (c). Whilst it was difficult to track the full extent of clearance along the lymphatic vessels, the hybrid image (d) of the injection site indicated that the camera can be used to show focal uptake in relation to surface anatomy.
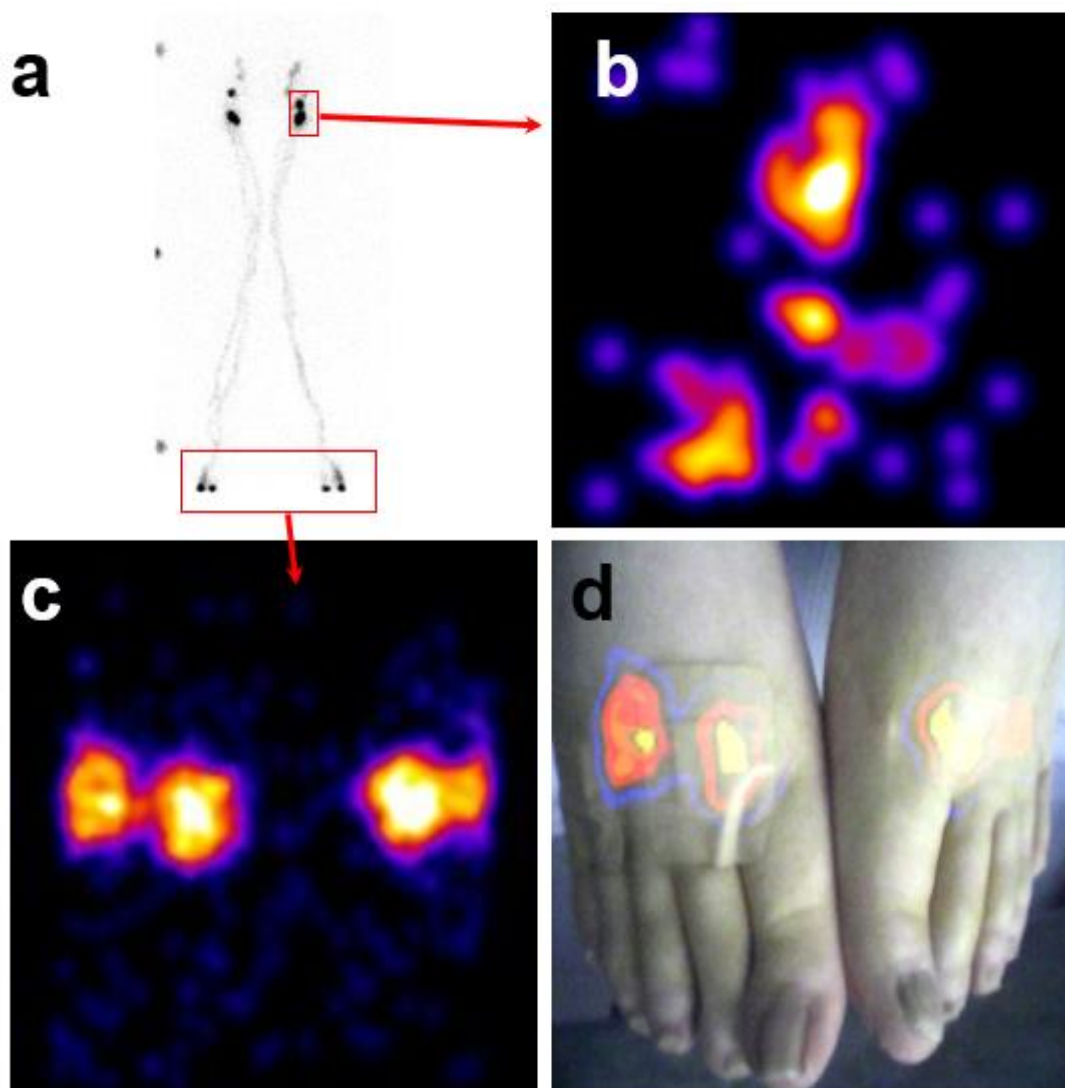
Figure 8.10: Example of the gamma and hybrid images acquired by HGC (1 mm pinhole collimator) in patient administered with 12 MBq of $^{99m}$Tc-nanocolloid at each injection site (two injections on each foot) undergoing lymphoscintigraphic imaging. Image (a) is an anterior planar image of lower extremities, produced by a standard LFOV gamma camera, 20 minutes following administration with a 17 minutes acquisition time showing focal uptake at the injection site and the inguinal region bilaterally with high activity on the left and right site. Image (b) is the gamma image acquired by HGC on the left inguinal region with 5 minutes acquisition time. Gamma image of the feet (c) was acquired by HGC positioned at a distance of 21 cm with 5 minutes imaging time, subsequently superimposed with the optical image (d).

### 8.3.5    Bone and labelled Leucocyte scintigraphy

For patients undergoing bone and leucocytes investigations, the imaging was focussed on regional scan instead of whole body scan. Whilst uptake of the scanning agent was visible in those regions of interest, these did not produce any dramatic results due to the lack of focal uptake at these sites in the patients studied. Figure 8.11 shows an example of bone scintigraphy undertaken with 1.5-mm-thick crystal and 1 mm diameter pinhole collimator HGC. Another example of regional bone scan showing radiotracer uptake at

patient's thumb acquired using HGC with 0.6 mm-thick crystal and 1 mm diameter pinhole (Figure 8.12).
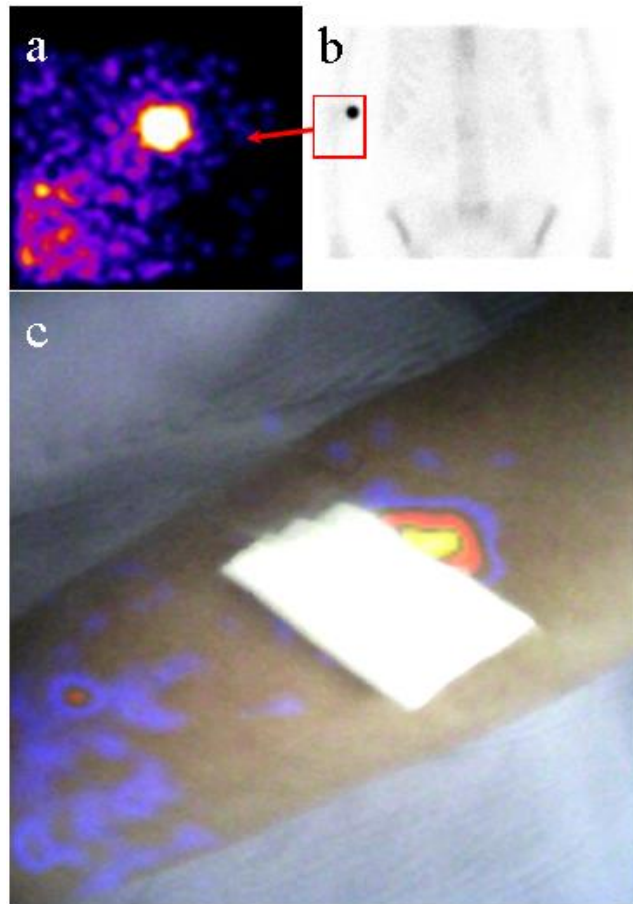


Figure 8.11: (a) Example of a gamma image of the injection site at patient's right arm acquired by HGC (1 mm pinhole collimator, SCD 27.5 cm, 250 s imaging time) of patient 020 undergoing bone scan. (b) Planar image of bone within abdominal region of the same patient acquired using the LFOV gamma camera. (c) Fused gamma image (a) and the optical image showing the injection site and regional radiotracer uptakes within the right elbow and forearm regions of the patient.
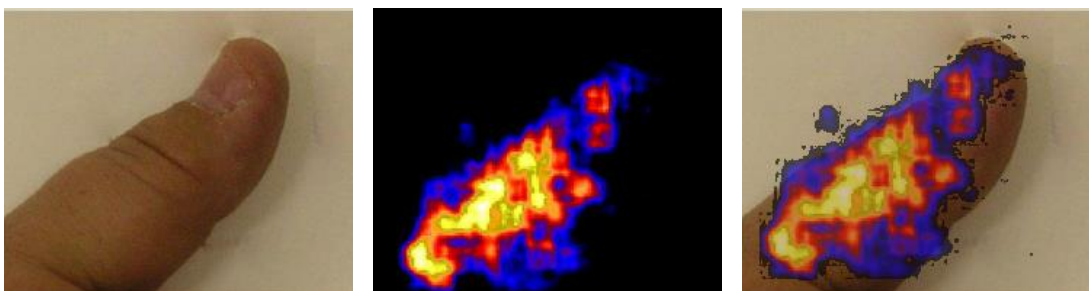


Figure 8.12: (a) Optical, (b) gamma and (c) hybrid images of right thumb of patient underwent bone scintigraphy. Images were undertaken with HGC positioned 45 mm away from the source, 3 hours following the administration of 600 MBq $^{99m}$Tc-hydroxymethylene diphosphate (HDP). (Image provided by Alan C. Perkins)

## 8.4 Discussion

This study has shown novel results of patient imaging using the HGC. It is believed that these are the first results of the use of a hybrid optical-gamma camera in a nuclear medicine clinic. At the time of writing there were no similar studies being carried out by other hybrid SFOV gamma cameras. Based on the literature search, most of the clinical applications of SFOV gamma camera have been reported were in radioguided surgery such as sentinel node localisation for breast [34, 47, 68, 207-209], melanoma [58, 210, 211], penile [63] as well as head and neck tumours [67, 209], radioguided occult lesion localisation [158], radioactive seed localisation [165] and primary hyperthyroidism [66, 212].

During gamma imaging, for a given SCD, crystal thickness or diameter of pinhole collimator, there is also a trade-off between sensitivity and resolution. During the initial stage of the camera development, the HGC was designed as a high spatial resolution imaging device [43]. This has limited the clinical performance of the camera until further improvements have been made to the camera head by increasing the crystal thickness and pinhole diameter. Increasing the thickness of the scintillator to 1.5 mm and the diameter of the pinhole collimator to 1 mm improved the camera sensitivity. This allowed the images to be recorded within 5 minutes.

This study provides the assessment of the imaging performance to determine the most appropriate areas for future clinical use. The initial studies showed that the SFOV gamma camera system was well suited to small organ imaging including thyroid and lacrimal drainage studies, where the radiopharmaceutical uptake could be clearly seen corresponding to the patient surface anatomy. The gamma images acquired by the HGC in patients undergoing bone and leucocyte scintigraphy were poor in quality caused by higher background noise in the acquired images. This may be resulted by insufficient detector shielding as discussed in Section 3.2.9 allowing the gamma-rays emitted from radiopharmaceutical distribution throughout the patient to be detected.

DaTscan studies were included as the performance of HGC in clinical imaging of ^{123}I source was particularly interesting. In previous publications, one study has reported that focal uptake might be visualised using planar imaging [213]. However, the results

obtained in this study have showed that the vertex planar images were not of diagnostic quality, which was due to the low sensitivity of the 0.5 mm pinhole collimator and 0.6 mm crystal thickness combination. Further investigations may be considered with the larger pinhole-crystal combination.

It is worth noting that the distributions of radiopharmaceutical at different time points within a patient will vary. As the study design aimed to minimise interruption to the routine imaging procedure, image acquisitions undertaken by HGC took place between the radiotracer administration and routine imaging times. This has posed a challenge in comparing the gamma images produced by the LFOV gamma camera and HGC as these images were acquired at different time points following administration of radiopharmaceutical. The differences may be minimised by minimising the gap between the imaging times for both imaging modalities. Guidance on the optimal imaging times was taken from the clinical guidelines published by international scientific and professional bodies as tabulated in Table 8.4. For example, the best imaging time for a DaTscan is quoted as between 3 and 6 hours following administration of the radiotracer [214], during which time the ratio of striatal to occipital $^{123}$I-ioflupane binding is stable.

Table 8.4: Recommended image acquisition duration and imaging time point.

| Procedure | Radionuclide | Duration of image acquisition (s) | Recommended post-injection imaging time |
|---|---|---|---|
| Lymphatic scan | $^{99m}$Tc | 600* | Immediately, 45 mins & 3 hours [215] |
| DaTscan | $^{123}$I | 1800 | 3-6 hours [214] |
| Lacrimal drainage scan | $^{99m}$Tc | 60 | Immediately [216] |
| Thyroid scintigraphy | $^{99m}$Tc | 300 | 15-30 mins [206] |
| | $^{123}$I | 600 | 3-24 hours |
| Bone scan | $^{99m}$Tc | 120-600 | 1 mins & 2 hours [217] |

| | | | |
|---|---|---|---|
| Leucocyte study | $^{99m}$Tc | 300-600 | 30 mins & 4 hours**[218] |

*Based on the scanning time of 10 cm/min and assumption of target length of 100 cm.
**Referred to diagnosis of abdominal abscess for adult patient.

It is believed that the combination of an optical camera with a gamma camera will have a number of benefits for small organ imaging and would be particularly suitable for intraoperative and interventional procedures. The optical imaging provides details of the patient's anatomical landmarks, while complement the physiological information as provided by the high resolution gamma imaging. This could lead to the use as a decisive tool in surgery, apparently for sentinel lymph node localisation and non-palpable breast tumour localisation using $^{125}$I seed and possibly the localisation of parathyroid glands and the detection of osteoid osteoma, in particular for cases where the injection site is situated adjacent to the radiotracer uptake. In addition, a handheld system may be used in surgical procedures in conjunction or as a replacement for a gamma probe where images can be obtained for inclusion in case notes, clinical audit and for medico-legal purposes.

## 8.5  Summary

This clinical study has demonstrated the feasibility and capability of HGC in clinical hybrid optical-gamma imaging in patients administered with $^{99m}$Tc and $^{123}$I labelled radiopharmaceuticals. The use of the hybrid imaging system has raised new possibilities for small organ imaging, where the localisation of radiopharmaceutical uptake can be presented in an anatomical context using superimposed optical imaging. The compact nature of the hybrid system offers the potential for bedside investigations and will be well suited for intraoperative and interventional imaging. This study has provided initial information that will be used as part of the process of tailoring this new technology for specific clinical applications.

# Chapter 9

# Discussion, Future Work and Conclusions

## 9.1 General discussions

The clinical speciality of nuclear medicine has benefitted from the continued development of imaging systems and radiopharmaceuticals. This thesis has examined the capabilities and the use of a new generation of SFOV gamma cameras, which is hoped will continue to extend the role of nuclear techniques for the benefit of patients. Specifically, the work has demonstrated the evolution and translation of a novel laboratory prototype hybrid optical-gamma camera to a stage where it has become a medical device with genuine potential for clinical applications.

The SFOV gamma camera utilised an EMCCD originating from photon detector applications in space research, coupled to a columnar-shaped CsI(Tl) crystal and a pinhole collimator to form the imaging detector. The gamma camera was co-aligned with an optical camera system, offering the ability for high resolution real time hybrid optical-gamma imaging. In practice the true ability of such a system can only be assessed by simulation and testing with phantoms, preclinical models and by clinical use.

The characterisation and image assessment work carried out in this thesis has showed the hybrid optical gamma camera was reliable for use in the laboratory and the clinic, even after shipping to the Netherlands for preclinical imaging. The work has demonstrated its use with a range of imaging radionuclides commonly used in diagnostic nuclear medicine procedures such as $^{99m}$Tc, $^{123}$I, $^{111}$In and the ability to detect $^{125}$I which has been shown to be of future interest for the localisation of occult breast lesions.

Part of the camera characterisation work was adapted from the testing scheme developed by Bugby *et al.* [105] and this was implemented on the pre-production camera system. Further characterisation work was proposed and successfully tested on the camera which included system uniformity, system sensitivity, detector head shielding leakage, optical-gamma image alignment and optical image quality. This work has been crucial for the objective assessment of the pre-production prototype Nebuleye camera and to compare its performance with the HGC and other SFOV gamma cameras such as the Crystalcam [71], which have been introduced for medical imaging.

In Chapter 4 preclinical work was undertaken using the camera to assess the imaging performance in animal studies, in this case to acquire images of mice administered with a newly developed dual modality probe. This was part of the camera development in order to expand the applications to preclinical imaging and has formed a basis for a future development to equip the camera system for near-infrared fluorescence imaging.

The use of SFOV gamma cameras in surgery is expanding rapidly and is taking nuclear medicine imaging procedures out of the traditional department setting. Ultimately the utility of bedside imaging and radioguided surgery depends upon the specificity of the radiopharmaceuticals that are available. Further development of the radiotracers coupled with the technological advances in cameras design will expand the range of procedures undertaken. The use of hybrid gamma cameras combining optical and luminescent/fluorescence imaging with gamma imaging will further expand the range of surgical applications undertaken in future.

In light of this, preparatory work was undertaken to bring the camera system into a surgical department as described in Chapters 6 and 7. Phantom simulations were developed to assess the capabilities of the camera for intraoperative imaging, specifically for SLNB in breast cancer surgery. Systematic camera tests were performed to examine the source detectability in difficult clinical scenarios such as deep seated nodes situated close to high activity at the injection site. This work suggested that the use of SFOV gamma cameras may complement the existing sentinel lymph node

localisation technique using non-imaging gamma probes. Other potential intraoperative imaging applications may include primary hyperparathyroidism, ectopic gland localisation and $^{125}$I radioactive seed localisation. Furthermore the gamma, optical and hybrid images produced may be used for inclusion in patient notes, clinical audit and for medico-legal purposes.

With the current camera technology design, there were some limitations that have been identified. The system sensitivity of the HGC fitted with a 1 mm diameter pinhole collimator (6.6 cps/MBq at SCD 50 mm) was extremely low in comparison with standard LFOV clinical gamma camera (125 cps/MBq, BrightviewX, Philips Healthcare, Milpitas, CA, USA). The relatively low sensitivity of the SFOV gamma camera was due to low detection efficiency and resulted in longer image acquisition times to record sufficient photon events to form a diagnostic quality image. If this camera is to be used for routine patient imaging, in particular in the operating theatre, this may be regarded as unacceptable and have other disadvantages affecting patient management [219]. The current weight of the camera head at 1 kg is quite heavy and the size of the Nebuleye was still considered relatively large for handheld use. The work in Chapter 7 to assess user motion is interesting, since this would suggest the acquisition time should not exceed two minutes during handheld use.

It was disappointing that the Nebuleye did not achieve CE marking as a medical device and as a consequence the clinical trial of SLNB in breast cancer did not go ahead. However, the clinical studies described in Chapter 8 have demonstrated the first results of use of the SFOV hybrid optical-gamma camera in medical imaging. This exploratory pilot study included patients undergoing bone, thyroid, lacrimal drainage and lymphatic imaging as well as DaTscan studies. Due to the compact design of the camera head with low profile photon detector, the camera was found to be suitable for small organ imaging at patient bedside. The most promising applications were found to be for thyroid scintigraphy and lacrimal drainage investigations where the uptake of radiotracer could be clearly seen. Further details were shown in the hybrid images for instance in the thyroid scintigraphy where the shape, size and position of the thyroid gland could be seen corresponding to the skin surface and in lacrimal drainage where

drainage of the tracer from the eye through the lacrimal duct could be identified in relation to patient surface anatomy.

It is widely acknowledged that there is a trade-off between system sensitivity and resolution of gamma cameras. The system spatial resolution of the HGC (2.43 mm at FWHM) with 1.5 mm-thick crystal and 1 mm diameter pinhole collimator was approximately three-fold better than the standard LFOV clinical gamma camera (7.4 mm at FWHM) used in medical research at Nottingham as tabulated in Table 3.9. With this high resolution ability, small objects situated adjacent to each other may be resolved. However, the system spatial resolution decreased with increase in SCD. This deterioration of system spatial resolution was apparent when the SFOV gamma camera was moved away from the study subject in order to increase the FOV. With the existing small field of view in the systems used this was considered to be a limitation.

Solutions to increase the system sensitivity may be considered by increasing the thickness of the CsI(Tl) crystal detector and widening the aperture of the pinhole collimator. Improvement of the HGC performance has been achieved by changing the crystal thickness from 0.6 mm to 1.5 mm and the pinhole size from 0.5 mm to 1 mm. The thicker crystal scintillator will have higher absorption rate for the incoming photons which improves the detection efficiency, especially for those photons with energies higher than $^{99m}$Tc, such as $^{131}$I (364 keV). However the problem with this approach is that this also causes multiple scattering of photons within the detector crystal resulting in degrading the spatial resolution of camera [14].

The use of solid-state detectors in SFOV gamma cameras may improve the spatial resolution and further reduce the space and weight of the camera head, compared to that of the current design of the HGC. The HGC utilises a pinhole collimator which also limits the camera sensitivity. However some strategies have to be proposed to improve this. Rogulski *et al.* [220] and Goorden *et al.* [221] have suggested the use of multiple pinhole collimators placed relatively close to the detector. This design has been applied in preclinical SPECT system [222] which has shown an improvement in spatial resolution while maintaining the system sensitivity. The drawback of the method was that it causes minification of the resulting image hence further reducing the FOV.

To overcome this limitation, the detector head of the HGC may need to be redesigned allowing for a combination of multiple detectors in one camera head. McAreavey *et al.* [77] have reported the design of $2 \times 2$ configuration of CZT detector module in a portable gamma camera. With this camera design and the combination of pinhole collimators, the FOV may be improved in comparison with the current version of HGC.

The operating temperature of the EMCCD was regulated by the Peltier cooler, which controlled the number of dark noise electrons to be generated within detector. This noise is proportional to the operating temperature of the CCD. As shown in the temperature stability test of the Nebuleye, the temperature of the CCD exceeded the recommended operating temperature limit within two hours after the system was powered up for use. At this stage the Nebuleye was not considered suitable for routine clinical use. For example such suboptimal performance could interrupt a surgical procedure when the camera is needed for a longer operating list. Hence, utilisation of an optimum cooling system design is crucial to prolong the duration of CCD temperature stability within the target range.

There is still a room to improve the uniformity of the gamma image acquired by the SFOV gamma cameras. No other sophisticated algorithms except blob detection technique was used in post-processing stage to enhance the image quality. On the other hand, camera head shielding design may need careful examination as they were a significant number of radiation leakage (details in Chapter 3), suspected through the gap between the shielding materials as shown in Figure 2.13. This may degrade the gamma image especially when imaging with sources of high activity or where activity is distributed throughout the patient.

It is clear that the combination of optical and gamma images provides added value in the clinical applications undertaken. High quality optical imaging is important for providing anatomical landmarks especially during surgery. In the circumstances when the camera is held close to the patient, the blockage of light or shadow on the ROI degrades the quality of optical image. Adding an external light source such as LED or laser beam at the edge of the camera head may illuminate the ROI while providing real time marking on the FOV frame at different SCDs and could be used to add a cross hair

mark on the subject surface. This could be beneficial especially in surgical procedures where the camera could be used as a guiding tool to localise sentinel nodes or tumours. The cross marking using a laser could be used to pinpoint the target and could guide the site of incision expose the target tissues.

## 9.2   Future work

This work has clearly demonstrated the feasibility and benefits of the SFOV hybrid optical gamma cameras in medical and preclinical imaging. Further work in this area of research is required to collect more clinical evidence and to assess further improvement in the camera performances. At time of writing, a further extended clinical trial (HRA reference number: 17/YH/0041) is still on-going to evaluate the performance of the HGC in a wider range of clinical investigations. Other clinical investigations undertaken so far include renal imaging, imaging of ectopic parathyroid adenoma and sentinel node localisation in patients with melanoma (Figure 9.1). Further imaging procedures should be carried out in patients administered with different radionuclides, such as $^{111}$In, $^{75}$Se, $^{131}$I and $^{201}$Tl. Moreover, further efforts to bring the camera into the surgical department should be carried out especially to perform the SLNB study in breast cancer surgery as specified in the protocol described in Chapter 6.
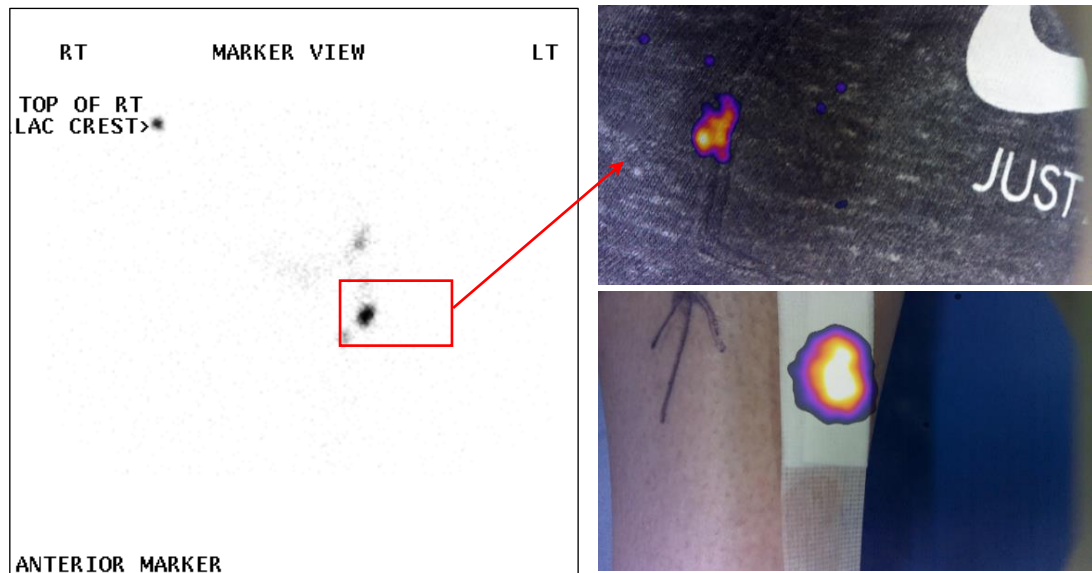


Figure 9.1: First sentinel node localisation study in patient with melanoma performed using the HGC with imaging time of 200 s. The hybrid images acquired at the injection site (bottom right, SSD 70 mm) and groin region (top right, SSD 40 mm) of patient, 38 minutes following administration of 20 MBq of $^{99m}$Tc-nanocolloid. (Left) Planar image of the pelvis region of the same patient, produced by a standard LFOV gamma camera, 186 minutes following administration with a 300 minutes acquisition time showing focal uptake at the groin region.

Further work focusing on the optimisation of the camera design as discussed earlier should be undertaken to enhance its performance as a medical device. This should include but not be limited to increasing system sensitivity and spatial resolution, enlarging the FOV of the camera, improving image post-processing and display, optimise the shielding of the camera head, the Peltier cooling system and the optical image display. Some work should be considered as part of the on-going clinical trial, including the utilisation of larger pinhole apertures, addition of extra features such as illumination of the surface being images and a laser marker on the camera surface as well as further modification of the software so that the optical and gamma image displays are automatically in the same orientation. In the long term, further optimisation work should be considered to improve the photon detection technology, camera head and collimator design, cooling technique and image post-processing methods.

Another important feature to add is the ability to estimate the depth of the target tissues showing radiotracer uptake. Pilot laboratory test results has been reported [37, 85] where the depth of the radionuclide source below the anatomical surface can be calculated by using the gamma and optical images generated by two well-defined geometrically separated hybrid camera systems. To fully implement this concept, the suggestion of combining multiple detectors in a compact single camera head may be considered, although maintaining the compact size of the camera head may be difficult to achieve.

There is an increasing interest in the use of combined gamma and near infrared fluorescent probes in preclinical and surgical imaging. Preliminary studies have been undertaken [37] using an in-house modified HGC and the addition of bespoke external excitation light source attached to the window of the camera head as described in Section 4.4.2.2 (Figure 9.2). This modified camera with the aid of an external excitation source has already produced the first hybrid gamma-fluorescent image as shown in Figure 9.3 however further optimisation will be crucial to improve the performance of this camera. With the introduction of hybrid gamma–NIRF probes in the clinic, it is envisaged that the ability of acquiring gamma and fluorescent image concurrently using the hybrid gamma cameras would be of great benefit for patients undergoing

intraoperative procedures such as SLNB and tumour excision. It is hoped that this thesis has contributed to the further development of these techniques.



Figure 9.2: Laboratory prototype of a co-aligned gamma-NIRF imaging system modified using HGC with an addition of a bandpass filter and a LED ring as the excitation light source. Image courtesy of University of Leicester.
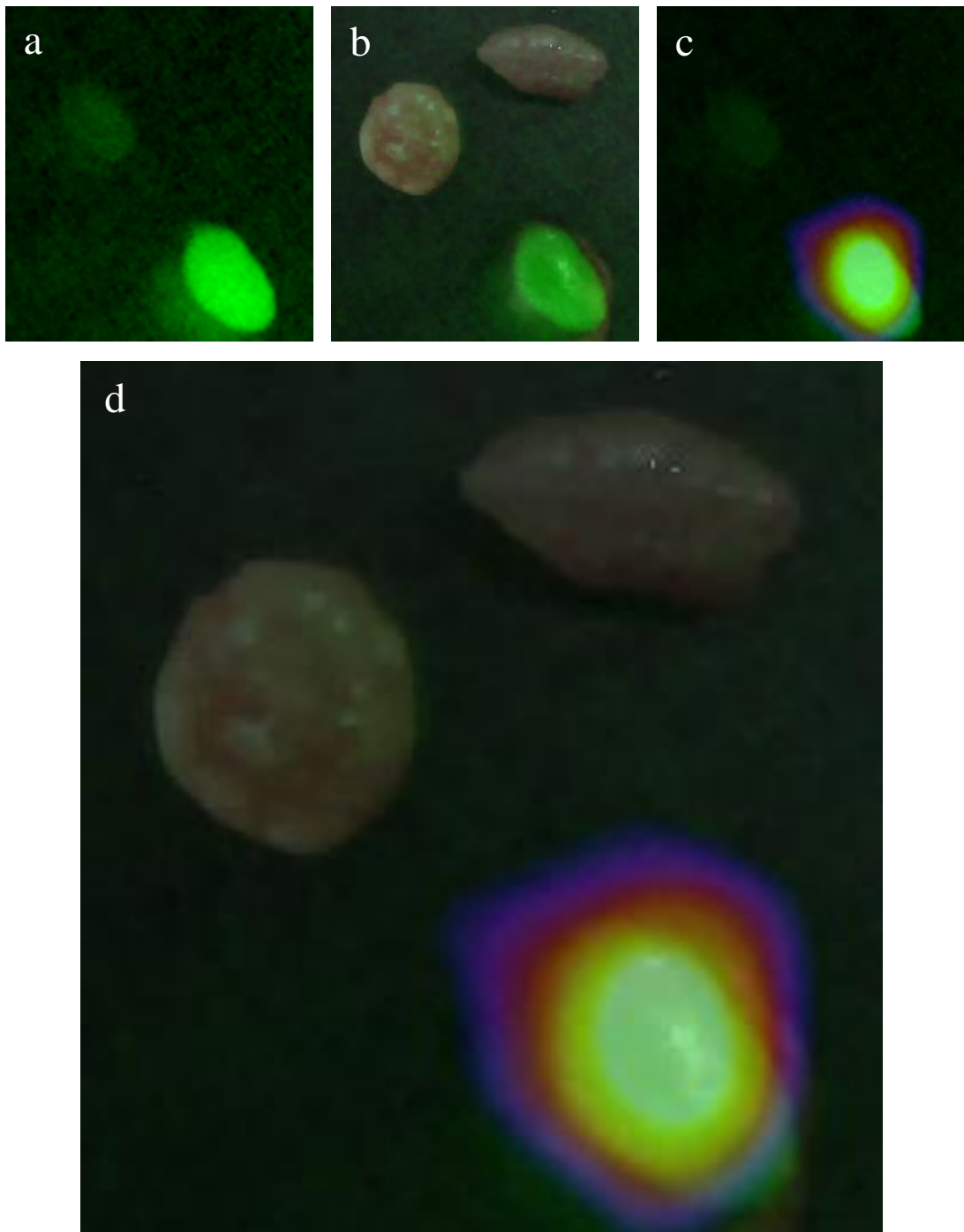
Figure 9.3: Example of (a) fluorescent, (b) hybrid optical-fluorescent, (c) hybrid fluorescent-gamma and (d) fused optical-fluorescent-gamma images of the excised tissues (kidney, tumour and muscle) acquired using the HGC handheld by operator. The fluorescent image was acquired separately using the modified HGC in the same experiment showing high uptake of fluorescence dye within the kidney. For better NIRF imaging quality, a commercial fluorescent imaging system (Artemis, Quest Medical Imaging, the Netherlands) was used to provide external excitation source.

## 9.3 Conclusions

- The work of this thesis has demonstrated the successful translation of a newly developed SFOV hybrid gamma camera into clinical use. A full testing scheme to characterise the hybrid components of the pre-production prototype camera was introduced and implemented, allowing the objective comparison of these cameras with other SFOV hybrid gamma cameras.

- Performance assessments were undertaken in clinical settings using bespoke phantoms, in particular for the assessment of the detectability of sentinel nodes in SLNB patients undergoing breast cancer surgery.

- Preparatory work to bring the camera into the surgical department was also completed, which included compliance with the regulatory requirements, clinical trial study design, the effects of operator motion, ergonomic of camera design and a routine quality control testing scheme was proposed.

- In addition experimental work was performed to explore the feasibility of the camera to detect clinically used radionuclides. This has confirmed the ability of the camera to detect energies ranging from $^{125}$I (35 keV) to $^{75}$Se (265 keV).

- The first clinical results of the use of the HGC for medical imaging was obtained in patients undergoing bone, thyroid, lacrimal drainage and lymphatic imaging. The camera demonstrated good potential for small organ imaging such as thyroid and lacrimal drainage scintigraphy.

- In addition, the preclinical imaging work has indicated the use of the SFOV hybrid optical gamma camera for imaging small animals where hybrid images may be of value for screening results in large animal numbers where SPECT imaging may be too time consuming.

# Appendices

## A. Matlab scripts

### A.1. Modify DICOM header

```
x=dicominfo('SFOV.dcm');
y=dicominfo('LFOV.0000');
z=y;
xfieldnames=fieldnames(x);
l=length(xfieldnames);



for i=1:l
    % xfieldnames = names of fields in SFOV
    % x = SFOV
    % y=LFOV
    % z=copy of LFOV

    if isfield(z, xfieldnames{i}) == 1
        z.(xfieldnames{i}) = x.(xfieldnames{i});
    end
    if strcmp(xfieldnames{i}, 'PixelSpacing') == 1
        z.(xfieldnames{i}) = [x.(xfieldnames{i});
x.(xfieldnames{i})];
    end
end

xim=dicomread('SFOV.dcm');
dicomwrite(xim, 'SFOV_new.dcm', z, 'CreateMode','Copy');
```

### A.2. Convert images from TIFF to DICOM format

```
% to convert tiff images to DICOM images in batch (within same
folder)
dirListing = dir('*.tiff');

counter=0;

for d = 1:length(dirListing)
    counter=counter+1;
    a=dirListing.name;
    b=imread(a);

    [pathstr,name,ext] = fileparts(a);
    dicomwrite(b, strcat(name,'.dcm'));
end
```

## A.3.    Analysis of uniformity test

```matlab
%Uniformity correction and quantification for SFOV gamma camera
%read two flood images and background image

a=dicomread('BCR1.dcm');
b=dicomread('image1.dcm');
c=dicomread('image2.dcm');

%convert from uint16 image to double image
%to change pixel intensity from int to floating number
a2=double(a);
b2=double(b);
c2=double(c);
%flood1 subtracted with background image and obtained max intensity
value
%normalised image with max int value
d=b2-a2;
max1=max(d(:));
e=d/max1;

%flood2 subtracted with background image and divided with
normalised image
f=c2-a2;
g=f./e;

%select ROI of image for quantification 110x110
Q=g(12:121,12:121);

%apply median filter (to replace outlier)
T=medfilt2(Q, [20 20], 'symmetric');

%quantification
mean=mean2(T);
stdev=std2(T);
max=max(T(:));
min=min(T(:));

%display corrected image in normalised scale
imshow(T ./ 80);

%obtained pixel profile
intensity1=T(50,:);

%display ROI of non-corrected image and obtained profile
I=c2(12:121,12:121);
imshow(I ./80);
mean3=mean2(I);
intensity2=I(50,:);
xlabel('Pixel');
ylabel('Normalised pixel intensity');
subplot(2,1,1),plot(intensity2/mean3);
subplot(2,1,2),plot(intensity1/mean);
```

# B. Questionnaire

The University of **Nottingham**
UNITED KINGDOM · CHINA · MALAYSIA

**University** *of* **Leicester**

Nottingham University Hospitals **NHS**
NHS Trust

## Compact Hybrid Optical-Gamma Camera Survey

**The purpose of this survey:**

The Universities of Nottingham and Leicester have developed a compact hybrid optical-gamma camera for intra-operative procedure and small organ imaging. The objective of this survey is to assess the system functionality to optimise its performance and safety in the clinical environment, particularly in operating theatre during surgical procedure. The data from this survey is needed for further device development before finalising the system configurations.

All information provided will be treated confidentially. The data will be used for device refinement and will be treated anonymously.

**Further information:**

For any further information about this study please contact:

| Prof. Alan C. Perkins | Mr. Aik Hao Ng |
|---|---|
| Professor of Medical Physics /Lead investigator | PhD Student |
| Radiological and Imaging Sciences | Radiological and Imaging Sciences |
| School of Medicine | School of Medicine |
| Alan.perkins@nottingham.ac.uk | msxahn@nottingham.ac.uk |
| Tel: 0115 82 31277 | Tel: 0115 823 1176 |

### Section A: General

1. Please indicate your first impression of the compact hybrid optical-gamma camera system by circling the number that best matches your opinion.

|  | Disagree |  |  |  | Agree |
|---|---|---|---|---|---|
| Suitable for use in the operating theatre | 1 | 2 | 3 | 4 | 5 |
| Visually attractive | 1 | 2 | 3 | 4 | 5 |
| Good surface finishing | 1 | 2 | 3 | 4 | 5 |
| Appropriate functionality | 1 | 2 | 3 | 4 | 5 |

2. Which of the following radiation detection device(s) would you prefer during the intra-operative procedure?
   (Please tick one)
   - ☐ Gamma camera only
   - ☐ Optical-gamma camera only
   - ☐ Both optical-gamma camera and gamma probe
   - ☐ Gamma probe only
   - ☐ Gamma camera and gamma probe
   - ☐ Other. Please specify: _____

## Section B: Safety and Performance

3. Do you have any safety concerns for use of the device in the operating theatre?

   ☐   Yes. Please specify:          ☐   No
   
   _____

4. Do you think that the hybrid optical/gamma images provided by the camera during the intra-operative procedure, when compared to gamma probe, provide additional values in the patient management? (Please circle the number that best matches your opinion)

| | Disagree | | | | Agree |
|---|---|---|---|---|---|
| Easier for localisation of uptake(s) | 1 | 2 | 3 | 4 | 5 |
| Provide dissection margin | 1 | 2 | 3 | 4 | 5 |
| Able to re-examine if there is a radioactive residue | 1 | 2 | 3 | 4 | 5 |
| Provide images as required for medical-legal purposes | 1 | 2 | 3 | 4 | 5 |

## Section C: Design concept and ergonomics

5. Which location do you consider the best for the trolley and the image display in the operating theatre? (Please tick one with reference to the diagram as below)

   ☐   Opposite the surgeon (A)        ☐   At the side of the surgeon (B)
   ☐   End of patient couch (C)         ☐   Other. Please specify:
   
                                            _____
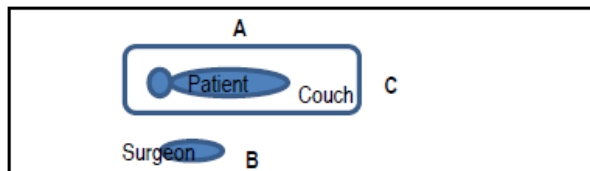


6. Which of the following applications would you like to have available when the cameras are in use? (Please circle the number that best matches your opinion)

| | Not necessary | | | | Essential |
|---|---|---|---|---|---|
| Real-time dynamic gamma image | 1 | 2 | 3 | 4 | 5 |
| Real-time optical video | 1 | 2 | 3 | 4 | 5 |
| Static gamma image | 1 | 2 | 3 | 4 | 5 |
| Static optical image | 1 | 2 | 3 | 4 | 5 |
| Static hybrid image (superimposed) | 1 | 2 | 3 | 4 | 5 |
| Dual-images comparison screen | 1 | 2 | 3 | 4 | 5 |
| Masking of high activities at injection site | 1 | 2 | 3 | 4 | 5 |
| Contrast enhancement | 1 | 2 | 3 | 4 | 5 |
| Variable colour scales | 1 | 2 | 3 | 4 | 5 |

| | Not necessary | | | | Essential |
|---|---|---|---|---|---|
| Measurement tools (eg. distance, line profile, etc) | 1 | 2 | 3 | 4 | 5 |
| Display of counts in hot spot | 1 | 2 | 3 | 4 | 5 |
| Editing tools/Marker | 1 | 2 | 3 | 4 | 5 |
| Other (please specify) | 1 | 2 | 3 | 4 | 5 |
| 1. _____ | 1 | 2 | 3 | 4 | 5 |
| 2. _____ | 1 | 2 | 3 | 4 | 5 |

7. Do you think the size and the weight of the camera head suitable for use in the operating theatre?

   ☐     Yes                        ☐     No

8. Do you feel comfortable when holding the camera head?

   ☐     Yes                        ☐     No

9. Do you think the size and the weight of the trolley suitable for use in the operating theatre?

   ☐     Yes                        ☐     No

10. Do you feel comfortable when moving the trolley?

    ☐     Yes                        ☐     No

11. Do you think the size and the weight of the moulded system and articulated arm suitable for use in the operating theatre?

    ☐     Yes                        ☐     No

12. Do you feel comfortable when moving the moulded system and articulated arm?

    ☐     Yes                        ☐     No

13. What do you think about the flexibility of the device manoeuvre? (Please circle the number that best matches your opinion)

| Not flexible | | | | Very flexible |
|---|---|---|---|---|
| 1 | 2 | 3 | 4 | 5 |

14. What is the acceptable image acquisition time for a single image to localise activity? (Please tick one)

    ☐   < 10 seconds            ☐   Between 10 seconds and 60 seconds

    ☐   Between 61 seconds and 120 seconds       ☐   Between 121 seconds and 180 seconds

    ☐   Other. Please specify:

    _____

**Section D: Sterility**

15. Does the system present any difficulties for maintaining sterility in theatre?

☐   Yes                              ☐   No

16. Would this be practical with the use of a sterile cover?

☐   Yes                              ☐   No

**Section E: Conclusion**

17. Are you interested in the technology of hybrid optical-gamma camera and would like to use it in your medical centre?

☐   Yes                              ☐   No

18. In additional to use in sentinel node localisation, are there any other surgical procedures which you think this camera might be useful?

19. Any other commends?

**Contact information of person completing this questionnaire**

| Name: | |
|---|---|
| Job title: | |
| Telephone: | |
| Email address: | |

**Thank you for your participation.**

# References

1. Morris, P. and A. Perkins. 2012. Diagnostic imaging. *The Lancet,* **379**(9825): 1525-1533.

2. Lawrence, J.H. 1940. Nuclear Physics and Therapy: Preliminary Report on a New Method for the Treatment of Leukemia and Polycythemia. *Radiology,* **35**(1): 51-60.

3. Siemens Medical Solutions USA. *Symbia T Series*. [Accessed on 31 August 2017]. Available from: https://www.healthcare.siemens.co.uk/molecular-imaging/spect-and-spect-ct/symbia-t.

4. Brigham and Women's Hospital. *Patient Education - Bone Scan*. [Accessed on 2 September 2017]. Available from: http://www.brighamandwomens.org/Departments_and_Services/radiology/services/nuclearmedicine/Patient/bone.aspx.

5. United Nations Scientific Committee on the Effects of Atomic Radiation. 2010. *UNSCEAR 2008 Report: Sources and effects of ionizing radiation, Volume I, Annex A–Medical radiation exposures*. New York: United Nations Available from: http://www.unscear.org/unscear/en/publications/2008_1.html.

6. United Nations Environment Programme. 2016. *Radiation: effects and sources*. Austria.

7. Saha, G.B. 2001. *Physics and Radiobiology of Nuclear Medicine*. 2nd edition. USA: Springer.

8. Yeong, C.H., M.H. Cheng, and K.H. Ng. 2014. Therapeutic radionuclides in nuclear medicine: current and future prospects. *Journal of Zhejiang University. Science. B,* **15**(10): 845-863.

9. Theobald, A.E., T. Theobald, and C.B. Sampson. 2011. *Sampson's Textbook of Radiopharmacy*. London: Pharmaceutical Press.

10. Livingood, J.J. and G.T. Seaborg. 1938. Radioactive iodine isotopes. *Physical Review,* **53**(12): 1015.

11. Cassen, B., L. Curtis, C. Reed, and R. Libby. 1951. Instrumentation for I-131 Use in Medical Studies. *Nucleonics,* **9**(2): 46-50.

12. Lawson, R.S. 2013. *The Gamma Camera: A Comprehensive Guide*. United Kingdom: Institution of Physics and Engineering in Medicine.

13. Mediso Medical Imaging System. *Nucline™ TH*. [Accessed on 1 August 2014]. Available from: http://www.mediso.com/.

14. Cherry, S.R., J.A. Sorenson, and M.E. Phelps. 2003. *Physics in Nuclear Medicine* Third edition. Philadelphia, PA: Elsevier.

15. Peterson, T.E. and L.R. Furenlid. 2011. SPECT detectors: the Anger Camera and beyond. *Physics in medicine and biology,* **56**(17): R145-R182.

16. Perkins, A.C. and J.E. Lees. 2016. *Gamma Cameras for Interventional and Intraoperative Imaging*. Boca Raton: CRC Press.

17. Saint-Gobain Crystals. *CsI(Tl), CsI(Na) Cesium Iodide Scintillation Material*. [Accessed on 3 September 2017]. Available from: http://www.crystals.saint-gobain.com/sites/imdf.crystals.com/files/documents/csitl-and-na-material-data-sheet_69771.pdf.

18. Knoll, G.F. 2000. *Radiation Detection and Measurement*. New York: John Wiley & Sons.

19. Powsner, R.A. and E.R. Powsner. 2006. *Essential Nuclear Medicine Physics*. 2nd edition. United Kingdom: Blackwell Publishing Ltd.

20. Kuhl, D.E. and R.Q. Edwards. 1963. Image Separation Radioisotope Scanning. *Radiology,* **80**(4): 653-662.

21. Hasegawa, B.H., E.L. Gingold, S.M. Reilly, S.-C. Liew, and C.E. Cann. 1990. Description of a simultaneous emission-transmission CT system. in *Medical Imaging '90*. Newport Beach, CA, United States: SPIE.

22. Muzic, R.F. and F.P. DiFilippo. 2014. PET/MRI – Technical Review. *Seminars in Roentgenology,* **49**(3): 242-254.

23. Mariani, G., L. Bruselli, T. Kuwert, E.E. Kim, A. Flotats*, et al.* 2010. A review on the clinical uses of SPECT/CT. *Eur J Nucl Med Mol Imaging,* **37**(10): 1959-85.

24. Selverstone, B., W.H. Sweet, and C.V. Robinson. 1949. The Clinical Use of Radioactive Phosphorus in the Surgery of Brain Tumors. *Annals of Surgery,* **130**(4): 643-651.

25. Perkins, A.C., P. Yeoman, A.J. Hindle, R.M. Vincent, M. Frier*, et al.* 1997. Bedside nuclear medicine investigations in the intensive care unit. *Nucl Med Commun,* **18**(3): 262-268.

26. Perkins, A.C. and J.G. Hardy. 1996. Intra-operative nuclear medicine in surgical practice. *Nucl Med Commun,* **17**(12): 1006-15.

27. Hurwitz, S.R., W.L. Ashburn, J.P. Green, and S.E. Halpern. 1973. Clinical Applications of a Portable Scintillation Camera. *Journal of Nuclear Medicine,* **14**(8): 585-587.

28. Digirad Corporation. *ergo™*. [Accessed on 1 August 2014]. Available from: http://www.digirad.com/cameras/ergo/.

29. Adolesco, A.B. *3D Mobile Gamma Camera - Cardiotom$^{TM}$*. [Accessed on 14 August 2015]. Available from: http://www.adolesco.se/.

30. Digirad Corporation. *2020tc Imager™*. [Accessed on 14 August 2015]. Available from: http://www.digirad.com/download/2020tc_s.pdf.

31. MiE Medical Imaging Electronics. *Picola Scintron®*. [Accessed on 15 August 2015]. Available from: http://www.mieamerica.com/index.php?id=1235&L=4.

32. DDD-Diagnostic A/S. *SoloMobile*. [Accessed on 15 August 2015]. Available from: http://www.ddd-diagnostic.dk/PD.pdf.

33. Barber, H.B., H.H. Barrett, W.J. Wild, and J.M. Woolfenden. 1984. Development of small in-vivo imaging probes for tumor detection. *IEEE Transactions on Nuclear Science,* **NS-31**(1): 599-604.

34. Engelen, T., B.M. Winkel, D.D. Rietbergen, G.H. KleinJan, S. Vidal-Sicart, *et al.* 2015. The next evolution in radioguided surgery: breast cancer related sentinel node localization using a freehand SPECT-mobile gamma camera combination. *Am J Nucl Med Mol Imaging,* **5**(3): 233-45.

35. Massari, R., A. Ucci, C. Campisi, F. Scopinaro, and A. Soluri. 2016. A novel fully integrated handheld gamma camera. *Nuclear Instruments and Methods in Physics Research Section A: Accelerators, Spectrometers, Detectors and Associated Equipment,* **832**: 271-278.

36. Sanchez, F., M.M. Fernandez, M. Gimenez, J.M. Benlloch, M.J. Rodriguez-Alvarez, *et al.* 2006. Performance tests of two portable mini gamma cameras for medical applications. *Medical Physics,* **33**(11): 4210-4220.

37. Lees, J.E., S.L. Bugby, M.S. Alqahtani, L.K. Jambi, N.S. Dawood, *et al.* 2017. A Multimodality Hybrid Gamma-Optical Camera for Intraoperative Imaging. *Sensors (Basel),* **17**(3).

38. Goertzen, A.L., J.D. Thiessen, B. McIntosh, M.J. Simpson, and J. Schellenberg. 2013. Characterization of a handheld gamma camera for intraoperative use for sentinel lymph node biopsy. in *IEEE Nuclear Science Symposium Conference Record*.

39. Mathelin, C., S. Salvador, D. Huss, and J.L. Guyonnet. 2007. Precise localization of sentinel lymph nodes and estimation of their depth using a prototype intraoperative mini gamma-camera in patients with breast cancer. *Journal of Nuclear Medicine,* **48**(4): 623-629.

40. Lees, J.E., S.L. Bugby, B.S. Bhatia, L.K. Jambi, M.S. Alqahtani, *et al.* 2014. A small field of view camera for hybrid gamma and optical imaging. *Journal of Instrumentation,* **9**(12): C12020.

41. Aarsvod, J.N., C.M. Greene, R.A. Mintzer, S.F. Grant, T.M. Styblo, *et al.* 2006. Intraoperative gamma imaging of axillary sentinel lymph nodes in breast cancer patients. *Phys Med,* **21** (Supp 1): 76-9.

42. Patt, B.E., M.P. Tornai, J.S. Iwanczyk, C.S. Levin, and E.J. Hoffman. 1997. Development of an intraoperative gamma camera based on a 256-pixel mercuric iodide detector array. *IEEE Transactions on Nuclear Science,* **44**(3): 1242-1248.

43. Lees, J.E., D.J. Bassford, O.E. Blake, P.E. Blackshaw, and A.C. Perkins. 2011. A high resolution Small Field Of View (SFOV) gamma camera: a columnar scintillator coated CCD imager for medical applications. *Journal of Instrumentation,* **6**.

44. Lees, J.E., D.J. Bassford, O.E. Blake, P.E. Blackshaw, and A.C. Perkins. 2012. A Hybrid Camera for simultaneous imaging of gamma and optical photons. *Journal of Instrumentation,* **7**.

45. Ng, A.H., P.E. Blackshaw, M.S. Alqahtani, L.K. Jambi, S.L. Bugby, *et al.* 2017. A novel compact small field of view hybrid gamma camera: first clinical results. *Nucl Med Commun,* **38**(9): 729-736.

46.  Pitre, S., L. Menard, M. Ricard, M. Solal, J.R. Garbay, *et al.* 2003. A hand-held imaging probe for radio-guided surgery: physical performance and preliminary clinical experience. *Eur J Nucl Med Mol Imaging,* **30**(3): 339-343.

47.  Kerrou, K., S. Pitre, C. Coutant, R. Rouzier, P.-Y. Ancel, *et al.* 2011. The Usefulness of a Preoperative Compact Imager, a Hand-Held γ-Camera for Breast Cancer Sentinel Node Biopsy: Final Results of a Prospective Double-Blind, Clinical Study. *Journal of Nuclear Medicine,* **52**(9): 1346-1353.

48.  Bricou, A., M.A. Duval, L. Bardet, A. Benbara, G. Moreaux, *et al.* 2015. Is there a role for a handheld gamma camera (TReCam) in the SNOLL breast cancer procedure? *Q J Nucl Med Mol Imaging,* (Mar 31).

49.  Netter, E., L. Pinot, L. Menard, M.A. Duval, B. Janvier, *et al.* 2009. Designing the scintillation module of a pixelated mini gamma camera: the spatial spreading behaviour of light. *IEEE Nuclear Science Symposium Conference Record,* **1-5**: 3300-3302.

50.  Netter, E., L. Pinot, L. Menard, M.A. Duval, B. Janvier, *et al.* 2009. The Tumor Resection Camera (TReCam), a multipixel imaging probe for radio-guided surgery. *IEEE Nuclear Science Symposium Conference Record,* **1-5**: 2573-2576.

51.  Russo, P., A.S. Curion, G. Mettivier, M. Esposito, M. Aurilio, *et al.* 2011. Evaluation of a CdTe semiconductor based compact gamma camera for sentinel lymph node imaging. *Medical Physics,* **38**(3): 1547-1560.

52.  Abe, A., N. Takahashi, J. Lee, T. Oka, K. Shizukuishi, *et al.* 2003. Performance evaluation of a hand-held, semiconductor (CdZnTe)-based gamma camera. *Eur J Nucl Med Mol Imaging,* **30**(6): 805-811.

53.  Fujii, T., S. Yamaguchi, R. Yajima, S. Tsutsumi, N. Uchida, *et al.* 2011. Use of a handheld, semiconductor (cadmium zinc telluride)-based gamma camera in navigation surgery for primary hyperparathyroidism. *Am Surg,* **77**(6): 690-3.

54.  Tsuchimochi, M. and K. Hayama. 2013. Intraoperative gamma cameras for radioguided surgery: technical characteristics, performance parameters, and clinical applications. *Phys Med,* **29**(2): 126-38.

55.  Tsuchimochi, M., K. Hayama, T. Oda, M. Togashi, and H. Sakahara. 2008. Evaluation of the efficacy of a small CdTe gamma-camera for sentinel lymph node biopsy. *Journal of Nuclear Medicine,* **49**(6): 956-962.

56.  Tsuchimochi, M., H. Sakahara, K. Hayama, M. Funaki, R. Ohno, *et al.* 2003. A prototype small CdTe gamma camera for radioguided surgery and other imaging applications. *Eur J Nucl Med Mol Imaging,* **30**(12): 1605-1614.

57.  Olcott, P.D., F. Habte, A.M. Foudray, and C.S. Levin. 2007. Performance characterization of a miniature, high sensitivity gamma ray camera. *IEEE Transactions on Nuclear Science,* **54**(5): 1492-1497.

58.  Olcott, P., G. Pratx, D. Johnson, E. Mittra, R. Niederkohr, *et al.* 2014. Clinical evaluation of a novel intraoperative handheld gamma camera for sentinel lymph node biopsy. *Phys Med,* **30**(3): 340-345.

59.     Ferretti, A., S. Chondrogiannis, A. Marcolongo, and D. Rubello. 2013. Phantom study of a new hand-held gamma-imaging probe for radio-guided surgery. *Nucl Med Commun,* **34**(1): 86-90.

60.     Chondrogiannis, S., A. Ferretti, E. Facci, M.C. Marzola, L. Rampin*, et al.* 2013. Intraoperative Hand-Held Imaging gamma-Camera for Sentinel Node Detection in Patients With Breast Cancer Feasibility Evaluation and Preliminary Experience on 16 Patients. *Clinical Nuclear Medicine,* **38**(3): E132-E136.

61.     Trotta, C., R. Massari, N. Palermo, F. Scopinaro, and A. Soluri. 2007. New high spatial resolution portable camera in medical imaging. *Nuclear Instruments & Methods in Physics Research Section A-Accelerators Spectrometers Detectors and Associated Equipment,* **577**(3): 604-610.

62.     Kopelman, D., I. Blevis, G. Iosilevsky, A. Reznik, A. Chaikov*, et al.* 2005. A newly developed intra-operative gamma camera: performance characteristics in a laboratory phantom study. *Eur J Nucl Med Mol Imaging,* **32**(10): 1217-1224.

63.     Brouwer, O.R., N.S. van den Berg, H.M. Mathéron, H.G. van der Poel, B.W. van Rhijn*, et al.* 2014. A Hybrid Radioactive and Fluorescent Tracer for Sentinel Node Biopsy in Penile Carcinoma as a Potential Replacement for Blue Dye. *European Urology,* **65**(3): 600-609.

64.     Fernández, M.M., J.M. Benlloch, J. Cerdá, B. Escat, E.N. Giménez*, et al.* 2004. A flat-panel-based mini gamma camera for lymph nodes studies. *Nuclear Instruments and Methods in Physics Research Section A: Accelerators, Spectrometers, Detectors and Associated Equipment,* **527**(1–2): 92-96.

65.     General Equipment for Medical Imaging, S.A. *Sentinella 102*. [Accessed on 16 Oct 2013]. Available from: http://www.gem-imaging.com/descargas/productos/sentinella102.pdf.

66.     Scerrino, G., S. Castorina, G.I. Melfa, C. Lo Piccolo, C. Raspanti*, et al.* 2015. The intraoperative use of the mini-gamma camera (MGC) in the surgical treatment of primary hyperparathyroidism Technical reports and immediate results from the initial experience. *Ann Ital Chir,* **86**.

67.     Vermeeren, L., R.A.V. Olmos, W.M.C. Klop, A.J.M. Balm, and M.W.M. van den Brekel. 2010. A Portable gamma-Camera for Intraoperative Detection of Sentinel Nodes in the Head and Neck Region. *Journal of Nuclear Medicine,* **51**(5): 700-703.

68.     Vidal-Sicart, S., L. Vermeeren, O. Sola, P. Paredes, and R.A. Valdes-Olmos. 2011. The use of a portable gamma camera for preoperative lymphatic mapping: a comparison with a conventional gamma camera. *Eur J Nucl Med Mol Imaging,* **38**(4): 636-641.

69.     Jung, J.H., Y. Choi, K.J. Hong, B.J. Min, S. Park*, et al.* 2007. Development of a dual modality imaging system: A combined gamma camera and optical imager. *IEEE Nuclear Science Symposium Conference Record,* **1-11**: 3762-3765.

70.     Ozkan, E. and A. Eroglu. 2015. The Utility of Intraoperative Handheld Gamma Camera for Detection of Sentinel Lymph Nodes in Melanoma. *Nuclear Medicine and Molecular Imaging,* **49**(4): 318-320.

71. Crystal Photonics. *Handheld USB-Gamma Camera "CrystalCam"*. [Accessed on 26 November 2014]. Available from: http://crystal-photonics.com/enu/products/cam-crystalcam--enu.htm.

72. Zuhayra, M., S. Dierck, M. Marx, Y. Zhao, R. Wilhelm*, et al.* 2015. Is the portable gamma camera "Crystal Cam" equal to the conventional gamma camera for the detection of SLNs of malignant melanoma. *Journal of Nuclear Medicine,* **56**(supplement 3): 1866.

73. EuroMedical Intruments. *Minicam 2*. [Accessed on 15 December 2015]. Available from: http://em-instruments.com.

74. Mathelin, C., S. Salvador, V. Bekaert, S. Croce, N. Andriamisandratsoa*, et al.* 2008. A new intraoperative gamma camera for the sentinel lymph node procedure in breast cancer. *Anticancer Research,* **28**(5 B): 2859-2864.

75. Aarsvold, J.N., R.A. Mintzer, C. Greene, S.F. Grant, T.M. Styblo*, et al.* 2003. Gamma cameras for intraoperative localization of sentinel nodes: Technical requirements identified through operating room experience. *IEEE Nuclear Science Symposium, Conference Record,* **1-3**: 1172-1176.

76. Kromek. *DMatrix™- Nuclear Imager Gamma Spectroscopy Detector/Imager and Software*. [Accessed on 22 August 2017]. Available from: http://www.kromek.com/index.php/medical/all-medical-products/dmatrix.

77. McAreavey, L.H., L.J. Harkness-Brennan, S.J. Colosimo, D.S. Judson, A.J. Boston*, et al.* 2017. Characterisation of a CZT detector for dosimetry of molecular radiotherapy. *Journal of Instrumentation,* **12**(03): P03001.

78. A. Soluri, R.M., C. Trotta, L. Montani, G. Iurlaro, A.M. Mangano, F. Scopinaro, R. Scafe`. 2005. New imaging probe with crystals integrated in the collimator's square holes. *Nuclear Instruments and Methods in Physics Research A,* **554**: 331-339.

79. Jung, J.H., Y. Choi, K.J. Hong, B.J. Min, J.Y. Choi*, et al.* 2009. Development of a dual modality imaging system: a combined gamma camera and optical imager. *Physics in Medicine and Biology,* **54**(14): 4547-4559.

80. Olcott, P.D., F. Habte, C.S. Levin, and A.M.K. Foudray. 2004. Characterization of Performance of a Miniature, High Sensitivity Gamma-Ray Camera. *IEEE Nuclear Science Symposium and Medical Imaging Conference Record,* **IV**: 3997-4000.

81. Salvador, S., V. Bekaert, C. Mathelin, J.L. Guyonnet, and D. Huss. 2007. An operative gamma camera for sentinel lymph node procedure in case of breast cancer. *Journal of Instrumentation,* **2**.

82. Haneishi, H., H. Shimura, and H. Hayashi. 2010. Image Synthesis Using a Mini Gamma Camera and Stereo Optical Cameras. *Ieee Transactions on Nuclear Science,* **57**(3): 1132-1138.

83. Menard, L., Y. Charon, M. Solal, P. Laniece, R. Mastrippolito*, et al.* 1998. POCI: A compact high resolution gamma camera for intra-operative surgical use. *IEEE Transactions on Nuclear Science,* **45**(3): 1293-1297.

84. Lees, J.E., G.W. Fraser, A. Keay, D. Bassford, R. Ott*, et al.* 2003. The high resolution gamma imager (HRGI): a CCD based camera for medical imaging.

*Nuclear Instruments & Methods in Physics Research Section A-Accelerators Spectrometers Detectors and Associated Equipment,* **513**(1-2): 23-26.

85.  Lees, J.E., S.L. Bugby, A.P. Bark, D.J. Bassford, P.E. Blackshaw, *et al.* 2013. A hybrid camera for locating sources of gamma radiation in the environment. *Journal of Instrumentation,* **8**(10): P10021.

86.  Mettivier, G., M.C. Montesi, and P. Russo. 2003. Design of a compact gamma camera with semiconductor hybrid pixel detectors: imaging tests with a pinhole collimator. *Nuclear Instruments and Methods in Physics Research Section A: Accelerators, Spectrometers, Detectors and Associated Equipment,* **509**(1–3): 321-327.

87.  Sanchez, F., J.M. Benlloch, B. Escat, N. Pavon, E. Porras, *et al.* 2004. Design and tests of a portable mini gamma camera. *Medical Physics,* **31**(6): 1384-1397.

88.  Menard, L., Y. Charon, M. Solal, M. Ricard, P. Laniece, *et al.* 1999. Performance characterization and first clinical evaluation of a intra-operative compact gamma imager. *IEEE Transactions on Nuclear Science,* **46**(6): 2068-2074.

89.  Habte, F., P.D. Olcott, C.S. Levin, and A.M. Foudray. 2007. Prototype parallel readout system for position sensitive PMT based gamma ray imaging systems. *IEEE Transactions on Nuclear Science,* **54**(1): 60-65.

90.  Turner, M.J.L., A. Abbey, M. Arnaud, M. Balasini, M. Barbera, *et al.* 2001. The European Photon Imaging Camera on XMM-Newton: The MOS cameras. *A&A,* **365**(1): L27-L35.

91.  Lumb, D.H., R.S. Warwick, M. Page, and A. De Luca. 2002. X-ray background measurements with XMM-Newton EPIC. *A&A,* **389**(1): 93-105.

92.  Lees, J.E., D. Bassford, G.W. Fraser, D. Monk, M. Early, *et al.* 2006. Investigation of scintillator coated CCDs for medical imaging. *IEEE Transactions on Nuclear Science,* **53**(1): 9-13.

93.  Frojdh, C., P. Nelvig, H.E. Nilsson, and C.S. Petersson. 1997. Simulation of the X-ray response of scintillator coated silicon CCDs. in *1997 IEEE Nuclear Science Symposium Conference Record.*

94.  RS Components Ltd. *Melcor CP 0.8_127_06L Thermoelectric Device.* [Accessed on 14 July 2017].

95.  e2v Technologies. *CCD97-00 Back Illuminated 2-Phase IMO Series Peltier Pack Electron Multiplying CCD Sensor.* [Accessed on 10 November 2014]. Available from: www.e2v.com/resources/account/download-datasheet/1487.

96.  J.E.Lees, S.L.Bugby, A.P.Bark, D.J.Bassford, P.E.Blackshaw, *et al.* 2013. A hybrid camera for locating sources of gamma radiation in the environment. *Journal of Instrumentation,* **8**.

97.  IDS Imaging Development Systems GmbH. *uEye XS Industrial Camera.* [Accessed on 9 February 2017]. Available from: https://en.ids-imaging.com/IDS/datasheet_pdf.php.

98.  Hall, D.J., A. Holland, and D.R. Smith. 2009. The use of automatic scale selection to improve the spatial and spectral resolution of a scintillator-coupled

EMCCD. *Nuclear Instruments & Methods in Physics Research Section A-Accelerators Spectrometers Detectors and Associated Equipment,* **604**(1-2): 207-210.

99. Pianykh, O.S. 2008. *Digital Imaging and Communications in Medicine (DICOM): A Practical Introduction and Survival Guide*. Verlag Berlin Heidelberg: Springer.

100. Gamma Technologies Ltd. *NebulEYE Mini Gamma Camera System v1.0 Instructions for use*. [Accessed on 5 September 2015].

101. National Electrical Manufacturers Association. *NEMA Standards Publication NU 1-2012 Performance Measurements of Gamma Cameras*. [Accessed on 28 March 2014].

102. International Electrotechnical Commission. *IEC 61675-2:2015 Radionuclide imaging devices - Characteristics and test conditions - Part 2: Gamma cameras for planar, wholebody, and SPECT imaging*. [Accessed on 13 October 2016].

103. International Atomic Energy Agency. 2009. *Quality assurance for SPECT systems*. Vienna: IAEA. Available from: http://www-pub.iaea.org/MTCD/publications/PDF/Pub1394_web.pdf.

104. Bhatia, B.S., S.L. Bugby, J.E. Lees, and A.C. Perkins. 2015. A scheme for assessing the performance characteristics of small field-of-view gamma cameras. *Phys Med,* **31**(1): 98-103.

105. Bugby, S.L., J.E. Lees, B.S. Bhatia, and A.C. Perkins. 2014. Characterisation of a high resolution small field of view portable gamma camera. *Phys Med,* **30**(3): 331-9.

106. Institute of Physics and Engineering in Medicine. 2003. *Quality Control of Gamma Camera Systems Report No. 86*. York: Institute of Physics and Engineering in Medicine.

107. Bugby, S.L., L.K. Jambi, and J.E. Lees. 2016. A comparison of CsI:Tl and GOS in a scintillator-CCD detector for nuclear medicine imaging. *Journal of Instrumentation,* **11**(09): P09009.

108. Philips Healthcare. *BrightView X and XCT specifications*. [Accessed on 03 May 2017]. Available from: www.philips.com/brightviewxct.

109. Jones, D.W., P. Hogg, and E. Seeram. 2013. *Practical SPECT/CT in Nuclear Medicine*. Springer London.

110. Wueller, D. 2006. Evaluating digital cameras. in *SPIE-IS&T Electronic Imaging*. SPIE.

111. International Organization for Standardization. *Technical Committee 42/Working Group 18: Electronic still picture imaging*. [Accessed on 09 May 2017]. Available from: https://www.iso.org/committee/48420.html.

112. Koren, N. 2006. The Imatest program: comparing cameras with different amounts of sharpening. in *Electronic Imaging 2006*. San Jose, California, United States.

113. Atkins, B. *Camera Lens Testing: Part 6 - Lens Testing for Resolution, Chromatic Aberration and Distortion*. [Accessed on 16 February 2017].

Available from: http://www.bobatkins.com/photography/technical/lens_sharpness.html.

114. Khalil, M.M., J.L. Tremoleda, T.B. Bayomy, and W. Gsell. 2011. Molecular SPECT Imaging: An Overview. *International Journal of Molecular Imaging,* **2011**.

115. Xie, B., M.A. Stammes, P.B. van Driel, L.J. Cruz, V.T. Knol-Blankevoort, *et al.* 2015. Necrosis avid near infrared fluorescent cyanines for imaging cell death and their use to monitor therapeutic efficacy in mouse tumor models. *Oncotarget,* **6**(36): 39036-49.

116. Vidal-Sicart, S., F.W. van Leeuwen, N.S. van den Berg, and R.A. Valdes Olmos. 2015. Fluorescent radiocolloids: are hybrid tracers the future for lymphatic mapping? *Eur J Nucl Med Mol Imaging,* **42**(11): 1627-30.

117. Bugby, S.L., J.E. Lees, and A.C. Perkins. 2017. Hybrid intraoperative imaging techniques in radioguided surgery: present clinical applications and future outlook. *Clinical and Translational Imaging,* **5**: 323–341.

118. de Jong, M., J. Essers, and W.M. van Weerden. 2014. Imaging preclinical tumour models: improving translational power. *Nat Rev Cancer,* **14**(7): 481-493.

119. de Kemp, R.A., F.H. Epstein, C. Catana, B.M.W. Tsui, and E.L. Ritman. 2010. Small-Animal Molecular Imaging Methods. *Journal of Nuclear Medicine,* **51**(Supplement 1): 18S-32S.

120. Mediso Medical Imaging Systems. *NanoScan SPECT Preclinical imaging system.* [Accessed on 3 September 2017]. Available from: http://www.mediso.com/uploaded/NSCSM_0816_web.pdf.

121. Mediso Medical Imaging Systems. *NanoScan PET Preclinical imaging system.* [Accessed on 3 September 2017]. Available from: http://www.mediso.com/uploaded/NPMPCB_0816_web.pdf.

122. van der Have, F., B. Vastenhouw, R.M. Ramakers, W. Branderhorst, J.O. Krah, *et al.* 2009. U-SPECT-II: An Ultra-High-Resolution Device for Molecular Small-Animal Imaging. *J Nucl Med,* **50**(4): 599-605.

123. Mediso USA. *nanoScan SPECT/CT.* [Accessed on 3 September 2017]. Available from: http://www.medisousa.com/preclinical/nanoscan/spect-ct.

124. Celentano, L., P. Laccetti, R. Liuzzi, G. Mettivier, M.C. Montesi, *et al.* 2003. Preliminary tests of a prototype system for optical and radionuclide imaging in small animals. *IEEE Transactions on Nuclear Science,* **50**(5): 1693-1701.

125. Autiero, M., L. Celentano, R. Cozzolino, P. Laccetti, M. Marotta, *et al.* 2005. Experimental study on in vivo optical and radionuclide imaging in small animals. *IEEE Transactions on Nuclear Science,* **52**(1): 205-209.

126. Kopelman, D., I. Blevis, G. Iosilevsky, O.A. Hatoum, A. Zaretzki, *et al.* 2007. Sentinel node detection in an animal study: Evaluation of a new portable gamma camera. *International Surgery,* **92**(3): 161-166.

127. Tsuchimochi, M., K. Hayama, M. Toyama, I. Sasagawa, and N. Tsubokawa. 2013. Dual-modality imaging with 99mTc and fluorescent indocyanine green

using surface-modified silica nanoparticles for biopsy of the sentinel lymph node: an animal study. *EJNMMI Res,* **3**(1): 33.

128. Alqahtani, M.S., J.E. Lees, S.L. Bugby, P. Samara-Ratna, A.H. Ng*, et al.* 2017. Design and implementation of a prototype head and neck phantom for the performance evaluation of gamma imaging systems. *EJNMMI Physics,* **4**(1): 19.

129. QRM Quality Assurance in Radiology and Medicine GmbH. *NEMA NU4 Micro-PET Image Quality Mouse Phantom.* [Accessed on 7 September 2017]. Available from: http://www.qrm.de/content/products/microct/micro-pet-iq.htm.

130. Data Spectrum Corporation. *Mini, Micro and Ultra Micro Phantoms, Inserts and Accessories.* [Accessed on 11 September 2017]. Available from: http://www.spect.com/products-micro.html.

131. University of Calgary. *Micro CT Laboratory.* [Accessed on 11 September 2017]. Available from: https://www.ucalgary.ca/microct/.

132. Segars, W.P., B.M.W. Tsui, E.C. Frey, G.A. Johnson, and S.S. Berr. 2004. Development of a 4-D digital mouse phantom for molecular imaging research. *Molecular Imaging and Biology,* **6**(3): 149-159.

133. Festjens, N., T. Vanden Berghe, and P. Vandenabeele. 2006. Necrosis, a well-orchestrated form of cell demise: Signalling cascades, important mediators and concomitant immune response. *Biochimica et Biophysica Acta (BBA) - Bioenergetics,* **1757**(9): 1371-1387.

134. Maiorano, E., M.M. Regan, G. Viale, M.G. Mastropasqua, M. Colleoni*, et al.* 2010. Prognostic and predictive impact of central necrosis and fibrosis in early breast cancer. Results from two International Breast Cancer Study Group randomized trials of chemoendocrine adjuvant therapy. *Breast cancer research and treatment,* **121**(1): 211-218.

135. Stammes, M.A., V.T. Knol-Blankevoort, L.J. Cruz, H.R.I.J. Feitsma, L. Mezzanotte*, et al.* 2016. Pre-clinical Evaluation of a Cyanine-Based SPECT Probe for Multimodal Tumor Necrosis Imaging. *Molecular Imaging and Biology*: 1-11.

136. Tremoleda, J.L., A. Kerton, and W. Gsell. 2012. Anaesthesia and physiological monitoring during in vivo imaging of laboratory rodents: considerations on experimental outcomes and animal welfare. *EJNMMI Research,* **2**(44).

137. Cancer Research UK. *Breast cancer statistics.* [Accessed on 26 July 2017]. Available from: http://www.cancerresearchuk.org/health-professional/cancer-statistics/statistics-by-cancer-type/breast-cancer.

138. Carlson, R.W., D.C. Allred, B.O. Anderson, H.J. Burstein, W.B. Carter*, et al.* 2009. Breast cancer. Clinical practice guidelines in oncology. *J Natl Compr Canc Netw,* **7**(2): 122-92.

139. Hack, T.F., L. Cohen, J. Katz, L.S. Robson, and P. Goss. 1999. Physical and psychological morbidity after axillary lymph node dissection for breast cancer. *J Clin Oncol,* **17**(1): 143-9.

140. Mansel, R.E., L. Fallowfield, M. Kissin, A. Goyal, R.G. Newcombe, *et al.* 2006. Randomized multicenter trial of sentinel node biopsy versus standard axillary treatment in operable breast cancer: The ALMANAC trial. *Journal of the National Cancer Institute,* **98**(9): 599-609.

141. Povoski, S.P., R.L. Neff, C.M. Mojzisik, D.M. O'Malley, G.H. Hinkle, *et al.* 2009. A comprehensive overview of radioguided surgery using gamma detection probe technology. *World Journal of Surgical Oncology,* **7**.

142. Vidal-Sicart, S. and R.A. Valdés Olmos. 2016. Synergism of SPECT/CT and portable gamma cameras for intraoperative sentinel lymph node biopsy in melanoma, breast cancer, and other malignancies. *Clinical and Translational Imaging,* **4**(5): 313-327.

143. International Atomic Energy Agency. 2015.Radiopharmaceuticals for Sentinel Lymph Node Detection: Status and Trends, in *IAEA Radioisotopes and Radiopharmaceuticals Series*. International Atomic Energy Agency: Vienna.

144. Giammarile, F., N. Alazraki, J.N. Aarsvold, R.A. Audisio, E. Glass, *et al.* 2013. The EANM and SNMMI practice guideline for lymphoscintigraphy and sentinel node localization in breast cancer. *Eur J Nucl Med Mol Imaging,* **40**(12): 1932-1947.

145. McCarter, M.D., H. Yeung, S. Yeh, J. Fey, P.I. Borgen, *et al.* 2001. Localization of the sentinel node in breast cancer: Identical results with same-day and day-before isotope injection. *Annals of Surgical Oncology,* **8**(8): 682-686.

146. van der Ent, F.W.C., R.A.M. Kengen, H.A.G. van der Pol, and A.G.M. Hoofwijk. 1999. Sentinel node biopsy in 70 unselected patients with breast cancer: increased feasibility by using 10 mCi radiocolloid in combination with a blue dye tracer. *Eur J Surg Oncol,* **25**(1): 24-29.

147. De Cicco, C., M. Cremonesi, A. Luini, M. Bartolomei, C. Grana, *et al.* 1998. Lymphoscintigraphy and radioguided biopsy of the sentinel axillary node in breast cancer. *Journal of Nuclear Medicine,* **39**(12): 2080-2084.

148. Mariani, G., L. Moresco, G. Viale, G. Villa, M. Bagnasco, *et al.* 2001. Radioguided Sentinel Lymph Node Biopsy in Breast Cancer Surgery*. *Journal of Nuclear Medicine,* **42**(8): 1198-1215.

149. Scopinaro, F., A. Tofani, G. di Santo, B. Di Pietro, A. Lombardi, *et al.* 2008. High-resolution, hand-held camera for sentinel-node detection. *Cancer Biotherapy and Radiopharmaceuticals,* **23**(1): 43-52.

150. Soluri, A., R. Massari, C. Trotta, A. Tofani, G. Di Santo, *et al.* 2006. Small field of view, high-resolution, portable gamma-camera for axillary sentinel node detection. *Nuclear Instruments & Methods in Physics Research Section A-Accelerators Spectrometers Detectors and Associated Equipment,* **569**(2): 273-276.

151. Wendler, T., K. Herrmann, A. Schnelzer, T. Lasser, J. Traub, *et al.* 2010. First demonstration of 3-D lymphatic mapping in breast cancer using freehand SPECT. *Eur J Nucl Med Mol Imaging,* **37**(8): 1452-1461.

152. Vidal-Sicart, S., P. Paredes, G. Zanon, J. Pahisa, S. Martinez-Roman, *et al.* 2010. Added Value of Intraoperative Real-Time Imaging in Searches for

Difficult-to-Locate Sentinel Nodes. *Journal of Nuclear Medicine,* **51**(8): 1219-1225.

153. Cady, B., M.D. Stone, J.G. Schuler, R. Thakur, M.A. Wanner, *et al.* 1996. The new era in breast cancer. Invasion, size, and nodal involvement dramatically decreasing as a result of mammographic screening. *Arch Surg,* **131**(3): 301-8.

154. Lovrics, P.J., S.D. Cornacchi, R. Vora, C.H. Goldsmith, and K. Kahnamoui. 2011. Systematic review of radioguided surgery for non-palpable breast cancer. *Eur J Surg Oncol,* **37**(5): 388-97.

155. Pleijhuis, R.G., M. Graafland, J. de Vries, J. Bart, J.S. de Jong, *et al.* 2009. Obtaining Adequate Surgical Margins in Breast-Conserving Therapy for Patients with Early-Stage Breast Cancer: Current Modalities and Future Directions. *Annals of Surgical Oncology,* **16**(10): 2717-2730.

156. Luini, A., S. Zurrida, V. Galimberti, and G. Paganelli. 1998. Radioguided Surgery of Occult Breast Lesions. *European Journal of Cancer,* **34**(1): 204-205.

157. Patel, A., S.J. Pain, P. Britton, R. Sinnatamby, R. Warren, *et al.* 2004. Radioguided occult lesion localisation (ROLL) and sentinel node biopsy for impalpable invasive breast cancer. *Eur J Surg Oncol,* **30**(9): 918-923.

158. Paredes, P., S. Vidal-Sicart, G. Zanon, N. Roe, S. Rubi, *et al.* 2008. Radioguided occult lesion localisation in breast cancer using an intraoperative portable gamma camera: first results. *Eur J Nucl Med Mol Imaging,* **35**(2): 230-235.

159. Bluemel, C., A. Cramer, C. Grossmann, G.W. Kajdi, U. Malzahn, *et al.* 2015. iROLL: does 3-D radioguided occult lesion localization improve surgical management in early-stage breast cancer? *Eur J Nucl Med Mol Imaging,* **42**(11): 1692-9.

160. Gray, R.J., C. Salud, K. Nguyen, E. Dauway, J. Friedland, *et al.* 2001. Randomized prospective evaluation of a novel technique for biopsy or lumpectomy of nonpalpable breast lesions: radioactive seed versus wire localization. *Ann Surg Oncol,* **8**(9): 711-5.

161. Arsenali, B., H.W.A.M.d. Jong, M.A. Viergever, D.B.M. Dickerscheid, C. Beijst, *et al.* 2015. Dual-head gamma camera system for intraoperative localization of radioactive seeds. *Physics in Medicine & Biology,* **60**(19): 7655.

162. van der Noordaa, M.E.M., K.E. Pengel, E. Groen, E. van Werkhoven, E.J.T. Rutgers, *et al.* 2015. The use of radioactive iodine-125 seed localization in patients with non-palpable breast cancer: A comparison with the radioguided occult lesion localization with 99m technetium. *Eur J Surg Oncol,* **41**(4): 553-558.

163. Goudreau, S.H., J.P. Joseph, and S.J. Seiler. 2015. Preoperative Radioactive Seed Localization for Nonpalpable Breast Lesions: Technique, Pitfalls, and Solutions. *RadioGraphics,* **35**(5): 1319-1334.

164. Pouw, B., L.J. der Veen, D. Hellingman, O.R. Brouwer, M.J. Peeters, *et al.* 2014. Feasibility of preoperative (125)I seed-guided tumoural tracer injection using freehand SPECT for sentinel lymph node mapping in non-palpable breast cancer. *EJNMMI Res,* **4**: 19.

165. Pouw, B., L.J. de Wit-van der Veen, F. van Duijnhoven, E.J. Rutgers, M.P. Stokkel*, et al.* 2016. Intraoperative 3D Navigation for Single or Multiple 125I-Seed Localization in Breast-Preserving Cancer Surgery. *Clin Nucl Med,* **41**(5): e216-20.

166. Britten, A., V.R. Newey, and R. Clarke. 2007. A computerized gamma probe simulator to train surgeons in the localization of sentinel nodes. *Nucl Med Commun,* **28**(3): 225-229.

167. Keshtgar, M.R.S., D.W. Chicken, W.A. Waddington, W. Raven, and P.J. Ell. 2005. A training simulator for sentinel node biopsy in breast cancer: a new standard. *Eur J Surg Oncol,* **31**(2): 134-140.

168. Leguevaque, P., S. Motton, F. Courbon, M. Ricard, I. Berry*, et al.* 2011. Evaluation of a trainer phantom in the learning phase of sentinel lymph node identification in breast cancer. *World J Surg,* **35**(5): 995-1001.

169. Krohn, T., F.A. Verburg, H. Brockmann, O.H. Winz, F.M. Mottaghy*, et al.* 2012. A phantom assessment of portable imaging and radio-guided surgery systems with technetium-99m and fluorine-18. *Nucl Med Commun,* **33**(5): 452-458.

170. Lees, J.E., D.J. Bassford, P.E. Blackshaw, and A.C. Perkins. 2010. Design and use of mini-phantoms for high resolution planar gamma cameras. *Applied Radiation and Isotopes,* **68**(12): 2448-2451.

171. Perkins, A.C., D. Clay, and S.C. Lawes. 2007. A simple low cost phantom for the quality control of SPECT cameras. *World Journal of Nuclear Medicine,* **6**(1): 35-39.

172. Uren, R.F., R.B. Howmangiles, J.F. Thompson, D. Malouf, G. Ramseystewart*, et al.* 1995. Mammary Lymphoscintigraphy in Breast-Cancer. *Journal of Nuclear Medicine,* **36**(10): 1775-1780.

173. Bosch, A.M., A.G. Kessels, G.L. Beets, J.D. Rupa, D. Koster*, et al.* 2003. Preoperative estimation of the pathological breast tumour size by physical examination, mammography and ultrasound: a prospective study on 105 invasive tumours. *Eur J Radiol,* **48**(3): 285-92.

174. Bellevre, D., C. Blanc Fournier, O. Switsers, A.E. Dugue, C. Levy*, et al.* 2014. Staging the axilla in breast cancer patients with (18)F-FDG PET: how small are the metastases that we can detect with new generation clinical PET systems? *Eur J Nucl Med Mol Imaging,* **41**(6): 1103-12.

175. Tsushima, H., T. Takayama, H. Kizu, T. Yamanaga, Y. Shimonishi*, et al.* 2007. Advantages of upright position imaging with medium-energy collimator for sentinel node lymphoscintigraphy in breast cancer patients. *Annals of Nuclear Medicine,* **21**(2): 123-128.

176. Rose, A. 1970. The visual process, in *Vision: Human and Electronic*, W. Low and M. Schieber. Springer US. 1-27.

177. Pouw, B., L.J. de Wit- van der Veen, M.P.M. Stokkel, C.E. Loo, M.-J.T.F.D. Vrancken Peeters*, et al.* 2015. Heading toward radioactive seed localization in non-palpable breast cancer surgery? A meta-analysis. *Journal of Surgical Oncology,* **111**(2): 185-191.

178.  Pieri, A., R. Milligan, A. Critchley, J. O'Donoghue, N. Sibal*, et al.* 2017. The introduction of radioactive seed localisation improves the oncological outcome of image guided breast conservation surgery. *Eur J Surg Oncol,* **43**(5): S12.

179.  Weber, G. *X-Ray attenuation & absorption calculator*. [Accessed on 10 August 2017]. Available from: http://web-docs.gsi.de/~stoe_exp/web_programs/x_ray_absorption/index.php.

180.  Pouw, B., I.M. van der Ploeg, S.H. Muller, R.A. Valdes Olmos, L.K. Janssen-Pinkse*, et al.* 2015. Simultaneous use of an (125)I-seed to guide tumour excision and (99m)Tc-nanocolloid for sentinel node biopsy in non-palpable breast-conserving surgery. *Eur J Surg Oncol,* **41**(1): 71-8.

181.  Garner, H.W., J.M. Bestic, J.J. Peterson, S. Attia, and D.E. Wessell. 2017. Preoperative radioactive seed localization of nonpalpable soft tissue masses: an established localization technique with a new application. *Skeletal Radiology,* **46**(2): 209-216.

182.  European Commission. *Medical devices*. [Accessed on 20 June 2017]. Available from: https://ec.europa.eu/growth/sectors/medical-devices/regulatory-framework_en.

183.  U.S. Food and Drug Administration. *Device Advice: Comprehensive Regulatory Assistance*. [Accessed on 20 June 2017]. Available from: https://www.fda.gov/MedicalDevices/DeviceRegulationandGuidance/default.htm.

184.  *The Medical Devices Regulations 2002*. [Accessed on 19 June 2017]. Available from: http://www.legislation.gov.uk/uksi/2002/618/introduction/made.

185.  British Standards Institution. *EN 60601 Medical Electrical Equipment and Systems*. [Accessed on 19 June 2017]. Available from: https://www.bsigroup.com/en-GB/medical-devices/our-services/en-60601/.

186.  British Standards Institution. *BS EN ISO 14971:2012 Medical devices. Application of risk management to medical devices*. [Accessed on 19 June 2017]. Available from: https://shop.bsigroup.com/ProductDetail/?pid=000000000030268035.

187.  British Standards Institution. *BS EN ISO 13485:2016 Medical devices. Quality management systems. Requirements for regulatory purposes*. [Accessed on 19 June 2017]. Available from: https://shop.bsigroup.com/ProductDetail?pid=000000000030353196.

188.  Medicines and Healthcare products Regulatory Agency. *Medical devices: conformity assessment and the CE mark*. [Accessed on 13 June 2017]. Available from: https://www.gov.uk/guidance/medical-devices-conformity-assessment-and-the-ce-mark#the-ce-marking.

189.  Sokole, E.B., A. Plachcinska, and A. Britten. 2010. Acceptance testing for nuclear medicine instrumentation. *Eur J Nucl Med Mol Imaging,* **37**(3): 672-681.

190.  *The Ionising Radiations Regulations 1999. SI 1999/3232*. [Accessed on 16 June 2017]. Available from: http://www.legislation.gov.uk/uksi/1999/3232/pdfs/uksi_19993232_en.pdf.

191. Association for the Advancement of Medical Instrumentation. *ANSI/AAMI HE75-2009: Human Factor Engineering-Design of Medical Devices*. [Accessed on 7 June 2017]. Available from: http://my.aami.org/aamiresources/previewfiles/HE75_1311_preview.pdf.

192. National Patient Safety Agency. Design for patient safety: user testing in the development of medical devices. [Accessed on 7 November 2014]. Available from: www.nrls.npsa.nhs.uk/design.

193. TheAverageBody.com. *Average Hand*. [Accessed on 16 June 2017]. Available from: http://www.theaveragebody.com/average_hand_size.php.

194. Canadian Centre for Occupational Health & Safety. *Hand Tool Ergonomics - Tool Design*. [Accessed on 19 September 2017]. Available from: https://www.ccohs.ca/oshanswers/ergonomics/handtools/tooldesign.html.

195. Sarkar, S., M.A. Oghabian, I. Mohammadi, A. Mohammadpour, and A. Rahmim. 2007. A linogram/sinogram cross-correlation method for motion correction in planar and SPECT imaging. *IEEE Transactions on Nuclear Science,* **54**(1): 71-79.

196. Darwesh, R., D. Clay, P.D. Hay, C. Kalirai, H. Rassoulian*, et al.* 2013. A three dimensional drive system for use with fillable emission phantoms for SPECT and PET imaging. *Phys Med,* **29**(6): 695-700.

197. van Dalen, J.A., W.V. Vogel, F.H.M. Corstens, and W.J.G. Oyen. 2007. Multi-modality nuclear medicine imaging: artefacts, pitfalls and recommendations. *Cancer Imaging,* **7**(1): 77-83.

198. Schmidlin, P. 1975. Development and comparison of computer methods for organ motion correction in scintigraphy. *Phys Med Biol,* **20**(3): 465-76.

199. Morgan, P. and R.W. Barber. 1992. Motion correction in 'static' scintigraphy. *Nucl Med Commun,* **13**(4): 246.

200. Administration of Radioactive Substances Advisory Committee. Notes for Guidance on the Clinical Administration of Radiopharmaceuticals and Use of Sealed Radioactive Sources. [Accessed on 30 May 2016]. Available from: https://www.gov.uk/government/uploads/system/uploads/attachment_data/file/492127/ARSAC_NfG_2016.pdf.

201. Parker, H.L., E. Tucker, E. Blackshaw, C.L. Hoad, L. Marciani*, et al.* Clinical assessment of gastric emptying and sensory function utilizing gamma scintigraphy: Establishment of reference intervals for the liquid and solid components of the Nottingham test meal in healthy subjects. *Neurogastroenterology & Motility*: e13122.

202. National Institute for Health and Clinical Excellence. Diagnostics Assessment Programme: SeHCAT (tauroselcholic [75selenium] acid) for the investigation of diarrhoea due to bile acid malabsorption: final scope. [Accessed on 18 July 2017]. Available from: https://www.nice.org.uk/guidance/dg7/documents/sehcat-final-scope2.

203. Dengel, L.T., M.J. More, P.G. Judy, G.R. Petroni, M.E. Smolkin*, et al.* 2011. Intraoperative Imaging Guidance for Sentinel Node Biopsy in Melanoma Using a Mobile Gamma Camera. *Annals of surgery,* **253**(4): 774-778.

204. Ng, A.H., D. Clay, P.E. Blackshaw, S.L. Bugby, P.S. Morgan*, et al.* 2015. Assessment of the performance of small field of view gamma cameras for sentinel node imaging. *Nucl Med Commun,* **36**(11): 1134-42.

205. Alqahtani, M.S., J.E. Lees, S.L. Bugby, L.K. Jambi, and A.C. Perkins. 2015. Lymphoscintigraphic imaging study for quantitative evaluation of a small field of view (SFOV) gamma camera. *Journal of Instrumentation,* **10**.

206. Society of Nuclear Medicine. *Society of Nuclear Medicine Procedure Guideline for Thyroid Scintigraphy V3.0.* [Accessed on 25 August 2017]. Available from: http://snmmi.files.cms-plus.com/docs/Thyroid_Scintigraphy_V3.pdf.

207. Bricou, A., M.A. Duval, Y. Charon, and E. Barranger. 2013. Mobile gamma cameras in breast cancer care - a review. *Eur J Surg Oncol,* **39**(5): 409-16.

208. Garbay, J., M. Ricard, J. Lumbroso, F. Rimareix, C. Uzan*, et al.* 2009. A new hand-held gamma camera for sentinel node detection in breast cancer. The Minicam experience in 50 cases. *Cancer Research,* **69**(2 Supplement): 1021.

209. Soluri, A., C. Trotta, F. Scopinaro, A. Tofani, C. D'Alessandria*, et al.* 2007. Radioisotope guided surgery with imaging probe, a hand-held high-resolution gamma camera. *Nuclear Instruments & Methods in Physics Research Section A-Accelerators Spectrometers Detectors and Associated Equipment,* **583**(2-3): 366-371.

210. van den Berg, N.S., O.R. Brouwer, B.E. Schaafsma, H.M. Matheron, W.M. Klop*, et al.* 2015. Multimodal Surgical Guidance during Sentinel Node Biopsy for Melanoma: Combined Gamma Tracing and Fluorescence Imaging of the Sentinel Node through Use of the Hybrid Tracer Indocyanine Green-(99m)Tc-Nanocolloid. *Radiology,* **275**(2): 521-9.

211. Brouwer, O.R., W.M.C. Klop, T. Buckle, L. Vermeeren, M.W.M. van den Brekel*, et al.* 2012. Feasibility of Sentinel Node Biopsy in Head and Neck Melanoma Using a Hybrid Radioactive and Fluorescent Tracer. *Annals of Surgical Oncology,* **19**(6): 1988-1994.

212. Ortega, J., J. Ferrer-Rebolleda, N. Cassinello, and S. Lledo. 2007. Potential role of a new hand-held miniature gamma camera in performing minimally invasive parathyroidectomy. *Eur J Nucl Med Mol Imaging,* **34**(2): 165-9.

213. Langford, J., P. Kemp, L. Bolt, S. Hoffmann, and J. Fleming. 2003. 55. DaTSCAN$^{TM}$: can a planar vertex view be of any use? *Nucl Med Commun,* **24**(4): 462.

214. Darcourt, J., J. Booij, K. Tatsch, A. Varrone, T. Vander Borght*, et al.* 2010. EANM procedure guidelines for brain neurotransmission SPECT using (123)I-labelled dopamine transporter ligands, version 2. *Eur J Nucl Med Mol Imaging,* **37**(2): 443-50.

215. British Nuclear Medicine Society. *Lymphoscintigraphy.* [Accessed on 27 August 2017]. Available from: https://www.bnms.org.uk/images/Lymphoscintigraphy_2016_NEW.pdf.

216. British Nuclear Medicine Society. *Lacrimal Scintigraphy.* [Accessed on 25 August 2017]. Available from: https://www.bnms.org.uk/images/Lacrimal_Scintigraphy_2016.pdf.

217. Van den Wyngaert, T., K. Strobel, W.U. Kampen, T. Kuwert, W. van der Bruggen*, et al.* 2016. The EANM practice guidelines for bone scintigraphy. *Eur J Nucl Med Mol Imaging,* **43**: 1723-1738.

218. Society of Nuclear Medicine. *Society of Nuclear Medicine Procedure Guidelinefor $^{99m}Tc$-Exametazime (HMPAO)-Labeled Leukocyte Scintigraphy for Suspected Infection/Inflammation*. [Accessed on 27 August 2017]. Available from: http://snmmi.files.cms-plus.com/docs/HMPAO_v3.pdf.

219. Peersman, G., R. Laskin, J. Davis, M.G. Peterson, and T. Richart. 2006. Prolonged Operative Time Correlates with Increased Infection Rate After Total Knee Arthroplasty. *HSS Journal,* **2**(1): 70-72.

220. Rogulski, M.M., H.B. Barber, H.H. Barrett, R.L. Shoemaker, and J.M. Woolfenden. 1993. Ultra-high-resolution brain SPECT imaging: simulation results. *IEEE Transactions on Nuclear Science,* **40**(4): 1123-1129.

221. Goorden, M.C., M.C. Rentmeester, and F.J. Beekman. 2009. Theoretical analysis of full-ring multi-pinhole brain SPECT. *Phys Med Biol,* **54**(21): 6593-610.

222. Beekman, F.J., F. van der Have, B. Vastenhouw, A.J. van der Linden, P.P. van Rijk*, et al.* 2005. U-SPECT-I: a novel system for submillimeter-resolution tomography with radiolabeled molecules in mice. *J Nucl Med,* **46**(7): 1194-200.

*"If I have seen further than others,*

*it is by standing upon the shoulders of giants."*

*-    Sir Isaac Newton*